Fall 2011

Phase-field simulation of dendritic growth under externally applied deformation

Masashi Yamaguchi
University of Iowa

PHASE-FIELD SIMULATION OF DENDRITIC GROWTH UNDER EXTERNALLY APPLIED DEFORMATION

by

Masashi Yamaguchi

An Abstract

Of a thesis submitted in partial fulfillment
of the requirements for the Doctor of
Philosophy degree in Mechanical Engineering
in the Graduate College of
The University of Iowa

December 2011

Thesis Supervisor: Professor Christoph Beckermann

ABSTRACT

Defects, i.e. hot tears, macrosegragation, and pores, formed in metal castings are a result of stresses and strains in the solid-liquid mushy zone. Numerical simulation of solidification of deforming dendrite crystal promises to improve insight into the mechanical behavior of mushy zones under an applied load. The primary goal of this thesis is to develop numerical methodologies for performing solidification simulation of deforming dendrites. Such simulation encounters difficulties associated with the interface dynamics due to phase change or interaction among the dendrites, and large visco-plastic deformation applied to them. Phase-field simulation of dendritic solidification is promising for the treatment of the complex interface dynamics. Free energy based formulation allows the model to incorporate bridging and wetting phenomena occurring at grain boundaries through an extra energy term which arises from a mismatch of the crystallographic orientation. The particle method would be attractive to handle large inelastic deformation without suffering mesh entanglement. In order to investigate the effect of solid deformations on the evolving microstructure, the material point method with elasto-visco-plasticity constitutive model is developed to couple to a phase-field model of solidification. The changes in the crystallographic orientation of a growing dendrite crystal due to solid deformation are carefully accounted for through the coupling methodology. The developed numerical framework is applicable to the simulation for single and multiple crystals, and is capable of handling complex morphological change. The wide variety of validations and practical problems solved in this thesis demonstrates the capability of investigating deformation behavior of growing crystals.

Abstract Approved: _____
Thesis Supervisor

_____
Title and Department

_____
Date

PHASE-FIELD SIMULATION OF DENDRITIC GROWTH UNDER EXTERNALLY APPLIED DEFORMATION

by

Masashi Yamaguchi

A thesis submitted in partial fulfillment
of the requirements for the Doctor of
Philosophy degree in Mechanical Engineering
in the Graduate College of
The University of Iowa

December 2011

Thesis Supervisor: Professor Christoph Beckermann

Graduate College
The University of Iowa
Iowa City, Iowa

CERTIFICATE OF APPROVAL

_____

PH.D. THESIS

_____

This is to certify that the Ph.D. thesis of

Masashi Yamaguchi

has been approved by the Examining Committee
for the thesis requirement for the Doctor of Philosophy
degree in Mechanical Engineering at the December 2011 graduation.

Thesis Committee: _____
Christoph Beckermann, Thesis Supervisor

_____
Jia Lu

_____
Colby Swan

_____
H.S. Udaykumar

_____
Olesya I. Zhupanska

ACKNOWLEDGEMENTS

It is a pleasure to thank those who made this thesis possible. First, I would like to express my deepest gratitude to my thesis supervisor, Prof. C. Beckermann, whose persistent encouragement and precise guidance enabled me to develop a deep understanding of the subject. This thesis would not have been possible without helps by my thesis committees in terms of understandings of interfacial dynamics and solid mechanics.

I would also like to extend my gratitude to Dr. R. Hardin and Dr. K. Carlson to provide prompt computational setup, fixation, the noteworthy advices and a lot of encouragements. I am indebted to many of my colleagues in the solidification laboratory in the University of Iowa to support and help me a lot for conducting research. I would like to thank the staff members of the Department of Mechanical Engineering and Computer Systems Support for their help and offering comfortable research environment.

I would also like to show my gratitude to Donald and Linda Palmer for their persistent care about our personal life, and it leads this thesis to a successful conclusion.

I also owe my deepest gratitude to Bridgestone Corporation for offering and supporting this precious opportunity to brush up my skills.

Finally, special thanks goes to my wife Ayako, my son Hinata and all my family for their unconditional support. Their continuous encouragement provided me a lot of motivations and energy source to overcome difficulties associated with a course of this thesis.

TABLE OF CONTENTS

LIST OF TABLES

Table

LIST OF FIGURES

Figure

LIST OF SYMBOLS

a	Depth of double-well potential (unit is energy)
α	Crystallographic orientation
$\vec{b}$	Body force vector
β	Kinetic coefficient
C	Some constant (no specific use)
$\boldsymbol{C_0}$	The fourth order elasticity tensor
c_p	Specific heat under constant pressure
c_{solid}	Speed of sound in the solid matter
d	Capillary length
d_x, d_y	Displacement in x and y direction
$d\lambda$	Plastic multiplier
δ_{ij}	Dirac delta function
D	Thermal diffusivity
Δt	Time increment
Δx,Δy	Spatial increment in x and y direction
e or e_{ij}	Deviatoric strain tensor
ε or ε_{ij}	Strain tensor
ε_0	Strength of anisotropy
ε_ϕ	Coefficient for gradient of phase-field in polycrystalline model
E	Young's modulus
$f(\phi,\theta)$	Double-well potential
f_Y	Yielding function
$F(\phi,\theta,\alpha)$	Free energy
$g(\phi)$	Monotonically increasing function with respect to ϕ
γ	Consistency parameter

γ_{lim}	Cut-off value used in cut-off inverse function
G	Shear modulus
H	Height
$h(\phi)$	Monotonically increasing function with respect to ψ
η	Coefficient on diffusion term of an orientation evolution equation
η_{visc}	Viscosity coefficient of Perzyna type visco-plasticity model
I	The second momentum of area
$j(\phi)$	Monotonically increasing function with respect to ψ
J_2	The second principal invariants of the deviatoric part of the Cauchy stress
κ	Interface curvature
K	Bulk modulus
l_p	Side length of material point (initial length is defined by l_{px0} and l_{py0} in x and y direction, respectively)
λ	Coupling coefficient between ϕ and θ
L	Length
L_f	Latent heat of fusion per unit volume
L_1, L_2	Norms
n	Normal distance to the interface
n_p	The number of material point in one direction within a background cell (n_p=2 is typically used in this thesis)
$\mathbf{n}$	Unit normal tensor to yield surface in **s** space
$\vec{n}$	Unit normal vector to the interface
v	Poisson's ratio
P	Coefficient on relaxation time in orientation evolution equation
P_l	Load
ϕ	Phase-field in the range of $-1 \leq \phi \leq 1$

ψ	Phase-field in the range of $0 \le \psi \le 1$
$\varphi = \tan^{-1}(\phi_y/\phi_x)$	Angle between fixed frame, i.e. x coordinate axis and $\vec{n}$
$\theta = (T-T_m)/(L/c_p)$	Dimensionless temperature
Q	Coefficient on relaxation time in phase-field equation (polycrystalline model)
q	Conserved noise term
R	Radial distance
ρ	Density
s and l of suffixes	s=solid, l=liquid
s or s_{ij}	Deviatoric part of the Cauchy stress
$\overline{S_{vp}}, \overline{\nabla S_{vp}}$	Weighted shape function and its gradient
σ or σ_{ij}	Cauchy stress tensor
σ_Y	Yield stress
t	Time
τ	Relaxation time
τ_p	Pseudo time
τ_{visc}	Relaxation time of Perzyna type visco-plasticity model
T	Temperature
T_m	Melting temperature
T_p	Time period
$\vec{v}_{ext}$	Velocity of external field
$\vec{v}_{grid}$	Grid velocity
v_{i}	Normal velocity to the interface
$\vec{v}_{liquid}$, $\vec{v}_{solid}$	Velocity of liquid and solid phase, respectively
V_{p}	Volume of material point
W	Interface thickness
ω or ω_{ij}	Spin tensor

Ω	Domain
Ω_p	Support domain of material point
x, y	Coordinates
ξ	Anisotropy
$\chi_p(\boldsymbol{x})$	Particle characteristic function
ζ	Non-conserved noise term
$\mathbf{1}$	The second order identity tensor
$<x> = (x+\|x\|)/2$	The Macaulay brackets
$<\bullet>$	Mean average value

CHAPTER 1

INTRODUCTION

1.1 Background and Motivation

Metal casting is a well-established manufacturing process to produce complexly shaped metalwares by utilizing solidification from liquid melt in a single operation. A recognized disadvantage of the process is formation of defects. Most of the defects are a result of solidification process. Porosities and hot tears are considered to be some of the most severe defects and may preclude applying castings to metal products which require high reliability or integrity, for example a suspension arm of an automobile. The main cause of the defect formation is a deformation in the mushy zone by various external loading during casting process, i.e. contact force applied by rolls in continuous casting and pressure casting, and a volume change associated with phase change [1]. Mechanical response and feeding of liquid melt in mushy zone influences the defect formation.

Mushy zones are characterized by partially solidified regions, and the structure is intermediate between microstructure and grain-scale macrostructure. Grain-scale macrostructure is a result of the following series of microstructure evolution. (i) Solid seeds randomly created in the liquid melt freely and evolve their morphologies, i.e. equiaxed or columnar dendrite structures, until impingements on one another occur. (ii) A coherent network is formed among dendrite structures. The network can become interlocked, and it begins to have mechanical strength. (iii) Liquid melt trapped inside the solid skeleton solidifies with the forming grain boundaries. In terms of mechanical response, the morphology of the solid evolved in the process of (i) is significant because it strongly affects on interlocking property in the process of (ii). A network of dendrites is interlocked at a relatively low solid fraction while a network of spheroidal or globular grains must have a higher solid fraction than dendritic network to have the same mechanical strength [2]. Deformation applied to the microstructure also has a significant

effect on the microstructure evolution. Figure 1. 1 (a)-(b) shows snapshots of preliminary experiments examining deformation of dendrite arms in the mushy zone by applied load which were performed at the University of Iowa's solidification laboratory. Two horizontally extended dendrite arms in succinonitril-3%water alloy are pushed in the horizontal direction. As indicated by an arrow in Figure 1. 1 (b), a bridging of side branches is observed. Complex phenomena taking place at the contact area, such as the formation and breakage of bridging, sliding motion among branches etc., would lead the microstructure change. Pores are formed in the process of (iii). Density change associated with phase change [3] or contraction/expansion of solid due to applied deformation [4] induces fluid flow to the part through a porous solid network. A lack of feeding of liquid melt to the part is a main cause of the formation of pores. Residual stress associated with rapid cooling or non-isothermal distribution causes dilatation of solid and leads a formation of hot tears. Shear deformation in mush during continuous casting is said to be one of the causes of macrosegregation, whose formation is strongly dependent on a relative velocity of liquid with respect to solid [5]. The deformation in mushy zones is strongly related to the formation of defects from various aspects.

Based on the above discussion, a numerical prediction of mushy zone deformation in the evolving microstructure scale should provide innovative insights to improve an existing casting process from the standpoint of the management of defect formation. Morphological change under applied deformation is one of the challenging aspects of the problem. A formation of bridges among branches and coarsening grains are determined by interfacial energy associated with crystallographic orientation mismatch among them. An approach with energetic considerations is necessary. Deformation of evolving microstructure is another challenging task. A breakage of the bridges and fragments of dendrite arms are a result of deformation applied to the parts, and it, in turn, affects the microstructure change. The solid itself behaves as elasto-visco plastic material at high temperatures, and possibly causes large deformation. A numerical method which handles

large deformation with evolving microstructure is essential. State-of-art numerical methodology designed to simulate the complex coupling phenomena would cover the limitations of experimental investigation in terms of resolution of time and length scale.

1.2 Literature Review

A brief overview of experimental and numerical work regarding mush zone/semi-solid deformation is described in this section.

1.2.1 Experimental investigations of mushy zone/semi-solid under deformation

Flemings [2] performs a series of experiments on alloy semi-solids in order to investigate a wide variety of topics, i.e. crystallization, ripening, interdendritic flow, and solid motion etc. One of the major experimental findings is a morphological change of the solid due to applied deformation. Higher shear rate results in more spheroidal microstructure than dendritic microstructure as shown in Figure 1. 2. This, in turn, affects on the mechanical strength of the material. For instance, shear strength of a dendritic microstructure is three orders of magnitude larger than that of a spheroidal microstructure at the early stage of microstructure evolution, i.e. when the solid fraction is 0.4. Contacts among crystals have an important role on generating shear stress against shear strain. When the fraction of solid is less than 0.9, deformation of the solid is mainly caused by grain-boundary sliding.

Recent advances in technology make it possible to visualize and analyze dynamic solidification processes in a microstructural scale. Billia et al. [6] employ in-situ and real time investigations of solidification dynamics with X-ray radiography. Dynamic morphological change of dendrites of aluminum alloy under the gravitational force is successfully captured. One fascinating result of their work is a bending of secondary dendrite arm caused by two precipitating equiaxed dendrite crystals (indicated by 1and 2 in Figure 1. 3). Reinhart et al. [7] demonstrates a similar experiment to Billa's work, and

showed that the stress caused by bending acting on the thin neck part where a secondary arm attaches to a primary arm is estimated by measuring bending angle. They conclude that a sudden and irrecoverable rotation of the secondary dendrite arm is caused by yielding at the thin neck due to stress concentration. Moreover, the mechanical response of the solid itself shows strain rate dependency (i.e. [8]). In-situ observations of the deformation behavior of a semi-solid Al-Cu alloy with the X-ray microtomography employed by Terzi et al. [9] show that the deformation in the semi-solid is highly inhomogeneous. The inhomogeneity is an important characteristic of semi-solid material with an applied deformation and is due to a different mechanical response of solid and liquid phases. Motion of liquid melt induced by solid contraction/expansion is also ascertained by the observation and a formation of pores is clearly shown to be a result of a lack of liquid feeding.

As a summary, the experimental investigations mentioned in above indicate the following:

(1) Mutual interaction between microstructure change and stress field through mechanical response of the solid network.
(2) Mechanical response of the solid itself follows elasto-visco-plastic material law.
(3) Fragmentation of dendrite arms arises from stress/strain localization associated with morphology of the solid structure.
(4) Deformation of the solid phase affects the formation of pores through the formation of void space and an induction of fluid flow.

Although the experimental facts listed above provide useful knowledge about the mushy zone/semi-solid under applied deformation, the measurement of various physical quantities, i.e. stress, strain, velocity, temperature etc., in a microscopic scale still have limitations. Complete control of experimental conditions, i.e. a control of nucleation of multiple seeds, is nearly impossible. Numerical methodology of the system can be essential to clarify the detailed mechanisms which explain the experimental results.

1.2.2 Numerical modeling of the mushy zone/semi-solid under deformation

1.2.2.1 Averaging model approach

Some numerical methodologies to investigate a mechanical response of mushy zone/semi-solid have been developed by researchers. One approach is based on an averaging model. Lalli [10] employs numerical analysis with averaged continuity and momentum equations based on a two phase model. The mushy zone is modeled as a mixture of regularly allocated globular grains and fluid in a unit cell. Mechanical equilibrium equations with a plasticity constitutive model are applied to compute the stress distribution within the solid phase while fluid flow is calculated based on D'Arcy's law. A one-dimensional axisymmetric compression simulation provides liquid fraction and stress distribution to evaluate the severity of segregation within the material. Monroe [11] introduces the effects of thermally induced strain and visco-plastic strain to the mechanical equilibrium equation for porous solids in order to investigate the deformation of casting material during an actual process. The constitutive model used in his study (Cocks model) accounts for solid fraction, temperature dependency of material properties, strain rate, strain, and hardening effect, so the effect of coherency of the solid network is considered through solid fraction dependent mechanical response. All model parameters are determined experimentally, and the model gives a good prediction of hot tear formation.

Such models are inherently phenomenological because the characteristics of microstructure within a unit cell are averaged out. To recover the characteristics, several model parameters such as solid fraction dependent constitutive behavior have to be experimentally specified, and thus the model itself is strongly problem dependent.

1.2.2.2 Deformation analysis of microstructure

In the averaging model approach, the mechanical response depending on microstructure is consolidated to model parameters. An attempt to avoid the phenomenological treatment and to consider the actual physics at the micro-scale structure has been made by modeling an actual microstructure. The model developed by Phillion et al. [12] is composed of multiple grain structures with liquid and pores (three-phase model) illustrated in Figure 1. 4. The grains are generated by the Voronoi tessellation technique such that the solid fraction of the model corresponds to that obtained by experiments, thus the geometry of the model is arbitrarily defined. Liquid is simply assumed to be a perfectly plastic material with very low yield stress. A notable result of their FEM analysis is that strain localization in liquid degrades macroscopic mechanical properties, and the localization is strongly influenced by grain size and porosity. This indicates that grain sliding is the possible cause of microstructure-dependent mechanical response. This fact also implies that a property of bridging and coarsening at the grain boundary is an influential factor of macroscopic mechanical response.

The FEM model developed by Fuloria et al. [13] reproduces an actual three-dimensional dendrite captured by X-ray microtomography. The experimentally measured constitutive relation of Al-Cu alloys, which is a function of plastic strain, strain rate, temperature, flow stress, and solid fraction, is used in the model. A columnar dendritic structure is compressed up to 5% macroscopic strain for different solid fractions. Flow stress obtained from their simulation shows good correlation with experimental data. Some limitations of their FEM analysis are reported. Firstly, a numerical divergence associated with contact, i.e. interdendritic impingements, restricts a simulation of more than 5% compression. Stress/strain localization should be expected within complicated dendritic structure even if the applied displacement to the dendritic structure is small with

respect to macroscopic scale. A capability for handling large deformation and contact is required for a numerical methodology of solid deformation.

Both methodologies are well developed to examine the stress-state in microscopic scale structure. However, neither of them combine microstructure evolution due to phase change and relaxation process taking place at contact region among dendrites.

1.2.2.3 Numerical analysis of microstructure evolution

The solidification phenomenon is a so-called moving boundary problem and is inherently difficult to solve. Limiting our interest to pure substances, the solidification phenomenon is governed by the following equations.

$$\frac{\partial \theta}{\partial t} = D\nabla^2 \theta \tag{1.2.1}$$

$$v_i = D\left(\left.\frac{\partial \theta}{\partial n}\right|_S - \left.\frac{\partial \theta}{\partial n}\right|_L \right) \tag{1.2.2}$$

$$\theta_i = -d(\alpha)\kappa - \beta(\alpha)v_i \tag{1.2.3}$$

The first equation is the heat conduction equation which is valid in bulk solid and liquid phases. The term $\theta=(T-T_m)/(L_f/c_p)$ denotes the dimensionless temperature, and T, T_m, L_f and c_p are temperature, melting point of planer interface, latent heat of fusion and specific heat under constant pressure, respectively. The term D is the thermal diffusivity which is assumed to be identical in both solid and liquid phases in this thesis. The second equation is the Stefan condition. Motion of the solid-liquid interface is expressed as energy conservation at the interface under phase transformation. The term v_i denotes the normal component of the interfacial velocity and n is the direction normal to the interface. The subscripts S and L stand for solid and liquid phase, respectively. The third equation is the Gibbs-Thomson effect which defines the equilibrium temperature of the solid-liquid interface. The temperature is shifted as a function of the mean curvature κ of the

interface and interfacial velocity. The coefficients $d(\alpha)$and $\beta(\alpha)$ are the capillary length and the kinetic coefficient, and are dependent on the crystallographic orientation α.

Numerical methodology for the moving boundary problem is generally divided into two major categories. One is called the fixed grid method, and another is the front tracking method [14]. The former method allows the interface to pass through fixed meshes whereas in the latter method computational grids follow the motion of the interface directly, i.e. by adapting grids to the interface. In the fixed grid method, additional numerical treatments satisfy the interfacial boundary conditions exactly at the interface, i.e. eq.(1.2.2) and (1.2.3), are essential. The front tracking method often sufferes from mesh entanglement due to large deformation and the complex topology of the interface. In this thesis, the fixed grid method is adopted to compute the complex morphological change of dendritic structures.

The fixed grid method is sub-categorized into the sharp interface method (SIM) and the diffuse interface method. The interface is tracked as a sharp entity in the former method while the latter method treats the interface as steep but sufficiently smooth transition. In the SIM, solid and liquid phases are completely separated by the interface, and the problem becomes a free boundary problem. The interface tracking method, i.e. volume-of-fluid (VOF) method [15], and a method to impose interfacial boundary conditions exactly at the interface are necessary to find the location and the motion of the interface. The level-set method [16] is regarded as a highly successful interface tracking method. The interface is tracked as a sharp discontinuity throughout computation while re-initialization is necessary to pursue an accurate calculation result. The ghost fluid method [17] makes it easy to impose interfacial boundary conditions. However, an actual implementation of the interface tracking method and imposing interfacial conditions is not a trivial procedure.

1.2.2.3.1 Phase field simulation of solidification

The phase-field method has been a popular computational method that has successfully been applied to various solidification problems, i.e. dendritic solidification of pure substance [18-19], and eutectic solidification [20], in the last decade as one of the diffuse interface methods. The main feature of the method is an introduction of an order parameter ϕ which denotes the phase at given location and time, A phase of ϕ=-1 and ϕ=1 refer the bulk liquid and solid phase, respectively. The phase field varies smoothly from bulk solid to liquid within the diffuse interface, thus the phase is treated as "diffuse" rather than the "sharp" interface used in the usual sharp interface method. A free energy model of the system is constructed as a thermodynamically consistent function of ϕ and θ [21]. The time evolution of the phase-field is determined by the time dependent Ginzburg-Landau (TDGL) type equation which ensures that the total free energy of the system decreases with time, and is solved in a single computational domain. The interface is implicitly evolved without any special treatment, so tremendous efforts regarding to an interface tracking and assignment of interfacial conditions are avoided. This is the significant advantage of the phase-field method over the sharp interface method, and the method is chosen to simulate microstructure evolution in this thesis.

1.2.2.3.2 Phase-field simulation of solidification with stress evolution

Phase-field solidification simulation with the evolution of the stress field is employed by Uehara et al. [22]. Elastic strain energy and plastic dissipation energy are additionally considered to derive their governing equations. Phase-field, temperature, and mechanical equilibrium equations with an elasto-plastic constitutive model are solved by finite difference and finite element methods. Heat release due to plastic deformation, thermal stress, and phase transformation stress is included in their model. Stress concentration around thin neck part and residual stress evolution around interdendritic

impingement region are computed as shown in Figure 1. 6. Stress distribution depends on the morphology of the microstructure. In their work, the simulation is performed in the confined computational domain, i.e. no displacement and traction boundary conditions are imposed on mechanical equilibrium equation. Stress is only induced by volumetric contraction/expansion due to temperature change or phase transformation, so the effect of an applied load on evolving microstructure is not considered. Furthermore, a bridging and a coarsening process at the interdendritic impingement region are not included.

Powell et al. [23] combine the phase-field equation with a unified equation of motion for both liquid and solid phases in order to simulate fluid-structure interaction. Non-uniform solid motion is only limited in the range of elastic regime, and volumetric change of the solid is neglected. Since the phase-field model should be extended to handle solidification phenomenon, a simulation of microstructure evolution with deforming solid phase is possible. However, the constitutive model is not suitable for an actual metallic material in the elastic range and plastic flow in the large deformation range (the model assumes incompressibility of the material). The authors note a possibility of an extension of the model to elasto-plastic and elasto-visco-plastic constitutive behaviors, but an actual methodology for an extension is not indicated.

1.2.2.3.3. Phase-field solidification simulation of polycrystalline material

As mentioned in the preceding section, a relaxation process, i.e. a bridging or a coarsening, at the interdendritic or grain impingement region, is an important factor on the resulting microstructure and the mechanical response against an applied load to the structure. The process is dependent on interfacial energies associated with crystallographic orientation mismatch at the dendrite or grain impingement region. The smallest unit of structure of metallic materials is a crystal lattice, and the structure

represents favorable sites for atoms which minimizes energy of the system. Therefore, the crystallographic orientation is determined by the direction where an atom favorably binds to the existing structure, thus the direction of anisotropy in the phase-field model corresponds to the direction. When two grains have different crystallographic orientations and lie next to each other, the status is unfavorable for the system in terms of energy. Grain rotation, grain boundary migration, and the introduction of dislocation occur in order to minimize energy of the system. Therefore a complex morphological change associated with bridging, a coarsening of grains, and the formation of a (dry or wetting) grain boundary is observed.

A polycrystalline phase-field model which can treat grain boundary formation and the grain coarsening process is developed by Warren et al. [24]. An energy penalty due to orientation mismatch is introduced to their free energy function, and its form is designed such that a grain rotation and a grain boundary migration are possible. Grain wetting is incorporated as a balance among solid-liquid surface energy and grain boundary energy. The model needs some numerical treatments for an actual implementation, but an evolution of multiple crystals with the complex relaxation phenomena associated with grain boundary is successfully computed as shown in Figure 1. 7.

Although there are some other numerical models which can handle from a single dendrite growth to multiple grain formation as statistical mechanics based model, i.e. cellular automaton, this kind of method is less compatible in terms of coupling with a continuum based model, i.e. solid deformation analysis with FEM. The length scale intended in molecular dynamics and phase-field crystal method (i.e. [25]) is too small in terms of multiple grain scale. In this sense, the choice of phase-field method should be feasible in order to perform the solidification simulation in a range of the length scale.

In summary, some research concerning numerical methods for mushy zone deformation with or without microstructure evolution is presented. Points are listed in the following:

(1) The averaging model requires empirically determined model parameters in order to consider characteristics of a microstructure whose length scale is smaller than the unit cell used in the model.

(2) Deformation analyses with a model based on an actual microstructure have been performed by some researchers. However, none of the models have treated microstructure changes due to phase change under the applied deformation. A numerical issue associated with contact and large deformation should be kept in mind for a choice of numerical method.

(3) Simulations of microstructure evolution under stress field evolution

1.3 Scope of This Thesis

This thesis addresses the deformation of dendrite structures based on micro-scale physics. Situations where this research can be applied are inherent in a variety of casting processes. These issues have received almost no research attention in the past as stated in the preceding section. This thesis is aimed at obtaining fundamental knowledge of the mechanical behavior of dendritic microstructures in mushy zones under applied external loads through numerical investigation. The scale focus of this thesis is from the microscopic scale where the solid-liquid interfaces can be directly resolved to the scale where solidification of clusters of dendrites is observed. Therefore, this thesis is focused primarily on developing a direct numerical simulation method of microstructure evolution under externally applied deformation. The thesis topic should be a first attempt to develop a physics-based model for deformation of the mushy zones with the consideration of the microstructure. The methodology should advance the fundamental

understanding of mushy zone deformation and provide innovative insights to control the formation of defects in an existing casting process.

In order to accomplish these goals, a suitable coupling methodology among “solidification”, “solid deformation with proper crystallographic orientation treatment”, and has to be developed. The methodology should advance the fundamental understanding of mushy zone deformation and provide innovative insights to control the formation of defects.

For solidification phenomenon, complex evolution of the microstructure has to be accurately tracked. For this purpose, the development of a phase field model is pursued. Since the method is a potential tool to handle the simulation of grain boundary formation, the feature should consider the change of crystallographic orientation due to solid deformation.

For solid deformation, localization of the deformation within the dendritic structure needs to be addressed. In order to represent shear dependent material constitutive behavior against mechanical loading, an elasto-visco-plastic material model will be included. A numerical method which has capability of handling large deformation should be applied to this aim.

Specific targets of this thesis are the following:

1 To develop a phase field model of dendritic solidification under externally applied loading with the appropriate crystallographic orientation treatement

2 To develop a structural analysis model of the solid phase which has the capability of handling large deformations and elasto-visco-plastic material behavior

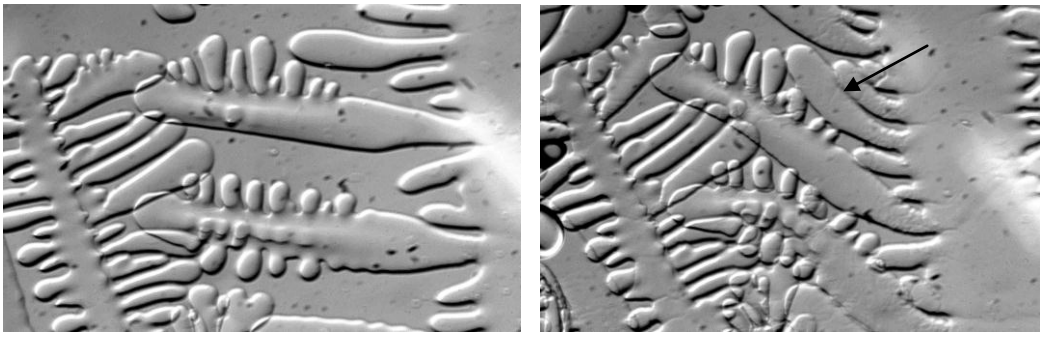

(a) (b)

Figure 1. 1 Experiments of the dendrite deformation under an applied load; two horizontally extended dendrite arms in a succinonitrile-3% water alloy are pushed in the horizontal direction; (a) before deformation; (b) after deformation.

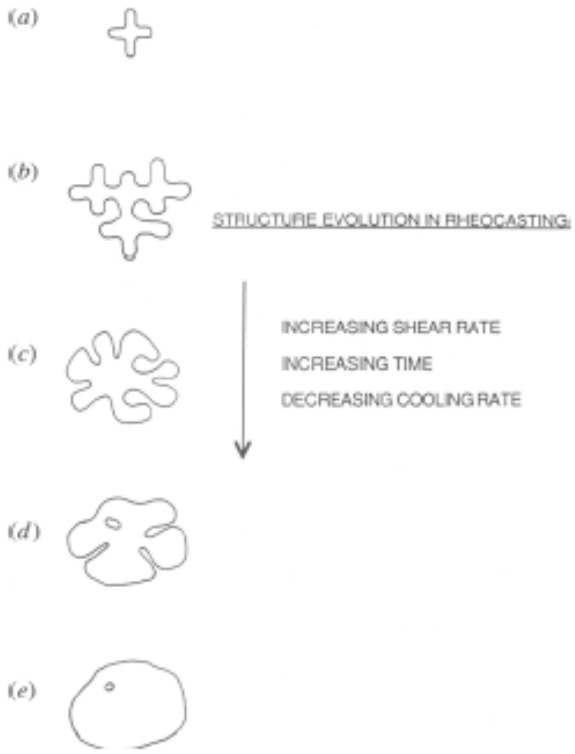

Figure 1. 2 Morphological change of solid body under applied shear.

Source: Flemings, M. *Metall. Mater. Trans.* **1991**, 22B, 269-293

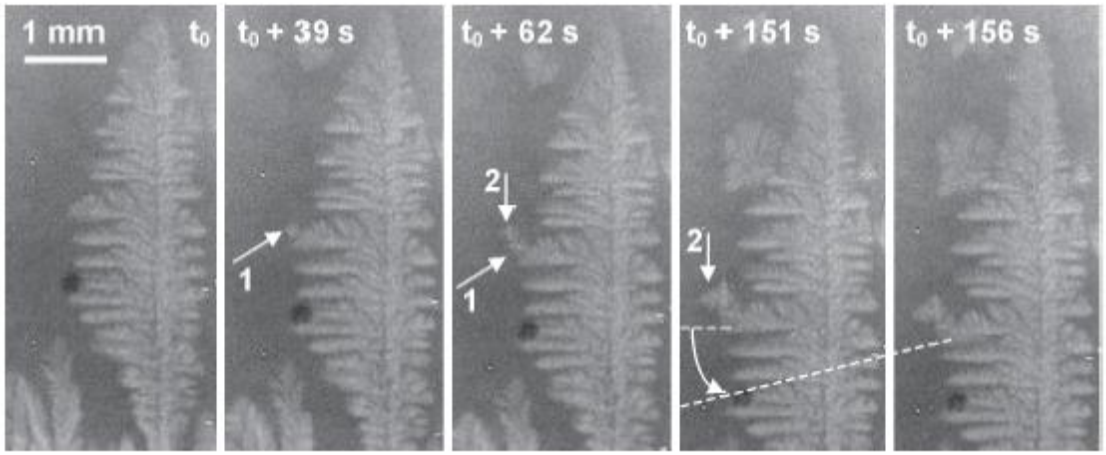

Figure 1. 3 A secondary arm bending due to two precipitating equiaxed dendrite crystals (indicated by 1 and 2).

Source: Billa, B. et al. *Trans. Indian Inst. Met.* **2007**, 60, 287-291

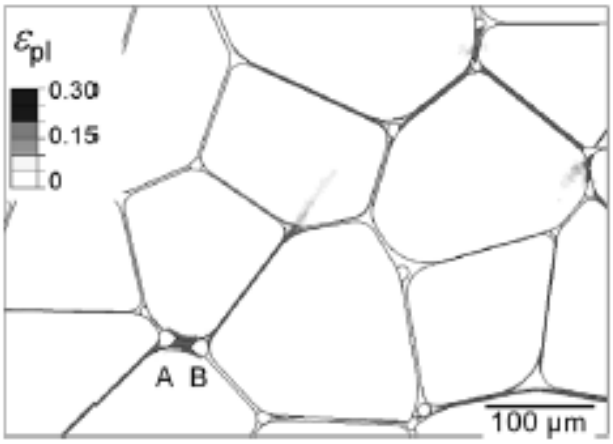

Figure 1. 4 Plastic strain contour obtained by FEM analysis with three phase model.

Source: Phillion, A.B. et al. *Acta Mater.* **2008**, 56, 4328-4338

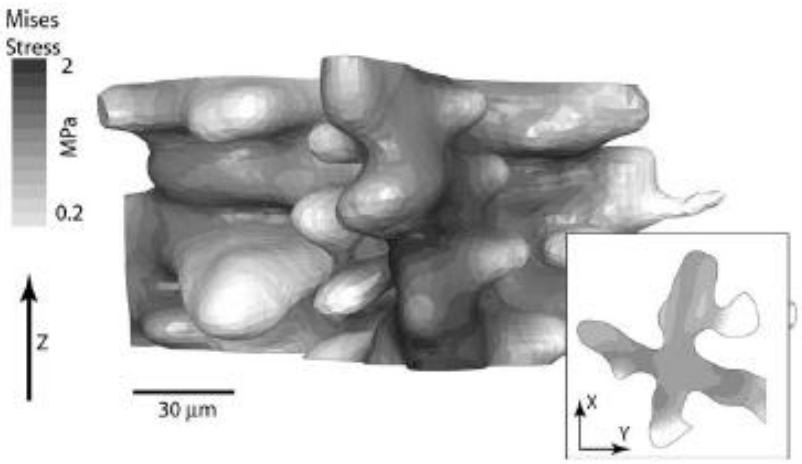

Figure 1. 5 Von Mises stress contour computed by FEM analysis with the model based on an actual dendritic microstructure captured by the X-ray microtomography.

Source: Fuloria, D.; Lee, P.D. *Acta Mater.* **2009**, 57, 5554-5562

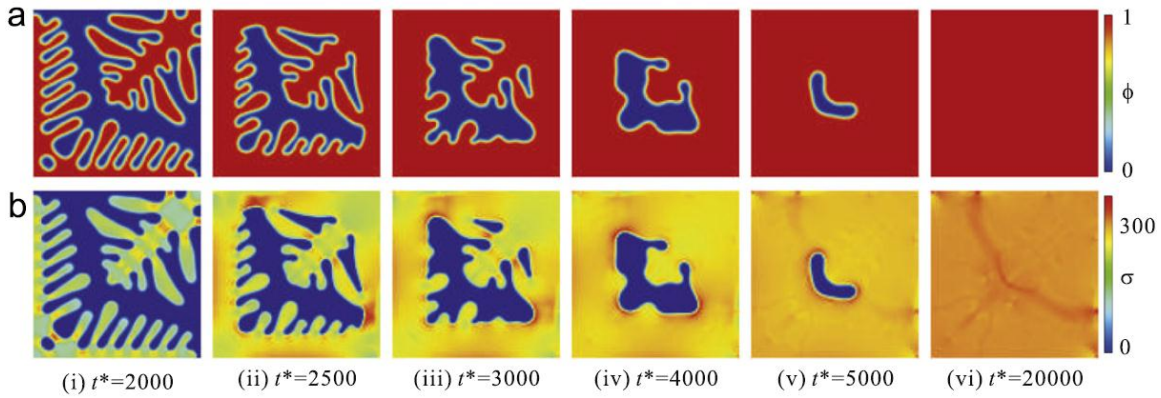

Figure 1. 6 A series of phase-field simulation of solidification coupled with stress/strain effect; (a) Phase-field and (b) Equivalent stress evolution

Source: Uehara, T. et al. *J. Cryst. Growth*. **2008**, 310, 1331-1336

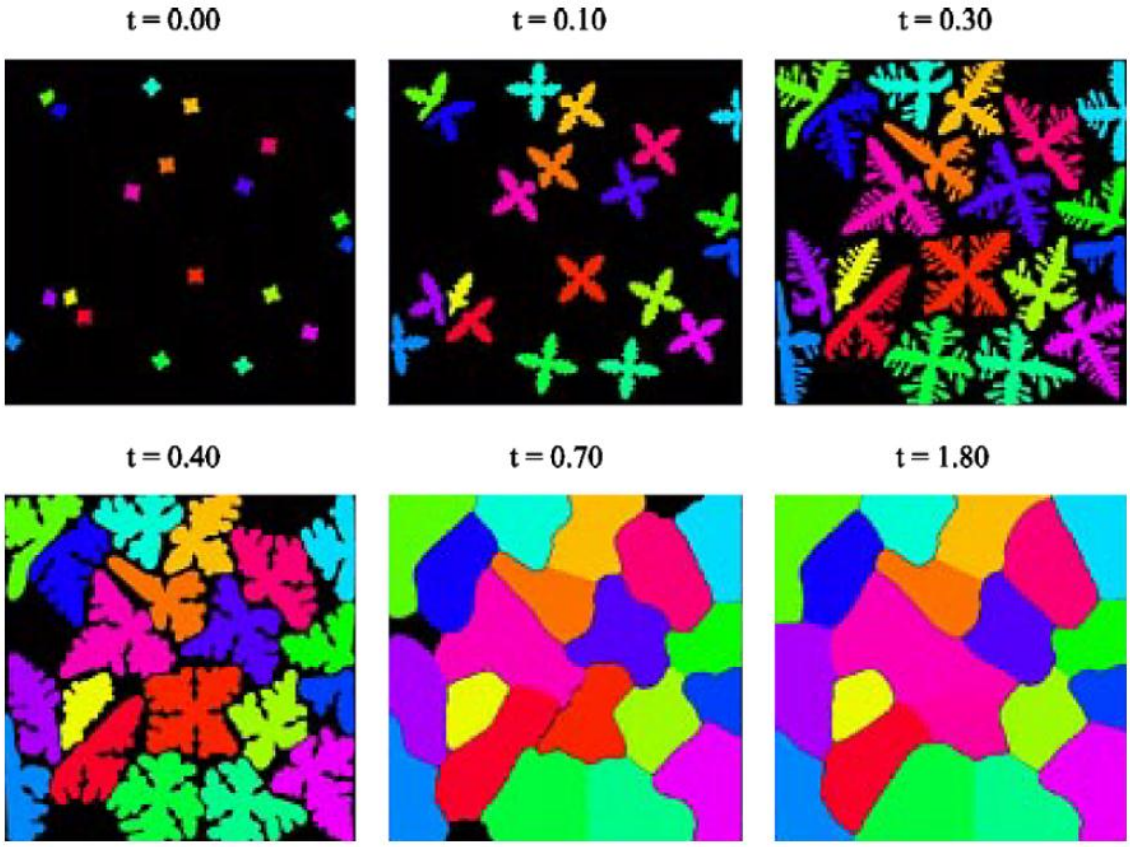

Figure 1. 7 A series of phase-field evolution (indicated by each dendrite or grain shape) and an evolution of crystallographic orientation (indicated by colors) employed by polycrystalline phase-field model.

Source: Warren J. A. et al. *Acta Mater*. **2003**,51,6035-6058

CHAPTER 2

METHODOLOGIES

Methodologies of numerical simulation of dendritic solidification with externally applied deformation are described in this section.

2.1 Strategy and Assumptions

As stated in the preceding introduction section, the major challenging aspects of dendritic solidification simulation with externally applied deformation are the following:

(1) Choice of the numerical method for dendritic solidification simulation and deformation simulation of the solid structure.
(2) Coupling methodology between the above two simulations with simplifications and assumptions.

The above topics are discussed in the following subsections.

2.1.1 Choice of numerical method

2.1.1.1 Dendritic solidification simulation

An evolution of the microstructure has to be correctly simulated by the methods presented in this thesis. Specifically, dendritic solidification of a single crystal and multiple grain formation as a result of impingements of the single crystals are of interest. Based on the discussion in chapter 1, a phase-field simulation of solidification should be a suitable choice to compute from single to multiple crystal growth. Thanks to the advantage of the phase-field method, tremendous work associated with interface tracking and imposing appropriate jump conditions at the interface are avoided. Instead, parameters in the model equations of the phase-field method have to be determined such that the result exactly replicates the result obtained by the sharp interface model. The

governing equations and determination procedure of the model parameters in the equations are presented in the later section.

2.1.1.2 Deformation analysis of solid structure

A complex stress distribution is expected within the structure due to (i) complicated solid morphology, (ii) interdendritic or grain impingements, and (iii) inelastic mechanical response of the solid material. The major requirements of a numerical method for solid deformation analysis are the following:

(1) Capability of handling large deformations and interdendritic/grain impingements.
(2) Easiness of reconstruction of the solid structure model during the sequence of computation.
(3) Inclusion of the elasto-visco-plasticity material model.

The finite element method (FEM) is a well-developed numerical method, and has been extensively applied to many kinds of problems in solid mechanics. However, the meshless method has also received considerable attention in the past decade as a tool to solve PDEs. Since the computation in the method relies on variables for material points as a representation of a solid body, the method naturally avoids mesh entanglement caused by the severe deformation observed in the usual mesh based FEM. Furthermore, the meshless method eliminates the cumbersome mesh construction process required in FEM which is basically due to rigid mesh connectivity. The meshless method has an attractive capability of handling repetitive solid model updates during a series of computations, and should be a suitable numerical method in terms of requirements (1)-(3) listed above.

Several kinds of meshless methods have been developed by researchers. The SPH (Smoothed Particle Hydrodynamics) method [26], the mesh-free Galerkin method [27], the vortex method [28], and the PIC (Particle-In-Cell) method [29] are some examples. In this thesis, the material point method (MPM) [30] is selected as a numerical

method for the solid deformation analysis. The MPM is originated from the PIC method, and has been applied to various problems such as deformation of composite material [31-32], compaction [33], fluid-structure interaction [34], fracture mechanics [35], geomechanics [36] etc. The main feature of the method is a usage of both Lagrangian and Eulerian descriptions. The solid body is represented by a collection of material points, and all of the information about the material properties and deformation history is tracked and held on the points (Lagrangian description). The equation of motion is solved by the aid of background grids which are typically fixed in space by mapping variables from the material points to the grid points. The grids are used as a computational scratch pad (Eulerian description). The method is free from the problem of mesh distortion while the deformation history is naturally delivered by material points. An insertion or relocation of material points should be relatively easier than a mesh based FEM. Mass and momentum conservation must be satisfied in the process. The use of Eulerian background cells also provides a better compatibility in terms of coupling with the other field variables which are governed by the Eulerian based equation as phase-field equation in this thesis.

At the initial stage of this research, the applicability of Lagrangian FEM (commercial FEM program ABAQUS and ANSYS) to our simulation methodology was examined. Nowadays, highly advanced mesh modification options, i.e. the arbitrary Lagrangian Eulerian method [37] and the adaptive meshing method [38], are available. These methods were applied to update our solid model associated with morphology change due to solidification. However, the modified solid model was typically composed of extremely fine elements due to the complexity of the morphology that occurs if the meshing criteria of commercial software are used, and often caused the termination of further computation. In order to specify own way of mesh modification, all meshing criteria should be implemented through the specific subroutines which are available in those software, which is a tremendous amout of work. Furthermore, inelastic material

behavior made the simulation more difficult. If a solid model is updated, the historical variables at Gaussian points on the updated model need to be specified as initial conditions for the further deformation analysis. In commercial software, a low order mapping method is used for the purpose, and iterative computation is performed such that the new stress state becomes consistent with the stress state before the model update. An updated model often was not available due to a convergence issue in the new stress state calculation process. As mentioned in chapter 1, contact analysis also presents difficulties. In the usual FEM analysis, the master and slave elements which represent a pair of contact elements should be defined for the contact analysis. Every time the solid model is updated, the elements must be found and determined automatically, and the code development is not trivial process. In terms of the solid model update and the stress determination process associated with the model update, the development of our own MPM code is decided. As we will discuss later, the calculation code is based on an explicit scheme, and no-slip contact is automatically satisfied. Those are also determining factors to select the MPM as a numerical method of solid deformation analysis.

2.1.2 Solution strategy and assumptions

Figure 2. 1 (a)-(b) show diagrams of the interactions among “phase-field”, “temperature”, and “solid stress field”. Figure 2. 1 (a) describes the case of full coupling among the fields while Figure 2. 1 (b) denotes the simplified coupling case applied to this thesis. Assumptions for the simplified coupling are described in the following subsections.

2.1.2.1 Phase-field – temperature field coupling

In the phase-field method, the free energy function of the system of concern is constructed. Basically, the free energy includes the information about two stable phases, i.e. solid and liquid in this thesis, described by the double-well potential and excess

surface energy. Since a stable phase is dependent on temperature, i.e. liquid phase is more stable than solid phase above melting point, the effect is considered through the introduction of a temperature dependent term for free energy (temperature → phase-field coupling).

Throughout this thesis, the densities of both solid and liquid phases are assumed to be equivalent. Under this assumption, a rate change of the phase field at an arbitrary spatial location denotes the rate change of solid mass created from liquid melt. As mentioned in chapter 1, the creation of solid mass due to phase change is accompanied by latent heat release. A source term for latent heat release is introduced to heat equation (phase-field → temperature coupling).

2.1.2.2 Phase-field – solid stress field coupling

Stress applied to the system of interest might induce phase transformation. However, it is mainly observed in solid-solid phase transformation, so the effect can be neglected. Instead, a change of solid shape is reflected in the solid model used in deformation analysis (phase-field → solid stress field coupling).

Solid stress may caused by phase change. The stress is induced by dilatation/contraction due to density change. As mentioned in the previous section, no density change due to phase change is assumed, and the effect is neglected. Alternatively, solid motion due to applied deformation is included as the advection velocity $\vec{v}_{solid}$ in the phase-field equation (solid stress field → phase-field coupling).

2.1.2.3 Temperature field – solid stress field

Thermal stress is induced by thermal expansion/contraction associated with a change of material properties due to temperature change or non-uniform temperature distribution within the solid structure. As pointed out by Dantzig and Rappaz [1], thermal stress is the major cause of hot tearing, but the effect is remarkable when the system is under rapid cooling, i.e. cooling from melting temperature to room temperature.

In this thesis, the solid phase is assumed to be held around the melting temperature and the thermal stress should be negligible. Heat generation associated with plastic deformation (dissipation) is not included this thesis. Instead, solid deformation is introduced as the advection velocity $\vec{v}_{solid}$ in the heat equation (solid stress field → phase-field coupling).

2.2 Equations

Equations used in dendritic solidification simulation with applied deformation are presented in the following subsections

2.2.1 Phase-field dendritic solidification simulation

Dendritic solidification of a pure substance is of interest in this thesis. The following non-conserved Allen-Cahn model given by Karma and Rappel [19] is solved as an evolution equation of phase-field ϕ.

$$\tau(\varphi)\left(\frac{\partial\phi}{\partial t}+\vec{v}_{ext}\cdot\nabla\phi\right)=\nabla\cdot\left[W^2(\varphi)\nabla\phi\right]-\frac{\partial F(\phi,\lambda u)}{\partial\phi}+\frac{\partial}{\partial x}\left[|\nabla\phi|^2W(\varphi)\frac{\partial W(\varphi)}{\partial\phi_x}\right]+\frac{\partial}{\partial y}\left[|\nabla\phi|^2W(\varphi)\frac{\partial W(\varphi)}{\partial\phi_y}\right] \quad (2.2.1)$$

where τ is a relaxation time (~10^{-10}[sec]), and W is an interface thickness. The term $F(\phi,\lambda\theta)=f(\phi)+\lambda\theta g(\phi)$ denotes the phenomenological bulk free energy. As mentioned in the previous section, "temperature θ → phase-field ϕ" coupling is considered by the $\theta g(\phi)$ term with a coupling parameter λ. A double-well potential $f(\phi)=-\phi^2/2+\phi^4/4$ is a typical choice to have two stable phases at ϕ=1 (solid) and ϕ=-1 (liquid), and an odd function $g(\phi)=\phi-2\phi^3/3+\phi^5/5$ is specified to represent a stable phase at given temperature θ. Anisotropy has an important role on the determination of the dendritic structure, and it reflects preferable growth directions. The effect is generally introduced through direction dependent parameters $\tau(\varphi)$ and $W(\varphi)$ in case no orientation

change during solidification is assumed. The term φ denotes the angle between the interface normal **n** and the fixed x-coordinate axis defined by

$$\varphi = \tan^{-1}\left(\frac{\phi_y}{\phi_x}\right) \tag{2.2.2}$$

where $\phi_x=\partial\phi/\partial x$ and $\phi_y=\partial\phi/\partial y$. The term $\mathbf{v}_{\text{ext}}$ represents the external field velocity given by

$$\vec{v}_{ext} = \psi\vec{v}_{solid} + (1-\psi)\vec{v}_{liquid} \tag{2.2.3}$$

The velocity is defined by the phasic average of the solid $\mathbf{v}_{\text{solid}}$ and the liquid velocity $\mathbf{v}_{\text{liquid}}$ through a fraction of solid $\psi=(1+\phi)/2$. Thus, the motion of phase-field is considered to be convection due to external field velocity.

2.2.2 Heat equation

The evolution of the dimensionless temperature field is described by the following heat conduction equation.

$$\frac{\partial\theta}{\partial t} + \vec{v}_{ext}\cdot\nabla\theta = D\nabla^2\theta + \frac{1}{2}\frac{d\phi}{dt} \tag{2.2.4}$$

The latent heat release at the solidification front is introduced through a source term as a function of rate change of ϕ. A factor of 1/2 on the rate change of phase-field term of the equation is for normalization (range of phase-field is $-1\le\phi\le1$). Convection by an external field velocity is also considered in the equation.

In order to have consistency between the phase-field model and the sharp interface model, solutions obtained by both models should be equivalent. The way to maintain the consistency in the phase-field model is called the thin-interface analysis [19] and is adopted in this thesis. The analysis defines relationships among model parameters appearing in eq.(2.2.1) and (2.2.4), and the details of the parameter determination will be presented in the later section.

2.2.3 Solid deformation

Phase-field simulation is classified as a numerical model of meso-scale phenomena. In the micro-scale, plasticity is characterized by the rearrangement of atoms, i.e. dislocation, sliding, and events taking place at grain boundary. The phenomena are numerically investigated by atomic scale analysis, i.e. molecular dynamics. However, the scalability of the method is not applicable to the scale of interest in this thesis due to its extensive computational cost, thus we limit our scope of solid deformation analysis in the range of continuum mechanics.

Under the above assumption, the equation of motion for solid structure can be written in the following form.

$$\rho \frac{d\vec{v}_{solid}}{dt} = \nabla \cdot \boldsymbol{\sigma} + \rho \vec{b} \tag{2.2.5}$$

Here ρ is the density, $\mathbf{v}_{\text{solid}}$ is again the velocity of solid phase, $\boldsymbol{\sigma}$ is the Cauchy stress tensor, and **b** is a body force vector. The equation is solved by the material point method (MPM) and its discritization and numerical procedure will be presented in a later section.

2.2.3.1 Constitutive equation

In order to solve eq.(2.2.5), a relationship between stress and strain (constitutive relation) is necessary. As pointed out in chapter 1, a consideration of non-linear mechanical response, i.e. visco-plasticity, is essential, so a rate form of the constitutive relation should be suitable. As commonly done, the total strain $\boldsymbol{\varepsilon}$ is decomposed into elastic $\boldsymbol{\varepsilon}^{e}$ and plastic part $\boldsymbol{\varepsilon}^{p}$.

$$\frac{d\varepsilon_{ij}}{dt} = \frac{d\varepsilon_{ij}^{e}}{dt} + \frac{d\varepsilon_{ij}^{p}}{dt} \tag{2.2.6}$$

We also assume that stress is generated only by the elastic part of the strain.

$$\frac{d\boldsymbol{\sigma}}{dt} = \mathbf{C_0} : \frac{d\boldsymbol{\varepsilon}^e}{dt} \tag{2.2.7}$$

where $\boldsymbol{C}_0$ is the fourth order elasticity tensor. A relation between strain and displacement is also needed to compute eq.(2.2.5). Generally, the strain rate is defined by a rate of deformation tensor.

$$\frac{d\boldsymbol{\varepsilon}}{dt} = \frac{1}{2}\left[\nabla\vec{v}_{solid} + \left(\nabla\vec{v}_{solid}\right)^T\right] \tag{2.2.8}$$

In order to describe the mechanical behavior of elasto-inelastic materials, the following pure elastic, elasto-perfectly plastic, and elasto-perfectly-visco-plastic material response are numerically implemented.

2.2.3.1.1 Elastic response

The linear-elastic material response can be represented by the following equation (tensor notation).

$$\sigma_{ij} = \frac{E}{1+\nu}\varepsilon_{ij} + \frac{E\nu}{(1+\nu)(1-2\nu)}\varepsilon_{ii}\delta_{ij} \tag{2.2.9}$$

where E and ν are Young's modulus and Poisson's ratio, respectively. The two dimensional plane strain condition is assumed throughout this thesis, i.e. $\varepsilon_{33}=\varepsilon_{13}=\varepsilon_{23}=0$. This condition gives us the relation $\sigma_{13}=\sigma_{23}=0$, $\sigma_{33}=\nu(\sigma_{11}+\sigma_{22})$. Using these relations, the resulting constitutive equation of linear-elastic material in vector-matrix representation is given by

$$\begin{bmatrix}\sigma_{11}\\ \sigma_{22}\\ \sigma_{12}\end{bmatrix} = \frac{(1-\nu)E}{(1+\nu)(1-2\nu)}\begin{bmatrix}1 & \nu/(1-\nu) & 0\\ \nu/(1-\nu) & 1 & 0\\ 0 & 0 & (1-2\nu)/2(1-\nu)\end{bmatrix}\begin{bmatrix}\varepsilon_{11}\\ \varepsilon_{22}\\ 2\varepsilon_{12}\end{bmatrix} \tag{2.2.10}$$

The constitutive relation is adopted to compute stresses for the inelastic material model.

2.2.3.1.2 Elasto-perfectly plastic response

Since the development of a material model for a specific material is not the primary objective of this thesis, a simple elasto-perfectly plasticity material model is assumed in some simulations. The von Mises yield criterion with the associative flow rule which is often used for general metallic material is introduced for inelastic material behavior. Since the material is assumed to be held around melting temperature, the assumption of no hardening effects (both isotropic and kinematic) should be justified.

The von Mises yielding function f_Y is represented by

$$f_Y(\sigma_{ij}) = \sqrt{s_{ij}s_{ij}} - \sqrt{\frac{2}{3}}\sigma_Y \leq 0 \tag{2.2.11}$$

where s_{ij} is the deviatoric part of the Cauchy stress, and σ_Y is the yield stress. Plastic strain $\boldsymbol{\varepsilon}^p$ is evolved by the following associative flow rule with a plastic multiplier $d\lambda$.

$$\frac{d\varepsilon_{ij}^p}{dt} = d\lambda \frac{\partial f_Y}{\partial \sigma_{ij}} = d\lambda \frac{s_{ij}}{\|s_{ij}\|} \tag{2.2.12}$$

where $d\lambda$ is a plastic multiplier. Stress is integrated by eq.(2.2.7) while satisfying eq.(2.2.11). The process is performed numerically by the radial return mapping method [39] which requires a single operation every single time step and is efficient in terms computational time (see appendix B for details of the numerical procedure).

2.2.3.1.3 Elasto-perfectly-visco-plastic response

Actual metallic materials show viscous response against imposed loading at high temperatures which means that the flow stress (dynamic yielding stress) is dependent on the rate of deformation. In order to incorporate the material behavior, a Perzyna type model [40] with classical J_2 associative flow rule is introduced in this thesis. The assumption of no hardening effect is also used for the same reason in the preceding section.

The von Mises yielding function is introduced as a loading function.

$$f_Y(\sigma_{ij}) = \sqrt{s_{ij}s_{ij}} - \sqrt{\frac{2}{3}}\sigma_Y \tag{2.2.13}$$

An evolution of visco-plastic strain follows the associative flow law as

$$\frac{d\varepsilon_{ij}^{vp}}{dt} = \gamma \frac{\partial f_Y(\sigma_{ij})}{\partial \sigma_{ij}} \tag{2.2.14}$$

where γ is a consistency parameter defined by

$$\gamma = \frac{\langle f_Y(\sigma_{ij}) \rangle}{\eta_{visc}} \tag{2.2.15}$$

η_{visc} is a viscosity coefficient which determines the decay time of the viscous response. $\langle \bullet \rangle$ denotes the Macaulay brackets, i.e. $\langle x \rangle = (x+|x|)/2$, so that the consistency parameter is activated when $f \geq 0$. The Perzyna type model allows the state of $f>0$ temporarily to have a strain rate dependent yield stress. Considering the above loading function and flow law, stress integration is performed by the radial return mapping method [39] the same way as the preceding purely plasticity model. Details of the numerical procedure are described in appendix B.

2.3 Fractional Step Method

Eq.(2.2.1) and (2.2.4) include convection terms due to the external velocity field. If the advection terms are absent, solution methodologies for stationary dendrite growth (i.e. [19]) are available. As a solution strategy for the equations, the fractional step or the operator split method (see, i.e. [37]) would be the suitable choice utilizing the existing solution methodologies.

Eq.(2.2.1) and (2.2.4) can be rewritten as the following simplified form.

$$\frac{\partial \mathbf{a}}{\partial t} + \vec{v}_{ext} \cdot \nabla \mathbf{a} = \mathbf{S} \tag{2.3.1}$$

where $\mathbf{a}=(\phi, \theta)$ and $\mathbf{S}=(S_\phi, S_\theta)$ represents R.H.S. of eq.(2.2.1) and (2.2.4). The equation is divided into two parts, i.e. "non-advection part" and "advection part", in the fractional step method.

$$\frac{\partial \mathbf{a}}{\partial t} = \mathbf{S} \tag{2.3.2}$$

$$\frac{\partial \mathbf{a}^*}{\partial t} + \vec{v}_{ext} \cdot \nabla \mathbf{a}^* = 0 \tag{2.3.3}$$

In these equations, a variable $\mathbf{a}^n$ at time level n is advanced to $\mathbf{a}^*$ at fictitious time level n*. As mentioned above, existing numerical methodologies can be applied to solve this step. Next, the variable $\mathbf{a}^*$ is advected by $\mathbf{v}_{\text{ext}}$, and $\mathbf{a}^{n+1}$ at time level n+1 is given by the second equation.

The time scale of the solidification process and the time scale of the solid deformation or fluid motion are inherently different. By splitting the governing equation into two subsets, i.e. eq.(2.3.2) and (2.3.3), a different time stepping size can be assigned to each equation. The ability to assign different stepping sizes is the main advantage of the fractional step method. In order to achieve an efficient computation, the numerical methodology is adopted in this thesis.

2.3.1 Numerical scheme of advection equation

A numerical scheme to solve the advection equation (2.3.3) is necessary for the fractional step method. Benson [37] points out that the advection scheme affects the overall accuracy of the method. According to Sun and Beckermann [41], a solution of the phase-field equation is quite sensitive to its profile, thus an advection scheme with a sufficient accuracy is essential to maintain the profile correctly during the advection.

The CIP (Cubic Interpolated Pseudo-particle or Constrained Interpolation Profile) method [42] is one of the advection schemes. The main characteristic of the CIP method is the use of both the variable and its spatial derivative to construct a piece-wise third

order polynomial within two neighbor nodes in one-dimensional case. A solution of the advection equation is determined to be a value at an upstream departure point which is found by tracing back along the polynomial (semi-Lagrangian way). The CIP method provides third order accuracy in space, which is the same order of accuracy as the CENO scheme used by Sun and Beckermann [41]. Thus, the CIP method is adopted as an advection scheme in this thesis. Details of the method and its implementation are presented in appendix A.

2.3.2 Validation: diagonal translation of a circle

Diagonal translation of a circle [41] is selected as a validation problem for an advection of the phase-field profile. A square computational domain whose side length is 1.0 is defined as illustrated in Figure 2. 2. The left bottom corner is set to be the origin of the coordinate system. Initially, a circle whose radius is 0.15 is located at (0.25, 0.25), and a phase-field profile is assigned to the circle (ϕ=1 is inside and ϕ=-1 is outside the circle). The phase-field profile is defined by the following hyperbolic tangent kernel function which is the steady state solution of phase-field equation (2.2.1).

$$\phi = -\tanh\left(\frac{n}{\sqrt{2}W}\right) \tag{2.3.4}$$

where n stands for a signed distance, i.e. $n \geq 0$ and $n < 0$ inside and outside the circle, respectively. Meshes of 80x80 and 160x160 are examined in this study. The interface thickness W is set to be $W=2\Delta x$ and $W=4\Delta x$ for 80x80 and 160x160 meshes, respectively. The external velocity field $\vec{v}_{ext}$ =(1.0,1.0) is imposed everywhere in the calculation domain until the center of the circle reaches at (0.75,0.75), then the circle is returned to the initial location by inverting the velocity field simultaneously.

Figure 2. 3 shows the phase field contours at initial state (left panels), half translation (center panels) and full translation (right panels) for (a) 80x80 and (b) 160x160 meshes. Circles travel diagonally while maintaining their outline within a

computational domain. The phase-field profiles along a horizontal center line passing through the center of the circle are illustrated in Figure 2. 4. No significant differences among the profiles are observed for both mesh configurations. The computed ϕ=0 contours are plotted in Figure 2. 5. The circular outline at full translation overlaps with the one at the initial state for both mesh configurations. Quantitative comparison of the ϕ=0 circular outlines is performed in the following way. The L_1 and L_2 error norms are defined as the error between the measured radius of the circle R_i based on the calculation results (bisection method is used to compute ϕ=0 contours) and the exact radius of the circle R_i^{ex} (R_i^{ex} =0.15 in this validation problem).

$$\varepsilon^{L_1} = \frac{\sum_{i=1}^{N} \left| R_i - R_i^{ex} \right|}{\sum_{i=1}^{N} R_i^{ex}}, \quad \varepsilon^{L_2} = \frac{\sqrt{\sum_{i=1}^{N} \left| R_i - R_i^{ex} \right|^2}}{\sum_{i=1}^{N} R_i^{ex}} \tag{2.3.5}$$

Figure 2. 6 shows the calculated L_1, L_2 norms with respect to the mesh size Δx. Simulations are performed with a constant interface thickness of W=0.01 and four different mesh sizes. The approximated curves are also presented in the figure, and the curves indicate that our calculation code shows 2.5-3rd order of accuracy. The order of accuracy is comparable to order of accuracy presented by Sun and Beckermann [41] (third-order CENO scheme). Therefore, the CIP method is a feasible choice for phase-field advection.

Additional simulations with different interface thickness W are performed. Meshes of size 160x160 are used, and the spatial increment Δx is fixed (a side length of the domain set to be unity). The L_1, L_2 norms with respect to $\Delta x' = \Delta x / W$ are shown in Figure 2. 7. As $\Delta x'$ increases, the error norms also increases. The sharper interface gives the larger error. As we will describe in detail later, the interface thickness W is only a free parameter in the phase-field equation. The value of W should be carefully determined if phase-field equation is combined with advection scheme. The value

$\Delta x' = \Delta x/W = 0.4$ is chosen in this thesis, so that the error associated with the combination is expected to be less than 0.1%.

2.4 Phase-Field Method

2.4.1 Parameter determination

Numerical parameters in the phase-field equation (2.2.1) and heat equation (2.2.4) need to be specified to recover solutions of the sharp interface dynamics eq.(1.2.1)-(1.2.3). The thin-interface asymptotic analysis [19] describes relationships among the parameters. Asymptotic analysis (or perturbation method) is performed for the inner (inside the diffuse interface) and outer region (outside the diffuse interface) while assuming the Peclet number $Pe = Wv_i/D$ to be a small parameter. By matching up the inner and outer solutions, the relationships are constructed. Although the mathematical details are not described here (see [19] for the details), the interfacial temperature is represented by the following form.

$$\theta_i = -\frac{Wa_1}{\lambda}\kappa - \frac{a_1}{\lambda}\frac{\tau}{W}\left[1 - \lambda\frac{W^2}{2D\tau}a_2\right]v_i \tag{2.4.1}$$

where $a_1 = 0.8839$ and $a_2 = 0.6267$ are constants obtained from the solvability integral for the given functional forms of $f(\phi) = -\phi^2/2 + \phi^4/4$ and $g(\phi) = \phi - 2\phi^3/3 + \phi^5/5$. Eq.(2.4.1) should recover the solution by sharp interface dynamics, i.e. eq.(1.2.3), then it gives the following relations.

$$d = \frac{Wa_1}{\lambda},\ \beta = \frac{a_1\tau}{\lambda W}\left[1 - \frac{\lambda W^2}{D\tau}a_2\right] \tag{2.4.2}$$

Since rapid cooling is not assumed in this thesis, the kinetic term is negligible, i.e. $\beta = 0$. Finally, the following relations are obtained among parameters.

$$\lambda = \frac{Wa_1}{d},\ \tau = \frac{a_1 a_2 W^3}{dD} \tag{2.4.3}$$

where λ, τ, and W are specified by eq.(2.4.3) because d and D are material properties. Generally, the interface thickness W is assumed to be a free parameter, and λ and τ are the values to be determined. As long as Peclet number Pe is kept small, the phase-field model recovers the solution using the sharp interface model.

2.4.2 Adding anisotropy

Anisotropy plays a crucial role on dendritic pattern selection, so the effect should be introduced to the phase-field model. Generally, the anisotropy is incorporated by allowing τ and W to depend on the local normal vector to the interface. In other words, the effect is included through surface energy and kinetics. The cubic or four-fold anisotropy, i.e. $\xi(\varphi)=1+\varepsilon_0\cos 4\varphi$, is introduced to τ and W such that $\tau(\varphi)=\tau_0\xi^2$ and $W(\varphi)=W_0\xi$. The term φ represents the angle between the x-axis of the fixed coordinate system and the local normal vector to the interface.

$$\varphi = \tan^{-1}\left(\frac{\phi_y}{\phi_x}\right) \tag{2.4.4}$$

where $\phi_x=\partial\phi/\partial x$ and $\phi_y=\partial\phi/\partial y$. In the above definition, a characteristic interface thickness W_0 and a time scale τ_0 is introduced. In the actual computation, eq.(2.2.1) is nondimensionalized by the scales, .i.e. $\nabla' = W_0\nabla$ and $t'=t/\tau_0$. Using the scaled variables, the dimensionless form of eq.(2.2.1) is given by

$$\begin{aligned}\left(1+\varepsilon_0\cos 4\varphi\right)^2\left(\frac{\partial\phi}{\partial t}+\vec{v}_{ext}\cdot\nabla'\phi\right) &= \nabla'^2\phi+\phi\left(1-\phi^2\right)-\lambda\left(1-\phi^2\right)^2\theta \\ &+\varepsilon_0\cos 4\varphi\left(2+\varepsilon\cos 4\varphi\right)\nabla'^2\phi \\ &-8\varepsilon_0\sin 4\varphi\left(1+\varepsilon\cos 4\varphi\right)\left(\varphi_x\phi_x+\varphi_y\phi_y\right) \\ &-16\varepsilon_0\left[\cos 4\varphi+\varepsilon\left(\cos^2 4\varphi-\sin^2 4\varphi\right)\right]\left(\varphi_y\phi_x-\varphi_x\phi_y\right)\end{aligned} \tag{2.4.5}$$

2.4.3 Change of crystallographic orientation due to solid deformation

Anisotropy is introduced to phase-field model depending on the angle φ defined by eq.(2.4.4). In the definition of φ, the angle is measured from a reference frame which is set to be the fixed x-coordinate axis in space. The phase-field simulation is performed under fixed Eulerian grids, thus it is a suitable definition. In the case where there is no solid deformation, the crystallographic orientation and the x-axis always correspond to each other during the simulation, i.e. Figure 2. 8 (a). However, since the crystallographic orientation reflects the crystal lattice structure of the solid phase, deformation imposed on the solid phase would cause a variation of the orientation within the solid structure. The x-axis and the orientation do not necessarily coincide with each other in that case, and the preferable growth direction should be changed by the change of orientation (Figure 2. 8 (b)).

One way to include the effect of the orientation change in phase-field model is by the introduction of an additional parameter α which represents an angle between the fixed x-axis and the crystallographic orientation as shown in Figure 2. 8 (b). By the introduction of α, the anisotropy should be determined based on an angle (φ-α). Modifications of $W(\varphi)\rightarrow W(\varphi-\alpha)$ and $\tau(\varphi)\rightarrow\tau(\varphi-\alpha)$ would be necessary. Due to the modifications, the following changes are required for φ_x and φ_y.

$$\begin{aligned}\varphi_x &\rightarrow \frac{\partial(\varphi-\alpha)}{\partial x'} = \frac{\phi_{yx}\phi_x - \phi_y\phi_{xx}}{\left|\nabla'\phi\right|^2} - \frac{\partial\alpha}{\partial x'} \\ \varphi_y &\rightarrow \frac{\partial(\varphi-\alpha)}{\partial y'} = \frac{\phi_{yy}\phi_x - \phi_y\phi_{xy}}{\left|\nabla'\phi\right|^2} - \frac{\partial\alpha}{\partial y'}\end{aligned} \tag{2.4.6}$$

The driving force of the orientation change is a rotation caused by solid deformation (translation does not affect on the change). The evolution of the orientation can be given by the following equation.

$$\frac{\partial \alpha}{\partial t'} + \vec{v}_{solid} \cdot \nabla' \alpha = \nabla' \times \vec{v}_{solid} = \frac{1}{2}\left(\frac{\partial v_{solid}}{\partial y'} - \frac{\partial u_{solid}}{\partial x'} \right) \tag{2.4.7}$$

The notation $\mathbf{v}_{solid}=(u_{solid}, v_{solid})$ is used here. Eq.(2.4.7) is of the same form as eq.(2.3.1), so that the fractional step method is also used to solve it.

As mentioned above, the crystallographic orientation is only meaningful in solid crystal, so the orientation cannot be defined in the liquid phase, i.e. $\phi<0$. However, the treatment of the liquit phase may cause some troubles in the actual numerical implementation because liquid part which will become the solid phase should have the same orientation as the solid into which the liquid part will be incorporated (the solid closest to the liquid part). Let us consider the following situation in the phase-field simulation. As shown in Figure 2. 9, a certain nodal point of liquid phase ($\phi<0$) is going to become solid phase ($\phi\geq0$) within a single computational time step. If there is no numerical treatment, the nodal point does not have any crystallographic orientation α when the phase-field equation (2.4.5) is solved because $\mathbf{v}_{solid}$ in eq.(2.4.7) is only defined in the solid phase. The nodal point may evolve in the wrong direction. In order to avoid the situation, some numerical treatment which assigns the same crystallographic orientation as the closest solid phase to the nodal point should be constructed and implemented in the phase-field model.

2.4.3.1 Numerical method of extending field variables

One possible way to achieve the treatment is the extension of the crystallographic orientation defined only in the solid phase to the liquid phase. Since the phase-field varies only across the interface, a unit normal to the interface is easily defined to be

$$\vec{n} = \frac{\nabla \phi}{|\nabla \phi|} \tag{2.4.8}$$

The vector points from the liquid to the solid phase. If the orientation at the interface is extended along the direction of the unit normal, the liquid phase should have the same orientation as the closest solid. The process would be numerically implemented with a PDE base extrapolation method [43]. A basic equation of the extrapolation is the following.

$$\frac{\partial \alpha}{\partial \tau_p} - \vec{n} \cdot \nabla \alpha = 0 \tag{2.4.9}$$

where τ_p is a pseudo time which is defined only for the numerical purpose. The equation is the same form as the advection equation, i.e. eq.(2.3.3). Since **-n** indicates the direction from solid to liquid, the equation leads an advection from the solid to the liquid phase. If the advection velocity is set to be zero in the solid phase, i.e. $\phi \geq 0$, the crystallographic orientation α at the interface is extended to the liquid phase. The equation (2.4.9) is solved until a steady state is established by setting criterion with some tolerance. For instance, the following residual is defined with α at *k*th and *k*+1th iteration (iteration of the pseudo time step).

$$\mathrm{Re}\, s \equiv \alpha^{k+1} - \alpha^{k} \tag{2.4.10}$$

In this thesis, a tolerance TOL=1.0e-6 is used. The CIP method is again used to solve the equation. In the steady state, i.e. $\tau_p \rightarrow \infty$, eq.(2.4.9) gives

$$\vec{n} \cdot \nabla \alpha = 0 \tag{2.4.11}$$

The equation denotes that α is kept constant along the normal direction to the interface. The minimum distance between some liquid part and its nearest neighbor solid is found by tracing the normal direction to the interface. The equation ensures that liquid phase has α of the nearest neighbor solid. Extension of α by eq.(2.4.9) in the order of the diffuse interface thickness is sufficient. The equation is only solved within a narrow band whose width is $6\Delta x$ (comparable to the diffuse interface thickness) while using a

flag which distinguishes the inside and outside of the diffuse interface for efficient computation.

In this thesis, the velocity of the liquid phase $\mathbf{v}_{\text{liquid}}$ in eq.(2.2.3) is not computed. However, $\mathbf{v}_{\text{liquid}}$ has to be estimated in the liquid phase to advect ϕ, θ, and α with $\mathbf{v}_{\text{ext}}$. Otherwise a jump in velocity would be formed at the interface, and it would cause some numerical instability. As a first approximation, the velocity of the solid phase is extended to the liquid phase in this thesis. The numerical procedure is simply performed with a replacement of $\alpha \rightarrow \mathbf{v}_{\text{ext}}$ in eq.(2.4.9). The profile of dimensionless temperature θ is more diffused than ϕ and α (the order of several times of diffuse interface thickness). Therefore, the velocity field should be extended beyond the interface thickness of the phase-field. From the definition of normal vector to the interface in eq.(2.4.8), the vector cannot be defined in the bulk phases, i.e. $\nabla\phi = 0$, so some numerical procedure is needed to have the normal vector beyond the diffuse interface thickness for solving eq.(2.4.9). The PDE base re-initialization scheme[16] is utilized for this purpose. From the steady state solution of phase-field equation, the singed distance from the interface n is represented by (inverse of eq.(2.3.4))

$$n = \frac{\sqrt{2}W}{2} \ln\left(\frac{1+\phi}{1-\phi}\right) \tag{2.4.11}$$

where n is only defined within the diffuse interface. Re-initialization is performed by the following PDE [16].

$$\frac{\partial n}{\partial \tau_p} + S(n)\left(|\nabla n| - 1\right) = 0 \tag{2.4.12}$$

where τ_p is again a pseudo time. The following function is adopted for $S(n)$.

$$S(n) = \frac{n}{\sqrt{n^2 + |\nabla n|^2 (\Delta x)^2}} \tag{2.4.13}$$

At the steady state, eq.(2.4.12) is reduced to

$$|\nabla n| = 1 \tag{2.4.14}$$

Then, n recovers the role of a signed distance function over the computational domain. Eq.(2.4.12) is solved by CIP method. The details of the numerical procedure are presented in appendix A.

The numerical methodology to consider the change of crystallographic orientation due to solid deformation described in this section is only applicable when the coupling between α and ϕ is negligible in terms of free energy. As mentioned in the preceding section, phenomena associated with grain impingements or grain boundary, i.e. bridging, and coarsening etc. are dependent on the state of free energies of the system. A mismatch of crystallographic orientation at the grain boundary acts as an energy penalty because disordered structure, i.e. dislocation, is formed at the region, consuming additional energy. This indicates that the free energy should be in the form of $F(\phi,\theta,\nabla\alpha)$, and includes coupling terms between ϕ and $\nabla\alpha$. This results additional terms related to $\delta F(\phi,\theta,\nabla\alpha)/\delta\phi$ and $\delta F(\phi,\theta,\nabla\alpha)/\delta\alpha$ in the evolution equation of ϕ and α, respectively. A polycrystalline phase-field model [24] incorporates the effect of the orientation mismatch on the free energy, but the simulation of the model is computationally more expensive. For the dendrite growth of single crystal, the orientation mismatch would not be a significant contribution to the system. Thus, simulations with the numerical methodology presented above will be presented in chapter 3 as the limiting case. In chapter 4, the polycrystalline phase-field model will be introduced to perform multi grain growth with forming grain boundaries.

2.4.3.2 Validation of the field variable extension: diagonal translation of a circle with extended velocity field

The methodology of field variable extension developed in the last section is examined in this section. Again, a diagonal translation of a circle is selected as the validation problem. Identical geometrical settings for the calculation domain and the

circle from the preceding test problem are used with 81x81 meshes. The interface thickness is set to be $W=2\Delta x$ in this test problem.

At each time step, (i) the velocity field is assigned only inside the circle at the beginning of every time step as shown in the lower left panel of Figure 2. 10. (ii)The phase-field ϕ is converted to the signed distance function n by eq.(2.4.11) within the diffuse interface region. (iii) n is extended to the whole computational domain using the re-initialization scheme given by eq.(2.4.12) as illustrated in the upper central panel of Figure 2. 10. (iv) The velocity field defined in (i) is extended outward the circle by eq.(2.4.9). (v) The circle with the phase-field profile is translated by the extended velocity field shown in the lower center and lower right panels of Figure 2. 10. As before, the velocity field $\vec{v}_{ext} = (1.0,1.0)$ is assigned until the circle reaches at (0.75,0.75) and it is inverted instantaneously.

Figure 2. 11 the left panel shows the computed ϕ=0contours. The circle at full translation corresponds well with that at the initial state. The phase-field profile along a horizontal centerline in the right panel of Figure 2. 11 also shows that the profile at the full translation is well maintained for one complete translation. The computed error norms determined by eq.(2.3.5) are L_1=3.1E-3 and L_2=3.3E-4. Based on the result, the proposed field variable extension scheme is successfully implemented and works correctly. The scheme should be applicable to actual numerical problems.

2.4.3.4 Validation of phase-field simulation of dendritic solidification under imposed external velocity

In addition to the numerical methodologies of the advection scheme and the field variable extension, an evolution of the dendritic microstructure is included in this thesis. The phase-field equation (2.4.5), the heat equation (2.2.3) and the evolution equation of crystallographic orientation (2.4.7) are solved under a given velocity field. The numerical results are compared with exact solutions.

2.4.3.4.1 Pure rotational velocity field

Dendrite growth under a rotational velocity field is examined in this section. A rectangular computational domain whose size is 641x1281 nodal points is used, and a circular solid seed is initially allocated at the center of the domain (ϕ=1 and θ=0 are specified inside the seed) as shown in Figure 2. 12. The dimensionless undercooling Δ=0.55 is set to liquid phase at the initial temperature and $\Delta x/W=\Delta y/W$=0.4 is used for spacing in x and y direction. Symmetric conditions are imposed on the left and the right walls while periodic conditions are assigned to the upper and the lower walls. All of the computational settings are specified in same manner as the phase-field simulation performed by Tong et al. [44] so that our numerical results can be compared with theirs. The rotation velocity is set to be π/40000 [rad/step]. An advection equation with rotational velocity is solved every 50 steps of phase-field simulation.

First, a series of simulations with parameters indicated in Table 2. 1 are performed to examine tip velocities. In the same table, the tip velocities obtained by the current study, data by Tong et al.[44], and the analytical result by microscopic solvability theory are presented for comparison. Significant differences are not observed among the data. Figure 2. 13 left panel shows plots of the trajectories of the four tips indicated in Figure 2. 12 right panel for the case where D=3, d_0/W_0=0.185, and ε=0.05. The dendrite tips move outward due to solidification, but the growth direction is changed by the external rotational velocity. As a result, a spiral like trajectory is observed up to 90 degrees rotation. The right panel of the same figure shows a time history of the tip velocities of the four tips. It can be seen that all tips grow evenly. Thus, our numerical methodology provides a correct simulation of dendrite growth. The phase-field contours of (a) no rotational velocity field, (b) rotational velocity field and consideration of crystallographic orientation change, and (c) (b) rotational velocity with no consideration of orientation change are presented in Figure 2. 14. Clearly, the contour obtained by condition (c) seems to be wrong since a pure rotation velocity field is imposed on whole

computational domain. A change of orientation must therefore be included in the phase-field equation.

2.4.3.4.2 Linear shear velocity field

Linear shear velocity is imposed on a computational domain in this section. The domain is schematically illustrated in the left panel of Figure 2. 15. The computational domain is defined by 641x641 grid points with $\Delta x/W_0=\Delta y/W_0=0.4$, and symmetric boundary conditions are imposed on all four sides. A circular solid seed is initially located in the middle of the left wall (ϕ=1 and θ=0 are specified inside the seed), and under-cooling is set to be Δ=0.55 in the liquid phase. The operating conditions are defined as D=3, d_0/W_0=0.185 and ε=0.05. The linear shear velocity field $\mathbf{u}_{\text{ext}}=(u_{\text{ext}}, v_{\text{ext}})$ is defined to be

$$\begin{aligned} u_{ext} &= 0 \\ v_{ext} &= -\frac{x}{L}\frac{\Delta x}{100} \quad [1/\text{time step}] \end{aligned} \tag{2.4.17}$$

where L denotes the side length of the computational domain (=640Δx). As shown in the right panel of Figure 2. 15, a horizontally-oriented dendrite arm evolves rightward and changes its direction to downward due to the imposed shear velocity field.

In order to evaluate the numerical result quantitatively, a comparison of a trajectory obtained from the simulation with the one obtained in a semi-analytical way is performed. A change of tip location (displacement) with respect to time due to convection by external velocity ($x_{\text{tip}}^{\text{ext}}(t)$, $y_{\text{tip}}^{\text{ext}}(t)$) is computed by the following equations.

$$\begin{aligned} x_{tip}^{ext}(t) &= 0 \\ y_{tip}^{ext}(t) &= \int_0^t v_{ext}\left(x_{tip}^{sol}(\tau)\right)d\tau \end{aligned} \tag{2.4.18}$$

Since external velocity in the *x* direction is absent, tip motion in the *x* direction is induced only by solidification. However, an analytical solution of the tip velocity is not available in the test case, so the tip locations in the *x* direction with respect to time $x_{\text{tip}}^{\text{sol}}(t)$ due to solidification are simply extracted from the numerical result, thus the procedure is semi-analytical. A change of crystallographic orientation α at the tip location is induced by rotation due to the imposed external velocity given by

$$\alpha(t) = \int_0^t \frac{\partial v_{ext}\left(x_{tip}^{sol}(\tau)\right)}{\partial y} d\tau \tag{2.4.19}$$

Due to the change of orientation α with respect to time, the direction of tip velocity is bended downward. By using α and the solidification velocity in the *x* direction $u_{\text{tip}}^{\text{sol}}$ (computed from $x_{\text{tip}}^{\text{sol}}$), the solidification velocity in *y* direction is computed by

$$v_{tip}^{sol} = u_{tip}^{sol} \tan\alpha \tag{2.4.20}$$

A change of tip location due to solidification can be expressed by

$$y_{tip}^{sol}(t) = \int_0^t v_{tip}^{sol}\left(x_{tip}^{sol}(\tau)\right) d\tau \tag{2.4.21}$$

Finally, semi-analytically obtained tip location in *y* direction would be given by a summation of the tip displacement caused by the external velocity and solidification.

$$y_{tip}^{total}(t) = y_0 + y_{tip}^{ext}(t) + y_{tip}^{sol}(t) \tag{2.4.22}$$

where y_0 is the initial tip position. An explicit Euler scheme is applied to the numerical integration of the above equations. A comparison of a trajectory directly obtained by numerical simulation with a trajecteory determined by the above semi-analytical method with components $y_{\text{tip}}^{\text{ext}}$ and $y_{\text{tip}}^{\text{sol}}$ is shown in Figure 2. 16. The trajectories correspond well with each other. The analysis shows that a change of crystallographic orientation due to imposed external velocity is properly introduced to phase-field model by the developed numerical methodology.

2.5 Material Point Method

The formulation and calculation procedure of the material point method (MPM) are briefly described in this section. Appendix B is also available for more detailed explanation of the derivations of some of the equations and notes for an actual numerical implementation.

2.5.1 Governing equations of material point method

As mentioned in the preceding section, The equations used in the MPM are the equations of motion (2.2.4), constitutive relation, and strain-displacement relation eq.(2.2.7). The solution methodology of the equations is based on a weak form of eq.(2.2.4) which is the same as the usual FEM. The weak form on the computational domain Ω is given by the following equation with an arbitrary test function $\delta \boldsymbol{w}$.

$$\begin{aligned}\int_\Omega \rho \frac{d\vec{v}_{solid}}{dt} \cdot \delta \mathbf{w} d\Omega &= \int_\Omega (\nabla \cdot \boldsymbol{\sigma}) \cdot \delta \mathbf{w} d\Omega + \int_\Omega \rho \vec{b} \cdot \delta \mathbf{w} d\Omega \\ &= \int_{\partial\Omega} \boldsymbol{\tau} \cdot \delta \mathbf{w} d\Omega - \int_\Omega \boldsymbol{\sigma} : \nabla \delta \mathbf{w} d\Omega + \int_\Omega \rho \vec{b} \cdot \delta \mathbf{w} d\Omega\end{aligned} \tag{2.5.1}$$

From the first to the second line, The Gauss divergence theorem is applied, and a traction $\vec{\tau} = \boldsymbol{\sigma} \cdot \vec{n}$ is defined on the domain boundary $\partial\Omega$. In the MPM, a solid body is represented by a collection of material points, and all information about the material properties and historical variables are carried by the points. Since eq.(2.5.1) is constructed based on continuous field variables while available variables are discretely distributed on the material points, the continuous field variables have to be reconstructed somehow from the discrete variables on material points.

In the MPM, the following particle characteristic function χ_p is defined to represent the support domain of each material point p at given location $\boldsymbol{x}$ and time t.

$$V_p = \int_\Omega \chi_p(\vec{x}, t) d\Omega \tag{2.5.2}$$

where V_p denotes a volume associated with each material point. The following aspect is also assumed for χ_p .

$$\sum_{p=1}^{N_p} \chi_p(\vec{x},t) = 1 \tag{2.5.3}$$

where N_p is the total number of material points. The equation indicates that χ_p satisfies the partition of unity at a given location $\boldsymbol{x}$. Using both eq.(2.5.2) and (2.5.3), any continuous field variable $f(\vec{x},t)$ is related to the discrete variable on material point f_p by the following equation (see appendix B.1.1 for the detailed derivation).

$$\sum_{p=1}^{N_p} f_p \int_\Omega \chi_p(\vec{x},t) d\Omega = \int_\Omega f(\vec{x},t) d\Omega \tag{2.5.4}$$

Introducing a relationship in eq.(2.5.4) to eq.(2.5.1) and a linear shape function $N_i(\vec{x})$ to $\delta\boldsymbol{w}$, the following equation is obtained (see appendix B.1.2 for the detailed derivation).

$$\sum_{p=1}^{N_p} m_p \frac{d\vec{v}_p}{dt} \bar{S}_{vp} + \sum_{p=1}^{N_p} \boldsymbol{\sigma}_p \cdot \nabla \bar{S}_{vp} V_p - \sum_{p=1}^{N_p} m_p \vec{b}(\vec{x}) \bar{S}_{vp} - \int_{\partial\Omega} \vec{\tau} \cdot N_i(\vec{x}) dS = 0 \tag{2.5.5}$$

where m_p and $\vec{v}_p$ are a mass and a velocity associated with each material point, respectively. The terms $\overline{S_{vp}}$ and $\overline{\nabla S_{vp}}$ denote a weighted shape function and its gradient, and specify a mapping way between a material point and a background nodal point.

$$\bar{S}_{vp} = \frac{1}{V_p} \int_{\Omega \cap \Omega_p} \chi_p(\vec{x},t) N_i(\vec{x}) d\Omega \tag{2.5.6}$$

$$\nabla \bar{S}_{vp} = \frac{1}{V_p} \int_{\Omega \cap \Omega_p} \chi_p(\vec{x},t) \nabla N_i(\vec{x}) d\Omega \tag{2.5.7}$$

Let us define a rate change of nodal momentum $\dot{\vec{p}}_i$ by the following equation.

$$\dot{\vec{p}}_i \equiv m_i \dot{\vec{v}}_i = \sum_{p=1}^{N_p} m_p \frac{d\vec{v}_p}{dt} \overline{S_{vp}} \tag{2.5.8}$$

where m_i and $\dot{\vec{v}}_i$ denote a nodal mass and a nodal acceleration. Internal and external force vectors are also defined by

$$\vec{f}_i^{\,\text{int}} = -\sum_{p=1}^{N_p} \boldsymbol{\sigma}_p \cdot \nabla \overline{S_{vp}} V_p$$
$$\vec{f}_i^{\,ext} = \sum_{p=1}^{N_p} m_p \vec{b}(\vec{x}) \overline{S_{vp}} + \int_{\partial\Omega} \tau \cdot N_i(\vec{x}) dS \tag{2.5.9}$$

Simplified form of eq.(2.5.5) is obtained with using the above defined vectors.

$$\dot{\vec{p}}_i = \vec{f}_i^{\,\text{int}} + \vec{f}_i^{\,ext} \tag{2.5.10}$$

The nodal equation of motion for each node is the equation to be solved in the actual computation.

2.5.2 Calculation procedure of the MPM

Nodal acceleration must be computed with nodal internal and external force by eq.(2.5.10) at every time step. In order to solve the equation, the material point variables are mapped to the fixed background nodes at the beginning of each time step. Since variables on the nodal points are always discarded before the mapping, the nodal points are simply used as a computational scratch pad. By using the continuous mapped nodal velocity field, a rate of deformation tensor or a strain rate at any location can be computed with using a linear shape function.

$$\begin{aligned}\dot{\boldsymbol{\varepsilon}}(\vec{x},t) &= \frac{1}{2}\left[\nabla\vec{v}(\vec{x}) + (\nabla\vec{v}(\vec{x}))^T\right] \\ &= \frac{1}{2}\left[\sum_{i=1}^{nnod} \nabla N_i(\vec{x}) \otimes \vec{v}_i + \sum_{i=1}^{nnod} \vec{v}_i \otimes \nabla N_i(\vec{x})\right]\end{aligned} \tag{2.5.11}$$

Introducing the relationship between the continuous and discrete variables given by eq.(2.5.4), a strain rate on each material point is then computed using eq.(2.5.11).

$$
\begin{aligned}
\dot{\boldsymbol{\varepsilon}}_p &= \int_{\Omega\cap\Omega_p} \dot{\boldsymbol{\varepsilon}}(\vec{x},t)\frac{\chi_p(\vec{x},t)}{V_p}\,d\Omega \\
&= \frac{1}{2V_p}\sum_{i=1}^{nnod}\Big[\int_{\Omega\cap\Omega_p}\nabla N_i(\vec{x})\chi_p(\vec{x},t)d\Omega\otimes\vec{v}_i + \\
&\qquad\qquad \vec{v}_i\otimes\int_{\Omega\cap\Omega_p}\nabla N_i(\vec{x})\chi_p(\vec{x},t)d\Omega\Big] \\
&= \frac{1}{2V_p}\sum_{i=1}^{nnod}\Big[\overline{\nabla S_{vp}}\otimes\vec{v}_i + \vec{v}_i\otimes\overline{\nabla S_{vp}}\Big]
\end{aligned}
\tag{2.5.12}
$$

Now the strain increment is available at each material point, and is used to update the stress state based on an appropriate constitutive relation. Using the updated stress at each material point $\boldsymbol{\sigma}_p$, the internal force vector on each background node is computed by eq.(2.5.9). Considering the external force vector, the nodal acceleration in eq.(2.5.10) is finally obtained. The nodal acceleration is used to update the location and the velocity of each material point using the nodal shape function.

The numerical procedure is briefly summarized as follows

(1) Initialization of material points
  (1-a) Generate material points $\vec{x}_p$ inside the continuum solid body
  (1-b) Assign material properties, i.e. particle volume, density, elastic modulus, and Poisson's ratio etc., and initial variables $\vec{v}_p, \boldsymbol{\sigma}_p, \boldsymbol{\varepsilon}_p$ etc.

(2) Discard the nodal variables m_i, $\vec{p}_i$, $\dot{\vec{p}}_i$, $\vec{f}_i^{\,\mathrm{int}}$, $\vec{f}_i^{\,ext}$

(3) Map variables from material points to the nodal points
  (3-a) Construct the weighted shape function $\overline{S_{vp}}$ and its gradient $\overline{\nabla S_{vp}}$ by eq.(2.5.6) and (2.5.7)
  (3-b) Assemble the material point variables to nodal points

$$
\begin{aligned}
m_i &= \sum_{p=1}^{N_p} m_p\overline{S_{vp}} \\
\vec{p}_i &= \sum_{p=1}^{N_p} m_p\vec{v}_p\overline{S_{vp}}
\end{aligned}
\tag{2.5.13}
$$

(4) Update the stress and strain on material points
  (4-a) The deformation rate tensor on each material point is constructed by eq.(2.5.12)

$$
\dot{\boldsymbol{\varepsilon}}_p = \frac{1}{2V_p}\sum_{i=1}^{nnod}\Big[\overline{\nabla S_{vp}}\otimes\vec{v}_i + \vec{v}_i\otimes\overline{\nabla S_{vp}}\Big]
$$

(4-b) Stress is updated based on a constitutive relation.

(5) Compute the internal and external forces on each node by eq.(2.5.9)

$$\vec{f}_i^{\,\text{int}} = -\sum_{p=1}^{N_p} \boldsymbol{\sigma}_p \cdot \nabla \overline{S_{vp}} V_p$$

$$\vec{f}_i^{\,ext} = \sum_{p=1}^{N_p} m_p \vec{b}(\vec{x}) \overline{S_{vp}} + \int_{\partial\Omega} \tau \cdot N_i(\vec{x}) dS$$

(6) Compute the rate of momentum on each node and update the momentum

(6-a) Compute the rate change of nodal momentum by eq.(2.5.10)

$$\dot{\vec{p}}_i = \vec{f}_i^{\,\text{int}} + \vec{f}_i^{\,ext}$$

(6-b) Compute the nodal momentum by explicit Euler scheme

$$\vec{p}_i^{\,n+1} = \vec{p}_i^{\,n} + \dot{\vec{p}}_i \Delta t \tag{2.5.14}$$

(7) Update the locations and velocity of the material points by using nodal variables

$$\begin{aligned} \vec{x}_p^{\,n+1} &= \vec{x}_p^{\,n} + \sum_{i=1}^{nnod} \overline{S_{vp}} \frac{\vec{p}_i}{m_i} \Delta t \\ \vec{v}_p^{\,n+1} &= \vec{v}_p^{\,n} + \sum_{i=1}^{nnod} \overline{S_{vp}} \frac{\dot{\vec{p}}_i}{m_i} \Delta t \end{aligned} \tag{2.5.15}$$

(8) Repeat (2)-(7) until the computation reaches the desired time step

The stress state is updated right after the variables on material points are mapped to the background nodal points in the above calculation sequence. The methodology is called update stress first (USF). In update stress last (USL) stresses are updated after computing new location and velocity of material points (after procedure 7 in the above outline) [45]. According to Buzzi et al.[46], the USF gives better energy conservation than the USL. For this reason, the USF is adopted in this thesis.

2.5.3 Weighted shape function

A weighted shape function $\overline{S_{vp}}$ and its gradient $\overline{\nabla S_{vp}}$ in eq. (2.5.6) and (2.5.7) define a way of mapping from the material points to the background nodal points and vice versa. Characteristics of the function strongly affect the calculation results.

Basically, the function is composed of a usual shape function $N_i(\boldsymbol{x})$ and a particle characteristic function χ_p, so that several options of χ_p are available.

In the original MPM [30], the following Dirac delta function is selected as the particle characteristic function.

$$\chi_p(\vec{x},t)=\delta(\vec{x}-\vec{x}_p) \tag{2.5.16}$$

The function gives expressions of $\overline{S_{vp}}=N_i(\vec{x}_p)$ and $\overline{\nabla S_{vp}}=\nabla N_i(\vec{x}_p)$. The use of the function has an advantage in terms of computational efficiency if Cartesian background cells are used. A given material point maps its variables only onto background nodes of the cell which the particle is contained in, and a given node maps its information only onto material points in adjacent cells. One disadvantage of the particle characteristic function is that it does not satisfy the partition of unity (it takes infinity at the particle location). Another disadvantage is called grid-crossing instability which typically occurs when a material point crosses a cell boundary. In this situation, the influence of a certain material point on some nodal points changes drastically. More specifically, the gradient of the weighted shape function, i.e. $\overline{\nabla S_{vp}}=\nabla N_i(\vec{x}_p)$ changes its sign by crossing the cell boundary. The discontinuous change often causes physically spurious oscillation [47], and it is not suitable for large deformation analysis.

In order to prevent undesirable spurious oscillation, the use of smoother weighted shape functions is effective. Bardenhagen et al. [47] chose the following Heaviside function as a particle characteristic function for one-dimensional case.

$$\chi_p(x,t)=\begin{cases}1 & \textit{for} \quad x\in\Omega_p \\ 0 & \textit{otherwise}\end{cases} \tag{2.5.17}$$

where, again, Ω_p denotes a support domain of a single material point. Variables associated with the particle are assumed to be uniformly distributed within the support domain. Typically a linear shape function is used for the shape function $N_i(\vec{x})$, i.e. for one-dimensional case

$$N_i(x)=\begin{cases}0 & |x-x_i|>\Delta x\\ 1+\dfrac{x-x_i}{\Delta x} & -\Delta x\le x-x_i\le 0\\ 1-\dfrac{x-x_i}{\Delta x} & 0<x-x_i\le\Delta x\end{cases} \tag{2.5.18}$$

where x_i is a location of background nodal point i and Δx is its spacing with neighbor nodes. The combination of eq.(2.5.17) and (2.5.18) for a weighted shape function is called the contiguous particles GIMP method [47]. By using the functions, $\overline{S_{vp}}$ and $\overline{\nabla S_{vp}}$ are represented by the followings.

$$\overline{S_{vp}}=\begin{cases}0 & |x_p-x_i|>\Delta x+l_p\\ \dfrac{1}{4\Delta x l_p}\left(x_p-x_i+\Delta x+l_p\right)^2 & -\Delta x-l_p\le x_p-x_i<-\Delta x+l_p\\ 1+\dfrac{x_p-x_i}{\Delta x} & -\Delta x+l_p\le x_p-x_i<-l_p\\ 1-\dfrac{\left(x_p-x_i\right)^2+l_p^2}{2\Delta x l_p} & -l_p\le x_p-x_i<l_p\\ 1-\dfrac{x_p-x_i}{\Delta x} & l_p\le x_p-x_i<\Delta x-l_p\\ \dfrac{1}{4\Delta x l_p}\left(\Delta x+l_p-x_p+x_i\right)^2 & \Delta x-l_p\le x_p-x_i\le\Delta x+l_p\end{cases} \tag{2.5.19}$$

$$\overline{\nabla S_{vp}}=\begin{cases}0 & |x_p-x_i|>\Delta x+l_p\\ \left(x_p-x_i+\Delta x+l_p\right)/\left(2\Delta x l_p\right) & -\Delta x-l_p\le x_p-x_i<-\Delta x+l_p\\ 1/\Delta x & -\Delta x+l_p\le x_p-x_i<-l_p\\ -\left(x_p-x_i\right)/\left(\Delta x l_p\right) & -l_p\le x_p-x_i<l_p\\ -1/\Delta x & l_p\le x_p-x_i<\Delta x-l_p\\ \left(x_p-x_i-\Delta x-l_p\right)/\left(2\Delta x l_p\right) & \Delta x-l_p\le x_p-x_i\le\Delta x+l_p\end{cases} \tag{2.5.20}$$

where $2l_p$ is the side length of the rectangular particle domain. For instance, profiles of $\overline{S_{vp}}$ and $\overline{\nabla S_{vp}}$ with Δx=1 and l_p=0.5Δx are plotted in Figure 2. 17 and Figure 2. 18, respectively. A solid line represents the weighted shape function and its gradient of the original MPM (use eq.(2.5.16) for a particle characteristic function) whereas the solid line with dots denotes those of GIMP. Since the particle domain is considered in the GIMP (domain of influence of GIMP is $|x_p\text{-}x_i|\le\Delta x+l_p$ while $|x_p\text{-}x_i|\le\Delta x$ for an original

MPM), a smoother transition near cell boundary is observed in the profile of a weighted shape function of GIMP. A gradient of the weighted shape function does not have a drastic change in terms of its sign. This characteristic of the shape function suppresses spurious oscillation when a material point is passing through the cell boundary. In this thesis, GIMP is applied to the solution methodology of MPM.

The above discussion is only for one-dimensional case. Extension of the weighted shape function to two-dimension is straightforward. Similar to the construction of the two-dimensional shape function, the relation $\overline{S_{vp}}(x, y) = \overline{S_{vp}}(x)\overline{S_{vp}}(y)$ is valid. Using this relationship, $\overline{\nabla S_{vp}}(x, y)$ is represented in a simple form (see appendix B for details).

2.5.4 Restriction of time step size

For computational simplicity, the lumped mass assumption is applied to construct the nodal mass matrix. Thanks to this assumption, the mass matrix is diagonalized, so that no matrix needs to be constructed and solved in eq.(2.5.10). An explicit time stepping scheme is typically chosen as a solution methodology. This is a significant advantage for our simulation in terms of handling large deformation, updating the solid structural model, and imposing the complicated material constitutive model. However, the explicit scheme is restricted by so-called CFL (Courant-Friedrichs-Lewy) condition. Since stress waves within the solid material must be resolved with the scheme, the time step size is limited by the wave speed (speed of sound in the solid matter). The speed of the longitudinal wave in a solid material c_{solid} is defined by the following equation (see i.e. [48]).

$$c_{solid} = \sqrt{\frac{K + 4G/3}{\rho}} \tag{2.5.21}$$

Where K and G denote the bulk modulus and the shear modulus, i.e. $K=E/3(1-2\nu)$ and $G=E/2(1+\nu)$. The CFL condition gives the following limitation on time increment.

$$\Delta t \leq \frac{\min(\Delta x, \Delta y)}{c_{solid}} \tag{2.5.22}$$

As mentioned in the above, the inelastic material model is also included in this thesis. Basically the speed of sound in the part where inelastic deformation occurs is smaller than in the part where fully elastic deformation takes place [48]. From this viewpoint, the limitation represented by eq.(2.5.22) should be valid for a simulation with inelastic deformation.

2.5.5 Treatment of large deformation

As stated in the above sections, information on the material point is mapped onto background grids which have an arbitrary configuration for every single time step in a MPM. Since the reference is always to a current configuration, the formulation is called the updated Lagrangian scheme (i.e.[49]). In addition, the incremental strain computed every time step is assumed to be small because the limitation of a time increment in eq.(2.5.22) is small. Because of this, the current and the deformed configuration within a single time step are assumed to be equivalent. This allows us to use the small strain formulation, i.e. eq.(2.2.7), to compute the strain increment for each incremental time step (nonlinear strain term is negligible).

2.5.5.1 Objective stress rate

One treatment is required to impose the constitutive relation on the solid material. A rate form of the stress-strain relationship, i.e. eq.(2.2.6), is used to handle non-linear material behavior. However, the rate change of a Cauchy stress tensor is not objective while the rate change of a strain rate tensor is objective. In order to satisfy the frame indifference, an objective stress rate tensor is used to impose the constitutive relation. Although there are some choices on an objective Cauchy stress rate, i.e. Truesdell rate and Green-Naghdi rate etc., the Jaumman stress rate is introduced to this thesis because of its simplicity in terms of actual numerical implementation. In order to remove the

effect of rigid body rotation from the stress tensor, the Jaumann rate of Cauchy stress $\hat{\boldsymbol{\sigma}}$ is represented by the following form.

$$\frac{d\hat{\boldsymbol{\sigma}}}{dt} = \frac{d\boldsymbol{\sigma}}{dt} + \boldsymbol{\sigma}\cdot\boldsymbol{\omega} - \boldsymbol{\omega}\cdot\boldsymbol{\sigma} \tag{2.5.23}$$

where $\boldsymbol{\omega}$ is a spin tensor defined by

$$\boldsymbol{\omega} = \frac{1}{2}\left(\frac{\partial v_i}{\partial x_j} - \frac{\partial v_j}{\partial x_i}\right) \tag{2.5.24}$$

The stress rate is now substituted into a rate form of the constitutive relation.

$$\frac{d\hat{\boldsymbol{\sigma}}}{dt} = \frac{d\boldsymbol{\sigma}}{dt} + \boldsymbol{\sigma}\cdot\boldsymbol{\omega} - \boldsymbol{\omega}\cdot\boldsymbol{\sigma} = \mathbf{C}_0 : \frac{d\boldsymbol{\varepsilon}}{dt} \tag{2.5.25}$$

Assuming $d\boldsymbol{\sigma}/dt \approx \Delta\boldsymbol{\sigma}/\Delta t$ and $d\boldsymbol{\varepsilon}/dt \approx \Delta\boldsymbol{\varepsilon}/\Delta t$, an incremental Cauchy stress becomes the following.

$$\Delta\boldsymbol{\sigma} = \mathbf{C}_0 : \Delta\boldsymbol{\varepsilon} + \left(\boldsymbol{\omega}\cdot\boldsymbol{\sigma} - \boldsymbol{\sigma}\cdot\boldsymbol{\omega}\right)\Delta t \tag{2.5.26}$$

Since USF (Update Stress First) method is used in this thesis, $\boldsymbol{\omega}$ in the R.H.S. of the equation is computed by the strain increment $\Delta\varepsilon^{n+1}$ at time step n+1. If we use $\boldsymbol{\sigma}^n$ at previous time step on the R.H.S of the equation, $\Delta\sigma^{n+1}$ is explicitly calculated.

2.5.5.2 Deformation of material point

Since a solid body is represented by a collection of material points, a material point itself is also deformed as the body is deformed. Due to the deformation of material points, the support domain of each point is changed. The change in the support domain of each material point is approximately tracked by a deformation gradient tensor $\mathbf{F}$ at the center of the material point (a time evolution of $\mathbf{F}$ is described in appendix B). Using $\mathbf{F}$, the area of the support domain A at the current time step can be described by

$$A = A_0 \det \mathbf{F} \tag{2.5.27}$$

where A_0 denotes the area of the support domain at the initial state. For an actual computation, the simplicity of the MPM is lost if a rotation of the support domain is

included. The procedure for the construction of the weighted shape function becomes complex (the calculation of the distance between a certain node and a certain point on the support domain of each particle becomes complicated). In this thesis, the support domain change is assumed to occur through a change of the side length in the *x* and *y* directions. Rotation of each support domain is not included. Specifically, side lengths of a current support domain in the *x* direction l_x and in the *y* direction l_y are computed by the following equation.

$$\begin{aligned} l_x^{n+1} &= \left(1+\Delta\varepsilon_{xx}^n\right) l_x^n \\ l_y^{n+1} &= \left(1+\Delta\varepsilon_{yy}^n\right) l_y^n \end{aligned} \tag{2.5.28}$$

From appendix B, the following relation is available for a time evolution of **F**.

$$\mathbf{F}^{n+1} = \left\{ \mathbf{I} + \left(\frac{\partial \mathbf{v}}{\partial \mathbf{x}} \right)^n \Delta t \right\} \cdot \mathbf{F}^n \tag{2.5.29}$$

By taking determinant of the equation,

$$\det \mathbf{F}^{n+1} = \det\left[\left\{ \mathbf{I} + \left(\frac{\partial \mathbf{v}}{\partial \mathbf{x}} \right)^n \Delta t \right\} \cdot \mathbf{F}^n \right] = \det\left\{ \mathbf{I} + \left(\frac{\partial \mathbf{v}}{\partial \mathbf{x}} \right)^n \Delta t \right\} \det \mathbf{F}^n \tag{2.5.30}$$

Since a small strain increment is assumed in this thesis, the equation can be approximated by

$$\begin{aligned} \det \mathbf{F}^{n+1} &\approx \left[\left(1+\Delta\varepsilon_{xx}^n\right)\left(1+\Delta\varepsilon_{yy}^n\right) - \Delta\varepsilon_{xy}^n \Delta\varepsilon_{yx}^n \right] \det \mathbf{F}^n \\ &\approx \left(1+\Delta\varepsilon_{xx}^n\right)\left(1+\Delta\varepsilon_{yy}^n\right) \det \mathbf{F}^n \end{aligned} \tag{2.5.31}$$

Eq.(2.5.28) should be a good approximation for a change of a support domain of each material point.

It should be noted that nodal mass is assembled by eq.(2.5.13). If some material points are close to cell boundaries, an extremely small nodal mass will be assembled to some nodes. This creates a phantom node which might have a large unphysical nodal acceleration associated with the procedure in eq.(2.5.15). In order to avoid this situation, a tolerance of mass *MTOL* is defined in the actual computation.

2.5.6 Treatment of contact

A contact phenomenon associated with an applied deformation is also of interest in this thesis, i.e. self contacts within single dendrite and contacts on grain boundaries. Numerical methods for the structural analysis should account for this phenomenon. Due to the use of background grids for solving the equation of motion, the no slip condition is automatically imposed on material points which are a contact pair because a single velocity field which is reproduced from the nodal velocity is imposed on those material points when the points are located in a common background cell (those material points behave as a single solid structure). In the actual phenomenon, a sliding motion would be observed, and would be dependent on the contact pressure and solid fraction of the region etc. A numerical algorithm which is capable of handling such sliding motion in MPM analysis has been developed by some researchers [53 and 54]. However, for numerical simplicity, only the no slip contact condition which is automatically included in MPM is considered in this thesis as a first approximation.

For instance, an impingement analysis of two squared solids with an elasto-perfectly plasticity constitutive model is performed in Figure 2. 19. The simulation is only to present the computational capability of the MPM to handle contact phenomenon, so the details of the material model etc. are omitted here.

The equivalent plastic strain (upper panels) and von Mises stress (lower panels) contours are presented at the initial state, 12.5%, 25%, and 37.5% compression (from left to right panels). The two squares are merged and compressed together without any special treatment. The capability of handling the contact in a simple manner is sufficient as a first approximation of the phenomenon in this thesis.

2.5.7 Validation of the material point method

In this section, benchmark problems are demonstrated to examine the accuracy of the material point method implemented in this thesis.

2.5.7.1 Validation of elastic response: Timoshenko cantilever problem

The elastic material behavior of the MPM is examined in this section (see 2.2.3.1.1 and appendix B for details of the model). The Timoshenko and Goodier cantilever problem is selected as the validation problem. The problem is employed to validate our material point method in the elastic regime. As shown in Figure 2. 20, a beam is placed on the left wall and vertical load is applied at the right tip of the beam. Analytical solutions of the horizontal displacement d_x and the vertical displacement d_y are given by the following equations [72].

$$\begin{aligned} d_x(x,y) &= \frac{P_l y}{6EI}\left[(6L-3x)x+(2+\nu)\left(y^2-\frac{H^2}{4}\right)\right] \\ d_y(x,y) &= -\frac{P_l}{6EI}\left[3\nu y^2(L-x)+(4+5\nu)\frac{H^2 x}{4}+(3L-x)x^2\right] \end{aligned} \tag{2.5.32}$$

Stress components are represented by

$$\begin{aligned} \sigma_{xx}(x,y) &= \frac{P_l(L-x)y}{I} \\ \sigma_{yy}(x,y) &= 0 \\ \tau_{xy}(x,y) &= -\frac{P_l}{2I}\left(\frac{H^2}{4}-y^2\right) \end{aligned} \tag{2.5.33}$$

where H is the height of the beam, L is the length of the beam, and P_l is the point force acting at the tip of the beam. $I = H^3/12$ is the second moment of area around z-axis, ν is Poisson's ratio and E is Young's modulus. As mentioned before, the plane strain condition is assumed. The geometrical settings of the beam are the same as the work done by Andersen et al. [73], L=8 and H=1. The beam is discretized into 32x4 background cells, and each cell is filled with 2x2 material points (a total of 512 material points) as illustrated in Figure 2. 20 lower panel. Boundary conditions are imposed as Figure 2. 21. For the left boundary, the centroid of the cross section of the beam is fixed in both x and y directions. The nodal points on the cross section are fixed only in the x direction. As

pointed out by Timoshenko et al. [72-74], the analytical solutions in the case described above are obtained only if the load P_l has the same parabolic distribution as τ_{xy} on the cross section at the tip. For this reason, the same parabolic profile as the shear stress is imposed on the right end of the beam as a loading condition. Specifically, the loading is numerically implemented in the form of an external acceleration (same as the body force term in eq.(2.5.5)) such that the summation of the acceleration becomes equivalent to a magnitude of the loading P_l. Since the material point method is a transient analysis, an immediate change of loading condition may cause vibrations within the beam. In order to avoid the undesired vibrations, the loading is assigned as the following cosine type moderate time variation.

$$F(t)=\begin{cases} 0 & \text{for } t \le 0 \\ \left\{\cos\left(\pi\dfrac{T_p-t}{T_p}\right)+1\right\}\dfrac{P_l}{2} & \text{for } 0 < t < T_p \\ P_l & \text{for } T_p < t \end{cases} \tag{2.5.34}$$

where T_p is the time period. Simulation is performed up to t=40 with setting T_p=20. A time increment Δt=0.001, Young's modulus E=3x10^7, Poisson's ratio ν=0.3, density of the beam ρ_0=10^3, and P_l=100 are used as the simulation conditions.

Figure 2. 22 represents time history of the vertical displacement at the right edge of the beam. The beam reaches an equilibrium state around t=20, so the comparison of the results at t=40 should be sufficient. A comparison of the vertical displacement along the horizontal centerline is plotted in Figure 2. 23. No significant difference is observed between our calculation results and the analytical solution. Contours of σ_{xx} on background Eulerian nodes are illustrated in Figure 2. 24. Tensile stress acts on the upper side of the beam whereas compression stress acts on lower side. The stress state is what we expected. Figure 2. 25 and Figure 2. 26 show profiles of σ_{xx} and τ_{xy} along the vertical centerline (at x=4) of the beam. The xx component of the stress corresponds well with the analytical result given by eq.(2.5.33). On the contrary, the xy component of

stress shows a stepwise profile, but its averaged profile seems to match with analytical one. As pointed by Andersen et al.[73], the profile is caused by the use of a linear shape function, i.e. eq.(2.5.18). The function can only describe a linear dependence on x or y within the background cell while the analytical solution of τ_{xy} is represented by a quadratic function of y. Thus, the lack of ability to construct higher order interpolation within the cell is the main cause of the profile. The issue would be improved by introducing a higher order shape function or a finer background mesh. For instance, the results obtained by meshes four times finer (64x8 background cells with 2048 material points) are presented in Figure 2. 27 and Figure 2. 28. The resolution of τ_{xy} is improved by the modification. Basically, the phase-field simulation is performed with quite fine meshes which can resolve the variations of phase-field and temperature within the diffuse interface. The issue of the stepwise distribution of τ_{xy} would not be significant.

2.5.7.2 Validation of elasto-plastic response: an elasto-plastic bar under tensile/compression loading

Elasto-plastic mechanical response is examined in this section (see 2.2.3.1.2 and appendix B for details of the model). A simple tensile and compression loading problem is designed and demonstrated. A dumbbell type specimen shown in Figure 2. 29 is defined (left panel) and discretized with 288 material points (right panel). On the top and bottom edges of the specimen, a displacement is imposed as the following function of time (through nodal velocity) such that both compression and tensile loading act on it.

$$\begin{aligned} d_x &= 0.0 \\ d_y &= A_0 \sin\left(\frac{2\pi}{T_p} t\right) \end{aligned} \tag{2.5.35}$$

where A_0 is the amplitude of the sine wave, and again T_p is the time period. The values A_0=0.01(maximum strain =0.5%) and T_p=40 are used in this validation. The mechanical properties of the specimen are specified as E=3x10^7, ν=0.3, and ρ_0=10^3 . In

addition, the yield stress σ_Y=6x10^4(yield at 0.2% tensile strain) is defined for the elasto-perfectly plasticity model.

The computed stress-strain curve is plotted in Figure 2. 30. In the graph, an equivalent stress σ_{eq} is defined by the von Mises stress with a sign that depends on σ_{yy}. As indicated in the graph, the plastic strain starts evolving exactly at the yield stress, and stress remains at the yield stress during the plastic deformation. Once the total strain reaches its maximum (0.5% which is determined by A_0), unloading takes place following the elastic regime. Since no anisotropy in terms of plasticity is considered, the specimen reaches yielding at the same magnitude of the yield stress as in the compression state. As a result, the specimen has stress due to plastic deformation even if the total strain returns back to zero. The stress-strain curve is exactly what we expected from the parameters and imposed displacement settings. From the validation presented,we can see that the elasto-perfectly plasticity model implemented in the MPM in this thesis should be adequate to use for an actual problem.

2.5.7.3 Validation of an elasto-visco-perfectly plastic response: an elasto-visco-plastic bar under tensile loading

The Elasto-perfectly-visco-plastic material model is examined in this section (see 2.2.3.1.3 and appendix B for details of the model). For the visco-plasticity model, a rate of change of deformation affects its dynamic yield stress, thus a constant displacement with respect to time is imposed as the boundary condition on the same specimen used in the preceding section (also the same discretization). In this validation, three different displacement boundary conditions, i.e. $d\varepsilon/dt$=4.0e-4, 8.0e-4, and 1.6e-3, are specified. The same parameter settings as the preceding section are used except for the relaxation time τ_{visco}=0.13 which defines the decay time of the viscous effect .

The computed stress-strain curves of the three strain rates are presented in Figure 2. 31. Higher imposed strain rate provides higher yielding stress. As presented in

appendix B, the Perzyna model with a function $\Phi(f_Y)= f_Y$ provides a linear dependence of the dynamic yield stress on the strain rate.

The numerical code of the MPM developed in this thesis possesses a capability of handling an elasto-perfectly-visco-plasticity constitutive behavior.

2.5.7.4 Validation: a rectangular bar with large shear deformation

In the last three sections, the basic characteristics of the constitutive models implemented in this study are examined. Validation presented in this section examines the capability of the MPM to handle large deformation. The shearing process of a rectangular bar with an elasto-perfectly plasticity constitutive law is computed. The same simulation is performed using FEM ANSYS 12.0 [75] for comparison purposes.

As illustrated in the left panel of Figure 2. 32 , a rectangular solid bar whose dimension is $L/2xL$ is defined, and a lateral displacement is imposed on both the upper and the lower surfaces of the bar. Vertical displacement is prohibited on the boundaries. The solid bar is represented by 25x50 cells for both the MPM analysis (background cell filled by 2x2 material points) and the FEM analysis (quadrilateral element with linear shape function). For the MPM analysis, the full computational domain is defined by 101x51 background nodes, and a phase-field is assigned to each node such that ϕ=0 corresponds to the solid outline (Figure 2. 32 right panel) at the initial state. The phase-field profile is advected by the solid deformation velocity with the methodology developed in the preceding section. The material properties of the solid bar are specified as E=200[GPa], Poisson's ratio ν=0.33, and yield stress σ_Y=400[MPa] for both the MPM and FEM analysis. In order to treat large deformation (geometrical non-linearity), an option of non-linear geometry NLGEOM is activated in the FEM analysis done by ANSYS 12.0.

The computed von Mises stress (left panels) and equivalent plastic strain (right panels) contours for both the MPM (upper panels) and the FEM (lower panels) at 40% shear strain (= displacement / height of the solid bar) are illustrated in Figure 2. 33. In the result of the MPM, material points lie on the deformed configuration, and the contour colors are overlaid on each material point. The increment of the equivalent plastic strain is computed by the following equation.

$$\Delta\bar{\boldsymbol{\varepsilon}}^{p}_{n+1} = \sqrt{\frac{2}{3}}\left\|\Delta\boldsymbol{\varepsilon}^{p}_{n+1}\right\| = \sqrt{\frac{2}{3}\,\Delta\boldsymbol{\varepsilon}^{p}_{n+1} : \Delta\boldsymbol{\varepsilon}^{p}_{n+1}} \tag{2.5.36}$$

Next, the total equivalent plastic strain is defined as a summation over time.

$$\bar{\boldsymbol{\varepsilon}}^{p}_{n+1} = \bar{\boldsymbol{\varepsilon}}^{p}_{n} + \Delta\bar{\boldsymbol{\varepsilon}}^{p}_{n+1} \tag{2.5.37}$$

As presented in the figure, most parts of the solid bar reach the yield stress, thus the deformation is considered to be large enough. Quite similar Mises stress and equivalent plastic strain distributions are observed for both the MPM and the FEM analysis. The left panel of Figure 2. 34 shows the profiles of the von Mises stress along the sampling lines indicated in the upper panels of Figure 2. 33 . Although small differences between two methods are observed, both profiles have quantitatively good agreement with each other. The computed solid outlines of both methods are also presented in Figure 2. 34 right panel. For the result of the MPM, ϕ=0 contour line is plotted as the solid outline. The MPM implemented in this thesis provides correct solid motion and advected phase-field profile due to the motion.

In order to show the computational capabilities of the MPM to handle large deformation, the deformation state at 60% shear is shown in Figure 2. 35. At this deformation state, the FEM analysis is terminated due to mesh collapse around corners of the solid bar. Therefore, the choice of the MPM as a numerical method of solid deformation should be suitable, and gives good performance even if it couples with phase-field advection.

(a)

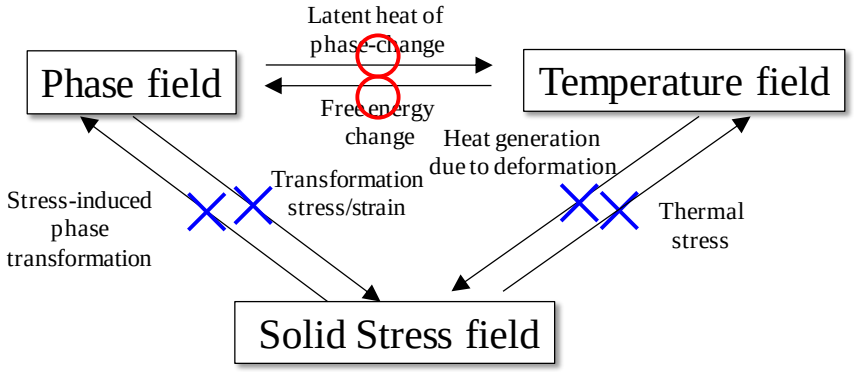

(b)

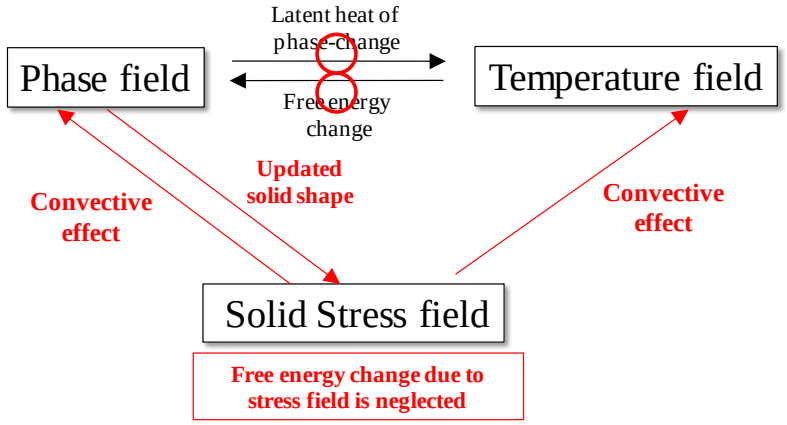

Figure 2. 1 Diagrams of interactions among three fields; (a) Interactions for full coupling; (b) Interactions simplified and considered in this thesis.

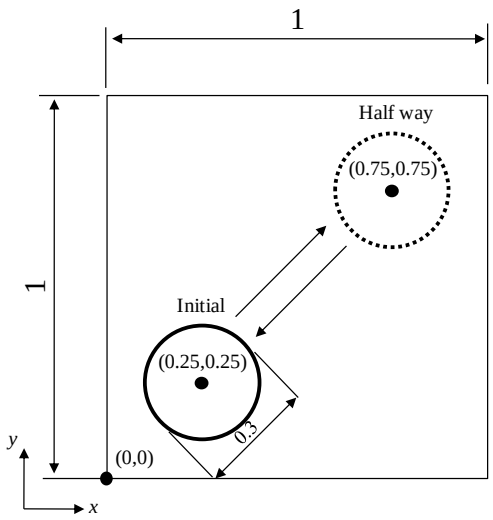

Figure 2. 2 Geometrical settings used in a diagonal translation of a circle problem; A circle is initially placed at (0.25, 0.25) and moves diagonally until its center reaches at (0.75, 0.75). Then, the circle moves back to an initial location.

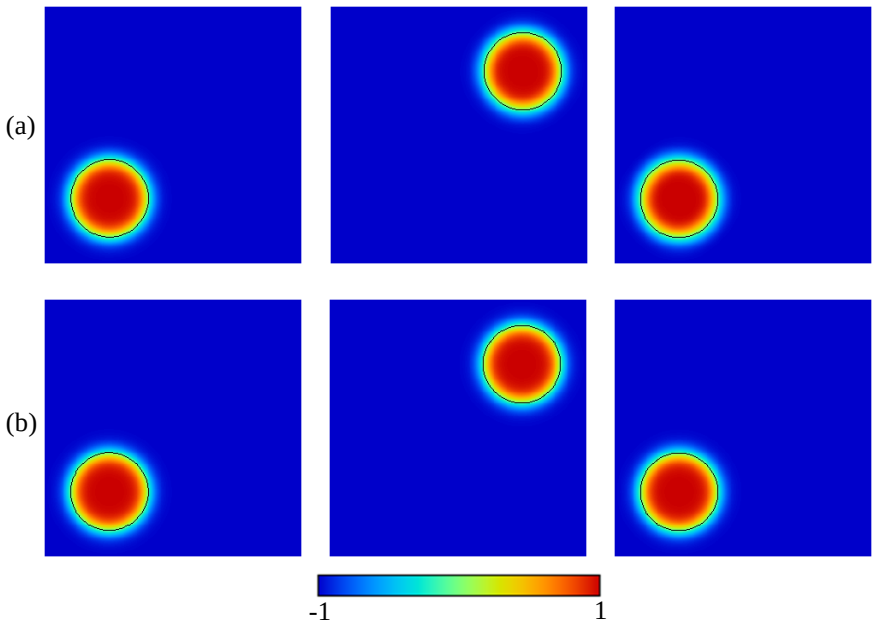

Figure 2. 3 Phase-field contours for a diagonal translation of a circle problem; (a) Meshes of 80x80; (b) Meshes of 160x160; Left panels: at initial state; central panels: at a half domain translation; right panels: at a full domain translation.

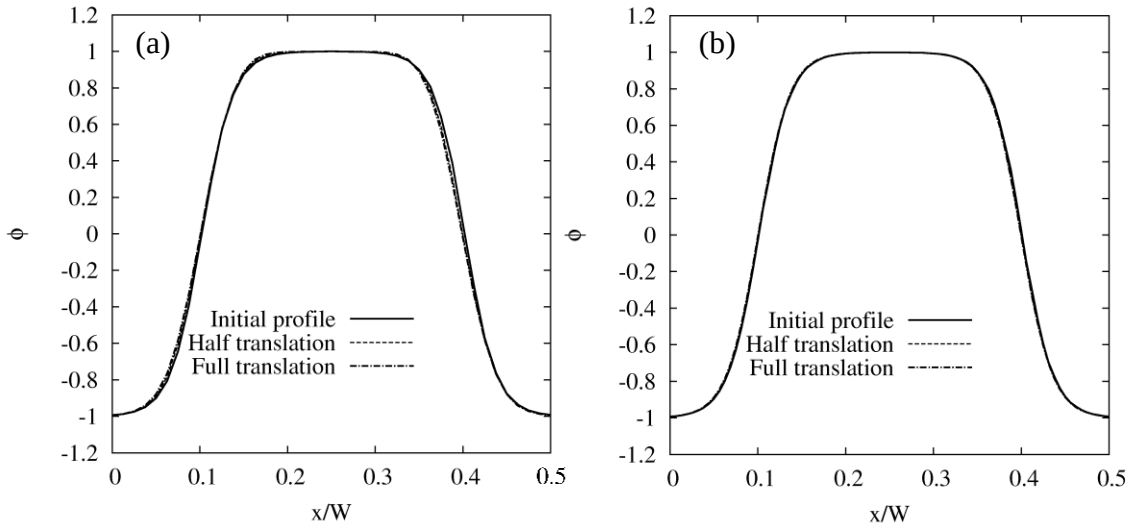

Figure 2. 4 Phase-field profiles along a horizontal center line passing through the center of the circle for three different states (initial, a half translation, and a full translation); (a) Meshes of 80x80; (b) Meshes of 160x160.

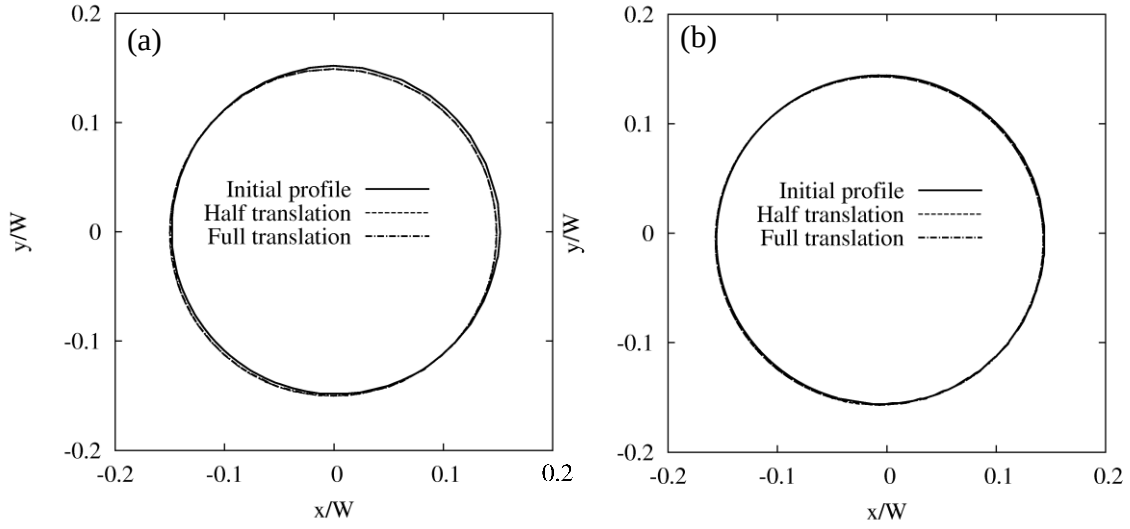

Figure 2. 5 Computed ϕ=0 contour lines for three different states (initial, a half translation, and a full translation); (a) Meshes of 80x80; (b) Meshes of 160x160; Centers of circles correspond with each other.

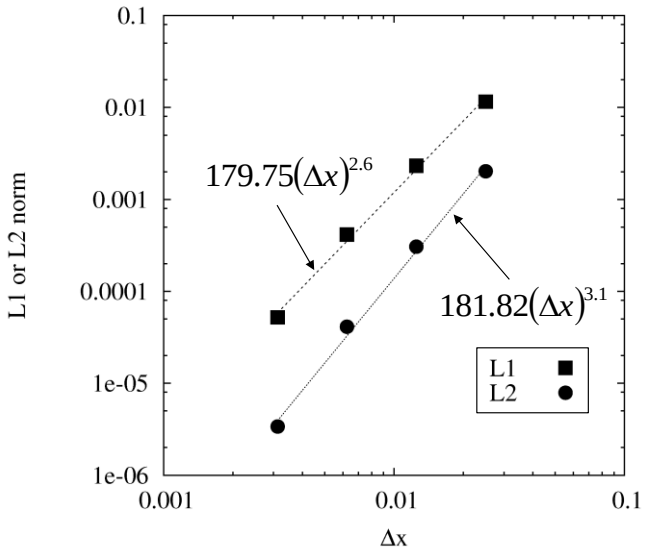

Figure 2. 6 L_1 and L_2 norms computed from a diagonal translation of a circle problem with different spatial increment Δx while an interface thickness W is fixed; Meshes of 160x160 are used; From fitted curves presented in the figure, an order of accuracy of the CIP method implemented in this thesis shows 2.6-3.1 order.

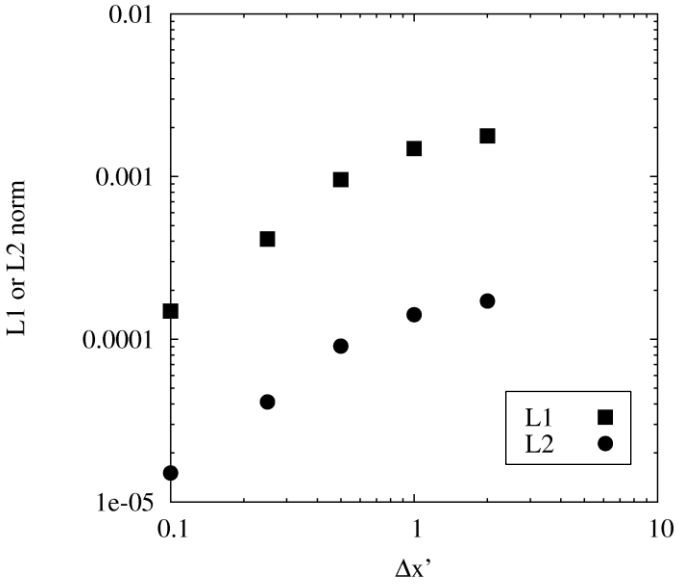

Figure 2. 7 L_1 and L_2 norms computed from a diagonal translation of a circle problem with different $\Delta x'=\Delta x/W$; W is varied while a special inclement Δx is fixed; Meshes of 160x160 are used.

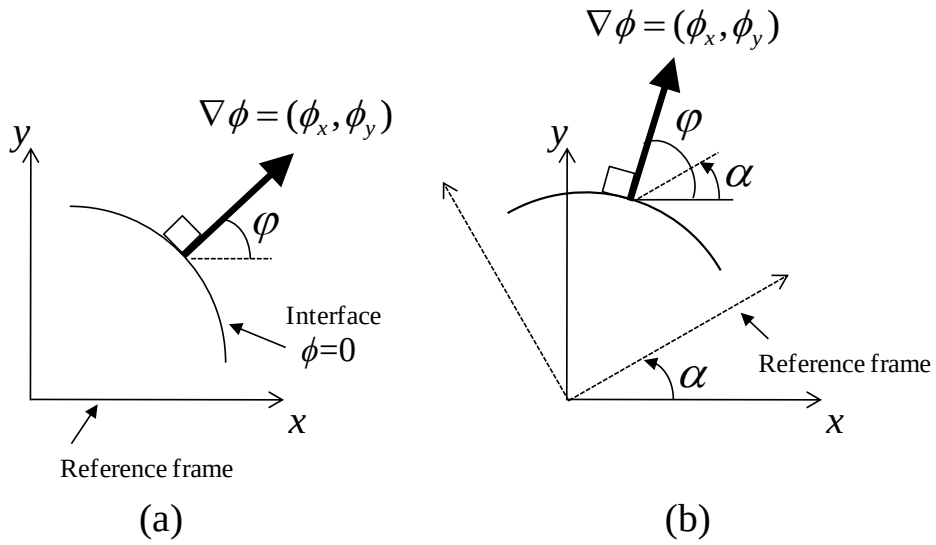

Figure 2. 8 Representations of a crystallographic orientation in the computational model; (a) Configuration at initial state or no deformation state; (b) Configuration at deformed state; Due to the applied deformation, a reference frame which aligns with the orientation direction is changed.

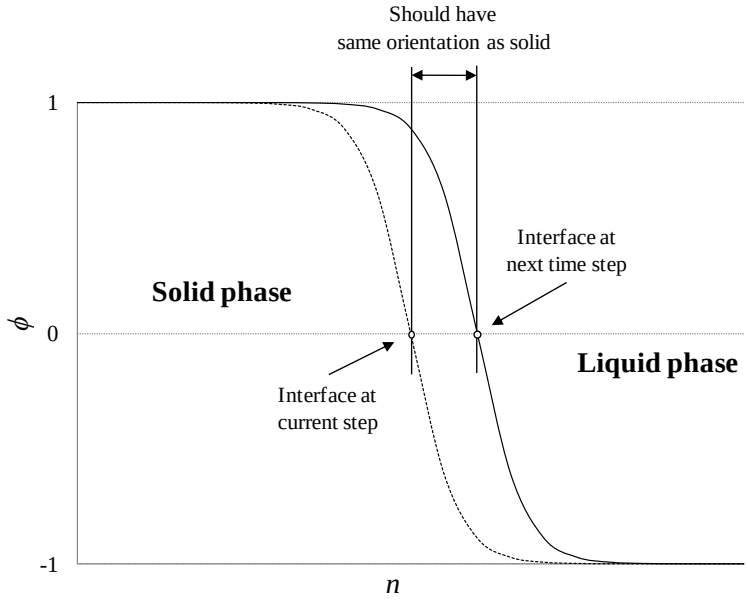

Figure 2. 9 A schematic of phase-field profiles across the interface at current (dashed line) and next time step (solid line); the portion where a liquid phase changes to a solid phase needs to have the same orientation as the closest solid phase.

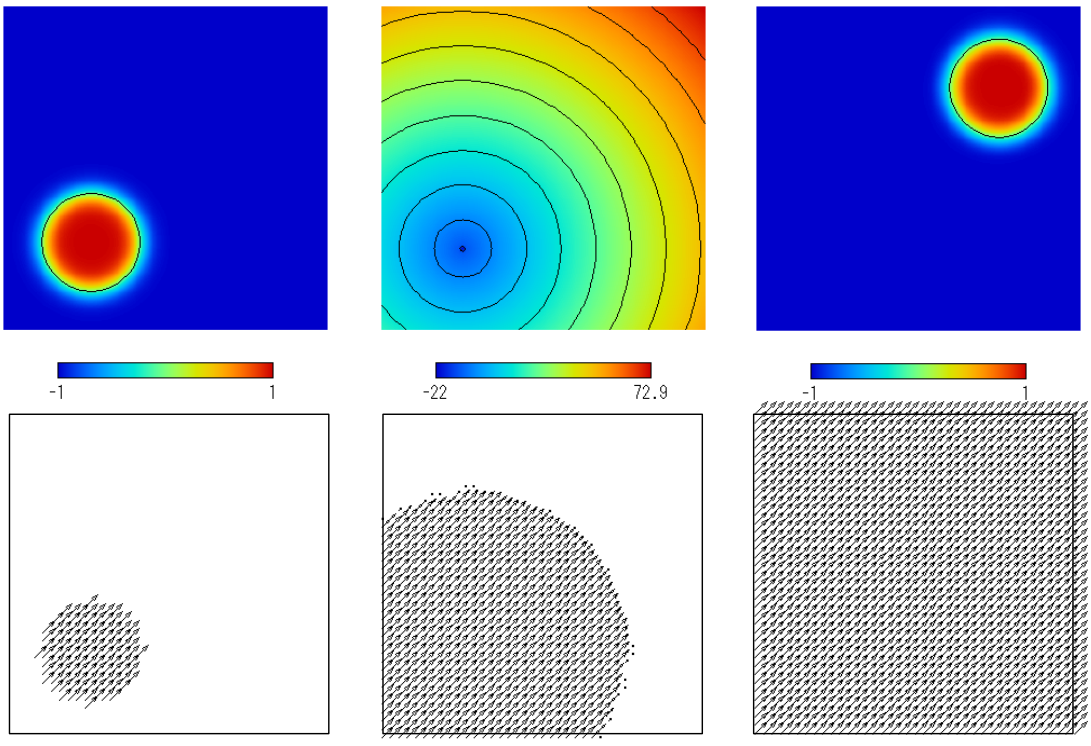

Figure 2. 10 A sequence of a diagonal translation of a circle problem with the extension of velocity field; Upper left panel: initial phase-field profile; Upper central panel: contours of the signed distance function converted from phase-field; Upper right panel: phase-field at a half translation; Lower panels: a sequence of the extension of velocity field at initial time step at initial substep (lower left panel) at a.half way of the extension (lower central panel), and at a full extension of velocity field (lower right panel). Velocity vectors are presented in the panels.

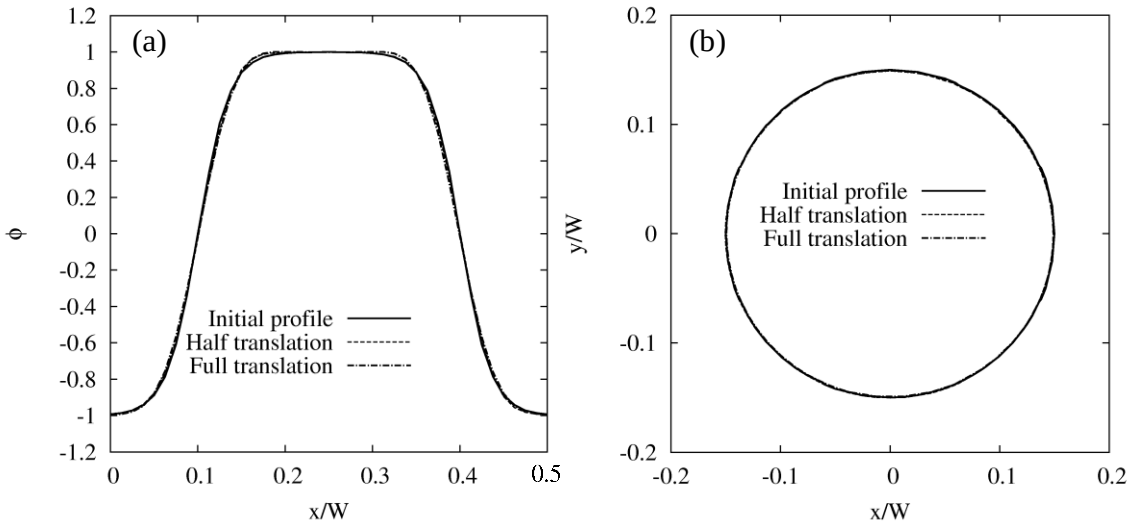

Figure 2. 11 Computed phase-field contours of a diagonal translation of a circle with the extension of velocity field extension; (a) Phase-field profiles along a horizontal center line passing through the center of the circle; (b) Computed ϕ=0 contour lines for three different states (initial, a half translation, and a full translation); Meshes of 80x80 are used.

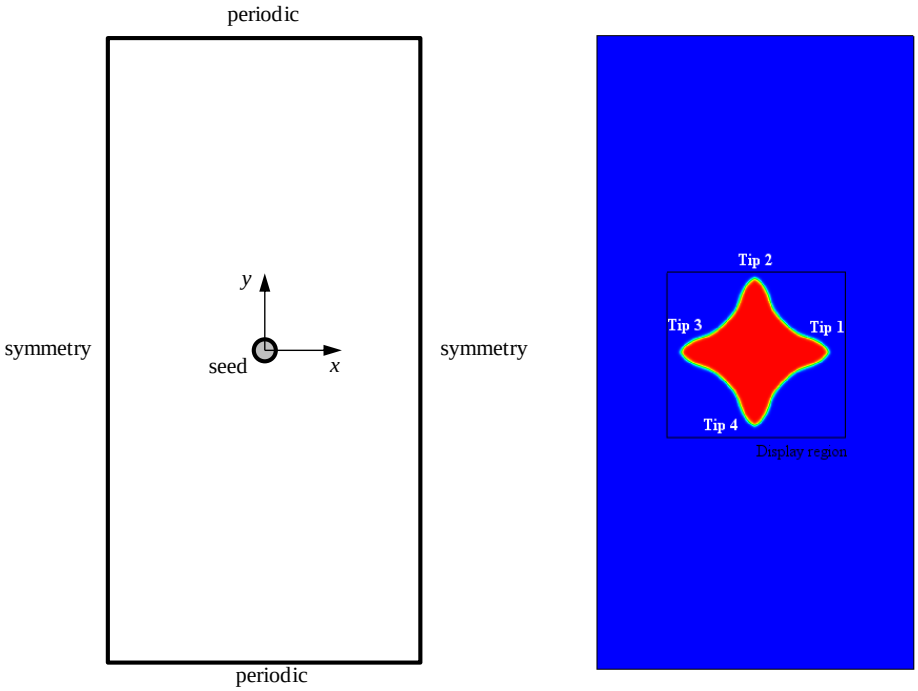

Figure 2. 12 Geometrical settings and boundary conditions of phase-field dendritic solidification under a given rotational velocity field; Right panel: a configuration of Tip1~Tip4 and magnified area which will be presented in the later figures.

D	d_0/W_0	ε	Vd_0/D			
			Exact	Data*	This study: No-rotation	This study: Rotation
4	0.139	0.05	0.0170	0.0175	0.0162	0.0164
3	1.185	0.05	0.0170	0.0175	0.0180	0.0180
4	0.139	0.03	0.0111	0.0112	0.0109	0.0108

Table 2. 1 Comparisons of dimensionless tip velocities with benchmark data

* Source: Tong, X.; Beckermann, C. *Phys. Rev. E* **2001**, 63, 061601

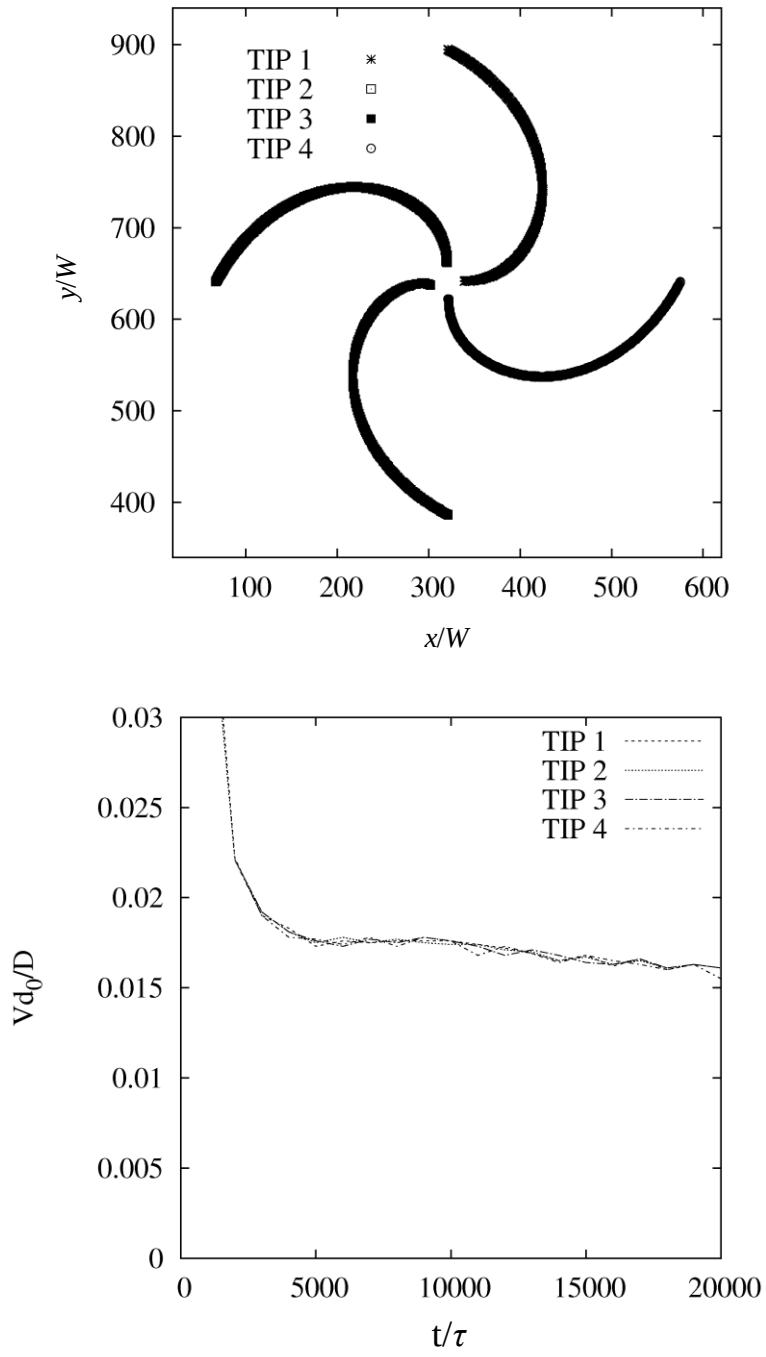

Figure 2. 13 Trajectories (upper panel) and time histories of dimensionless tip velocity (lower panel) of TIP 1~TIP 4 up to 90° rotation (D=3,d_0/W_0=0.185,ε=0.05)

.

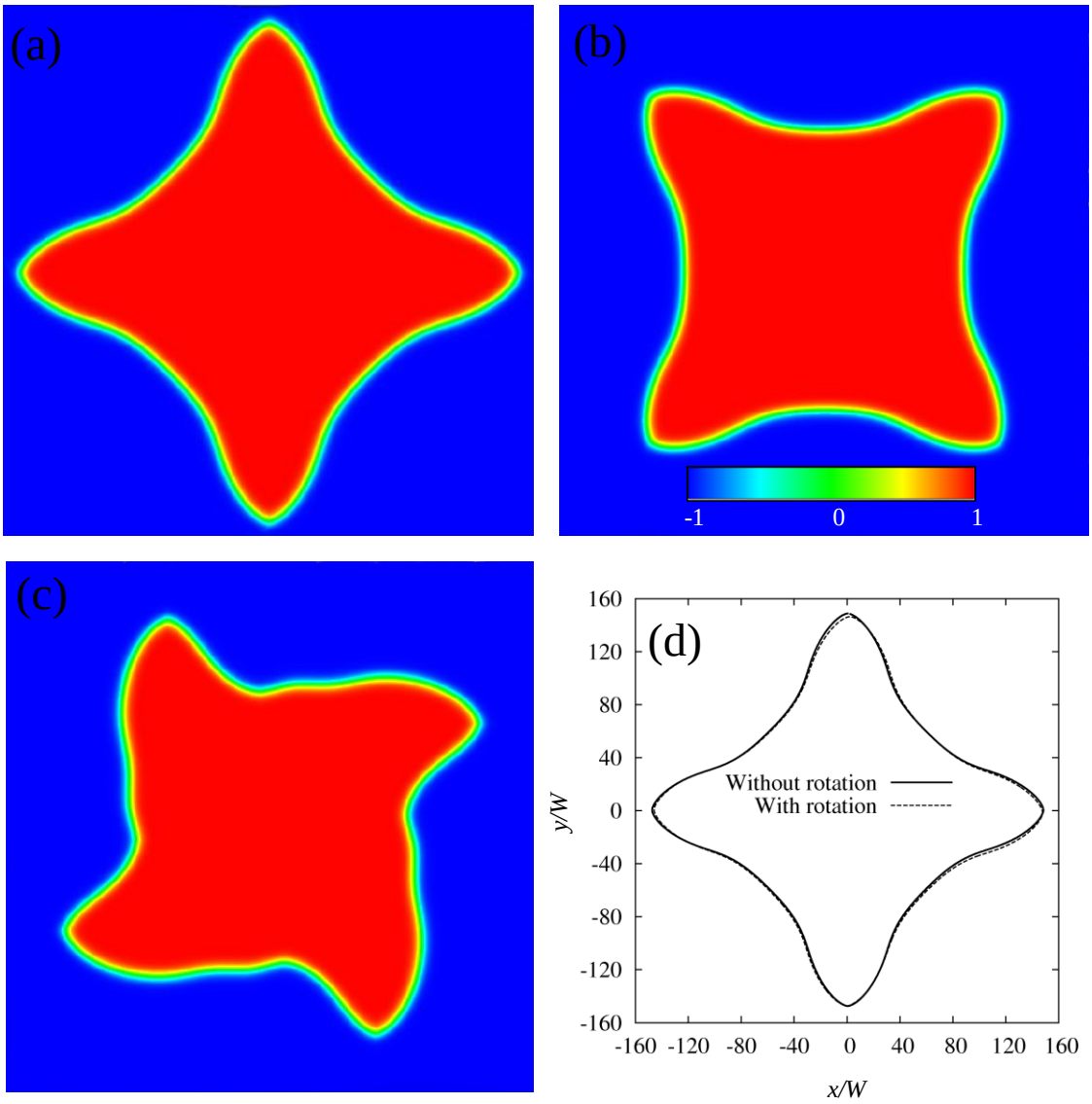

Figure 2. 14 Phase field contours of three different operating conditions (D=3,d_0/W_0=0.185,ε=0.05); (a) Without rotation, (b) With rotation at 45 degrees and a change of orientation angle is reflected in the phase-field equation; (c) With rotation at 45 degrees, and no consideration is made for a change of orientation angle in the phase-field equation; (d) Computed ϕ=0 contours of (a) and (b).

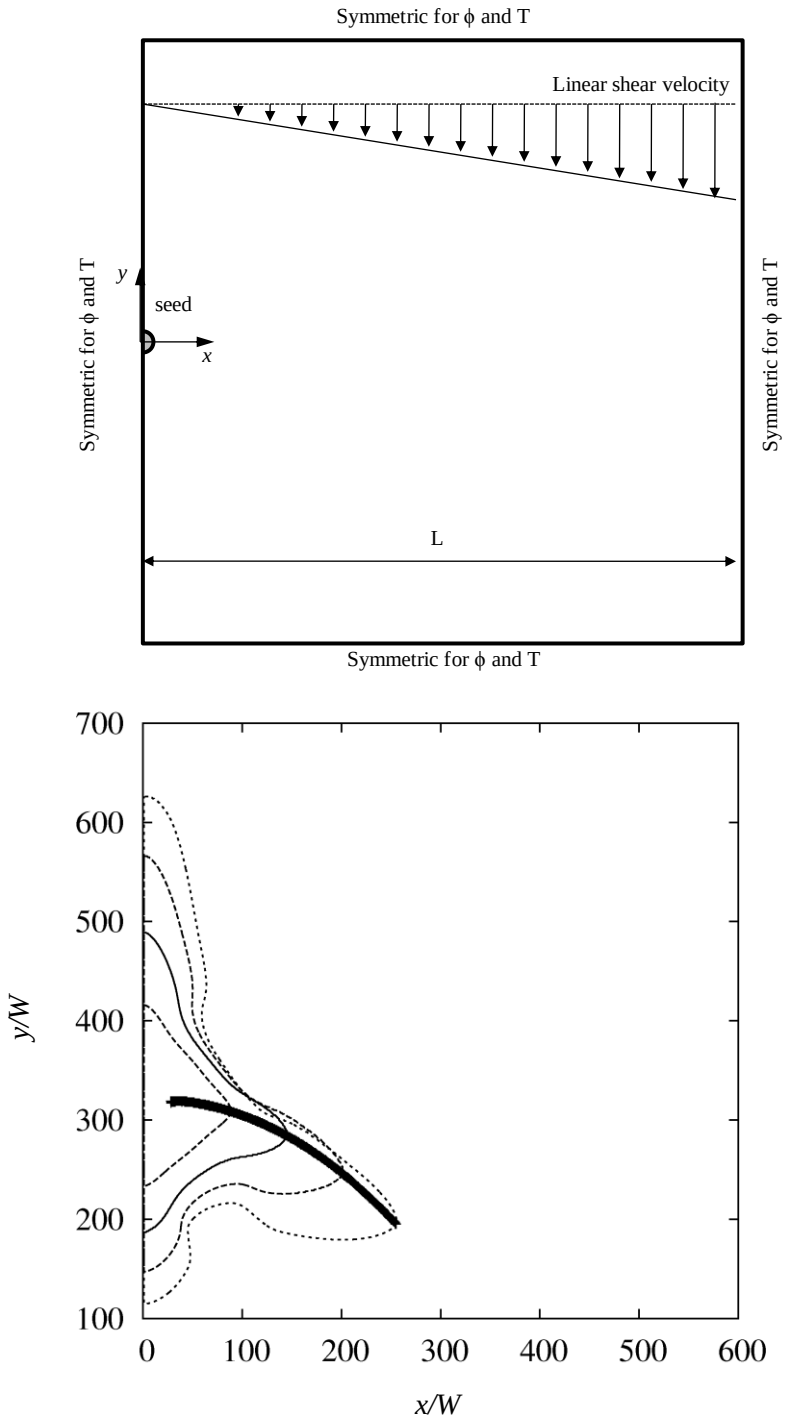

Figure 2. 15 Computational settings of dendrite solidification under a given linear shear velocity field (upper panel) and computed ϕ=0 contours at every 5000 time steps with a trajectory of dendrite tip (lower panel); D=3,d_0/W_0=0.185,ε=0.05 are used.

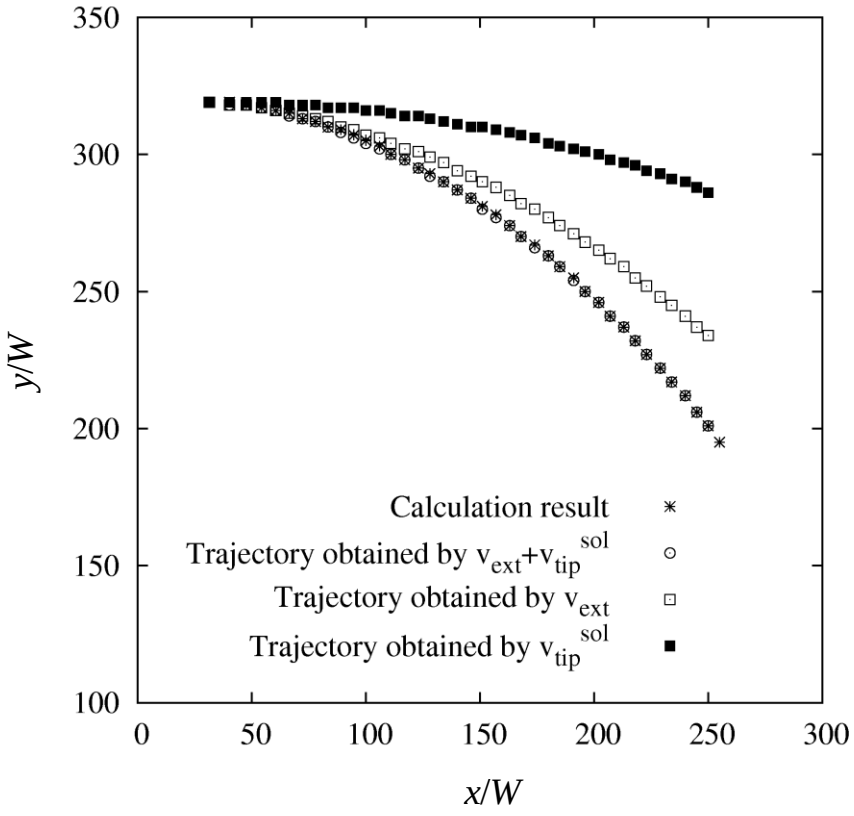

Figure 2. 16 Trajectories of growing dendrite tip under linear shear velocity field for four different cases; A trajectory directly obtained by phase-field simulation (cross mark), a trajectory obtained by only considering imposed external velocity (open square), a trajectory obtained by only considering tip solidification velocity with semi-analytical way (filled square), and a trajectory obtained by considering both external velocity and tip velocity (open circle).

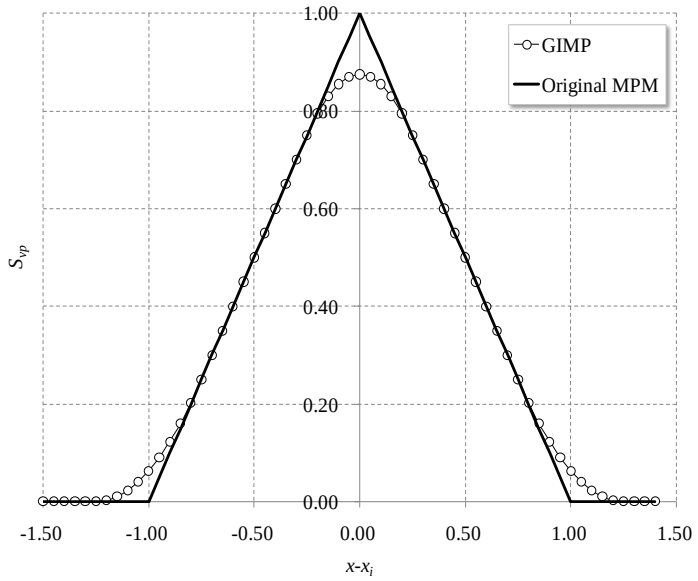

Figure 2. 17 Weighted shape function of the original MPM and the GIMP

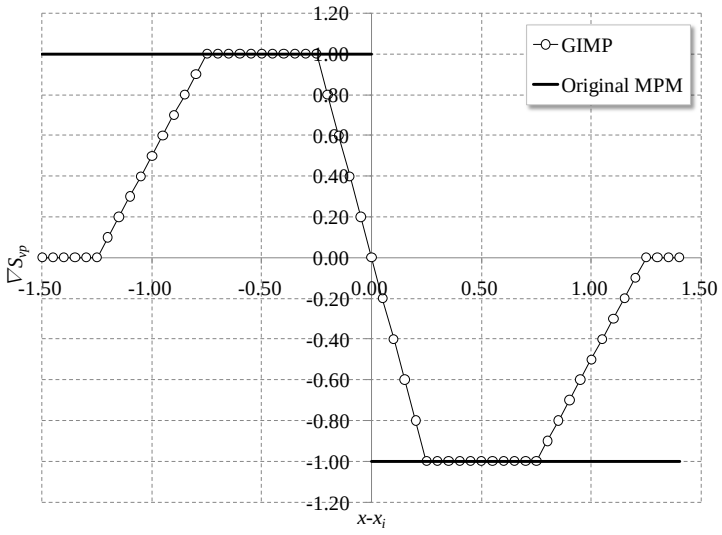

Figure 2. 18 Gradient of weighted shape function of the original MPM and the GIMP

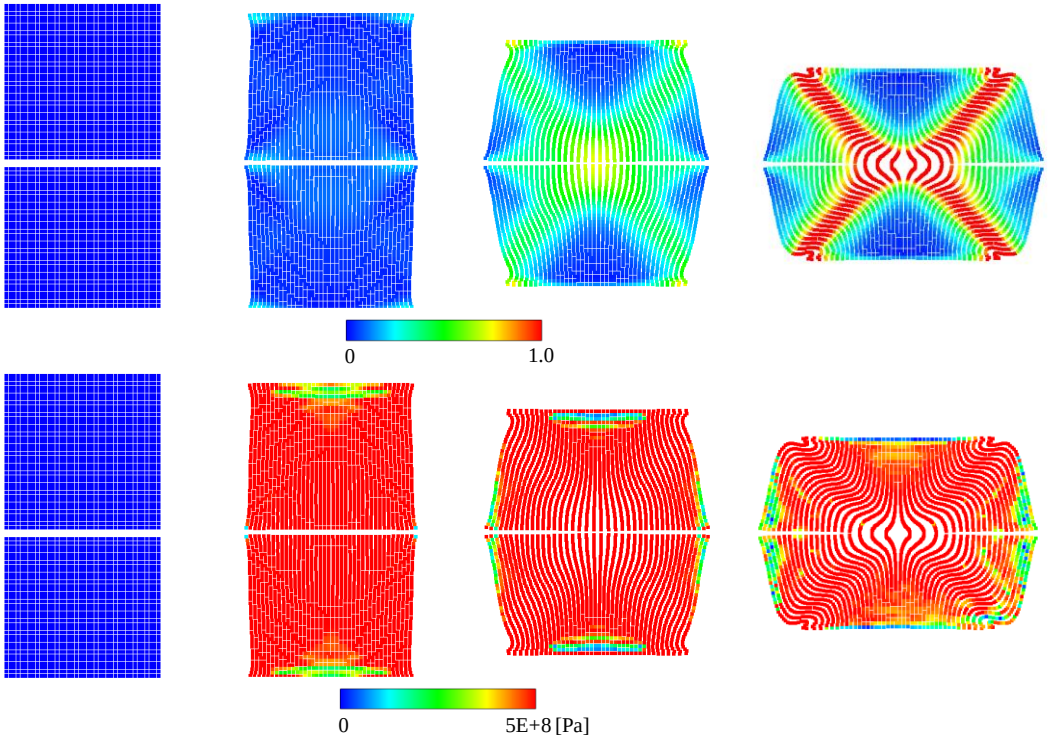

Figure 2. 19 Impinging two squares under compression loading; Upper panels: equivalent plastic strain; Lower panels: von Mises stress at initial state (left panels), at 12.5% compression (panels in the second column from the left), at 25% compression (panels in the third column from the left), and at 37.5% (right panels); No slip contact condition is automatically introduced in the MPM analysis.

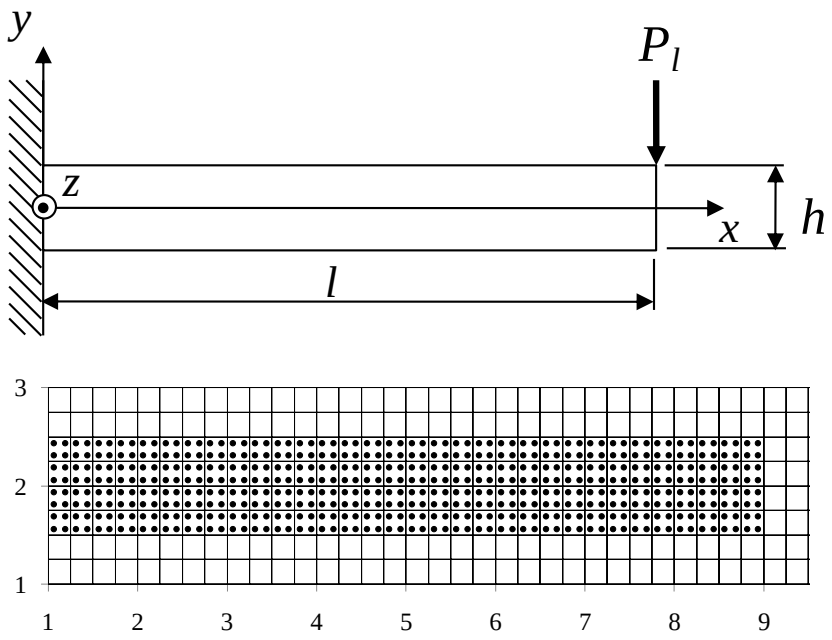

Figure 2. 20 Geometrical settings of the Timoshenko cantilever problem (upper panel) and initial distribution of material points (lower panel)

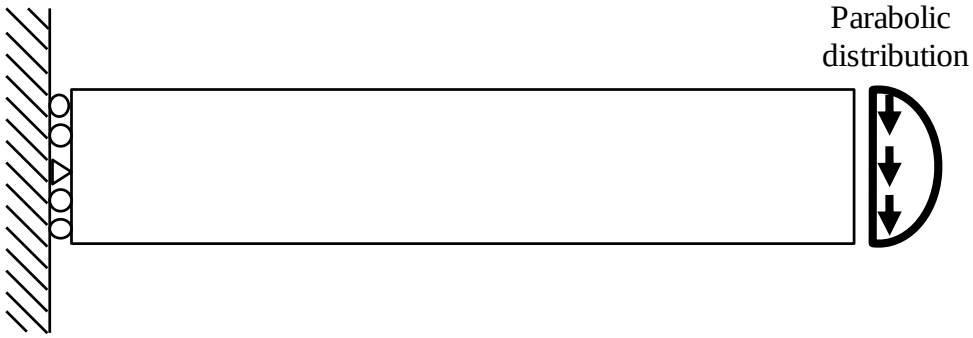

Figure 2. 21 Boundary and loading conditions of the Timoshenko cantilever problem.

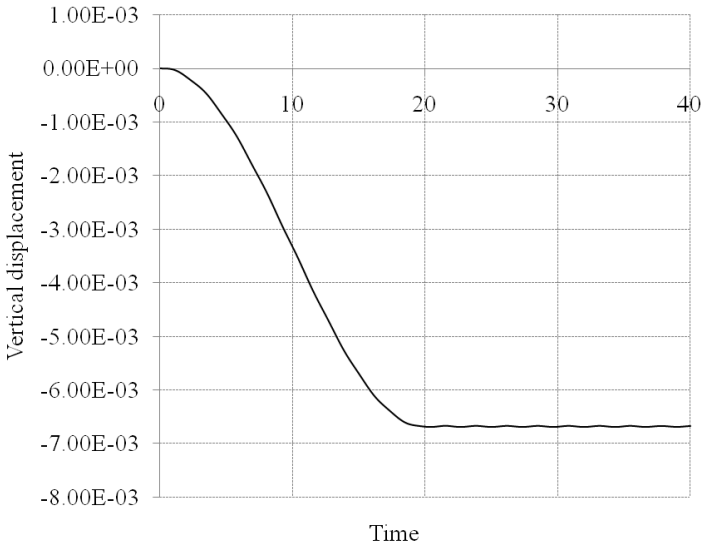

Figure 2. 22 A time history of vertical displacement of the tip of the beam

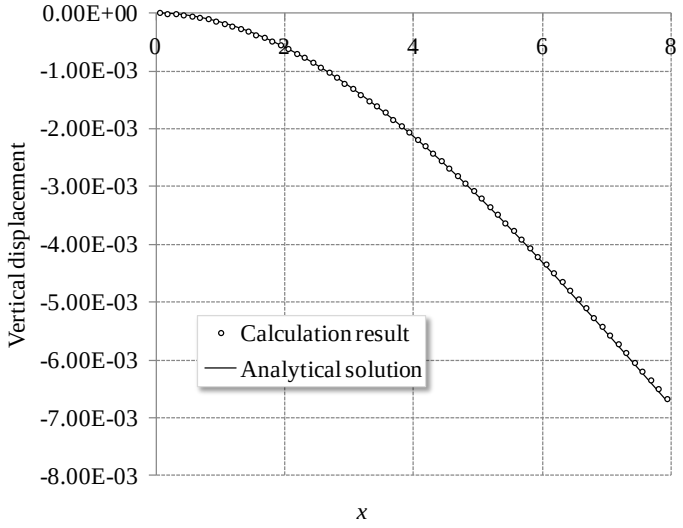

Figure 2. 23 A comparison of the vertical displacement along the horizontal centerline of the beam between calculation result (open circle) and analytical solution (solid line).

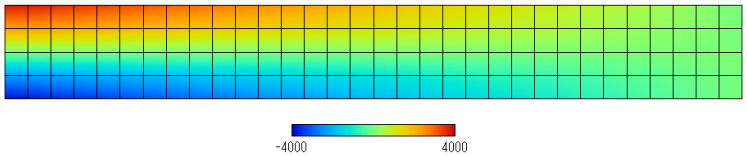

Figure 2. 24 Contours of σ_{xx} on background nodes; the background cells which include material points are only presented.

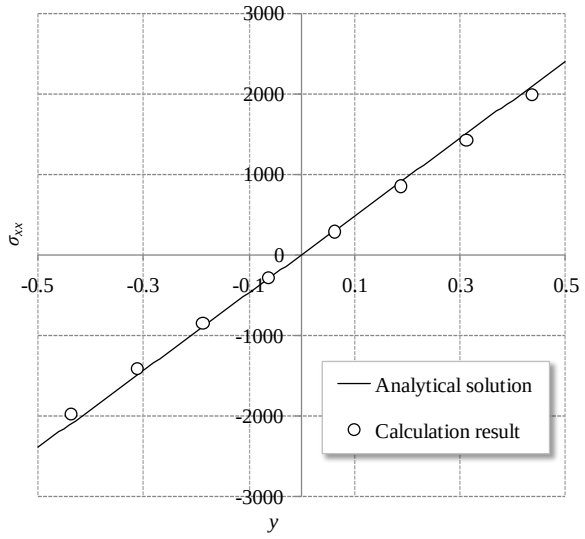

Figure 2. 25 Comparison of σ_{xx} profiles along vertical centerline (the line at x=4); computed stress (open circle) and analytical one (solid line) are plotted; computational result is by background cells of 32x4 with 512 material points.

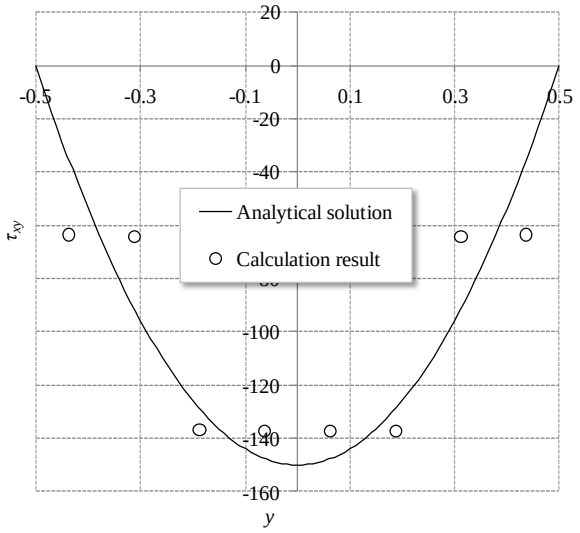

Figure 2. 26 Comparison of τ_{xy} profiles along vertical centerline (the line at x=4); computed stress (open circle) and analytical one (solid line) are plotted; computational result is by 32x4 background cells with 512 material points.

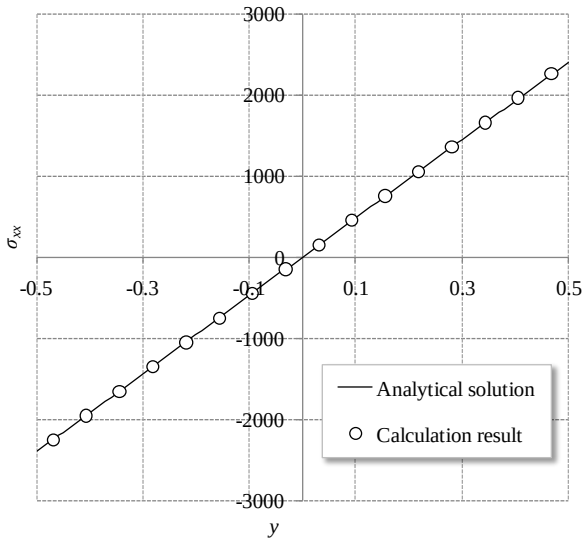

Figure 2. 27 Comparison of σ_{xx} profiles along vertical centerline (the line at x=4); computed stress (open circle) and analytical one (solid line) are plotted; computational result is by 64x8 background cells with 2048 material points.

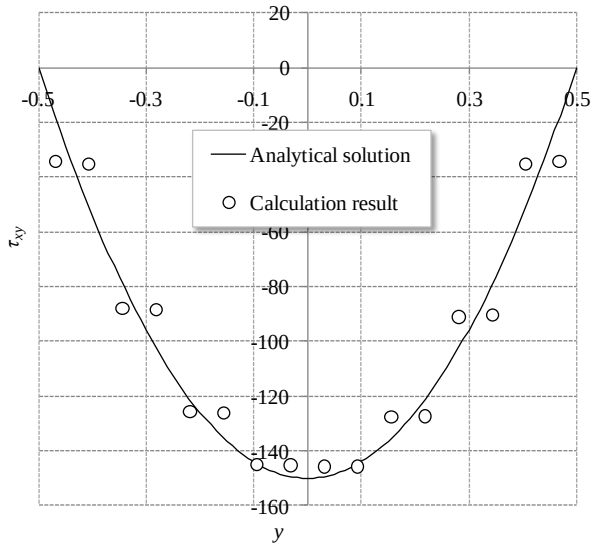

Figure 2. 28 Comparison of τ_{xy} profiles along vertical centerline (the line at x=4); computed stress (open circle) and analytical one (solid line) are plotted; computational result is by 64x8 background cells with 2048 material points.

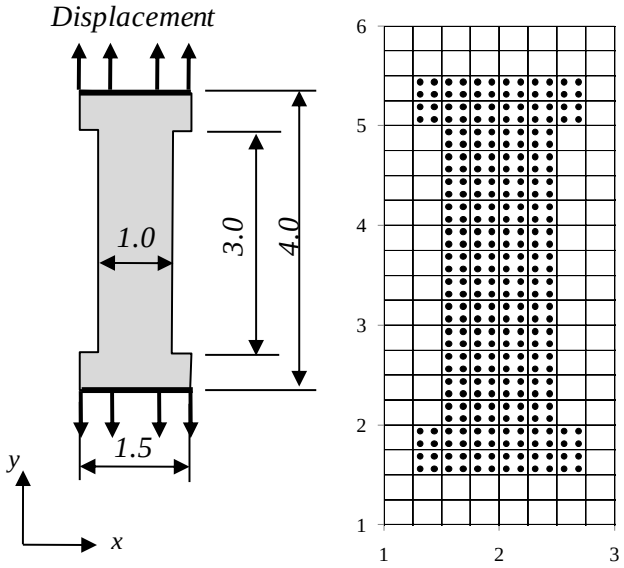

Figure 2. 29 Geometries of a dumbbell type specimen with imposed boundary conditions (left panel) and initial allocation of material points (right panel); Only a portion of the computational domain is presented.

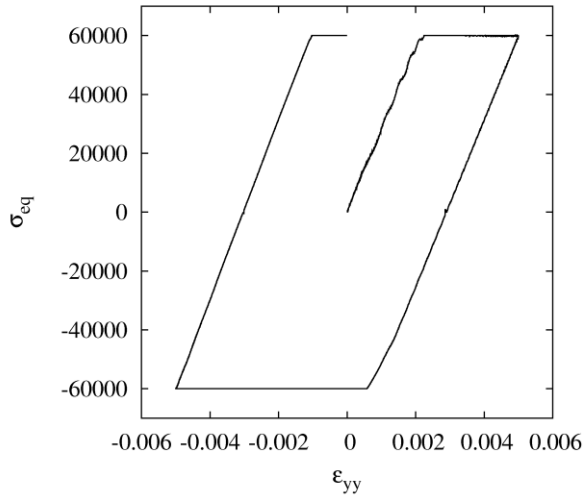

Figure 2. 30 Computed stress-strain curve by the validation of the tensile/compression loading with elasto-perfectly plasticity material model.

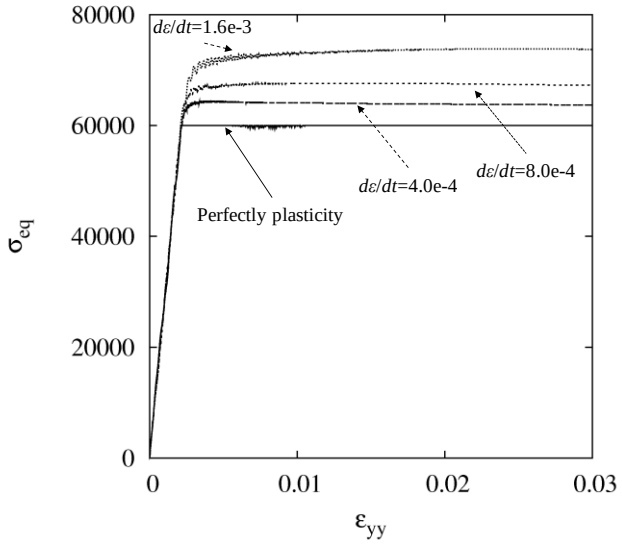

Figure 2. 31 Computed stress-strain curves of perfectly plasticity model, $d\varepsilon/dt$=4.0e-4, $d\varepsilon/dt$=8.0e-4, and $d\varepsilon/dt$=1.6e-3; Conditions of strain rate are indicated by arrows in the graph.

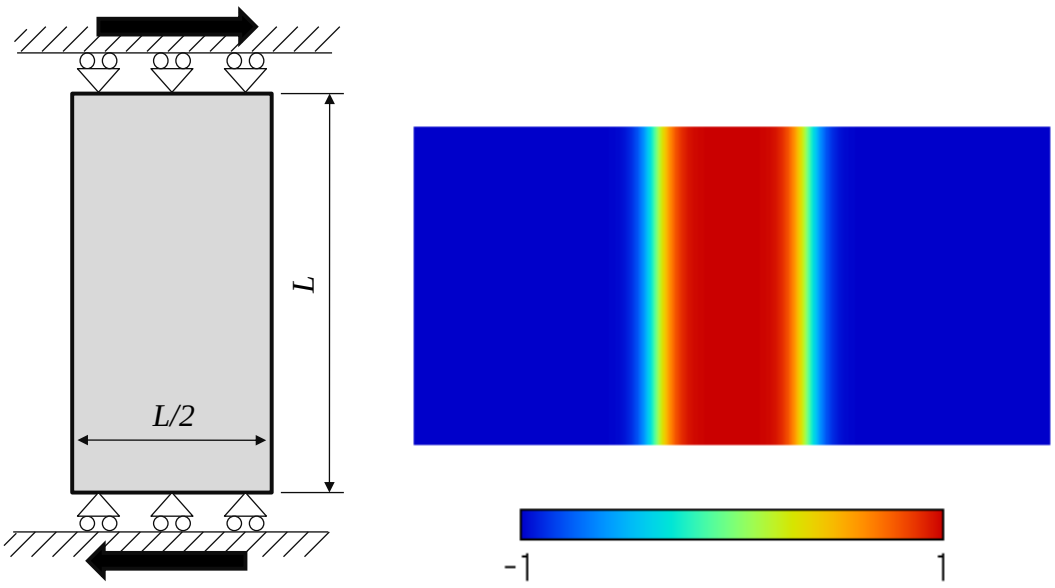

Figure 2. 32 Geometries and mechanical boundary conditions of a rectangular elasto-perfectly plastic bar under shear deformation (left panel), and initial phase-field profile defined on the background nodes (right panel); phase-field is advected by the velocity due to solid deformation computed by the MPM analysis.

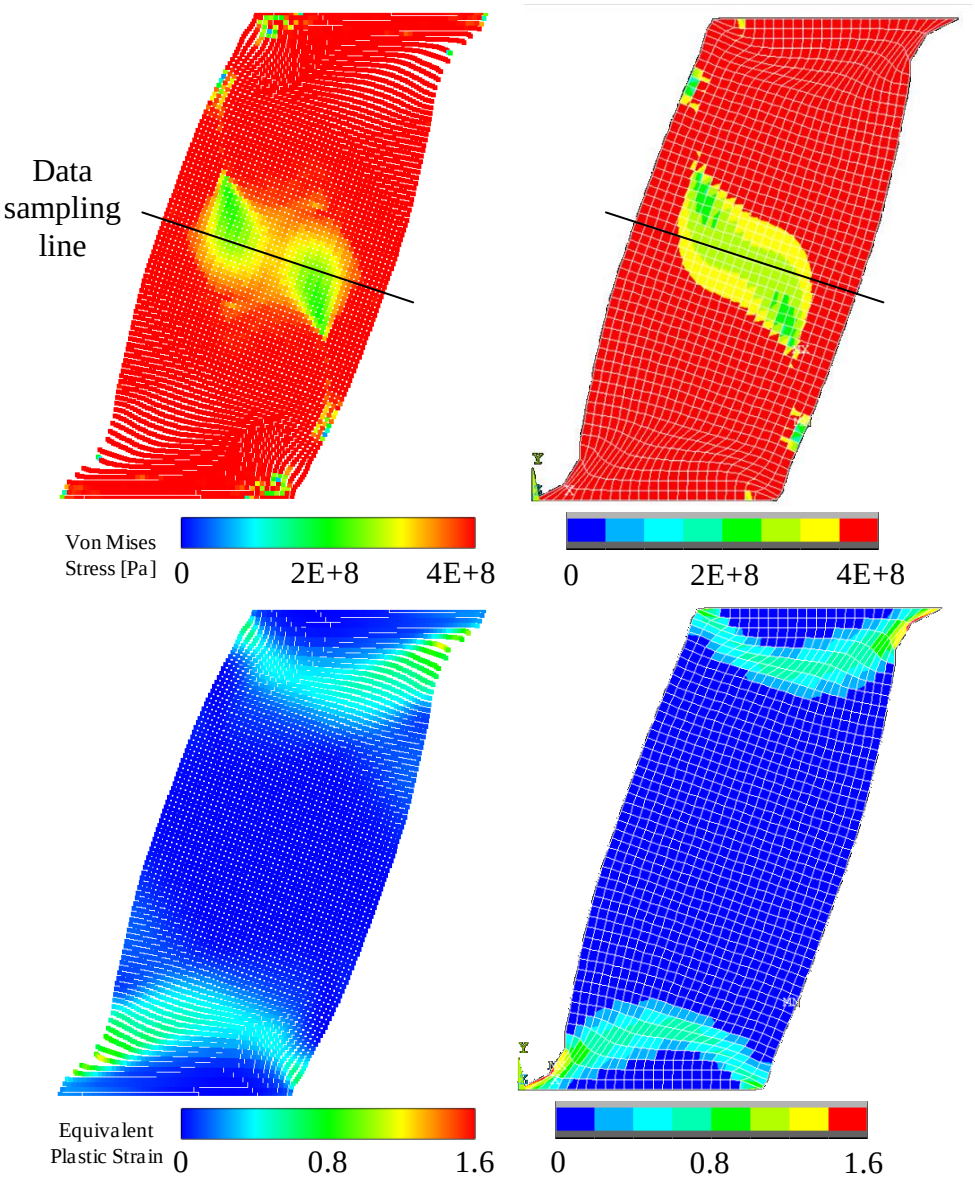

Figure 2. 33 Computed contours of von Mises stress (upper panels) and equivalent plastic strain (lower panels) at 40% shear of the MPM (left panels) and FEM using ANSYS 12.0 (right panel); contour colors are overlaid on material points for the result of the MPM analysis.

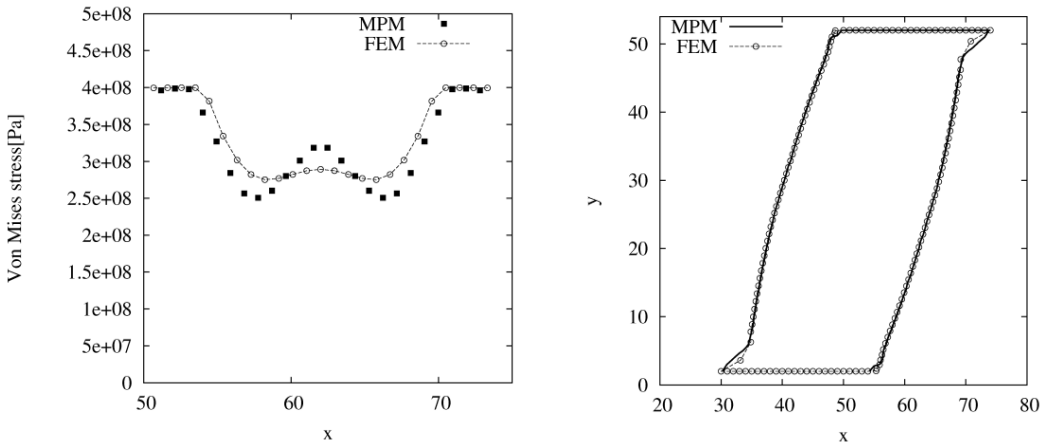

Figure 2. 34 Profiles of von Mises stress along a sampling line indicated in figure 2.33 upper panels (left panel), and outlines of solid bar (right panel) at 40% shear; ϕ=0 contour is presented as the outline of the MPM analysis.

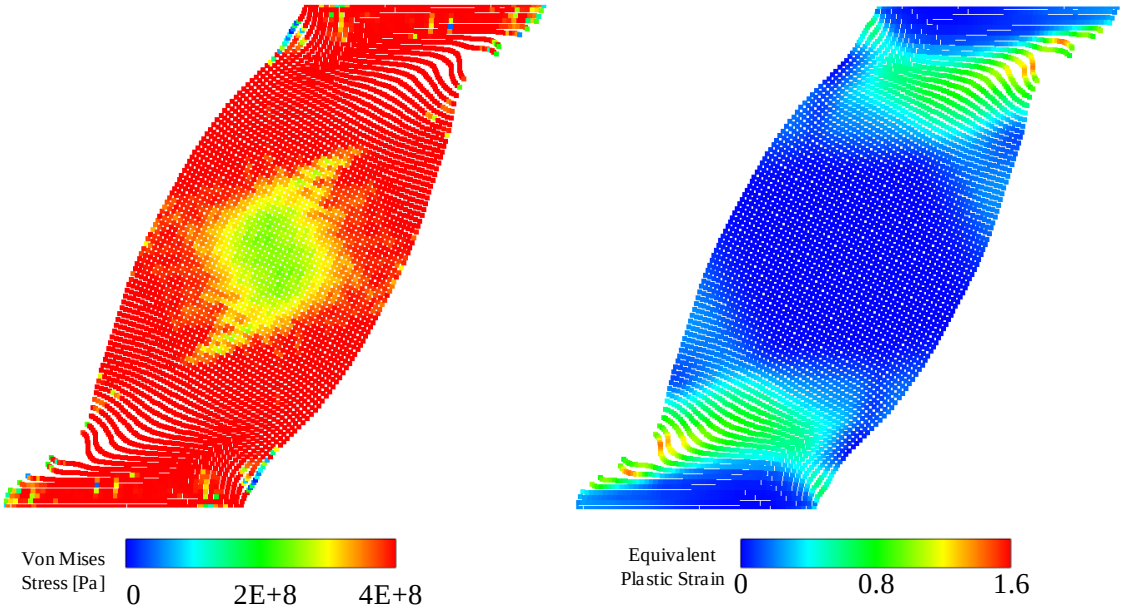

Figure 2. 35 Computed contours of von Mises stress (left panel) and equivalent plastic strain (right panel) at 60% shear of the MPM analysis; contour colors are overlaid on material points for the result of the MPM analysis.

CHAPTER 3

PHASE-FIELD SINGLE DENDRITIC SOLIDIFICATION SIMULATION WITH APPLIED DEFORMATION

Solidification simulations of a pure substance under externally applied loading are employed in chapter 3 and 4. The simulation with a single dendrite is of interest in this chapter. In addition to the numerical methodology developed in chapter 2, some numerical treatments associated with morphological change and the motion of computational boundaries are necessary. The additional numerical treatments are presented and validated first, and then some numerical experiments with assembled methodologies are performed.

3.1 Successive Update of Solid Structural Model in the MPM due to Morphological Change

The solid structure is successively and complexly evolved due to the phase change in a sequence of our simulation. Thus, the solid structural model used in the MPM has to be properly updated based on the latest solid geometry at every single computational time step. One of the major reasons for introducing the MPM as a numerical method of solid deformation analysis is the simplicity in terms of the modification of the solid structural model compared to a general Lagrangian FEM. By making use of the characteristics of the particle method, the following numerical procedure for the solid model modification is constructed and implemented in this thesis.

3.1.1 Assumptions and strategy

The numerical procedure for updating the solid structural model needs to satisfy the conservation mass and momentum like the governing equations themselves. Basically, since the mass associated with each material point does not change throughout the computation of the usual MPM without phase change, total mass conservation is

automatically guaranteed. In order to consider the mass change of the solid phase due to phase change in the MPM analysis, the mass change has to be correctly reflected through the mass of the material points which reside around the solid-liquid interface. An additional numerical procedure should be constructed for that purpose. For numerical simplicity, the following assumptions are made for the procedure.

(i) Density change associated with phase change is neglected.

(ii) The solidified part within single time step does not have any deformation history.

(iii) The phase-field represents the correct fraction of solid.

Some researchers (i.e.[76]) emphasize the importance of the density change between solid and liquid phases upon solidification through convection, but the convection of the liquid phase is out of the scope of this thesis, thus the effect is neglected. As stated in chapter 2, thermal stress and transformation stress are assumed to be absent, so that initial strain/stress is not caused within the newly formed solid part. By this assumption, the newly formed solid part would not affect the conservation of momentum. Due to assumptions (i) and (ii), the phase-field would represent the correct fraction of solid $\psi=(1+\phi)/2$ in the newly solidified part within a single computational time step. Thus, mass conservation is taken care of in the solid model update procedure using a fraction of solid defined by phase-field.

3.1.2 Update procedure of solid structural model

At the initial state, the phase-field $\phi(\mathbf{x},t)$ is defined by the hyperbolic tangent profile, i.e. eq.(2.3.4) such that the $\phi=0$ contour corresponds to solid-liquid interface. Depending on the phase-field $\phi(\mathbf{x}_p,t)$ at each material point location $\mathbf{x}_p$, a volume associated with each material point would be defined by the following way since no deformation is assumed at the initial state.

$$V_p = \int_{\Omega\cap\Omega_p} \frac{\phi(\vec{x})+1}{2} \chi_p(\vec{x}) d\Omega \tag{3.1.1}$$

where χ_p is the particle characteristic function mentioned before. A support domain of the material point is approximated by the rectangular area l_{px0}xl_{py0} . For instance, $l_{px0}=\Delta x/n_p$ and $l_{py0}=\Delta y/n_p$ if two material points $n_p=2$ are assumed in the fully solidified background cell ($\phi=1$) for each direction, i.e. n_pxn_p points per two dimensional cell. Eq.(3.1.1) should be simplified by the following.

$$V_p = \frac{\phi(\vec{x}_p)+1}{2} l_{px0} l_{py0} \tag{3.1.2}$$

By setting the reference density ρ_0 from assumption (i), the mass of each material point is denoted by

$$M_p = \rho_0 V_p \tag{3.1.3}$$

For every single computational time step, the solid-liquid interface is advanced by phase-field simulation. Due to the solidification, the mass of the solid phase is increased. Therefore the change of mass has to be properly reflected in the solid structural model used in the MPM. The following three cases, i.e. Figure 3. 1 (a) and (b), are considered in the procedure. As shown in Figure 3. 1 (a), an advanced interface intersects with two sides of a background cell, but no existing material points are inside the cell. In that case, two material points are simply inserted at the intersections. From assumption (ii), the points do not have any deformation history; l_{px0}xl_{py0} is assumed to be a full support domain of the point. Using the phase-field at the location of newly inserted material point, its volume is defined by eq.(3.1.2). Since the interface passes over a background cell by spending several time steps, the cell may have some existing material points when the interface is advanced as shown in Figure 3. 1(b). In the case where $n_p=2$ is assumed, four particles in total are the maximum number of particles allowed to exist in each cell if the cell is not deformed. In the situation where a point is inserted in a cell which already has four points, some existing points are merged with the newly inserted point such that the total number of particles does not exceed four. As a strategy of the merging

procedure, the closest existing material point to the inserted point is determined and the points are merged together (Figure 3. 1 (b) right panel). Historical variables of the closest point are simply transferred to the merged point. In order to make use of the arrays used for variables of the material points, a stack array with a first in first out sequence is utilized to store the information of the temporarily removed material point (the closest point to the interface point).

There is also a case where no material points are included in a background cell which is assumed to be fully solid phase. Since the equation of motion is solved on the background nodes by mapping the variables of material points on the nodes, the solid cell in the absence of material points does not contribute to the equation. The situation might cause separation or fragmentation as a worst scenario even if the solid part is assumed to be continuous. The numerical procedure to avoid the situation is included in our computations. Throughout the simulation, the phase-field resides on the background nodes, so the phase-field value of each background cell is computed as an average of the values of the nodes which compose the cell ϕ_{cell} (simply arithmetic average is used in the actual implementation). If $\phi_{\text{cell}} \geq 0$ and the cell does not have any material points at the interface, material points are inserted into the cell. The cell averaged historical variables and volumes evaluated by the phase-field value at the inserted location are assigned to the inserted points for the numerical simplicity.

3.1.3 Model validation

The above suggested numerical procedure for the solid structural model update is validated in this section. For validation purposes, a known phase-field profile and motion are assumed on a 151x151 computational domain. Nine solid grains shown in the left panels of Figure 3. 2 are initially allocated in the domain. Each grain is defined by an arbitrary *m*-fold shape, i.e. a radial distance from the center and the interface *R* is given by

$$R = R_0\left[1+\varepsilon_0 \cos\left(m\Theta\right)\right] \tag{3.1.4}$$

where R_0 is the reference radius, ε_0 is the strength of anisotropy, and Θ is the angle between the x-axis and a given location. Using the variation of R, the phase-field is assigned to each grain as a hyperbolic tangent profile given by eq.(2.3.4) (Figure 3. 2 upper left panel). Based on the phase-field profile and the strategy mentioned in the last section, material points are allocated within the solid body (Figure 3. 2 lower left panel, n_p=2). The solid-liquid interface associated with each grain is moved outward with an arbitrary constant speed during computation by defining R_0 as a function of time. During the computation, deformation of solid phase is not assumed. As time progresses, the distribution of material points is updated while following the motion of the phase-field (from Figure 3. 2 lower left to lower right panels).

Based on assumption (ii) presented in 3.1.2, the mass computed from the phase-field is considered to be exact throughout the computation. Using the phase-field on the background nodes, the following total mass of the solid phase can be calculated.

$$M_l^{total} = \sum_l \rho_0 \frac{1+\phi_l}{2} \Delta x \Delta y \tag{3.1.5}$$

On the other hand, each material point has own mass, so the total mass associated with material points is given by

$$M_p^{total} = \sum_p M_p \tag{3.1.6}$$

The numerical procedure mentioned in the last section is constructed such that the mass calculate by eq.(3.1.5) and (3.1.6) is equivalent. Figure 3. 3 shows a time history of the two different masses. The total mass computed by eq.(3.1.5) (solid line) and (3.1.6) (dashed line with cross shape plots) correspond well with each other. Successive changes of the solid phase due to solidification by phase-field analysis would be correctly introduced into the MPM through updates of the structural model.

3.2 Numerical Treatment Associated with Boundary Motion

3.2.1 Strategy and methodology

Deformation of the solid phase is a result of imposed external loading through a body force, an enforced displacement or force, and so on. In this thesis, the solid deformation is assumed to be caused by enforced displacement through the motion of rigid walls as observed in pressure castings. A Cartesian grid is adopted to compute the phase-field and the heat equation. Since the wall displacement imposed in a single time step does not necessarily correspond to the spacing of the grids, it is possible for the wall to stay between the grids. In order to perform an accurate and correct phase-field simulation, the boundary conditions are properly imposed at the correct boundary locations. The ALE (Arbitrary Lagrangian Eulerian) formulation [55 and 56] and cut-cell approach (i.e. [57]) are utilized for the purpose.

The key point of the numerical procedure is the usage of both activated and deactivated computational domains. A full computational domain is composed of the two sub-domains as shown in Figure 3. 4. The treatment allows the activated computational domain to change its configuration flexibly depending on the boundary wall motion. For the sake of computational simplicity, the moving walls are assumed to be flat and correspond to boundaries of the activated computational domain. Thus, the boundary conditions of phase-field and heat equations are imposed at the moving walls. As the moving wall translates, the spacing between the node on the wall and its neighbor node becomes smaller. Spacing is one of the determining factors of the time step size in an explicit time stepping scheme used to solve the phase-field and heat equations; the smaller spacing restricts the time increment to smaller value. It is not a desirable situation in terms of efficient computing. In order to avoid the inefficiency, nodes on the boundary wall are switched such that the minimum spacing is kept more than $\Delta x_0/2$

where Δx_0 is the reference spacing uniformly defined in the full computational domain. Using this treatment, the time increment is also maintained to be greater than some critical value. The numerical procedure of the boundary node switching is briefly explained with Figure 3. 5. At time $t=t$, the boundary node is assumed to be node i (Figure 3. 5 upper panel), and the boundary moves rightward with time. At $t+\Delta t$, the spacing between node i and its neighbor node $i+1$ becomes smaller, but is still more than $\Delta x_0/2$ (Figure 3. 5 middle panel). In this case, the boundary node is not switched with the other node. At $t+2\Delta t$, the spacing between i and $i+1$ should be less than $\Delta x_0/2$ if i remains as the boundary node. By switching the boundary from node i to $i+1$, the minimum spacing is kept greater than $\Delta x_0/2$ (Figure 3. 5 lower panel).

In the actual numerical implementation, the ALE formulation [55] is adopted to compute variables on switching nodes. Using the ALE form, the governing equations in the general form (eq.(2.3.1)) are represented by

$$\frac{d\mathbf{a}}{dt} + \left(\vec{v}_{ext} - \vec{v}_{grid}\right) \cdot \nabla \mathbf{a} = \mathbf{S} \tag{3.2.1}$$

where $\mathbf{v}_{\text{grid}}$ denotes the velocity of the grid point which is available only when the switching of boundary nodes takes place.

$$\frac{d\mathbf{a}}{dt} = \frac{\partial \mathbf{a}}{\partial t} + \vec{v}_{grid} \cdot \nabla \mathbf{a} \tag{3.2.2}$$

In the case shown in the lower panel of Figure 3. 5 , $\mathbf{v}_{grid}$ is defined at node i as the velocity to return to the original regular interval and on $i+1$ as the velocity to translate from the regular interval to the boundary wall. The CIP method is modified to be able to handle irregular spacing and applied to solve eq.(3.2.1) with operator split methodology. Irregular grid allocation is also considered in the implementation. The cut cell approach is adopted for this purpose. A 9-point Laplacian (see i.e. appendix of [41]) is used as a discretization of the Laplacian term in the phase-field equation in order to avoid an orientation dependency. However, the discretization is derived with a uniform spacing in

the x and y directions, and it is impossible to construct the 9-point Laplacian with irregular spacing (the formulation for the case $\Delta x_0 \neq \Delta y_0$ is possible, but the formulation for irregular spacing within the same direction is impossible). For that reason, 5-point Laplacian with irregular spacing is used as a discretization only for the boundary nodes. The form is given by

$$\nabla^2 \phi_{ij} = A\phi_{i+1j} + B\phi_{i-1j} + C\phi_{ij+1} + D\phi_{ij-1} - (A+B+C+D)\phi_{ij} \quad (3.2.3)$$

for the Laplacian at node (i,j) on Cartesian grids. Coefficients from A to D are specified as

$$A = \frac{2}{\Delta x_2(\Delta x_1 + \Delta x_2)}, \quad B = \frac{2}{\Delta x_1(\Delta x_1 + \Delta x_2)}$$
$$C = \frac{2}{\Delta y_2(\Delta y_1 + \Delta y_2)}, \quad D = \frac{2}{\Delta y_1(\Delta y_1 + \Delta y_2)} \quad (3.2.4)$$

$\Delta x_1 = x_i - x_{i-1}$, $\Delta x_2 = x_{i+1} - x_i$, $\Delta y_1 = y_j - y_{j-1}$, $\Delta y_2 = y_{j+1} - y_j$ are nodal spacing around node (i,j). Since the semi-implicit ADI scheme is used to solve the heat equation, irregular spacing is considered through the modification of coefficient matrix.

3.2.2 Model validation

The following validation is designed to examine the performance of the boundary node switching treatment. A series of 1280x640 computational meshes are defined as a full computational domain, and a 640x640 activated computational domain is created on the leftmost side of the full domain as shown in Figure 3. 6 upper panel. A solid seed (ϕ=1 is assigned inside the seed, otherwise ϕ=-1) is allocated at the middle of the left wall of the activated domain. The parameters D=3, d_0/W_0=0.185, ε=0.05, and Δ=0.55 are chosen for the validation. The flux free boundary condition is imposed on whole boundaries of the activated domain throughout the simulation. The activated domain is translated rightward with a constant speed $\mathbf{v}_{\text{domain}}$ (Figure 3. 6 lower panel), i.e. $\mathbf{v}_{\text{ext}} = \mathbf{v}_{\text{domain}}$, and no convection in the liquid melt is assumed. Thus, the solid seed evolves

its dendrite structure within a moving computational domain. Every 50 iterations of the phase-field and heat equations, the activated computational domain is translated to rightward with $0.05\Delta x$ based on eq.(3.2.1). The tip velocity and the translation speed of the activated domain are almost comparable.

Figure 3. 7 shows the phase-field contours (a) at initial state, (b) without, and (c) with activated domain motion at 100,000 time steps of phase-field simulation (the activated computational domain travels $100\Delta x$ from the left edge of the full domain). The gray region in the figure represents the deactivated computational domain where no calculation is performed. Basically, there is no difference in terms of computational settings of figure (b) and figure (c) except for the motion of the computational domain; the outlines of the dendrite for both conditions should be equivalent. Figure 3. 8 plots a comparison of the computed ϕ=0 contours with (solid line) and without (dashed line) motion for the activated computational domain (overlapped by matching both centers of dendrite). No significant differences are observed between two outlines. Although the numerical treatment is relatively simple, the phase-field simulation of solidification is performed under the motion of the computational domain.

3.3 Numerical Model of Thermal Noise

The side branches on the main dendirtic structure are generated by the selective amplification of the fluctuated interface. The main source of the fluctuation of the interface is thermal noise. Karma et al.[59] developed the phase-field model of dendritic sidebranching with thermal noise. In their study, since the interface noise is assumed to be negligible compared to the bulk noise, an introduction of the thermal noise term through bulk terms in the phase-field and heat equation is justified. The governing equations are given by

$$\frac{\partial \phi}{\partial t} = \nabla^2 \phi + \phi\left(1-\phi^2\right) - \lambda\theta\left(1-\phi^2\right)^2 + \varsigma(\mathbf{r},t)$$
$$\frac{\partial \theta}{\partial t} = D\nabla^2\theta + \frac{1}{2}\frac{d\phi}{dt} - \nabla\mathbf{q}(\mathbf{r},t) \tag{3.3.1}$$

where ζ and $\mathbf{q}$ denote non-conserved and conserved noise, respectively. Terms related to convection and anisotropy are omitted here for simplicity. Fluctuations of the noise are assumed to follow the Gaussian distribution whose mean variations are defined by

$$\left\langle \zeta(\mathbf{r},t)\zeta(\mathbf{r}',t')\right\rangle = 2F_\phi \delta(\mathbf{r}-\mathbf{r}')\delta(t-t')$$
$$\left\langle q_m(\mathbf{r},t)q_n(\mathbf{r}',t')\right\rangle = 2DF_u \delta_{mn}\delta(\mathbf{r}-\mathbf{r}')\delta(t-t') \tag{3.3.2}$$

where m=x,y, n=x,y for the two dimensional case. The terms $\delta(\mathbf{r}\text{-}\mathbf{r}')$ and $\delta(t\text{-}t')$ denote Dirac delta functions. The following relation is assumed for constants F_ϕ and F_u.

$$F_\phi = \lambda J F_u \tag{3.3.3}$$

where J=16/15 is a constant obtained by the solvability integral for the function $p(\phi)=\phi$[59]. In order to implement the noise terms, eq.(3.3.2) is rewritten by the following discrete forms.

$$\left\langle \zeta_{ij}\zeta_{i'j'}\right\rangle = \frac{2F_\phi}{\Delta t \Delta x^2}$$
$$\left\langle q_{m,ij}q_{n,i'j'}\right\rangle = \frac{2DF_u}{\Delta t\Delta x^2}\delta_{mn}\delta_{ii'}\delta_{jj'} \tag{3.3.4}$$

Absolute values of variation of those noise terms are then given by

$$\left\langle \zeta_{ij}^2\right\rangle = \frac{2F_\phi}{\Delta t\Delta x^2}, \left\langle q_{x,ij}^2\right\rangle = \left\langle q_{y,ij}^2\right\rangle = \frac{2DF_u}{\Delta t\Delta x^2} \tag{3.3.5}$$

Theaussian distribution of the noise terms are generated by the Box-Muller transform method [65] which is able to produce normal random values. First, two uniform random values R_{n1} and R_{n2} where $0 \le R_{n1} \le 1$ and $0 \le R_{n2} \le 1$ are generated. Then, Box-Muller transform is performed by the following equations.

$$T_1 = \sqrt{-2\ln(R_{n1})}\sin(2\pi R_{n2})$$
$$T_2 = \sqrt{-2\ln(R_{n1})}\cos(2\pi R_{n2}) \tag{3.3.6}$$

T_1 and T_2 are normal random numbers which lie in the normal distribution [0,1] and are independent on each other. For instance, Figure 3. 9 shows the distributions of normal random values by the Box-Muller transformation with three different numbers of sampling data and an exact normalized Gaussian distribution, i.e.

$$p(x) = \frac{1}{\sqrt{2\pi}}\exp\left\{-\frac{(x-x_0)^2}{2}\right\} \tag{3.3.7}$$

where $p(x)$ is a probability density function, x is a support. Here, the mean x_0 and variance are set to be zero and one, respectively. Larger sampling numbers produce a closer profile to an exact Gaussian distribution, but the profiles computed by the Box-Muller transformation give closer profile to the normal distribution for any numbers of sampling data. Using this method, the final forms of noise terms in the actual implementation are represented by

$$\zeta(\mathbf{r},t) = T_1\sqrt{\langle\zeta_{ij}^2\rangle} \quad or \quad T_2\sqrt{\langle\zeta_{ij}^2\rangle}$$
$$\mathbf{q}(\mathbf{r},t) = \left(T_1\sqrt{\langle q_{x,ij}^2\rangle}, T_2\sqrt{\langle q_{y,ij}^2\rangle}\right) \tag{3.3.8}$$

Here, the mean value of ζ and $\mathbf{q}$ are set to be zero. As pointed out in [44] and [59], the fluctuation in the phase-field equation is small, so only thermal noise $\mathbf{q}$ is implemented through a source term in the ADI method. Figure 3. 10 represents the phase-field contour computed by the above phase-field model with a thermal noise term. For the example 1200x800 nodal points are used, and D=3, d_0/W_0=0.185, ε=0.06, Δ=0.55, and F_u=1.0e-3 are defined in the calculation. Fluctuations are observed on the interface of the dendrite.

3.4 Single Dendrite Growth under Compression Loading

In this section, simulations of single dendrite growth under compression loading are presented. (i) Dendrite structure with elasto-perfectly-plasticity model; (ii) (i) with including thermal noise; and (iii) (ii) but with elasto-perfectly-viscoplasticity model are of interest in this section. For all simulations, 1200x800 meshes are prepared as a full computational domain. Initially, a solid seed is located at the center of the computational domain, and it freely evolves its dendritic structure until dendrite tips reach to both top and bottom surfaces under the flux free boundary condition. Then, both surfaces move such that they apply compression loading to the dendritic structure (Figure 3. 11). Mechanical boundary conditions are imposed through nodal velocity.

3.4.1 Example 1

The elasto-perfectly-plasticity constitutive model is applied to represent mechanical response of the dendritic solid structure. For phase-field and temperature analysis, values of $\Delta t'$=0.01, $\Delta x'$=0.4, d_0/W_0=0.185, ε=0.015, D=3.0, and Δ=0.55 are assigned, and the flux free boundary condition is used. For the MPM structural analysis, values of E=50.0[GPa], ν=0.33, ρ=7.8e3[kg/m3], and σ_Y=5.0[MPa] are used. These properties are typical values for metal at higher temperature (i.e. [58] and see appendix B), and no specific material is not assumed here. The dimensionless equation (see appendix B) is solved for the MPM analysis.

Figure 3. 12 shows contours of the phase-field (the left most panels), von Mises stress (panels in the second column from the left side), equivalent plastic strain (panels in the third column from the left side), and crystallographic orientation (the rightmost panels) at initial state (upper panels), at 5% compression (panels in the second row), at 10% compression (panels in the third row), and at 15% compression (lower panels). Since contact takes place at the dendrite tips located at the top and bottom, plastic strain starts evolving from that region, i.e. contour of plastic strain at 5% compression. Then,

gradually the center region of the dendrite has stress as the imposed deformation becomes larger.

3.4.2 Example 2

The fluctuated interface is incorporated through the thermal noise term described in 3.3 for the sake of examining the capability of our numerical methodology to handle more complex geometries. Mechanical properties and parameters used in the MPM analysis and phase-field simulation are the same as those in example 1 except for ε=0.06 and F_u=1.0x10^{-3} . Figure 3. 13 shows a sequence of the simulation. The illustrated contours are the same as those seen in example 1. Yielding initially occurs at the contact portions of the dendrite with the upper and lower walls, and then the yielding part moves toward the center of the dendrite, i.e. Mises stress and plastic strain contour at 30% compression. This is same result as presented in example 1. Orientation of the dendrite is varied by the imposed compression. For instance, the variation is caused by the clockwise rotation around the right hand side of the dendrite tip on the upper wall. The deformation is reasonable considering Poisson's effect due to the compression (the solid portion is expanded and flows rightward whereas the solid on the wall is fixed on it). Interestingly, the magnitude of the orientation change (see contours of orientation since initially the orientation is all set to be zero) depends on that of the plastic strain. This indicates that the plastic flow might be the major source of the orientation change within the single dendrite structure. Figure 3. 14 shows the computed ϕ=0 contours of the dendrites with (red line) and without (black line) deformation at 10, 20, and 30% compression. Outlines of the laterally extended arms are almost same regardless of deformation since their contribution on load bearing is small. On the contrary, the vertically extended arms are compressed and get thick as the deformation becomes larger. As shown in Figure 3. 15, stress concentrations are computed at the necked part of the

complexly fluctuated dendrite structure. From this viewpoint, stresses and strains should be correctly computed within the evolving dendritic structure.

3.4.3 Example 3

The visco-plasticity constitutive model is introduced in addition to the model presented in example2. The value of η_{visc} (viscosity coefficient) is set to be 100 (see appendix B for the parameter determination), otherwise all mechanical properties and parameters are the same as those of example 2. The characteristics of the dendrite deformation are almost same as the characteristics observed in the elasto-perfectly-plasticity model (Figure 3. 16). The computed ϕ=0 contours of the elasto-perfectly-plasticity model (solid line) and the elasto-perfectly-viscoplasticity model (red line) are presented in Figure 3. 17. There are small differences between results of the two constitutive models. For instance, Figure 3. 17 shows a close-up image of the rectangular area (blue line in the same figure). Smaller deformation or plastic flow is observed for the viscoplasticity model since the viscous effect gives higher flow stress than the static case. The basic deformation state should be determined by the flow law applied to the constitutive model.

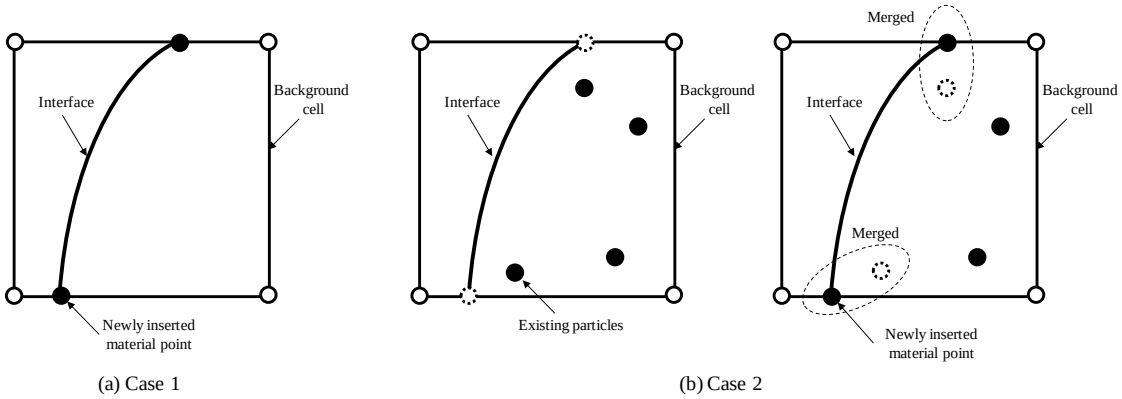

Figure 3. 1 Schematics of the insertion and the relocation of material points associated with an advanced interface due to solidification; (a) Case 1: a background cell does not have preexisting material points. Material points are newly inserted at the intersections of two sides of the cell with the interface; (b) Case 2: a background cell has four preexisting material points (left panel). The closest preexisting point to the intersections of the interface is merged with the newly inserted point (right panel).

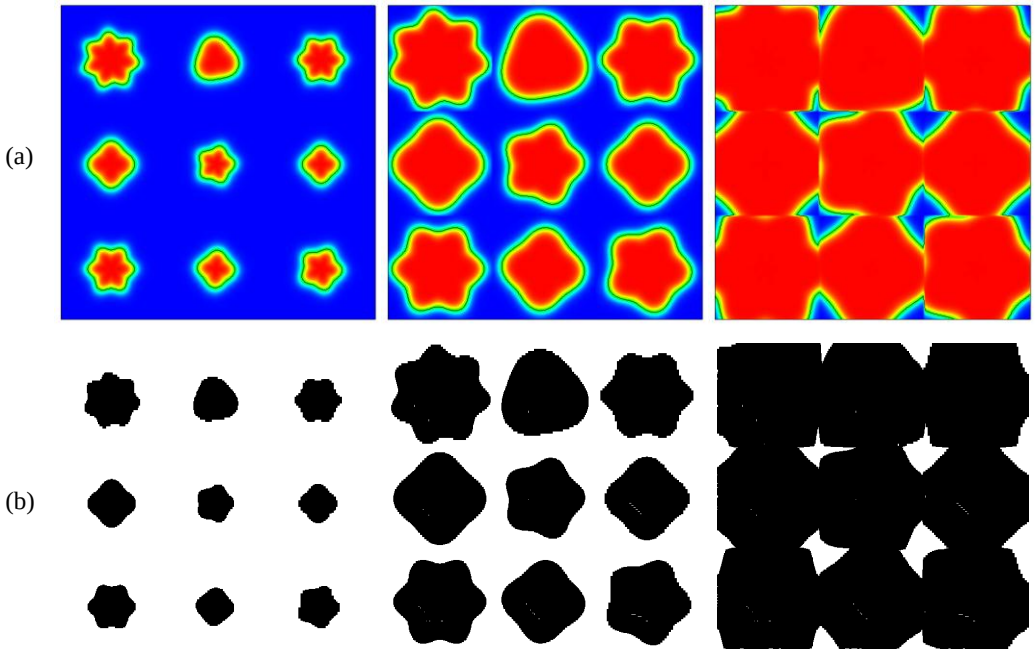

Figure 3. 2 Validation of numerical procedure of solid structural model update; (a) Phase-field contours associated with ϕ=0 line contour at initial state (left panel), intermediate time step (center panel), and final time step (right panel); (b) Allocation of material points.

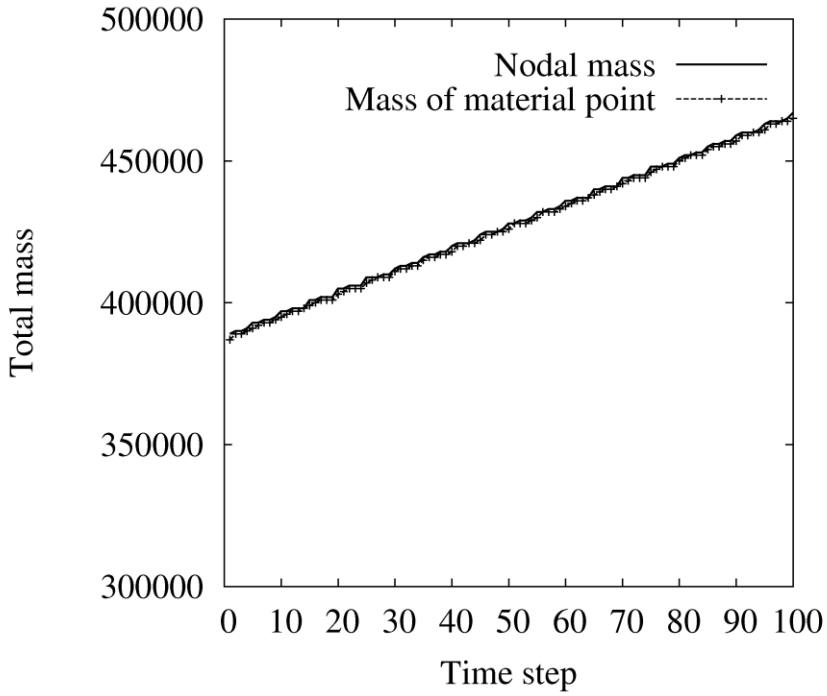

Figure 3. 3 A time history of total mass of the solid phase computed from phase-field on the background nodes (solid line) and the mass associated with the material points (dashed line with cross shape plots)

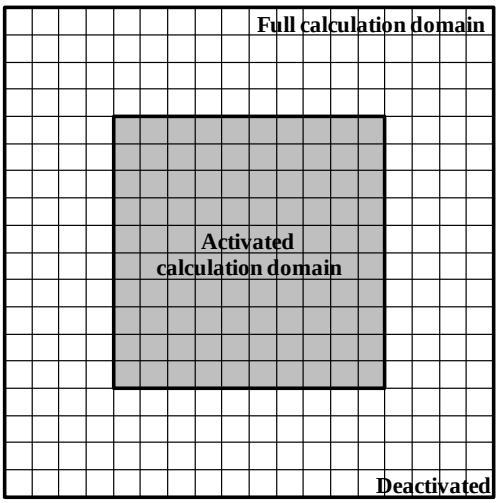

Figure 3. 4 A schematic of computational domain of phase-field and heat equation; A full computational domain is composed of an activated and a deactivated sub-domains.

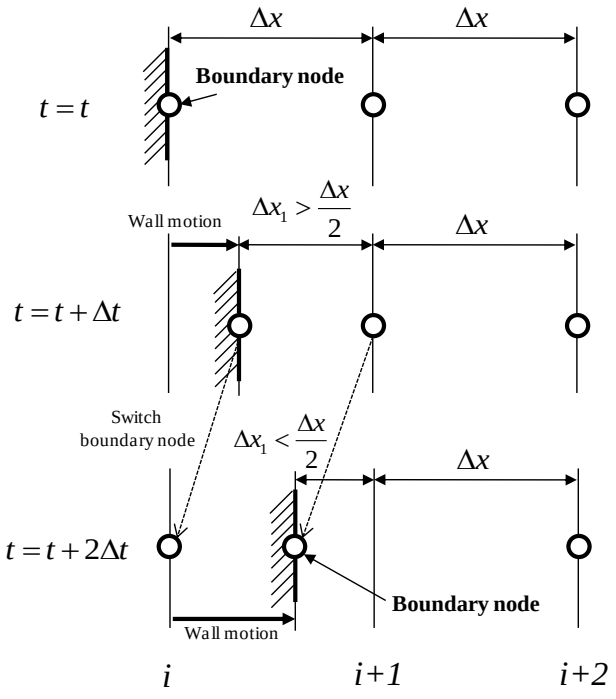

Figure 3. 5 Schematics of numerical procedure of boundary node switching; node *i* is assumed to be the boundary node at $t=t$. If the spacing between the boundary node and its neighbor node $i+1$ is less than $\Delta x_0/2$, the boundary node is switched to $i+1$ (lower figure).

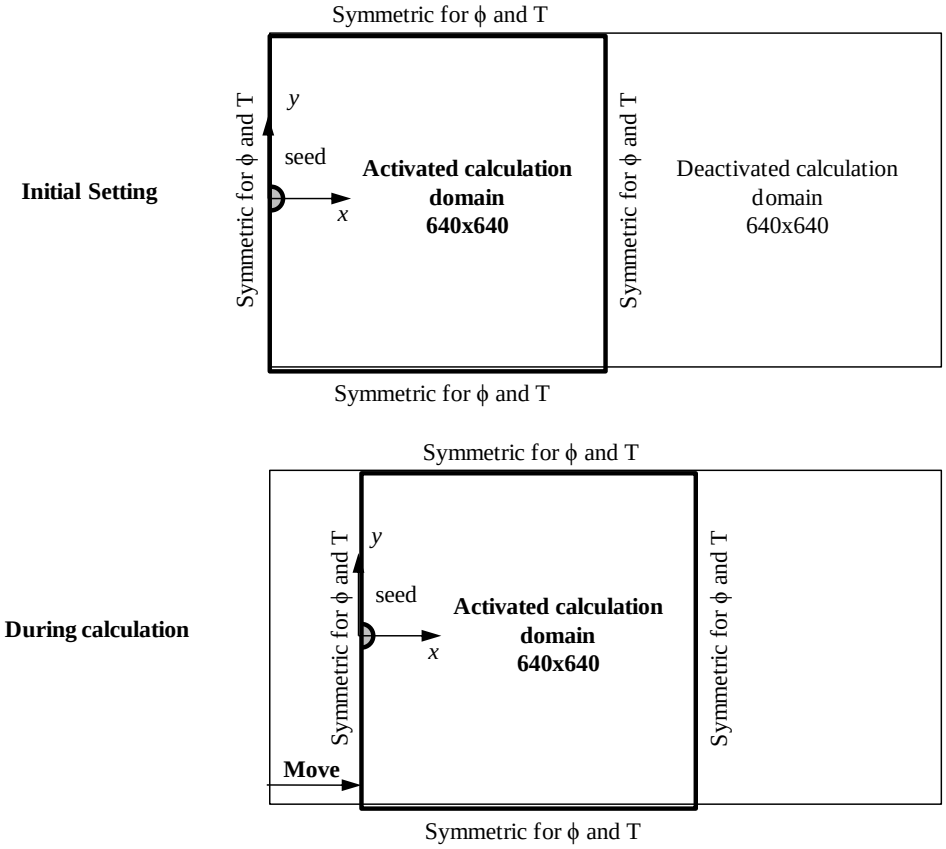

Figure 3. 6 Schematics of a validation of boundary node switching procedure; upper panel: initial conditions. 640x640 activated domain is placed within 1280x640 full computational domain; lower panel: boundary conditions of phase-field and heat equations. Activated domain is translated rightward with evolving solid seed.

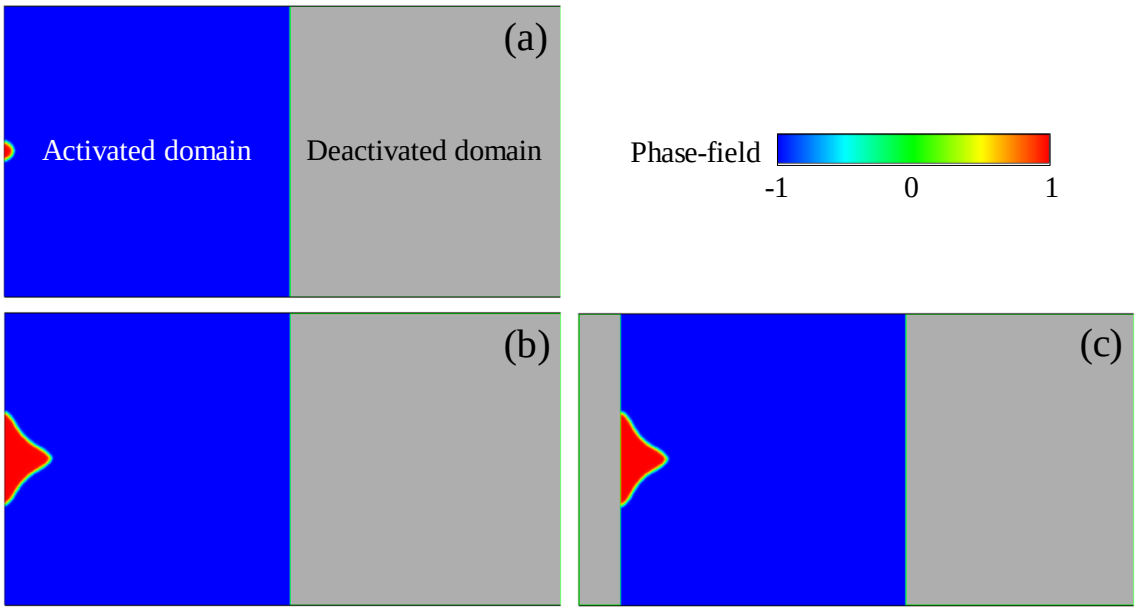

Figure 3. 7 Phase-field contours of validation problem of moving wall treatment; Gray region represents deactivated computational domain where no calculation is performed; (a) at initial state; (b) at after 100,000 steps of phase-field simulation without an activated domain motion; (c) at after 100,000 steps of phase-field simulation with an activated domain motion

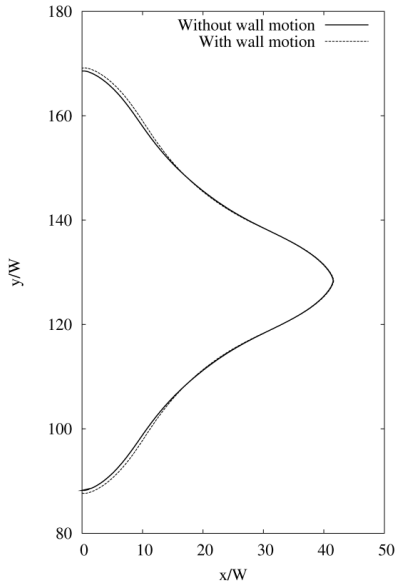

Figure 3. 8 A comparison of computed ϕ=0 contours with (solid line) and without motion of activated computational domain (dashed line).

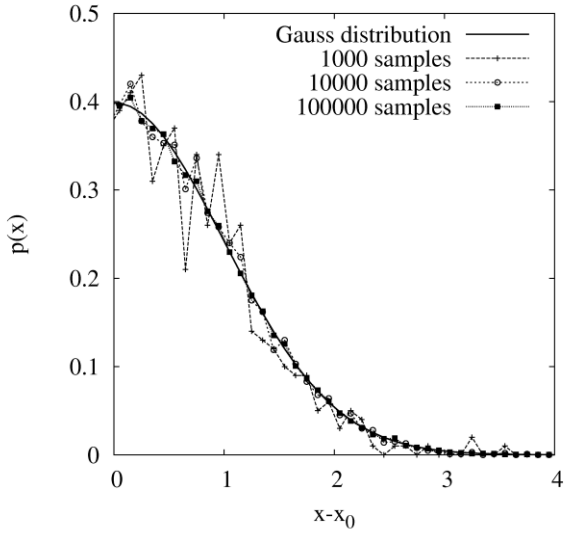

Figure 3. 9 Distributions of normal random values by Box-Muller transformation with the different number of samples. For a symmetry, only half of the distribution is presented. An exact Gaussian profile (solid line), profile obtained by Box-Muller transformation with 1000 data samples (dotted line with cross-shaped plots), with 10,000 data samples (dotted line with circular plots), and with 100,000 data samples (dotted line with square plots) are compared.

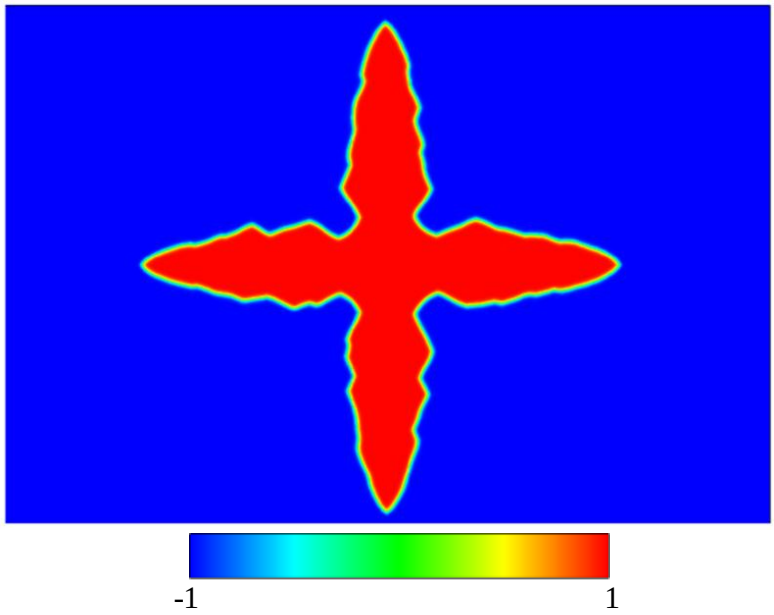

Figure 3. 10 Phase-field contour computed by phase-field model with thermal noise. (D=3, d_0/W_0=0.185, ε=0.06, Δ=0.55, and F_u=1.0e-3)

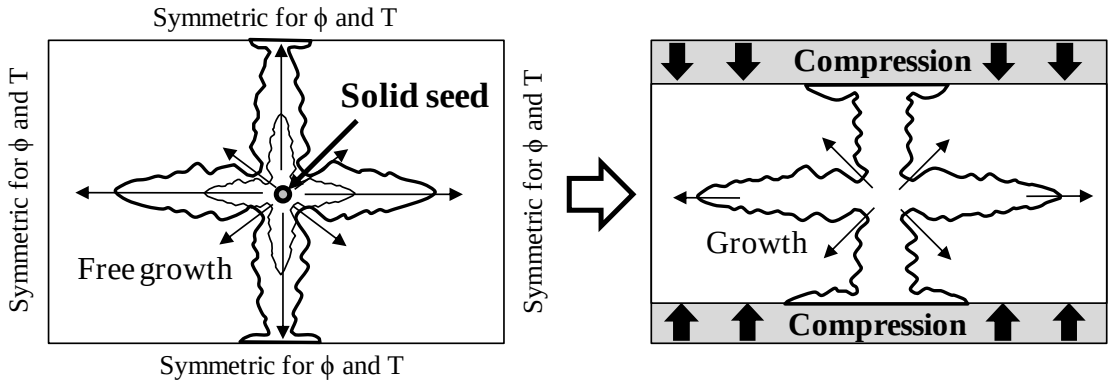

Figure 3. 11 A schematic of phase-field dendritic solidification simulation with externally applied compression loading; Left panel: initial and boundary conditions of phase-field solidification simulation. A solid seed freely evolves its dendritic structure until dendrite tips reach to upper and lower boundaries; Right panel: after the free dendrite growth, upper and lower walls move such that the dendritic solid structure is compressed.

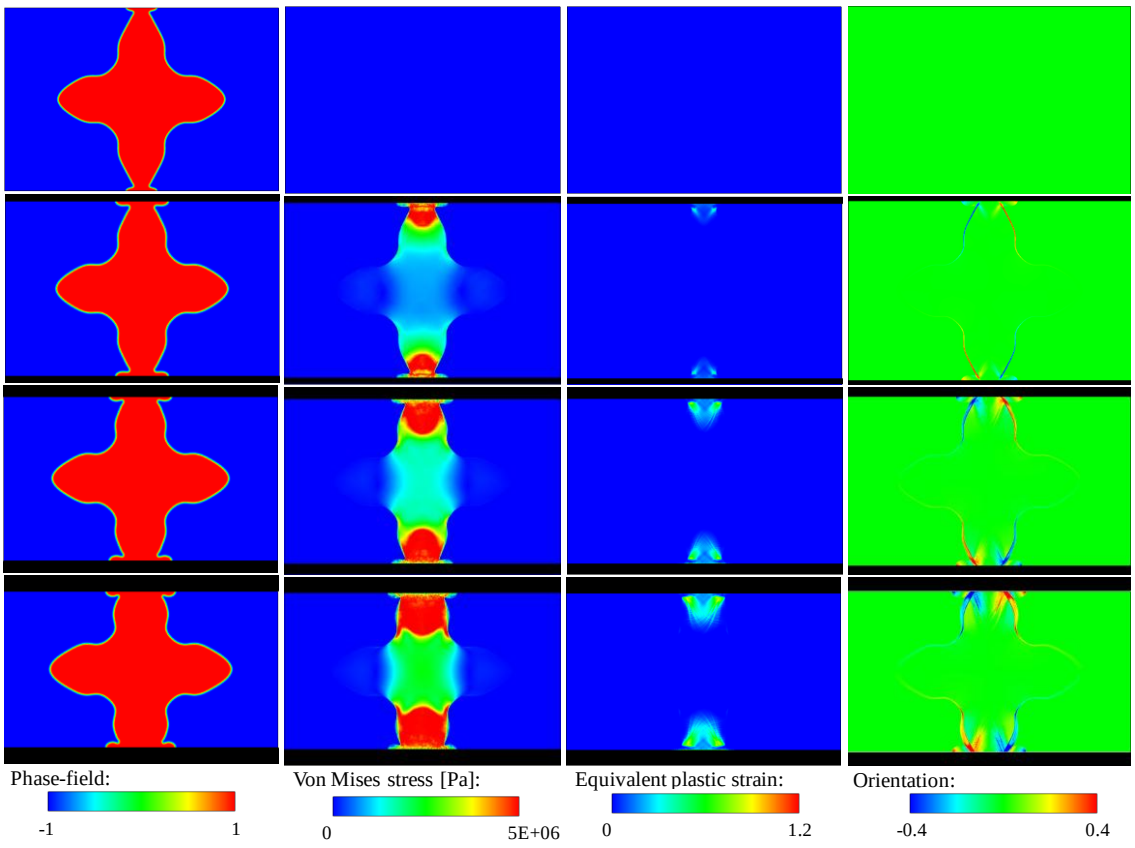

Figure 3. 12 Phase-field simulation of dendritic solidification under compression loading; Left panels: phase-field contours; second panels from the left: von Mises stress; third panels from the left: equivalent plastic strain; right panels: crystallographic orientation; Upper panels: initial state; panels of the second row: 5% compression; panels of the third row: 10 % compression; and lower panels: 15% compression. Black parts denote walls.

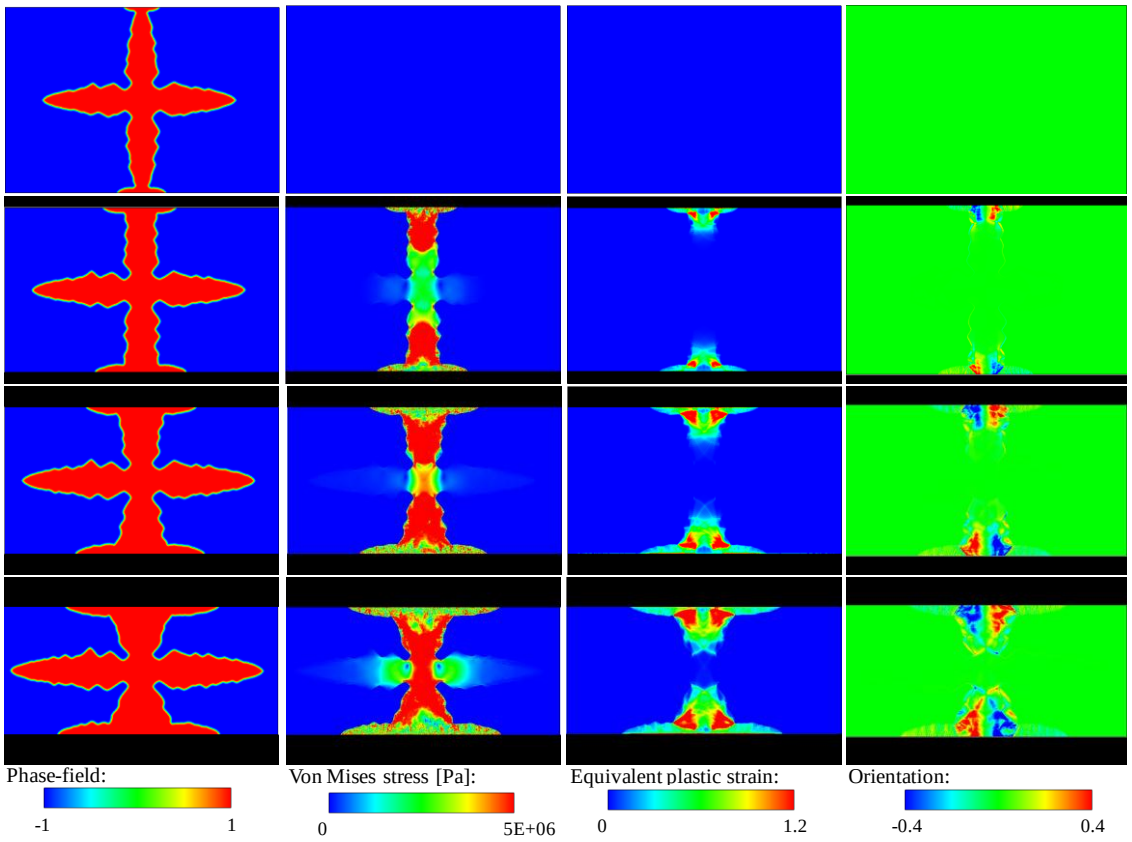

Figure 3. 13 Phase-field simulation of dendritic solidification under compression loading with thermal noise (F_u=1.0e-3); Left panels: phase-field contours; second panels from the left: von Mises stress; third panels from the left: equivalent plastic strain; right panels: crystallographic orientation; Upper panels: initial state; panels of the second row: 10% compression; panels of the third row: 20 % compression; and lower panels: 30% compression. Black parts denote walls.

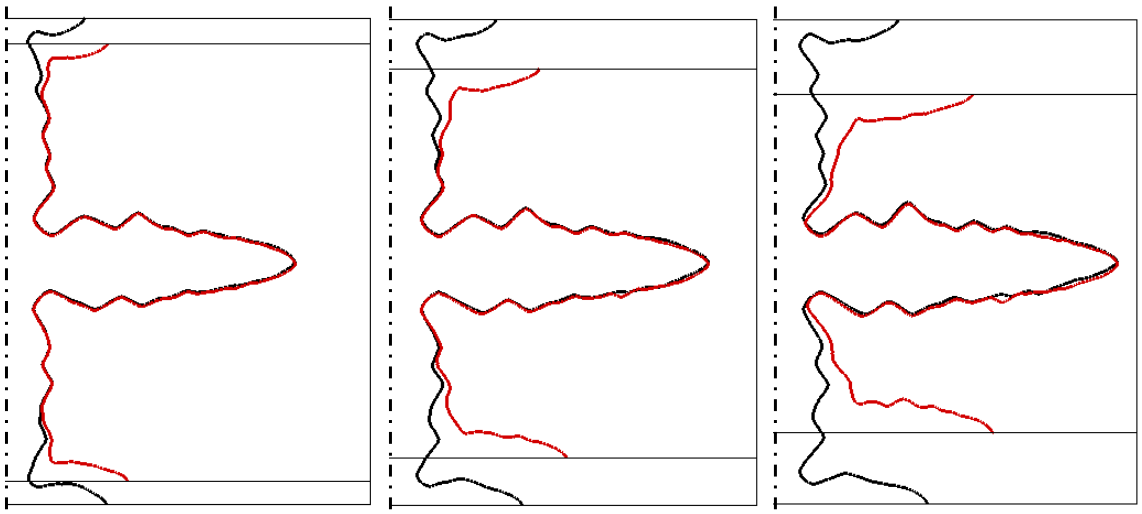

Figure 3. 14 Comparisons of computed ϕ=0 contours of evolving noised dendrite with (red line) and without (black line) compression loading at 10% (left panel), 20% (center panel), and 30% (right panel) compression; only a right half domain is presented.

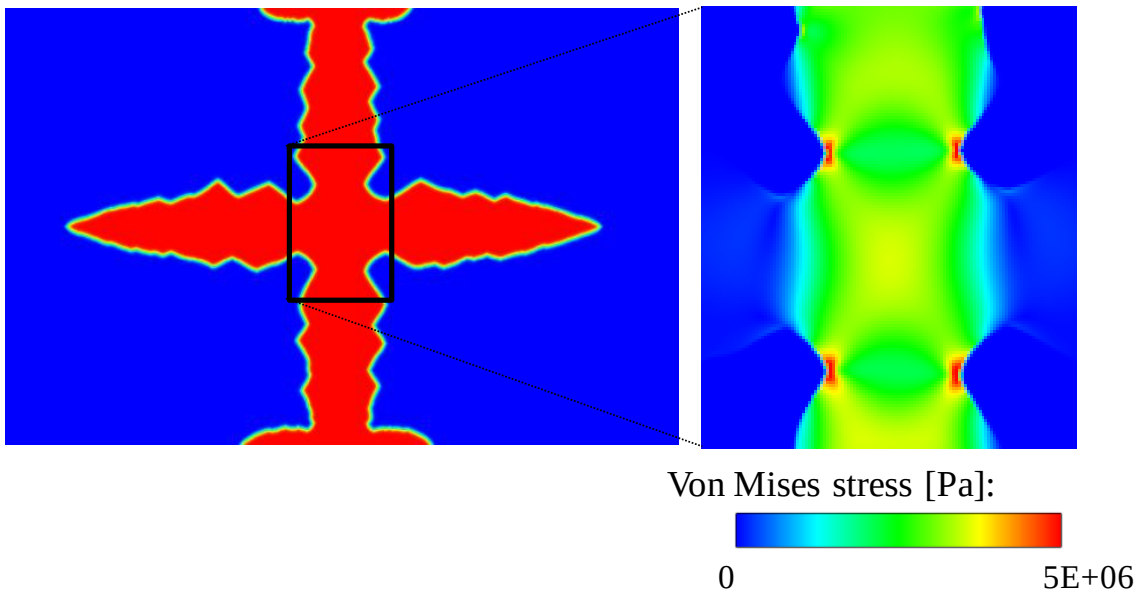

Figure 3. 15 Close-up image of dendrite under compression loading (right panel); rectangular region presented in the left panel (phase-field contour) is magnified and Mises stress is shown.

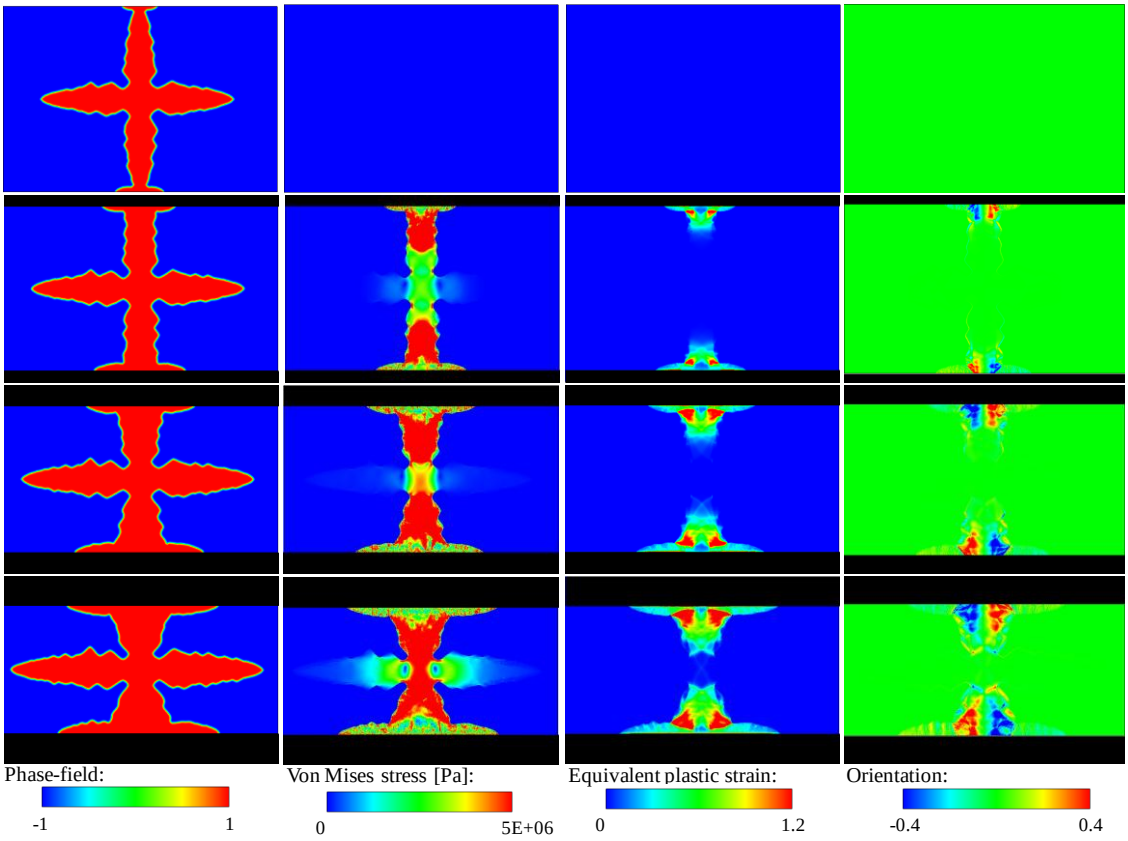

Figure 3. 16 Phase-field simulation of dendritic solidification under compression loading with thermal noise (F_u=1.0e-3); elasto-perfectly-visco-plasticity constitutive model is applied; Left panels: phase-field contours; second panels from the left: von Mises stress; third panels from the left: equivalent plastic strain; right panels: crystallographic orientation; Upper panels: initial state; panels of the second row: 10% compression; panels of the third row: 20 % compression; and lower panels: 30% compression. Black parts denote walls.

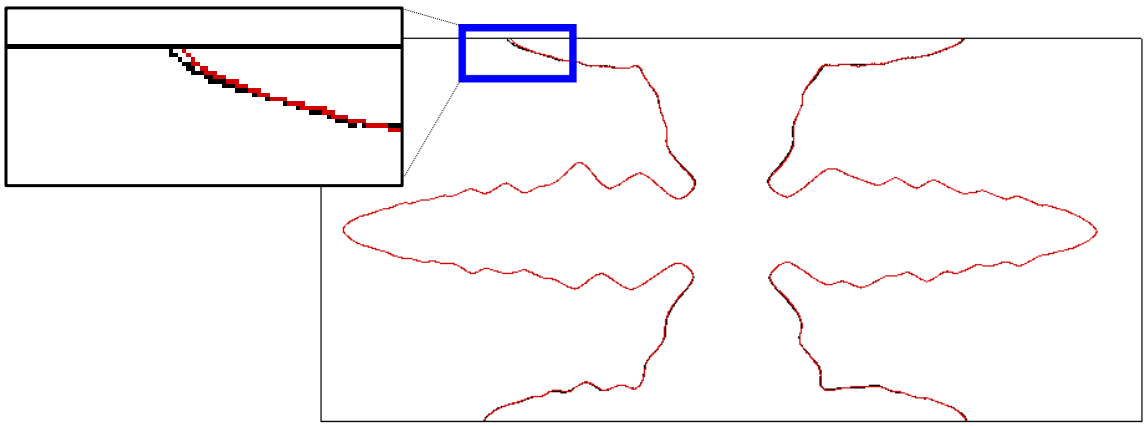

Figure 3. 17 Comparisons of computed ϕ=0 contours at 30% compression for elasto-perfectly-viscoplasticity (red line) and elasto-perfectly-plasticity (black line) constitutive model; a rectangular area indicated by thick blue line is magnified.

CHAPTER 4

PHASE-FIELD MULTIPLE DENDRITIC SOLIDIFICATION SIMULATION WITH APPLIED DEFORMATION

As stated in chapter 2, the computation of multiple dendrite growth is complicated by interfacial energies associated with the solid-liquid interface and grain boundaries. In this chapter, a numerical model to handle multiple dendrite growth is incorporated into the model developed in chapters 2 and 3. An explanation of the model is briefly presented and simulations of multiple dendrite growth with externally applied deformation are demonstrated.

4.1 Introduction

Each dendrite crystal or grain has its own crystallographic orientation which originally reflects its lattice structure and corresponds to its preferable growth direction. As multiple solid grains grow and the solid fraction increases, grain impingements take place. If the grains have different orientations, an orientation mismatch may occur around the impinging region and results in the formation of grain boundaries. Since the grain boundary separates two regions of the same crystal structure but of different orientation, the lattice structure in the region is incomplete. From this viewpoint, the grain boundary is considered to be a lattice defect (i.e. dislocations) Excess energy should be required to introduce the defects within some material. The final configuration of the macro grain structures would be determined by the minimization of free energy of the system of concern. In some case, a relaxation process to reduce orientation mismatch will occur, i.e. a grain rotation, grain coarsening, and grain boundary migration, while in other cases a wetting grain boundary (does not form grain boundary) will appear. Some energetic treatments should be necessary to simulate the solidification phenomena with multiple grains.

The phase-field model used in chapter 3 only considers a change of growth direction (orientation angle change) due to externally applied deformation, but does not include the effect of orientation mismatch on the solidification process. The orientation mismatch is considered to be an energy penalty (excess energy) in terms of the free energy of the system from the above discussion, so an appropriate model should incorporate a free energy term to simulate multiple dendrite growth with externally applied deformation.

Basically, two distinct approaches are available for the phase-field solidification simulation with multiple grains. One is the so-called multi-phase-field model, i.e. [51] and [52]. In this model, a set of order parameters (i.e. *N* parameters for *N* grains) is introduced, where each parameter represents the phase of each grain (the free energy function is modified to have *N* minima in the bulk free energy term). By doing so, *N* distinct crystallographic orientations are assigned to *N* grains, so that the energy penalty term due to orientation mismatch among grains can be included in the model. However, the restriction of the model is that the finite number of grains and distinct crystallographic orientations are allowed to be set. In this thesis, self contact within a single crystal is of interest in addition to the inter-dendritic impingements. Therefore, continuous variation of orientation is anticipated due to applied deformation. In this sense, the multi-phase-field model is not suitable to handle the situation.

Another model is called the KWC (Kobayashi-Warren-Carter) model [50] or polycrystalline phase-field model. An order parameter which represents the crystallographic orientation is introduced to the model. Since an orientation mismatch should be expressed by the spatial gradient of the crystallographic orientation, i.e. $\nabla\alpha$, the energy penalty term associated with the orientation mismatch is assumed to be proportional to the gradient. The formation of the grain boundary is computed through an interaction term between the phase-field and orientation (mismatch). The model is capable of handling a continuous variation of orientation field, thus it will be a suitable

choice to include the effect of multiple grain impingements on our numerical methodology.

4.2 Evolution Equations of KWC Phase-field Model

In this section, the formulation of the KWC phase-field model [24] is briefly explained. The crystallographic orientation $\alpha(\vec{x},t)$ at a given location and time is used in the same way as the preceding section.

4.2.1 The form of free energy

The total free energy of the system *F* of the KWC phase-field model is given by the following equation.

$$F = \int_{\Omega}\left(\frac{\varepsilon_{\phi}^{2}}{2}\Gamma\left(|\nabla\phi|,\alpha-\varphi\right)+ f(\phi,T)+h(\phi)s|\nabla\alpha|+\frac{\eta^{2}}{2}j(\phi)|\nabla\alpha|^{2}\right)dV \qquad (4.2.1)$$

The first term on the R.H.S. of the equation is an anisotropic surface energy term whose magnitude is controlled by ε_ϕ where ε_ϕ has the same meaning as the interface thickness $W(\mathbf{n})$ in chapter 2, but with a different dimension (ε_ϕ^2 has a dimension of [Energy density. Length^2]). The following form is considered for the surface energy term.

$$\Gamma\left(|\nabla\phi|,\alpha-\varphi\right)=\left(c_1+c_2\xi(\varphi-\alpha)\right)|\nabla\phi| \qquad (4.2.2)$$

where the function ζ has *N*-fold symmetry, i.e.

$$\xi\left(\varphi+\frac{2\pi}{N}\right)=\xi(\varphi) \qquad (4.2.3)$$

Angle φ is the angle between a fixed reference frame, i.e.the *x*-coordinate axis, and the direction normal to the interface. The definition is same as the defination presented in chapter 2, i.e. $\varphi=\tan^{-1}(\phi_y/\phi_x)$. Due to the representation in eq.(4.2.2), an anisotropy is imposed depending on the crystallographic orientation α. The specific form of eq.(4.2.2) is defined to be

$$\Gamma\left(|\nabla\phi|,\alpha-\varphi\right)=\left(1+\varepsilon_0\cos 4(\alpha-\varphi)\right)|\nabla\phi| \qquad (4.2.4)$$

The second term on R.H.S. of eq. (4.2.1) is again the bulk free energy density. Since there should be two stable phases, a double-well potential term with a temperature dependent term is applied in the same way that the phase-field model was used in chapters 2 and 3.

$$f(\phi,T)=\frac{a^2}{8}\left(-\frac{\phi^2}{2}+\frac{\phi^4}{4}\right)+\frac{a^2}{32}+f_{sol}\,p(\phi) \tag{4.2.5}$$

The coefficient a denotes the depth of the double-well, and a^2 has the dimension of energy density. The following forms of f_{sol} and $p(\phi)$ (monotonically increasing function) have been suggested.

$$f_{sol}=L\left(\frac{T}{T_m}-1\right)$$
$$p(\phi)=\begin{cases}\dfrac{15}{16}\left(\phi-\dfrac{2}{3}\phi^3+\dfrac{\phi^5}{5}\right)+\dfrac{1}{2} & \textit{Type I}\\[2ex] \dfrac{(1+\phi)^2}{4}(2-\phi) & \textit{Type II}\end{cases} \tag{4.2.6}$$

The type I function gives the same expression as our phase-field equation mentioned in the chapter 2 in case orientation related terms are excluded.

The third and fourth terms of eq.(4.2.1) are allowed to have a grain boundary, i.e. $\nabla\alpha\neq 0$, and grain motion, respectively. The coefficients s and η affect the strength of coupling between ϕ and α, and η also relates to the thickness of grain boundary. The functions $h(\phi)$ and $j(\phi)$, are monotonically increasing functions with respect to ϕ such that $\alpha(\mathbf{x},t)$ vanishes in the bulk liquid phase, i.e. ϕ=-1. In the polycrystalline phase-field model, the following functions have been proposed.

$$h(\phi)=j(\phi)=\frac{(1+\phi)^2}{4} \tag{4.2.7}$$

4.2.2 Evolution equations of ϕ and α

The evolution equations of ϕ and α are obtained from the variational equations of the free energy function $F(\phi, \alpha)$ using the same procedure used for obtaining the phase-field equation for single dendrite growth in chapter 2 (rate change of ϕ and α is assumed to be proportional to their gradient flow direction). In the case of an isotropic surface free energy, i.e. $\Gamma = |\nabla\phi|$, the following evolution equations can be obtained.

$$\begin{aligned}\{Q(\phi,\nabla\alpha)\tau_\psi\}\frac{\partial\phi}{\partial t} &= -\frac{\delta F}{\delta\phi} \\ &= \varepsilon_\phi^2\nabla^2\phi - \frac{\partial f(\phi,T)}{\partial\phi} - \frac{\partial h(\phi)}{\partial\phi}s|\nabla\alpha| - \frac{\partial j(\phi)}{\partial\phi}\frac{\eta^2}{2}|\nabla\alpha|^2\end{aligned} \tag{4.2.8}$$

$$\begin{aligned}\{P(\phi,\nabla\alpha)\tau_\alpha\}\phi^2\frac{\partial\alpha}{\partial t} &= -\frac{\delta F}{\delta\alpha} \\ &= \nabla\cdot\left[j(\phi)\eta^2\nabla\alpha + h(\phi)s\frac{\nabla\alpha}{|\nabla\alpha|}\right]\end{aligned} \tag{4.2.9}$$

For coefficients Q and P, the following forms are proposed.

$$\begin{aligned}&Q = 1 \\ &P = P(\eta|\nabla\alpha|), \quad where\ \ P(w) = 1 - e^{-\beta w} + \frac{\mu}{\eta}e^{-\beta w}\end{aligned} \tag{4.2.10}$$

where μ and β denote coefficients, μ=10^3 and β=10^5 are used in this study. The function P controls the relaxation time of the orientation evolution in the bulk solid grain, i.e. $|\nabla\alpha| = 0$ and the grain boundary region. A larger μ corresponds to a smaller diffusivity of orientation; which implies smaller grain rotation, and vice versa. In addition to the above evolution equations, temperature is computed by the heat equation in the same form as the equation introduced in chapter 2.

$$\frac{\partial\theta}{\partial t} = D\nabla^2\theta + \frac{1}{2}\frac{\partial\phi}{\partial t} \tag{4.2.11}$$

Basically, a symmetric boundary condition is imposed on heat equation, and has the same meaning as an adiabatic boundary condition. Since the computational domain

has finite size, the released latent heat due to phase change is accumulated in the domain, thus the domain is heated. At some moment, the dendrite growth would be suppressed because the latent heat is not sufficiently removed from the solidification front due to the temperature increase. In order to obtain an equilibrium multiple solid grain structure, a cooling term is introduced to eq.(4.2.11), i.e.

$$\frac{\partial \theta}{\partial t} = D\nabla^2\theta + \frac{1}{2}\frac{\partial \phi}{\partial t} + c(\theta_0 - \theta) \tag{4.2.12}$$

where c is the coefficient for cooling effect, and θ_0 (<0) is the reference temperature. The cooling term is activated several time steps from the beginning of the simulation.

4.3 Validation and Example of KWC Phase-field Model

4.3.1 Validation: formation of dihedral angle between impinging two grains

Some tips for an actual numerical implementation (model parameter determination, a solution methodology of an evolution equation for orientation, and one-dimensional validation problem) are described in appendix C. In this section, a two-dimensional simulation of impinging two grains is performed as a validation of the numerical program of the polycrystalline phase-field model presented in this thesis. Two-dimensional full equations (eq.(4.2.5), (4.2.6), and (4.2.8) or (4.2.9)) are to be solved, and a dihedral angle ξ_{di} formed between two grains at the equilibrium state is examined.

Before proceeding with the numerical simulations, analytical solutions of the dihedral angle in case of η=0 limit are briefly mentioned (see [24] for more mathematical details) first. The energy associated with the grain boundary is calculated by integrating free energy density over the grain boundary region. The form of the equation is

$$\gamma_{bc} = \frac{a\varepsilon_{\phi}}{3}\left[1-\left(\frac{1+\phi_{\min}}{2}\right)^{3}\right] \tag{4.3.1}$$

where ϕ_{min} is the phase-field ϕ at the center of the grain boundary, and is represented by

$$\phi_{\min} = 1-\frac{2\Delta\alpha}{\Delta\alpha_{c}} \tag{4.3.2}$$

The term $\Delta\alpha_c$ is the critical angle mismatch which is defined by

$$\Delta\alpha_{c} = \frac{a\varepsilon_{\phi}}{s} \tag{4.3.3}$$

Since the phase-field is allowed to have a value in the range of $-1\leq\phi\leq1$, a grain boundary is not formed if $\Delta\alpha>\Delta\alpha_c$ in the KWC phase-field model (wetting boundary). If the system has a wetting boundary, an usual solid-liquid interfacial energy γ_{ls} should be computed by an integration of free energy density over the diffuse interface region in the absence of orientation mismatch ($\Delta\alpha=0$).

$$\gamma_{ls} = \frac{a\varepsilon_{\phi}}{6} \tag{4.3.4}$$

From eq.(4.3.1) and (4.3.4), the following insight into the KWC phase-field model is obtained. In order to create a grain boundary, a pair of solid-liquid interfaces which are impinging each other should be necessary, with the energy cost to create the two interfaces given by $2\gamma_{ls}=a\varepsilon_{\phi}/3$ from eq.(4.3.4). On the contrary, the energy required to form grain boundary at $\Delta\alpha=\Delta\alpha_c$ is represented by $\gamma_{bc}(\Delta\alpha_c)=a\varepsilon_{\phi}/3$ from eq.(4.3.1). The energy cost to form a wetting boundary and the energy cost to form a grain boundary are balanced at $\Delta\alpha=\Delta\alpha_c$. Therefore, forming wetting boundary is favorable if $\Delta\alpha>\Delta\alpha_c$ in the model. The dihedral angle ξ_{di} observed at a triple point shown in Figure 4. 1 is given by the following Young's equation (force balance at the triple point).

$$\cos\left(\frac{\xi_{di}}{2}\right) = \frac{\gamma_{bc}}{2\gamma_{ls}} \tag{4.3.5}$$

Eq.(4.3.1), (4.3.4), and (4.3.5) give the following analytical expression of the dihedral angle ξ_{di} in the case of η=0 limit, and the dihedral angle is compared with the one obtained by numerical simulation.

$$\xi_{di} = 2\cos^{-1}\left(\frac{\gamma_{bc}}{2\gamma_{ls}}\right) \tag{4.3.6}$$

For the numerical simulation, two grains are placed next to one another, and ϕ=1 and α=$\pm\Delta\alpha$/2 are assigned inside the grains. Values of ϕ=-1, α=0 are assigned to liquid phase as initial conditions (Figure 4. 2 (a) and (b)). The value θ=0 is imposed as the initial temperature. The method of parameter determination used by Warren et al. [24] is adopted such that the dimensionless model parameters are set to be $\tilde{\varepsilon}_\phi = 1.0, \tilde{s} = 0.94, \tilde{\eta} = 0.53, \tau'_\alpha = 0.1$(diffuse interface thickness $W_0 (= \tilde{\varepsilon}_\phi)$ and relaxation time τ_0 are used for characteristic length and time scale). The operation conditions are set such that ε_0=0.0, d_0/W_0=0.185, $\Delta x/W_0$=0.4, and D=3.0. Since the initial curvature is defined without considering Gibbs-Thomson effect, the system tries to establish new equilibrium state. Some parts of the grain melt back and cool the interface region until the temperature of the region and the melting point determined by the interface curvature become equivalent.

In order to compare the numerical result with its analytical solution given by eq.(4.3.6), the interface curvature is measured by fitting two true circles to ϕ=0 interface contours at 300000 steps (an equilibrium of the system is assumed to be established at this stage). Using the obtained centers of the two circles and radii, a dihedral angle is geometrically computed. Figure 4. 3 shows the phase-field contours for four different orientation mismatches ($\Delta\alpha/\Delta\alpha_c$=0.19, 0.38, 0.57, and 1.5). As the mismatch becomes larger, the dihedral angle becomes smaller. For instance, a wetting boundary is observed in the case of $\Delta\alpha/\Delta\alpha_c$=1.5. Figure 4. 4 plots the dihedral angles as a function of orientation mismatch. The analytical solution given by eq.(4.3.6) is indicated by a solid

line whereas the numerical solutions are represented by square dots. The dihedral angle decreases with increasing orientation mismatch, and the tendency is due to a dependency of the grain boundary energy on the orientation mismatch represented by eq.(4.3.1). Since the analytical solution is computed under the assumption of η=0, there is a difference between the analytical and numerical solution, but the polycrystalline phase-field model represents the behavior of grain boundary formation well. The upper panel of Figure 4. 5 shows the relationship between orientation mismatch and grain boundary energy which is normalized by the solid-liquid interfacial energy $2\gamma_{ls}$. In the range of small orientation mismatch, the grain boundary energy has an almost linear dependency on the orientation mismatch. The dependency is the same as the dependancy analytically obtained by Read-Shockley [69]. As previously mentioned, if the orientation mismatch is more than its critical value $\Delta\alpha_c$, the grain boundary energy is maintained at $2\gamma_{ls}$ (since less energy is required to form a wetting boundary in the state). In the lower panel of the same figure, the experimental results of the relationship between orientation mismatch and grain boundary energy for tin and lead are plotted [70]. The dependency of each material qualitatively agrees well with the dependency obtained by numerical simulation (upper panel of the same figure). Since γ_{ls} depends on the material, the value should be adjusted by a parameter a and ε_ϕ in eq.(4.3.4) if a specific material is considered. The term $\Delta\alpha_c$ is also shown in the figure as the angle at which the boundary energy converges to a constant value. That value can be controlled by the parameter s in eq.(4.3.3) if we want. In this thesis,a specific material is not assumed, so the parameter determination proposed by Warren et al. is adopted (see appendix C for more details).

4.3.2 Example: isothermal impingement simulation of four grains

In the preceding section, the basic characteristic of the polycrystalline phase-field model are examined, and it is shown that the model can qualitatively present the actual behavior of the grain boundary, i.e. the relationship between orientation mismatch and grain boundary energy. In this section, the impingements of four grains are simulated to form a complete solid grain structure.

As shown in Figure 4. 6 for equally sized circular grains are allocated to four corners of calculation domain whose size is 201x201. The parameter settings are the same as those in the last section, except that a constant temperature θ=-0.1 is imposed on the system throughout the simulation. Flux free boundary conditions are imposed on all variables.

Three different computational settings are investigated (Figure 4. 6 (a)~(c)). For case (a), the left two grains have α=0 whereas right two grains have $\alpha=\pi/8$. No orientation mismatch exists between left two and right two grains, so they are merged together. As a result, a planar grain boundary is formed in the vertical direction. For case (b), the left two grains have the same α=0, and they are merged together. Contrary to example a, an orientation mismatch $\Delta\alpha=\pi/4$ exists between right two grains, so a grain boundary is formed between the two grains. Since three different orientations coexist in the system, a dihedral angle is formed at the triple junction. For case (c), the three different orientations used in case (b) are imposed on the system, but the upper left and lower right grains have the same orientation. This results in a merged grain structure of those two grains. In this way, a multiple grain structure is formed through the interactions of orientation mismatch among the grains by the polycrystalline phase-field model.

4.3.3 Example: non-isothermal simulation of multiple grain impingements

For a more practical application, in addition to the model used in the last section, thermal diffusion is included through the heat equation. The computational domain is expanded to 1201x1201, and 50 seeds are randomly allocated in the domain. Crystallographic orientation α is also randomly assigned to each solid seed such that the value stays within $-\pi/4 \leq \alpha \leq \pi/4$. The same model parameters as the last section are used except ε_0=0.05 and Δ=0.55 are applied to form the dendritic structure. In this calculation, a cooling term in (4.2.12) is activated after t/τ_0=50. The values c=10and θ_0=-0.2 are used to obtain a completely solidified grain structure. The flux free boundary condition is adopted.

Figure 4. 7 shows a series of the simulation. At an early stage of the simulation, each solid seed freely evolves its structure, and then impingements between the grains take place. Depending on the orientation mismatch, grain boundaries are formed among grains. As the simulation goes, the coarsening process is also observed. Grain boundaries formed by small orientation mismatches typically vanish by matching the orientation of one of the grains with the orientation of its neighbor, so that the number of grains reduces with time. The numerical program of the polycrystalline phase-field model proposed in this thesis should work with a larger system (see appendix C for a simulation of multiple grain growth with thermal noise).

4.4 Modeling of the Mechanical Behavior of the Grain Boundary

Mechanical connections among grains, i.e. bridging, are determined depending on the state of the free energy of the system, and have a considerable effect on the relative motions among the grains. For instance, if two adjacent grains form a bridge between them, the grains behave as a single solid structure. On the contrary, individual motions

are expected for each grain when a wetting boundary is formed between two. A grain boundary in the polycrystalline phase-field model is represented by the phase-field as a value in the range of $-1<\phi<1$ at the equilibrium state. Since the motion of the liquid phase is not computed in this thesis, the phase-field dependent mechanical properties (assign mechanical properties of solid phase for $\phi=1$ and those of liquid phase for $\phi=-1$. Otherwise mechanical properties in between solid and liquid phase is imposed for $-1<\phi<1$) do not provide a good representation of the grains at the grain boundary. In this thesis, the simply mechanical properties of solid phase are imposed if $\phi\geq 0$, otherwise no contribution of mechanical response is assumed for the case where $\phi<0$.

The introduction of anisotropic constitutive behavior into the MPM should be possible (i.e. [32]), and would be a future work.

4.4.1 Test simulation of examining mechanical behavior of a grain boundary

A simple test simulation to check the mechanical behavior of a grain boundary is examined. No anisotropy ($\varepsilon_0=0.0$) is assumed, and $\tilde{\varepsilon}_\phi = 1.0, \tilde{s} = 0.94, \tilde{\eta} = 0.53$, $\tau'_\alpha = 0.1$, $d_0/W_0=0.185$, $\Delta x/W_0=0.4$, and $D=3.0$ are set as operation conditions. The flux free boundary condition is applied to the whole boundary. Initially, a planar solid is placed in the computational domain (401x1201 grid nodes), and the region is separated into two sub-domains where each sub-domain has its own orientation (Figure 4. 8 upper panels). In one case (a), an orientation mismatch is imposed such that $\Delta\alpha/\Delta\alpha_c=1.39$. In case (b), a lower orientation mismatch $\Delta\alpha/\Delta\alpha_c=0.13$ is assigned. The solid region is exposed to the undercooled liquid ($\Delta=0.55$), thus it evolves upward while forming a grain boundary. As shown in the lower panels of the same figure, the grain boundary formed in case (a) has $\phi<0$ whereas $\phi>0$ is observed in case (b). Therefore, the solid region in case (a) should behave as two individual solid parts while in case (b) it deforms as one unified solid structure. As shown in Figure 4. 9, a forced displacement is imposed on the left and right

walls such that grains are pulled apart. The sliding boundary condition is used on the bottom wall.

Figure 4. 10 shows the phase-field contours of case (a) and (b) at the initial state (upper panels) and at 15% tensile deformation (lower panels). For case (a), grains are pulled apart while evolving their solid structure. On the contrary, solid grains behave as one solid in case (b). In this way, the grain boundary is assumed to be a complete solid or complete liquid depending on its phase-field value in this thesis.

4.5 Multiple Grain Growth under Applied Deformation

Solid deformation analysis is coupled with the polycrystalline phase-field model in this section. First, multiple globular growths under shear deformation are simulated as a relatively simple test calculation. Then, the deformation analysis of dendrite structures with fine side-branches is presented.

4.5.1 Example 1: multiple globular grain growth under imposed shear deformation

4.5.1.1 Calculation settings

As shown in the upper panels of Figure 4. 11 , 14 solid seeds are initially allocated in a zigzag alignment. For each seed, the crystallographic orientation is randomly assigned. No anisotropy (ε_0=0.0) is assumed, and $\tilde{\varepsilon}_{\phi} = 1.0, \tilde{s} = 0.94, \tilde{\eta} = 0.53$, $\tau'_{\alpha} = 0.1$, d_0/W_0=0.185, $\Delta x/W_0$=0.4, and D=3.0 are specified as model parameters. The flux free boundary condition is used. First, the solid seeds evolve their structure without deformation until some bridging is formed among them (Figure 4. 11 lower panels). Although the initial allocation of seeds is quite simple and regular, a complex multiple grain structure appears even at this stage since angle mismatches among grains are different depending on their location. After the initial

evolution of the solid seeds, shear deformation is imposed to the solid structure through enforced displacement of the top and bottom walls (Figure 4. 12).

4.5.1.2 Results

Figure 4. 13 illustrates Mises stress (left panels) and the equivalent plastic strain (right panels) at 0% (upper panels), 10% shear (panels in the second row), 20% (panels in the third row), and 40% shear (lower panels). The deformation concentrates on narrow portions of the solid structure at the early stage, i.e. at 10 and 20% shear; the portions have a relatively higher plastic strain than the other part of the solid structure. After the remaining liquid parts residing among grains are solidified, i.e. at 40% shear, traces of plastic deformation are found around the grains initially located in the middle row. A remarkable effect of the applied deformation on the evolving grain structure is observed around the seed located at the rightmost side in the middle row. As indicated in the magnified images of the region in Figure 4. 14, the seed is translated to leftward by the enforced displacement acting on the solid allocated on the lower wall which is connected to the seed. Due to the translation, the liquid part allocated between the solid and its neighbor on the left side solidifies faster than it would solidigy in the case without the shear deformation, i.e. Figure 4. 17 upper panel. Figure 4. 15 and Figure 4. 16 show the contours of the phase-field and crystallographic orientation as a function of time. The imposed shear deforms the distribution of crystallographic orientation as well as the solid structure (phase-field) itself (see also Figure 4. 17 lower panel). The simulation proves the impact of applied deformation on the evolving grain structure.

4.5.2 Example 2: evolving dendrites with thermal noise under imposed shear

4.5.2.1 Calculation settings

In order to show the capability of our methodology to handle more complex microstructure, a thermally fluctuated interface is introduced in this section. Most of the model parameters are identical to those used in the example 1, but ε_0=0.08 and Δ=0.8 are defined to form fine and complex side branching. The setting of ε_0 and Δ is unrealistic in the practical situation, so this problem is only for test purposes.

First, three solid seeds are placed on the bottom wall, and their orientations are aligned with the coordinate axes. Flux free boundary conditions are applied on the all boundaries for all fields. The seeds initially evolved within the under-cooled melt until their dendrite tips reach to the upper wall. Then, shear loading is imposed on the dendrite structure through enforced displacement on the upper and lower walls (Figure 4. 19).

4.5.2.2 Results

Contours of Mises stress (left panels) and equivalent plastic strain (right panels) as a function of time are presented in Figure 4. 20. Since the noised dendrites have quite complicated solid structures, stress concentration is observed in the narrow portions of the dendrites. As the result of the concentration of the deformation, plastic strain is accumulated in these portions. Figure 4. 21 shows the phase-field (left panels) and crystallographic orientation (right panels) of the same simulation. As the imposed displacement becomes larger, the orientations of vertically extended dendrites are changed by the bending motion. The constraints of *y*-displacement on the moving walls might cause a relatively large rotation of the solid lying on the wall. Variations of orientation within dendrites due to imposed deformation create mismatches of the orientations among the dendrites.

In the preceding simulation, the liquid portions that reside among dendrites are heated up due to latent heat released from the solid-liquid interface. In order to obtain a complete solid structure, the cooling effect is incorporated to the simulation. Figure 4. 22 shows Mises stress (left panels) and the equivalent plastic strain (right panels). The deformation due to self-contact or interdendritic impingements is observed as well as the concentration of the deformation in the narrow portion of the dendrites. Figure 4. 24 shows the same contour of equivalent plastic strain at 30% shear as Figure 4. 22, but the range of the contour is magnified. Plastic strain has been developed in the region of deformation concentration and impingements taking place. As shown in Figure 4. 23, once the liquid portions among dendrites are solidified (lower left panel), coarsening takes place among the grains where orientation mismatch exists (lower right panel). As a result, some grain boundaries (although the boundaries are almost close to the solid phase) are formed within the solid structure which originally had uniform orientation field (Figure 4. 25).

4.5.3 Example 3: evolving dendrite with thermal noise under imposed compression loading

4.5.3.1 Calculation settings

In this section, the same simulation as the preceding section is used but imposing compression loading is performed. Model parameters are identical to those used in example 2. The symmetric condition is assumed for computational simplicity, thus only one quarter of the domain is actually solved as shown in Figure 4. 26. A solid seed is initially placed at the lower left corner of the domain, and it evolves until the vertically extended dendrite arm reaches the upper wall. Then, compression loading is imposed with the mechanical boundary condition presented in the same figure.

4.5.3.2 Results

The complex dendrite structure is compressed while evolving its solid structure as shown in Figure 4. 27 (see i.e. phase-field contours). As seen in example 2, plastic strain is mainly developed in the narrow portions of the dendrites and the parts where self-contact taking place. The distribution of crystallographic orientation changes in time due to the deformation and relaxation process. For instance, the side branches of the dendrite around the upper wall have own orientation angles at 5% since they behave as different grains. However, those branches are connected together as a result of relaxation process on orientations, i.e. at 10%. At 20% compression, the orientation mismatch still exists within the connected solid structure. Numerical methodology developed in this thesis can describe the relaxation or coarsening process within the complex solid structure during deformation.

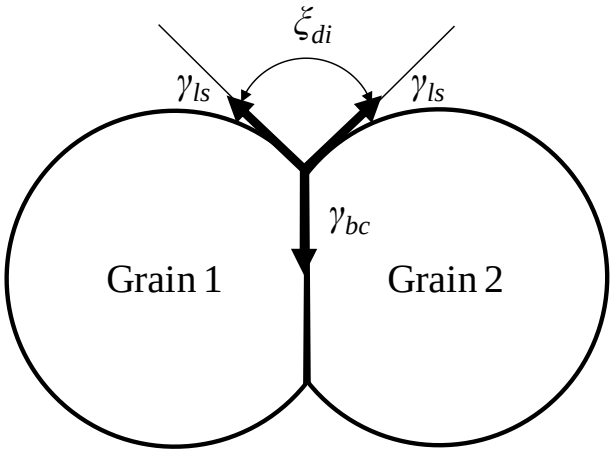

Figure 4. 1 A schematic of force balance at a grain boundary of two impinging grains

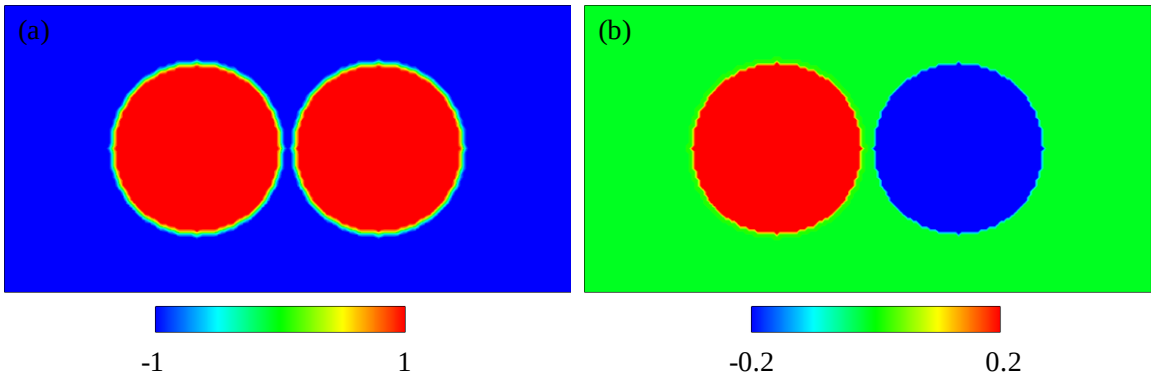

Figure 4. 2 Initial condition of 2-D numerical simulation of two impinging grains; (a) phase-field; (b) orientation field.

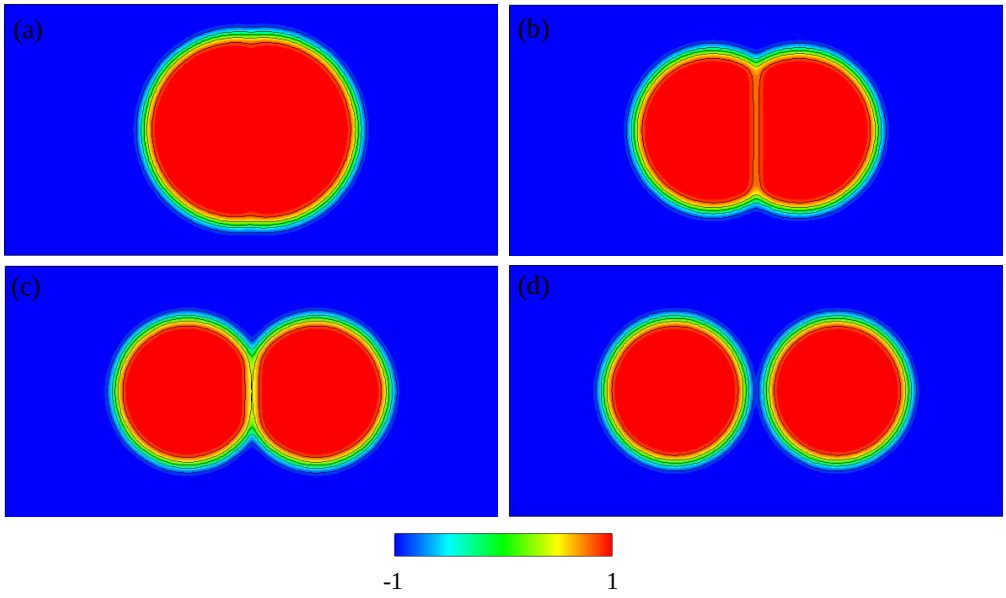

Figure 4. 3 Phase-field contours of four simulations of two impinging grains at steady state; (a) $\Delta\alpha/\Delta\alpha_c$=0.19; (b) $\Delta\alpha/\Delta\alpha_c$=0.38; (c) $\Delta\alpha/\Delta\alpha_c$=0.57; (d) $\Delta\alpha/\Delta\alpha_c$=1.5; Contour lines indicate phase-field values ϕ=-0.8-0.8 in increments of 0.4.

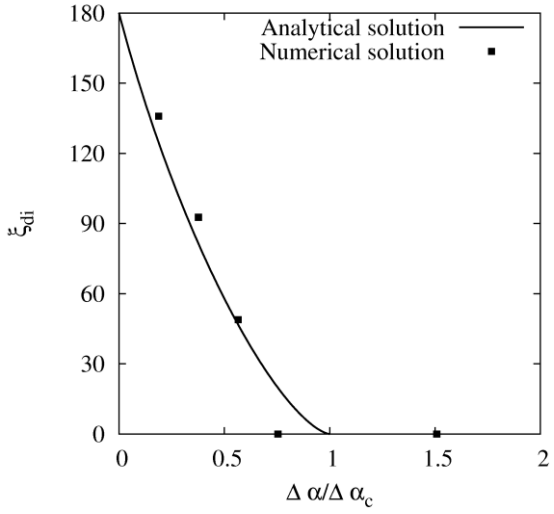

Figure 4. 4 A relation between angle mismatch $\Delta\alpha/\Delta\alpha_c$ and dihedral angle ξ_{di} for analytical (solid line) and numerical result (square dots).Two-dimensional simulation of two impinging grains. Left panel: phase-field contour of impinging grains (upper panel: $\Delta\alpha/\Delta\alpha_c$=0.67; lower panel: $\Delta\alpha/\Delta\alpha_c$=1.33) ; and right panel: relation between angle mismatch and dihedral angle

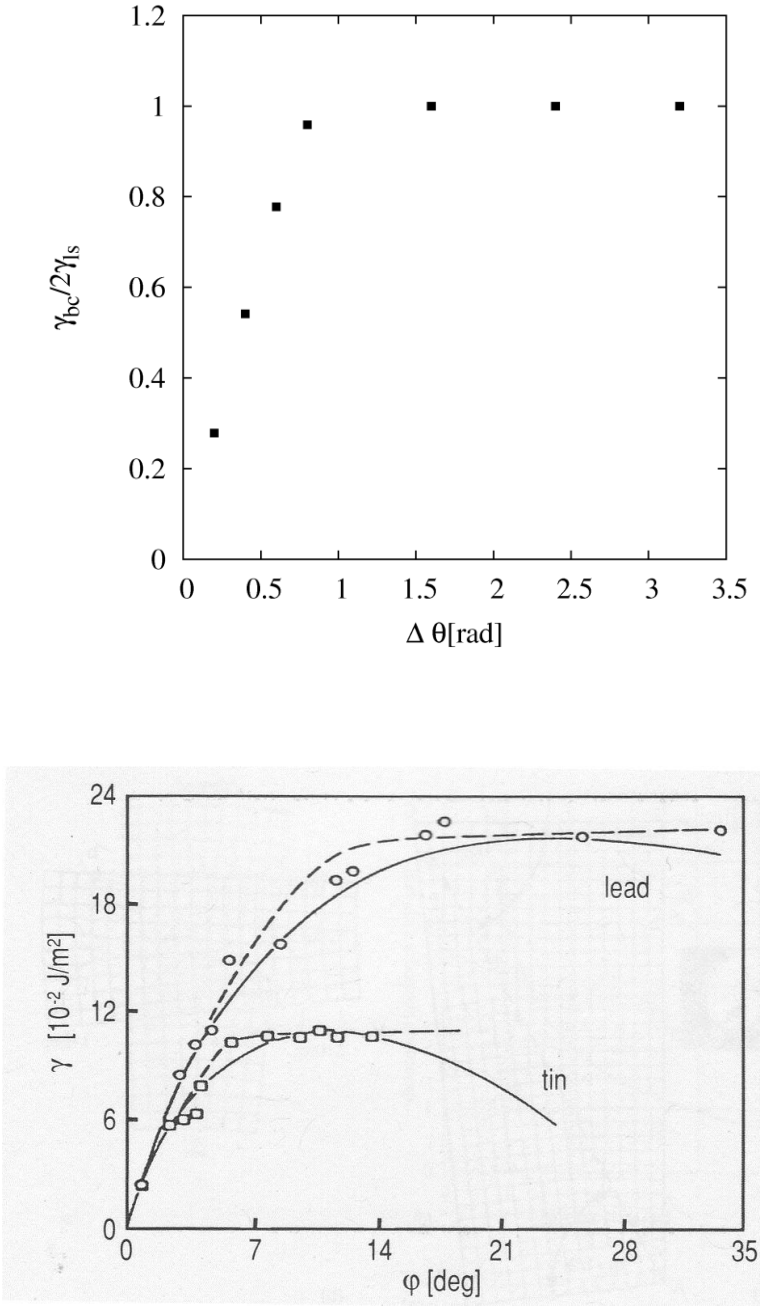

Figure 4. 5 Grain boundary energy as a function of an orientation mismatch; Upper panel: numerical result (grain boundary energy is normalized by solid-liquid interfacial energy); Lower panel: experimental values obtained from the source indicated below.

Source: Gottstein G. and Shvindlerman L.S. *Grain boundary migration in metals 2nd edition*. **2010**, CRC press.

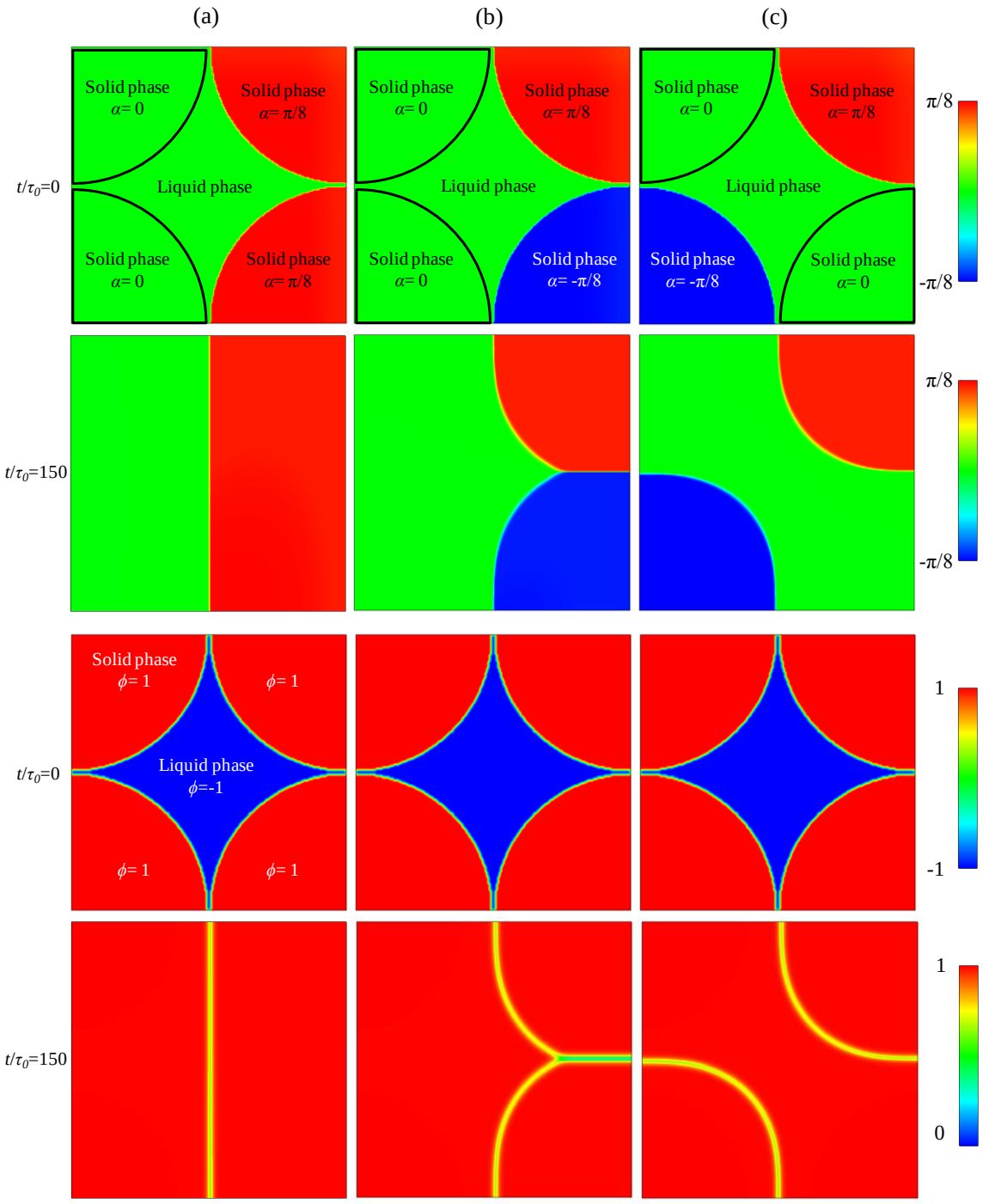

Figure 4. 6 Simulation of impinging four circular grains; panels in top two rows: orientation field at initial state (upper panels) and at t/τ_0=150 (lower panels); panels in bottom two rows: phase-field at initial state (upper panels) and at t/τ_0=150 (lower panels); three different initial settings (a)~(c) are examined.

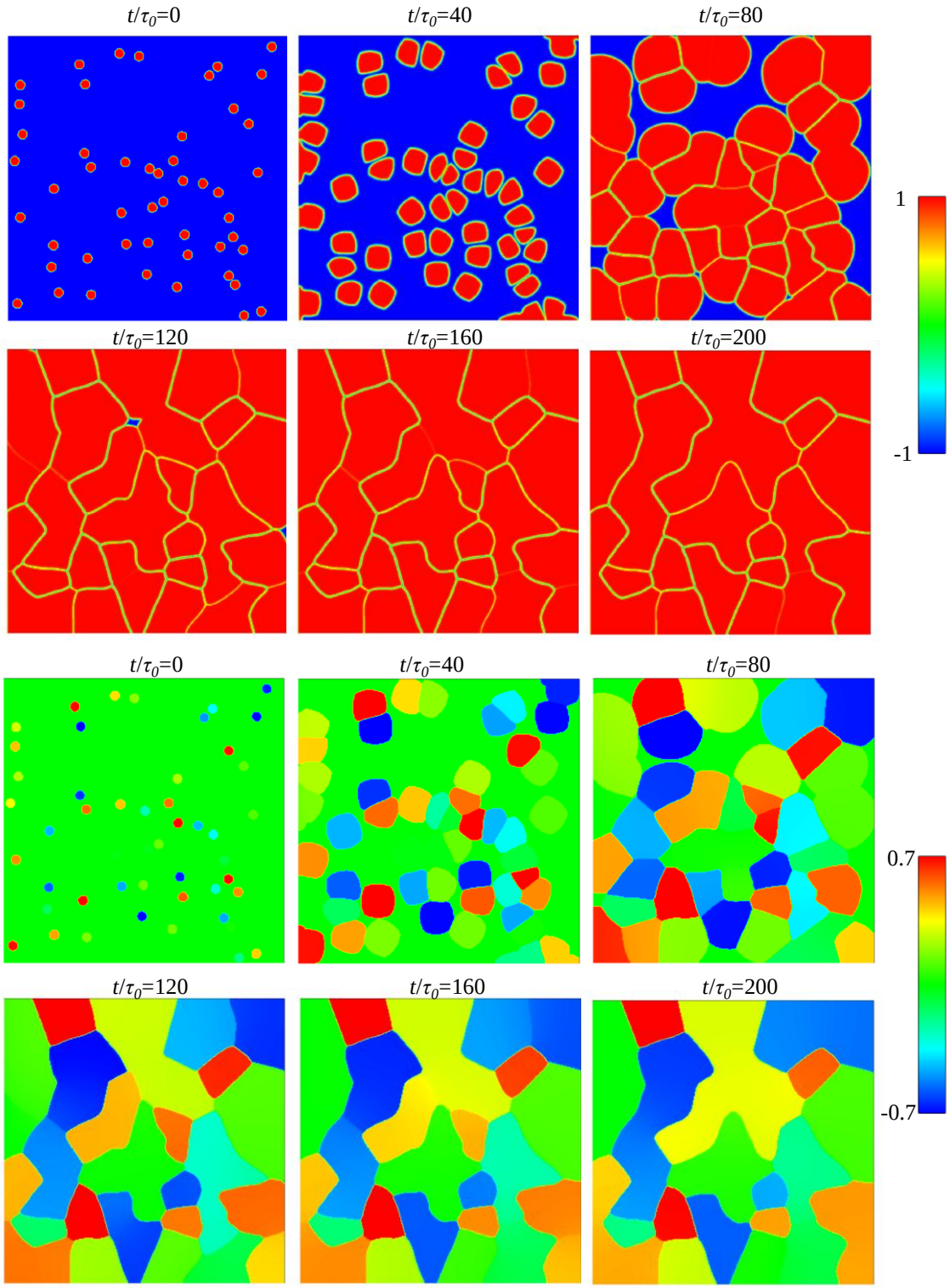

Figure 4. 7 Non-isothermal polycrystalline phase-field simulation; upper panels: phase-field at different stages; lower panels: orientation field at different stages; randomly allocated 50 solid seeds grow and form grain boundaries.

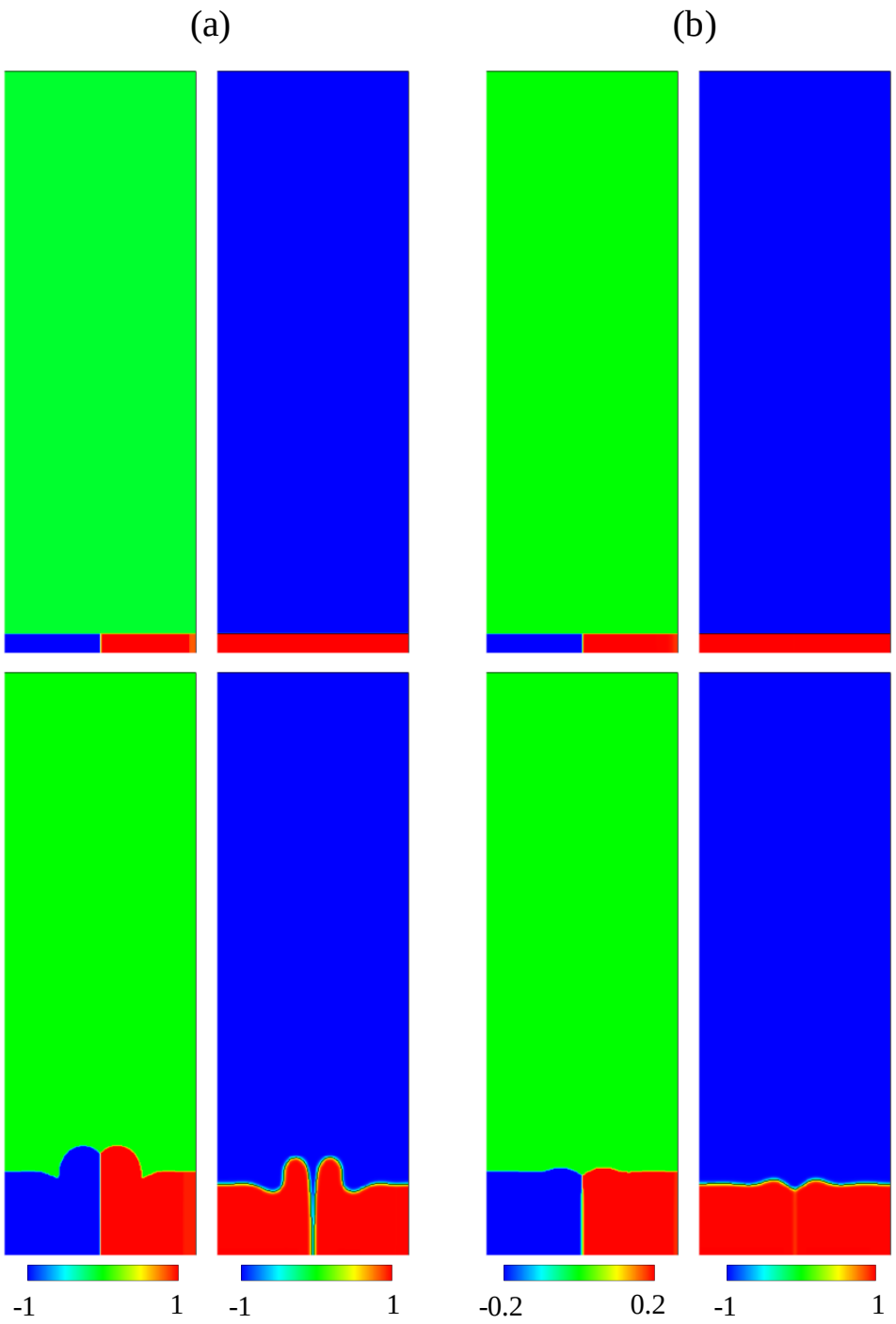

Figure 4. 8 Initial evolution of orientation field (left panels) and phase-field (right panels) for (a) high and (b) low orientation mismatch; upper panels: initial conditions; lower panels: after 60000 steps.

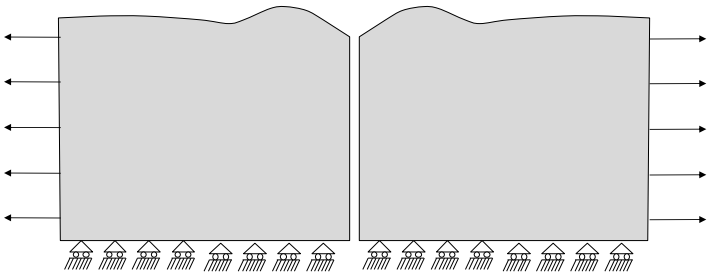

Figure 4. 9 Mechanical boundary condition of polycrystalline phase-field simulation with deformation by tensile loading.

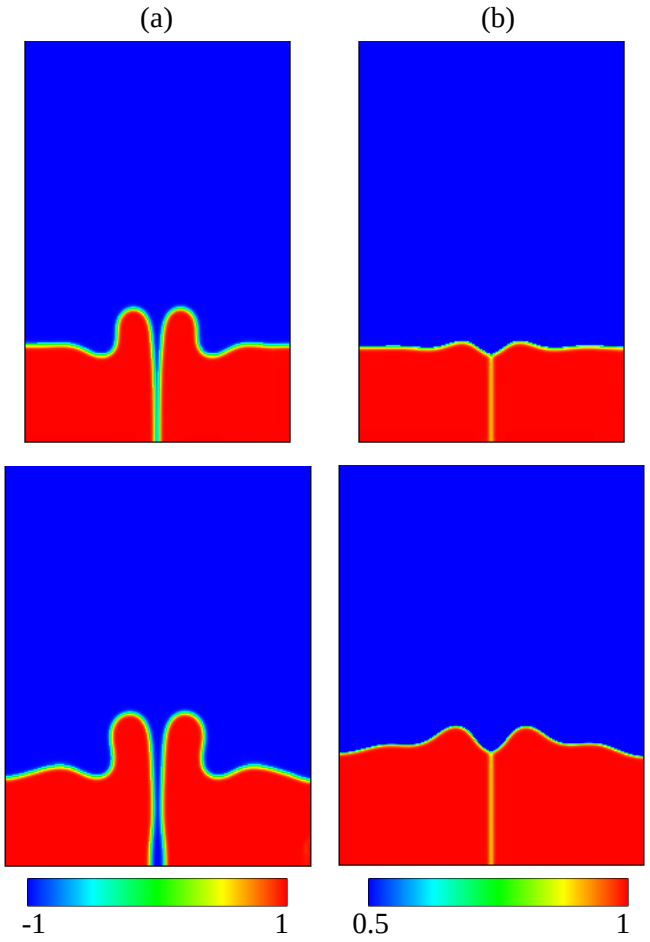

Figure 4. 10 Simulation results by phase-field polycrystalline model with MPM deformation analysis for (a) high and (b) low orientation mismatch; forced displacement is imposed such that grains are pulled apart to right and left; upper panels: at 0% tension; lower panels: at 15% tension.

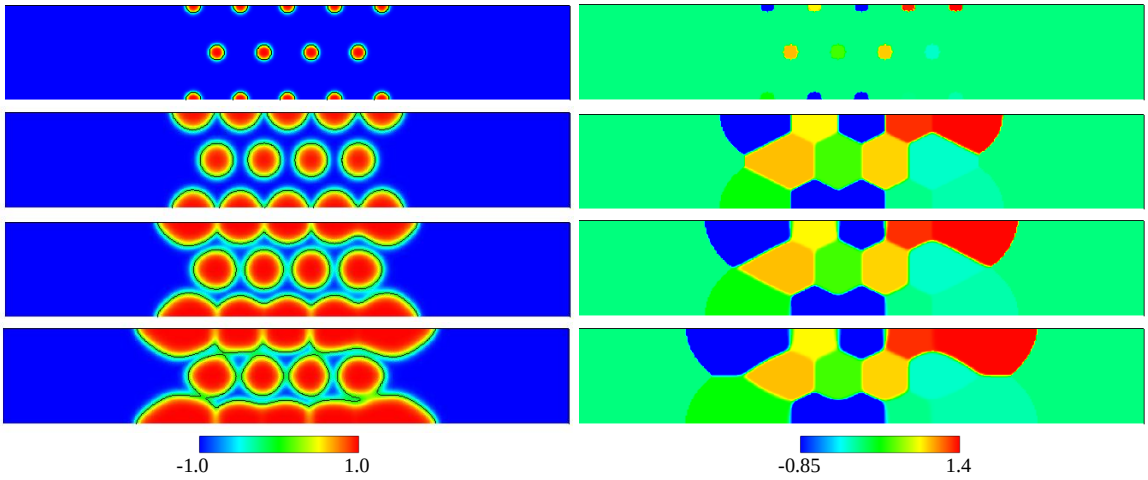

Figure 4. 11 Initial evolution of phase-field (left panels) and orientation field (right panels) of multiple globular grains for four different states.

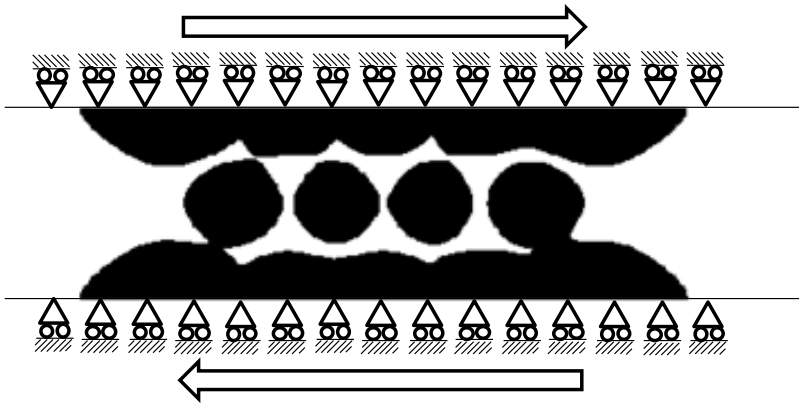

Figure 4. 12 Mechanical boundary condition of the MPM analysis imposed on the evolving multiple globular solids.

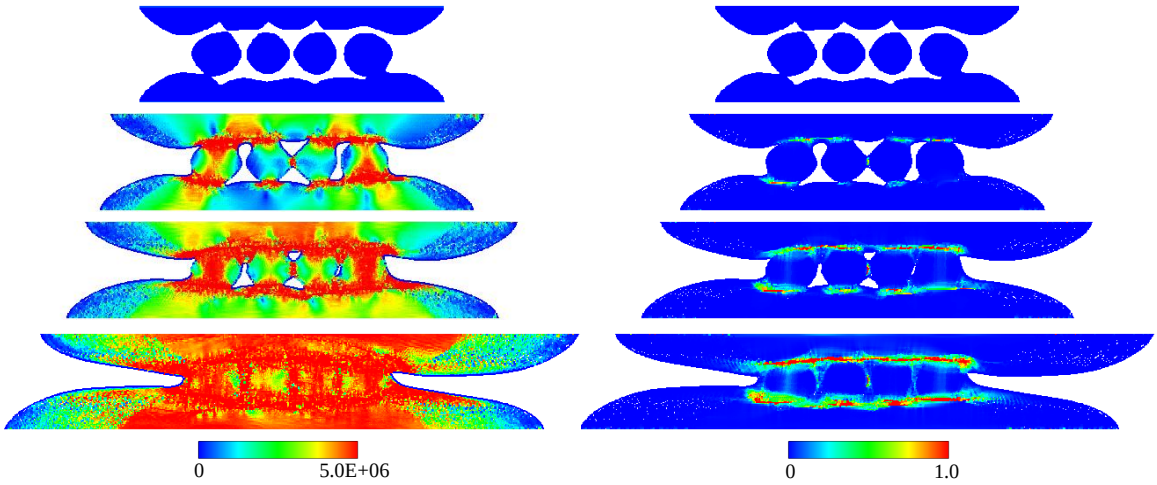

Figure 4. 13 Multiple globular growth under shear loading; left panels: von Mises stress; right panels: equivalent plastic strain at 0% shear (upper panels), at 10% shear (panels in the second row), at 20% shear (panels in the third row), and at 40% shear; contours are overlaid on material points.

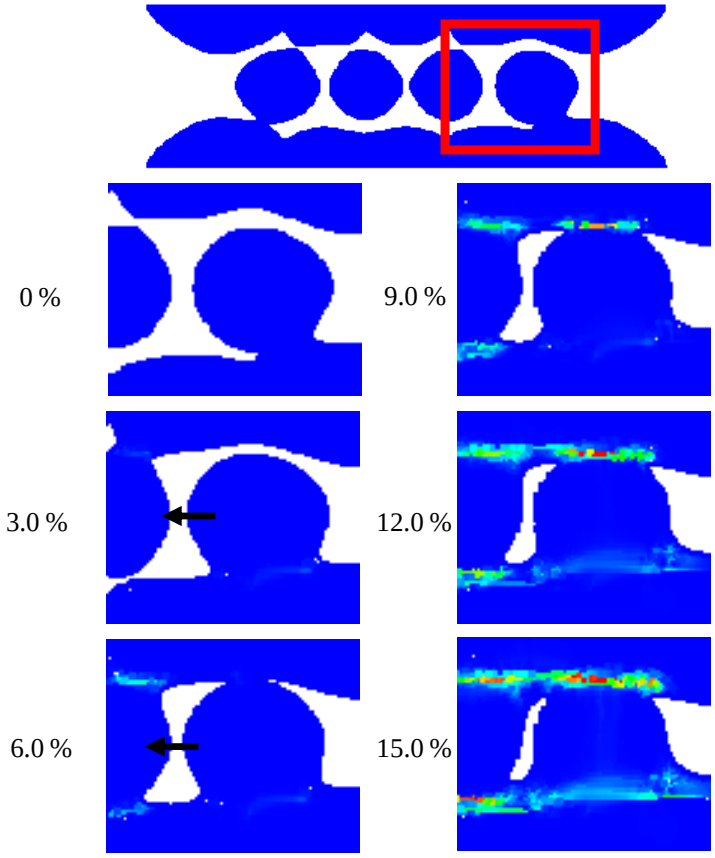

Figure 4. 14 Close-up images of material points; a rectangular domain presented in the upper panel is magnified; contours of equivalent plastic strain is overlaid on the material points; Images up to 15.0% shear deformation are presented; a solid grain moves leftward due to imposed displacement.

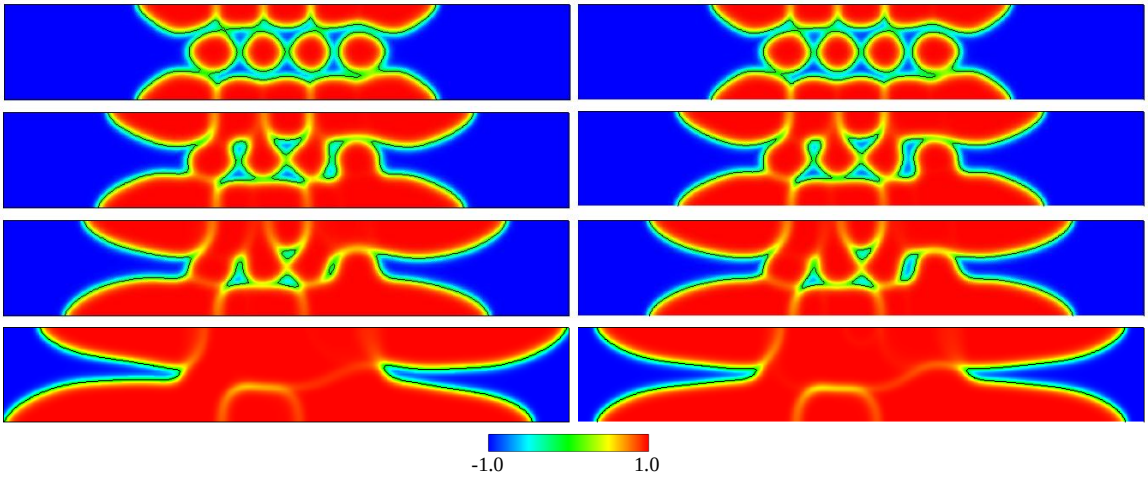

Figure 4. 15 Comparisons of phase-field contours with (left panels) and without (right panels) shear deformation at 0% (upper panels), at 10% (panels in the second row), at 20% (panels in the third row), and at 40% (lower panels).

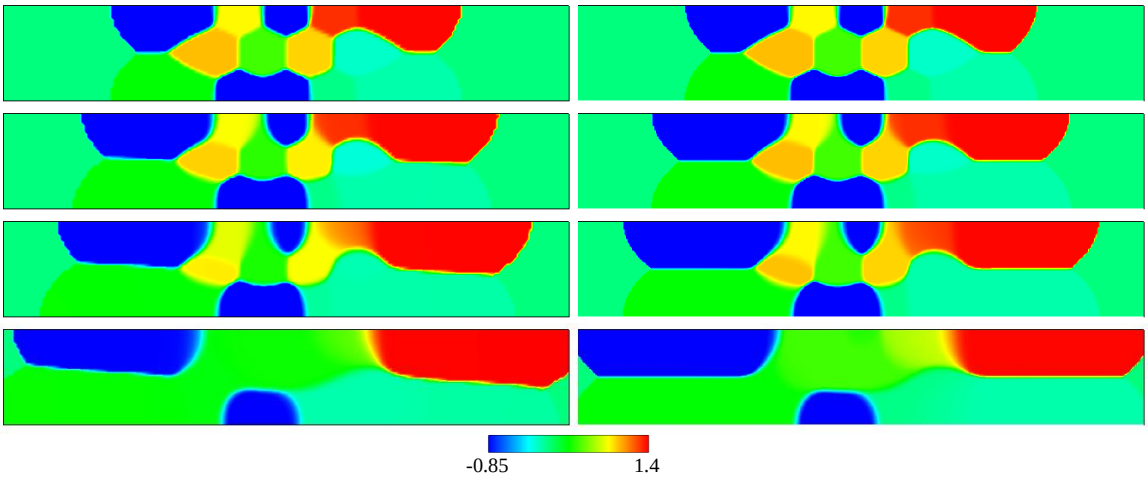

Figure 4. 16 Comparisons of crystallographic orientation contours with (left panels) and without (right panels) shear deformation at 0% (upper panels), at 10% (panels in the second row), at 20% (panels in the third row), and at 40% (lower panels).

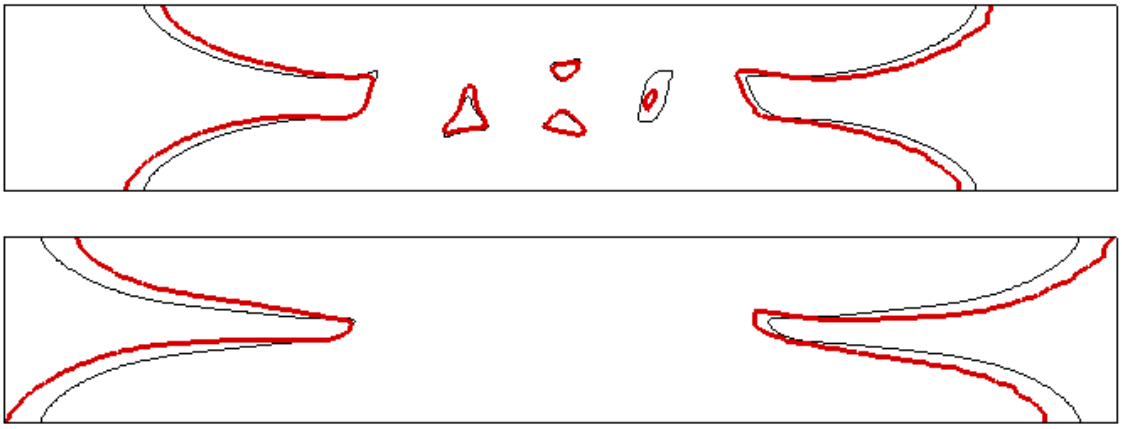

Figure 4. 17 Comparisons of computed ϕ=0 contours of growing multiple globular with (thick red line) and without (black line) shear deformation at 20% (upper panel) and 40% shear (lower panel).

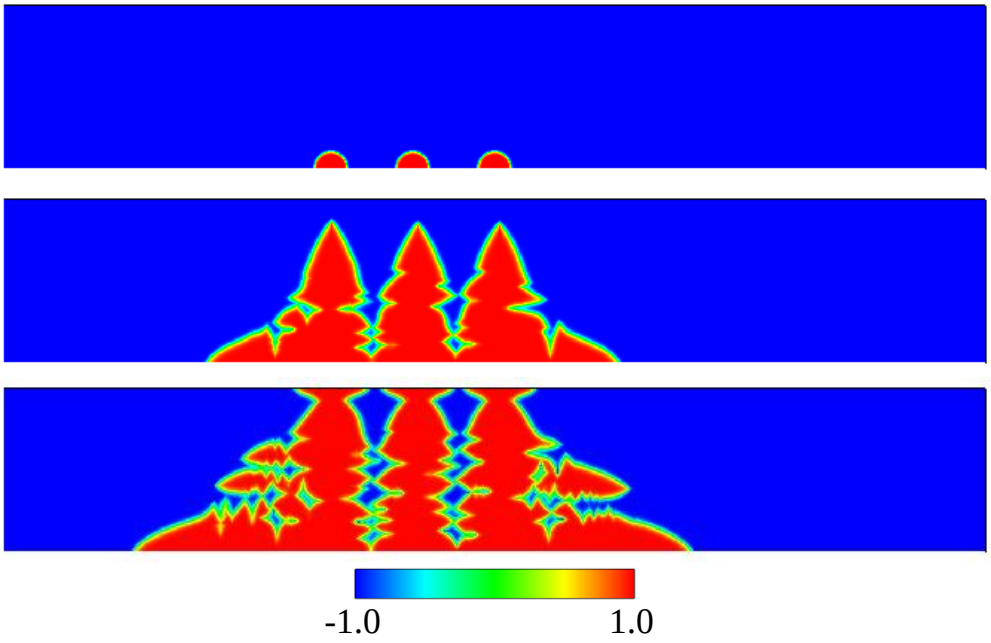

Figure 4. 18 Initial stage of free dendrite growth; Three solid seeds are initially placed on the bottom wall, and their orientations are aligned with coordinate axes, i.e. α=0, (upper panel); The seeds evolves until tips of the dendrites reach to the upper wall (middle and lower panels).

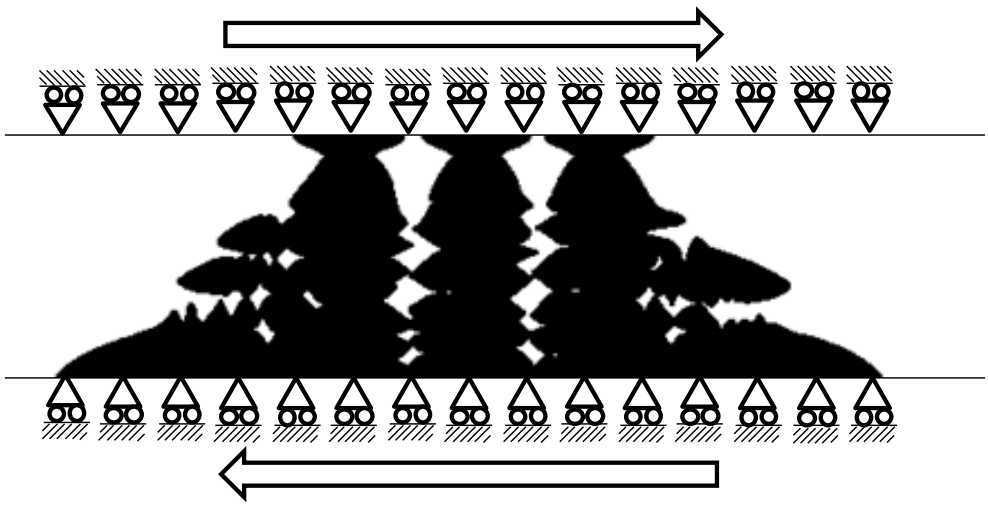

Figure 4. 19 Mechanical boundary condition of the MPM analysis for evolving dendrites under shear; displacement is imposed through upper and lower boundaries such that dendrites are sheared.

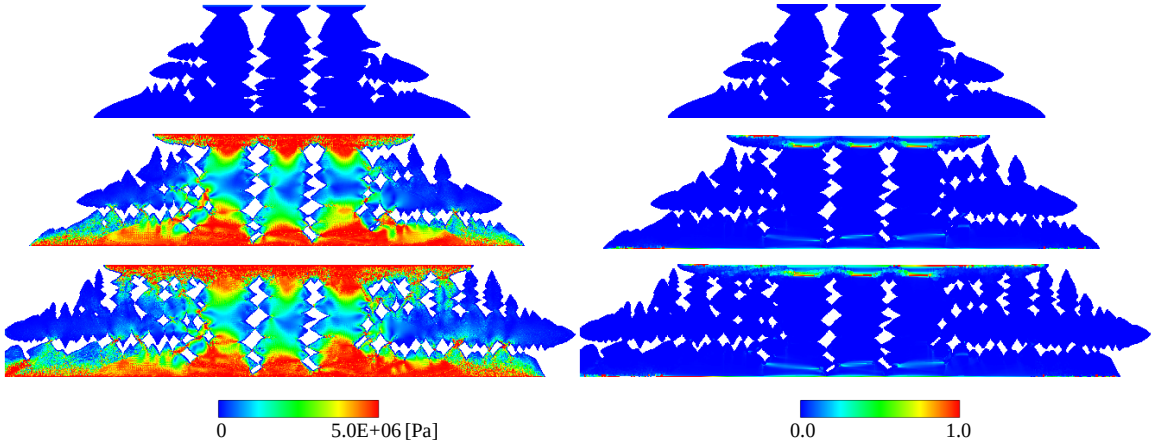

Figure 4. 20 Dendrite growth with thermal noise (ε=0.08 and Δ=0.8) under shear; left panels: von Mises stress; right panels: equivalent plastic strain at 0% shear (upper panels), at 15% shear (middle panels), and 30% shear (lower panels)

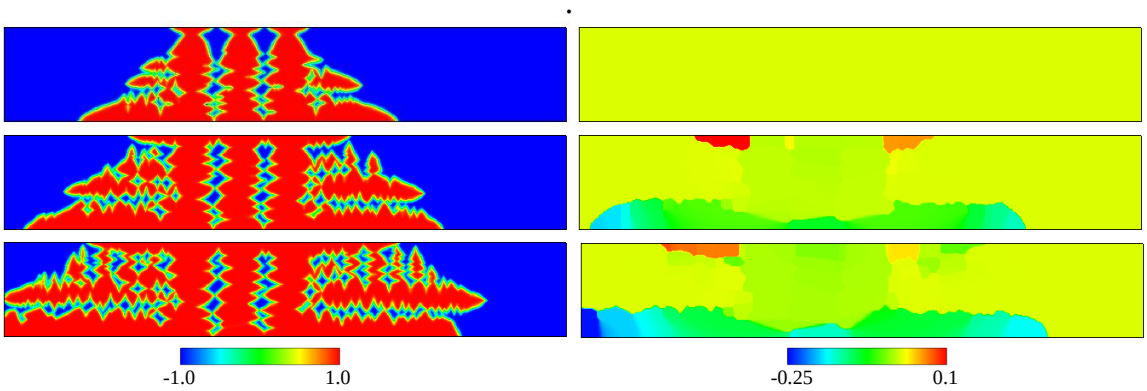

Figure 4. 21 Dendrite growth with thermal noise (ε=0.08 and Δ=0.8) under shear; Left panels: phase-field; Right panels: orientation field at 0% shear (upper panels), at 15% shear (middle panels), and 30% shear (lower panels)

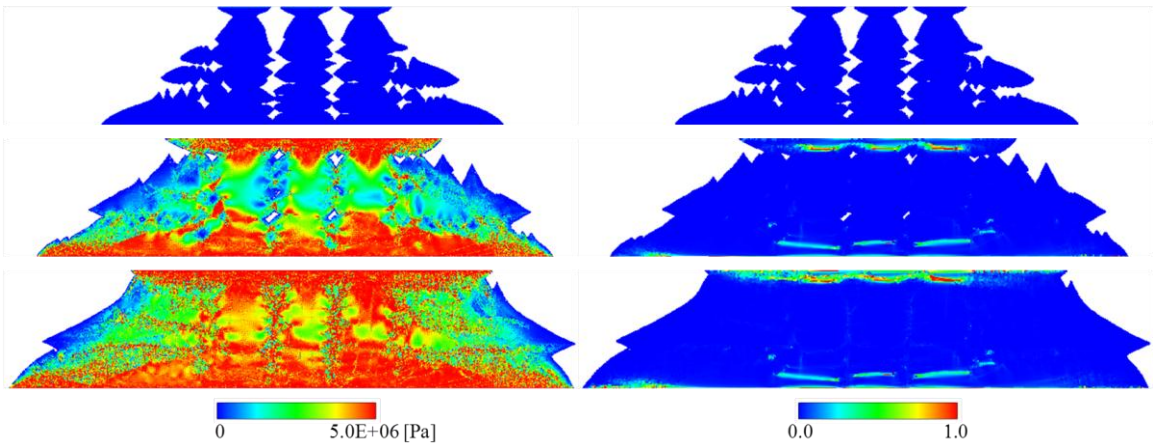

Figure 4. 22 Dendrite growth with thermal noise (ε=0.08 and Δ=0.8) under shear; left panels: von Mises stress; right panels: equivalent plastic strain at 0% shear (upper panels), 15% shear (middle panels), 30% shear (lower panels); cooling term in heat equation (4.1.12) is activated when solid deformation reaches 12% shear

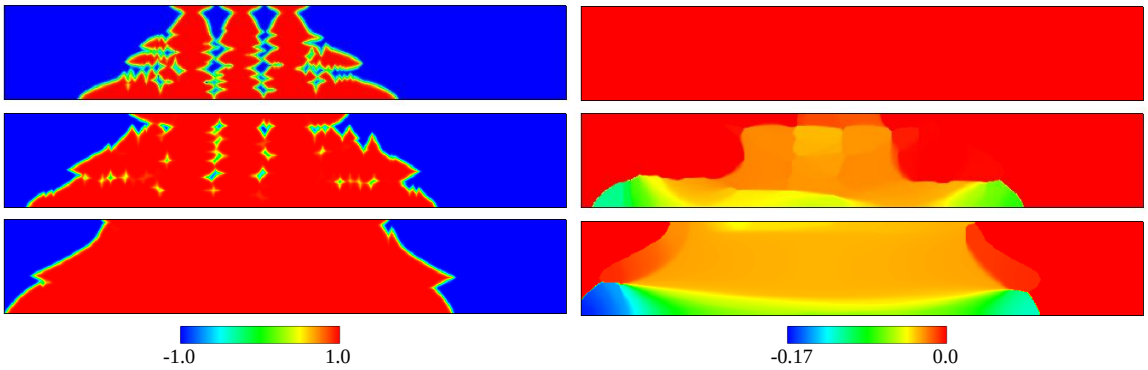

Figure 4. 23 Dendrite growth with thermal noise (ε=0.08 and Δ=0.8) under shear; left panels: phase-field; right panels: orientation field at 0% shear (upper panels), 15% shear (middle panels), and 30% shear (lower panels); cooling term in heat equation (4.1.12) is activated when solid deformation reaches 12% shear.

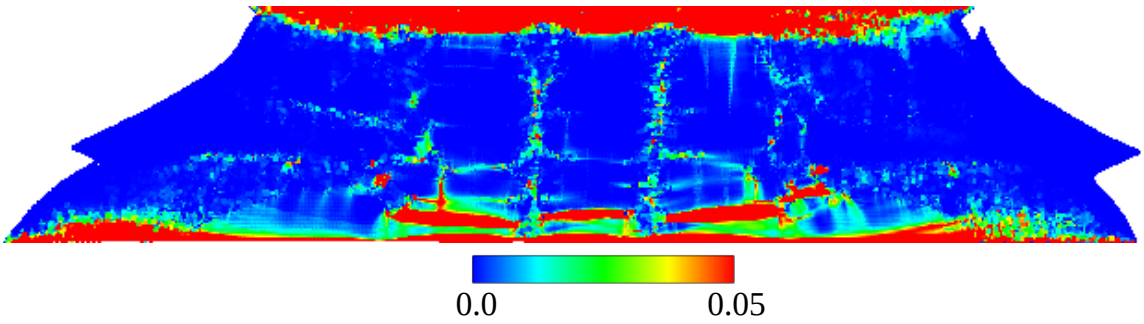

Figure 4. 24 Contour of equivalent plastic strain at 30% shear same as presented in Figure 4. 23 with the different range.

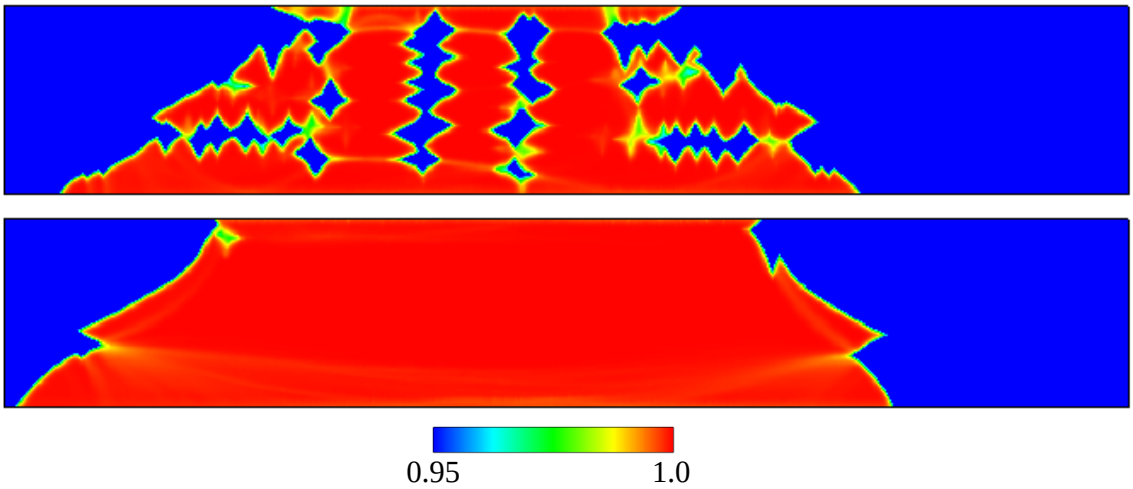

Figure 4. 25 Phase-field contours at 15% and 30% shear that are same figures presented in Figure 4.23 in the range of $0.95 \leq \phi \leq 1.0$.

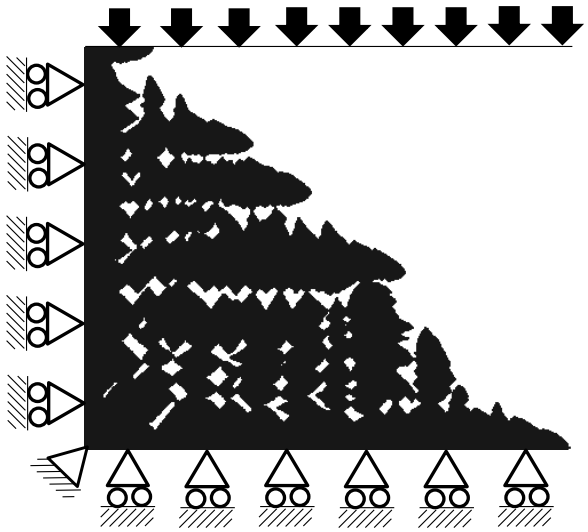

Figure 4. 26 Boundary conditions of MPM structural analysis; symmetric condition is assumed on left and bottom boundary;

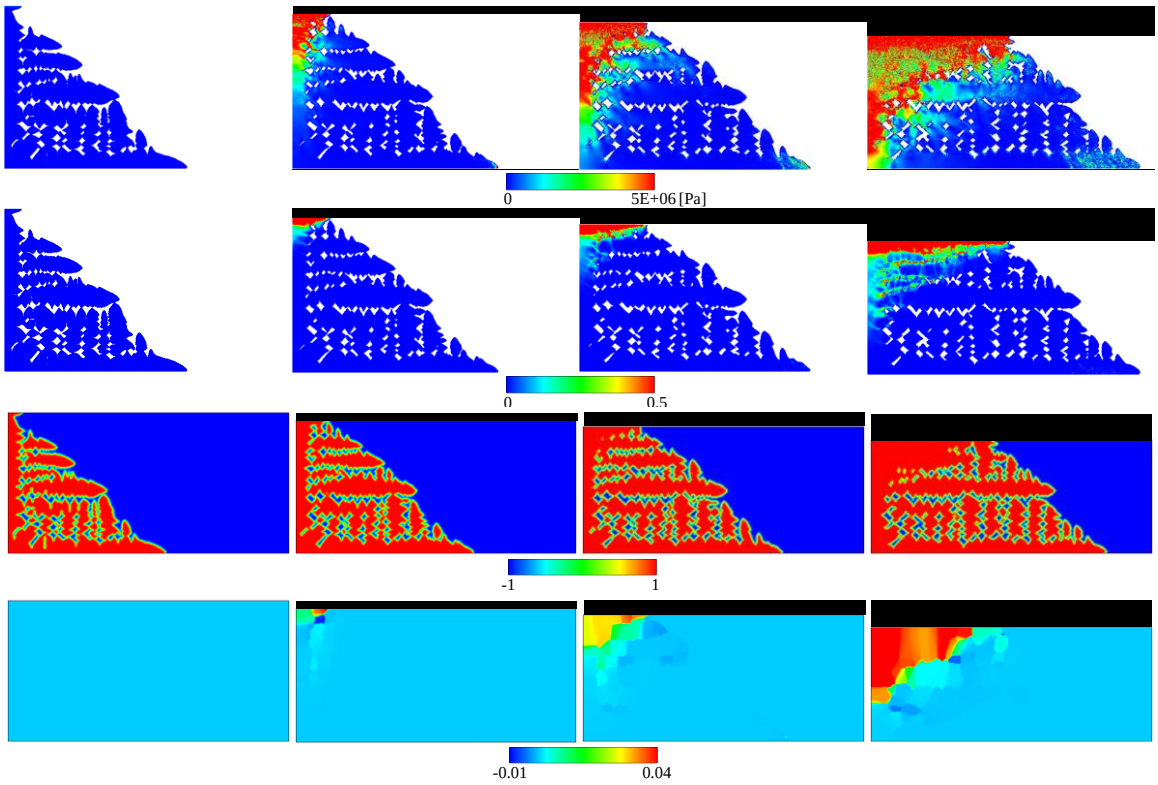

Figure 4. 27 Dendrite growth with thermal noise (ε=0.08 and Δ=0.8) under compression loading; upper panels: Mises stress; panels in the second row: equivalent plastic strain; panels in the third row: phase-field; lower panels: crystallographic orientation at 0% compression (left panels), 5 % (panels in the second column), 10% (panels in the third column), and 20% compression.

CHAPTER 5

CONCLUSIONS AND RECOMMENDATIONS FOR FUTURE WORK

5.1 Conclusions

Understanding of mechanical behavior of the evolving microstructure under applied external loads is important for a further understanding of the formation of defects such as hot tears and micro-pores. The primary objective of this thesis is to develop a promising numerical framework for modeling dendritic solidification with a deforming solid structure while addressing micro-scale physics. The novelty of this thesis is that the numerical simulation is based on the scale of evolving microstructure. The utilization of both Lagrangian and Eulerian approaches is the main feature of the numerical strategy. The phase-field simulation of solidification based on Eulerian approach makes the treatment of interface dynamics easier, and the extension of the model to the polycrystalline phase-field model allows the user to consider complex interdendritic phenomena. The material point method which is based on both Lagrangian and Eulerian descriptions is coupled with the phase-field model to simulate large solid elasto-viscoplastic deformation without the mesh collapse which is generally found in Lagrangian FEM. Through coupling, the changes in the crystallographic orientation of the evolving crystals due to applied deformation are accounted for. The examples presented in this thesis demonstrate the feasibility and capability of the numerical framework.

5.2 Recommendations for Future Work

The following aspects are recommendations for future work.

- Although the fluid flow of the liquid melt is not of interest in this thesis, the flow as a result of solid-liquid interaction should affect on the characteristics of solidification mainly through convection (solid deformation due to fluid flow is assumed to be

small [77-78]). For instance, fluid flow would be induced by the grain motion observed in the example 1 of chapter 4. The leftward motion of the grain might produce rightward flow on the upper side of the grain, i.e. Figure 4.14, and the flow will enhance heat transfer and thus solidification around the portion. Isolated liquid/gas pores will be formed earlier in this case than they would be in the case without fluid flow. The numerical methodology by Sun et al. [79] should be feasible. In the method, the velocities of solid and liquid phases are independently defined, and a matching of both velocities based on asymptotic analysis is performed within the diffuse interface. The developed methodology of field variable extension would be applicable to it.

- Contacts among the solid grains in the MPM are approximately introduced through common background cells. In the actual situation, more complicated phenomena, i.e. frictional contact or relative sliding between crystals, might be observed. For a more correct treatment of the contacts, the contact, sliding and separation model [53] would be available. However, the determination of mechanical properties associated with friction due to the contact is another challenging issue.
- Although the constitutive models used in this thesis is isotropic, so-called crystal plasticity should be observed within the deformed single crystal is in the scale of micro- range [86]. Since a constitutive relationship has to reflect the glide of dislocation etc. within the crystal, it should be anisotropic. Introduction of anisotropic mechanical response to the MPM would be possible [62].
- Excess energy associated with elastic strain energy and dissipation energy due to plastic deformation are not considered in this thesis for the simplicity of computation, but they should affect the morphological change of the deforming solid structure somehow, i.e. a change in the timing of bridging among crystals. The above energy terms would be incorporated by reference to the model developed by Uehara et al. [22].

- Simulations reported in this thesis were limited to two-dimensional applications. Extension of the methodology to three dimensional applications should be relatively easy in terms of both the three-dimensional phase-field polycrystalline model [82] and the three dimensional material point method [83]. However, the computational cost will be drastically increased. The parallel computing technique and the adaptive grid approach (i.e. [84] and [85]) should also be investigated to overcome the difficulty.

APPENDIX A

THE CIP METHOD

The CIP method [42] introduced as an advection scheme in this thesis is briefly described in this section.

A.1 Solution Methodology of the CIP Method

The simplest form of a hyperbolic type equation for one-dimensional case is represented by the following advection equation.

$$\frac{\partial f}{\partial t} + u\frac{\partial f}{\partial x} = 0 \qquad \text{(A.1.1)}$$

where f is an arbitrary variable and u is the advection velocity. When the constant velocity is assumed within the whole computational domain, the equation represents a simple translation of f with the constant velocity u.

A brief numerical procedure of the CIP method is the followings. An initial profile (solid line in Figure A. 1(a)) travels to a new location (dashed line in Figure A. 1 (a)) after given time step Δt. Although an exact solution (dashed line in Figure A. 1 (a)) is represented by a continuous expression, f on discrete nodal points represented by black dots in Figure A. 1 (b) is the only information available in the actual numerical computation. A profile of f among nodal points needs to be computed in the simulation, for instance, to obtain $\partial f/\partial x$ at a certain nodal point. For that purpose, a certain profile should be assumed based on the discrete data points. One possible choice is a use of the first order upwind scheme, and the scheme gives a polygonal line profile among the data points. The resulting profile is totally different from an exact solution. This is the main cause of numerical diffusion during the computation. In order to reduce the error, both a variable f and its spatial derivative $\partial f/\partial x$ are stored on each nodal point, and used to construct the better profile among nodes as shown in Figure A. 1 (c). This is the main strategy of CIP method.

The information of $\partial f/\partial x$ is also advected with the advection velocity which is not necessarily constant. By taking derivative of eq.(A.1.1) with respect to x, the following equation is obtained.

$$\frac{\partial f'}{\partial t} + u\frac{\partial f'}{\partial x} = -f'\frac{\partial u}{\partial x} \tag{A.1.2}$$

where $f' = \partial f / \partial x$. The fractional step approach is applied to solve eq.(A.1.2) in the CIP method. Same as mentioned in section 2.3, the equation is separated into "advection phase" and "non-advection phase" .

$$\frac{\partial f'}{\partial t} + u\frac{\partial f'}{\partial x} = 0 \tag{A.1.3}$$

$$\frac{\partial f'}{\partial t} = -f'\frac{\partial u}{\partial x} \tag{A.1.4}$$

By solving eq.(A.1.3) and (A.1.4) sequentially, solutions of f' which is advected by the advection velocity is computed.

A.2 The CIP Method for 1-D Case

For 1-D case, eq.(A.1.1), (A.1.3) and (A.1.4) are equations to be solved. Advection equations eq.(A.1.1) and (A.1.3) are solved by semi-Lagrangian way in the CIP method. First, the following cubic Hermite interpolation is formed with f and $f'^n = (\partial f / \partial x)^n$ on node *i* and its upwind node *iup* at time step *n*.

$$F_i(x) = a_i X^3 + b_i X^2 + f'^n_i X + f^n_i \tag{A.2.1}$$

where $X = x - x_i$ is a distance between arbitrary location x and node i. Since four variables f^n_i, f^n_{iup}, f'^n_i, f'^n_{iup} are available, coefficients a_i and b_i can be determined by the following continuity conditions on the upwind node *iup*.

$$\begin{aligned} F_i(x_{iup}) &= f^n_{iup} \\ F'_i(x_{iup}) &= f'^n_{iup} \end{aligned} \tag{A.2.2}$$

Then, a_i and b_i are

$$a_i = \frac{f'_i + f'_{iup}}{\Delta x^2} + \frac{2\left(f_i - f_{iup}\right)}{\Delta x^3} i\,\mathrm{sgn}$$
$$b_i = \frac{3\left(f_{iup} - f_i\right)}{\Delta x^2} - \frac{2f'_i + f'_{iup}}{\Delta x} i\,\mathrm{sgn} \tag{A.2.3}$$

In the above eq.(A.2.3), the following definitions are used.

$$\mathrm{sgn}(u) = \begin{cases} +1 & for\ u \geq 0 \\ -1 & for\ u < 0 \end{cases} \tag{A.2.4}$$

$$\begin{aligned} i\,\mathrm{sgn} &= -\mathrm{sgn}(u) \\ iup &= i + i\,\mathrm{sgn} \\ \Delta x &= \left|x_{iup} - x_i\right| \end{aligned} \tag{A.2.5}$$

Although u is a function of both x and t, the advection velocity u is assumed to be constant during time increment Δt when Δt is small enough. This is the major assumption of the CIP method. Under the assumption, the following relationships are available.

$$\begin{aligned} f_i^{n+1} &= f(x_i, t+\Delta t) = f(x_i - u\Delta t, t) = F(x_i - u\Delta t) \\ f'^{*}_i &= f'(x_i, t+\Delta t) = f'(x_i - u\Delta t, t) = F'(x_i - u\Delta t) \end{aligned} \tag{A.2.6}$$

Updated values of f_i and f_i' on node i are determined as values at upwind point on the profile of the previous time step. If the distance between node i and the upwind node is defined by $\xi = -u\Delta t$, eq.(A.2.1), (A.2.3) and (A.2.6) give the following equations.

$$\begin{aligned} f_i^{n+1} &= F(x_i - u\Delta t) = a_i\xi^3 + b_i\xi^2 + c_i\xi + d_i \\ f'^{*}_i &= F'(x_i - u\Delta t) = 3a_i\xi^2 + 2b_i\xi + c_i \end{aligned} \tag{A.2.7}$$

Through the above process, solutions of eq.(A.1.1) and eq.(A.1.3) are computed.

After updated variables in (A.2.7) are obtained, non-advection phase is calculated based on eq.(A.1.4) with the explicit Euler scheme for the time derivative and the central

difference scheme for the spatial derivative. Finally, values of updated variables f_i^{n+1} and $f_i'^{n+1}$ are obtained.

$$\frac{f'^{n+1}_i - f'^{*}_i}{\Delta t} = -f'^{*}_i \frac{u^n_{i+1} - u^n_{i-1}}{2\Delta x} \tag{A.2.8}$$

A.3 The CIP Method for 2-D Case

A two-dimensional advection equation is solved by the following way. The equation to be solved is

$$\frac{\partial f}{\partial t} + u\frac{\partial f}{\partial x} + v\frac{\partial f}{\partial y} = 0 \tag{A.3.1}$$

where the external advection velocity field is denoted by $\vec{u}_{ext} = (u, v)$. By taking derivative of eq.(A.3.1) with respect to *x* and *y*, the following equations for the spatial derivatives of *f* are given.

$$\begin{aligned}
\frac{\partial f_x}{\partial t} + u\frac{\partial f_x}{\partial x} + v\frac{\partial f_x}{\partial y} &= -\frac{\partial u}{\partial x} f_x - \frac{\partial v}{\partial x} f_y \\
\frac{\partial f_y}{\partial t} + u\frac{\partial f_y}{\partial x} + v\frac{\partial f_y}{\partial y} &= -\frac{\partial u}{\partial y} f_x - \frac{\partial v}{\partial y} f_y
\end{aligned} \tag{A.3.2}$$

where $f_x = \partial f / \partial x$ and $f_y = \partial f / \partial y$. The fractional step approach is applied to the equations.

[Advection phase]

$$\begin{aligned}
\frac{\partial f_x}{\partial t} + u\frac{\partial f_x}{\partial x} + v\frac{\partial f_x}{\partial y} &= 0 \\
\frac{\partial f_y}{\partial t} + u\frac{\partial f_y}{\partial x} + v\frac{\partial f_y}{\partial y} &= 0
\end{aligned} \tag{A.3.3}$$

[Non-advection phase]

$$\frac{\partial f_x}{\partial t} = -\frac{\partial u}{\partial x} f_x - \frac{\partial v}{\partial x} f_y$$
$$\frac{\partial f_y}{\partial t} = -\frac{\partial u}{\partial y} f_x - \frac{\partial v}{\partial y} f_y \qquad \text{(A.3.4)}$$

In order to solve the advection phase eq.(A.3.1) and (A.3.3), a time increment Δt is assumed to be negligibly small, which is the same assumption made in the one-dimensional case. This assumption gives

$$f(x, y, t + \Delta t) = f(x - u\Delta t, y - v\Delta t, t) \qquad \text{(A.3.5)}$$

The following cubic interpolation is formed with nodal values f and their gradients f_x and f_y.

$$F(x, y) = \sum_{l=0}^{3} \sum_{m=0}^{3} C_{lm} X^l Y^m \qquad \text{(A.3.6)}$$

where $X=x-x_i$ and $Y=y-y_j$ are distances between an arbitrary location (x, y) and node (i, j) on the Cartesian coordinate system. For 2-D, four nodal points (i, j), (iup, j), (i, jup), and (iup, jup) are available where iup and jup represent upwind nodal points in x and y direction, respectively. Eq.(A.3.6) is formed with 12 known variables on the above four nodal points (f,f_x,f_y)x4. Several choices of coefficients C_{lm} are possible.

Type A interpolation [42] is used. The function has a simple form.

$$\begin{aligned} F(x, y) = {} & C_{30} X^3 + C_{20} X^2 + \alpha_{ij} X + f_{ij} \\ & + C_{03} Y^3 + C_{02} Y^2 + \beta_{ij} Y \\ & + C_{21} X^2 Y + C_{11} XY + C_{12} XY^2 \end{aligned} \qquad \text{(A.3.7)}$$

where $\alpha = f_x = \partial f / \partial x, \beta = f_y = \partial f / \partial y$.

Ten coefficients need to be determined in this interpolation. Continuities of f, f_x, f_y on (i, j), (iup, j), (i, jup) and a continuity of f on (iup, jup) are used for that purpose. The continuity conditions give the following equations.

$$
\begin{aligned}
&F(0,0) = f_{ij}, \quad F_x(0,0) = \alpha_{ij}, \quad F_y(0,0) = \beta_{ij} \\
&F(0,\Delta y_{jup}) = f_{ijup}, \quad F_x(0,\Delta y_{jup}) = \alpha_{ijup}, \quad F_y(0,\Delta y_{jup}) = \beta_{ijup} \\
&F(\Delta x_{iup},0) = f_{iupj}, \quad F_x(\Delta x_{iup},0) = \alpha_{iupj}, \quad F_y(\Delta x_{iup},0) = \beta_{iupj} \\
&F(\Delta x_{iup},\Delta y_{jup}) = f_{iupjup}
\end{aligned}
\tag{A.3.8}
$$

iup, *jup*, Δx_{iup}, and Δy_{iup} are defined by

$$
\begin{aligned}
&i\,\mathrm{sgn} = -\mathrm{sgn}(u) \\
&iup = i + i\,\mathrm{sgn} \\
&\Delta x_{iup} = x_{iup} - x_i
\end{aligned}
\tag{A.3.9}
$$

$$
\begin{aligned}
&j\,\mathrm{sgn} = -\mathrm{sgn}(v) \\
&jup = j + j\,\mathrm{sgn} \\
&\Delta y_{jup} = y_{jup} - y_j
\end{aligned}
\tag{A.3.10}
$$

Resulting coefficients are obtained as follows with the above notations.

$$
\begin{aligned}
C_{30} &= [-2f_{iupj} + 2f_{ij} + (\alpha_{ijup} + \alpha_{ij})\Delta x \cdot i\,\mathrm{sgn}] / (\Delta x^3 \cdot i\,\mathrm{sgn}) \\
C_{20} &= [3f_{iupj} - 3f_{ij} - (\alpha_{iupj} + 2\alpha_{ij})\Delta x \cdot i\,\mathrm{sgn}] / (\Delta x^2) \\
C_{03} &= [-2f_{ijup} + 2f_{ij} + (\beta_{ijup} + \beta_{ij})\Delta y \cdot j\,\mathrm{sgn}] / (\Delta y^3 \cdot j\,\mathrm{sgn}) \\
C_{02} &= [3f_{ijup} = 3f_{ij} - (\beta_{ijup} + 2\beta_{ij})\Delta y \cdot j\,\mathrm{sgn}] / \Delta y^2 \\
C_{21} &= [A - (\alpha_{iupj} - \alpha_{ij})\Delta x \cdot i\,\mathrm{sgn}] / (\Delta x^2 \Delta y \cdot j\,\mathrm{sgn}) \\
C_{11} &= [-A + (\alpha_{ijup} + \alpha_{ij})\Delta x \cdot i\,\mathrm{sgn} + (\beta_{iupj} + \beta_{ij})\Delta y \cdot j\,\mathrm{sgn}] \\
&\quad / (\Delta x \cdot i\,\mathrm{sgn}\ \Delta y \cdot j\,\mathrm{sgn}) \\
C_{12} &= [A - (\beta_{iupj} + \beta_{ij})\Delta y \cdot j\,\mathrm{sgn}] / (\Delta x \cdot i\,\mathrm{sgn}\ \Delta y^2)
\end{aligned}
\tag{A.3.11}
$$

Where $A=f_{ij}-f_{ijup}-f_{ijup}+f_{iupjup}$ is defined. The following updated variables are obtained with notations $\xi=-u\Delta t$ and $\eta=-v\Delta t$.

$$
\begin{aligned}
f_{ij}^{n+1} &= f\left(x-u\Delta t, y-v\Delta t, t\right) = F\left(x-u\Delta t, y-v\Delta t\right) \\
&= C_{30}\xi^3 + C_{20}\xi^2 + \alpha_{ij}^n\xi + f_{ij}^n + C_{03}\eta^3 + C_{02}\eta^2 + \beta_{ij}^n\eta \\
&\quad + C_{21}\xi^2\eta + C_{11}\xi\eta + C_{12}\xi\eta^2 \\
\alpha_{ij}^* &= f_x\left(x-u\Delta t, y-v\Delta t, t\right) = F_x\left(x-u\Delta t, y-v\Delta t\right) \\
&= 3C_{30}\xi^2 + 2C_{20}\xi + \alpha_{ij}^n \\
&\quad + 2C_{21}\xi\eta + C_{11}\eta + C_{12}\eta^2 \\
\beta_{ij}^* &= f_y\left(x-u\Delta t, y-v\Delta t, t\right) = F_y\left(x-u\Delta t, y-v\Delta t\right) \\
&= 3C_{03}\eta^2 + 2C_{02}\eta + \beta_{ij}^n \\
&\quad + C_{21}\xi^2 + C_{11}\xi + 2C_{12}\xi\eta
\end{aligned}
\tag{A.3.12}
$$

Based on the above procedure, eq.(A.3.1) and (A.3.3) are solved. In addition, non-advection phase eq.(A.3.4) needs to be calculated to have spatial derivatives of *f*. The explicit Euler in time and the central difference in space are applied to the discretisation.

$$
\begin{aligned}
\frac{\alpha_{ij}^{n+1}-\alpha_{ij}^n}{\Delta t} &= -\frac{u_{i+1j}^n - u_{i-1j}^n}{2\Delta x}\alpha_{ij}^* - \frac{v_{i+1j}^n - v_{i-1j}^n}{2\Delta x}\beta_{ij}^* \\
\frac{\beta_{ij}^{n+1}-\beta_{ij}^n}{\Delta t} &= -\frac{u_{ij+1}^n - u_{ij-1}^n}{2\Delta y}\alpha_{ij}^* - \frac{v_{ij+1}^n - v_{ij-1}^n}{2\Delta y}\beta_{ij}^*
\end{aligned}
\tag{A.3.13}
$$

After the above calculation, updated variables of f, f_x, f_y at time level n+1 are finally obtained.

The continuity condition at (*iup*,*jup*) only satisfies about f not f_x and f_y. An accuracy of the type A interpolation around (*iup*,*jup*) might be issue. In order to improve the accuracy, type B interpolation is proposed [80] and it introduces continuity conditions of f_x and f_y at the point (*iup*,*jup*). As pointed out by Yabe et al. [81], an order of accuracy of type B interpolation is almost same as type A interpolation. A validation in section 2.3.1.1 proves the fact, thus its applicability to our study should be sufficient.

A.4 Level-Set Method with the CIP Method

A governing equation of the level set method presented in the main chapter is given by

$$\frac{\partial F}{\partial t} + S(F)(|\nabla F| - 1) = 0, \quad S(F) = \frac{F}{\sqrt{F^2 + |\nabla F|^2 \Delta x^2}}$$

In order to solve the equation by the CIP method, the equation is transformed as follows.

$$\frac{\partial F}{\partial t} + \left\{ \frac{S(F)\nabla F}{|\nabla F|} \right\} \cdot \nabla F = S(F)$$

The transformed equation can be divided into "non-advection phase" and "advection phase".

$$\frac{\partial F^*}{\partial t} = S(F)$$

$$\frac{\partial F}{\partial t} + \vec{u} \cdot \nabla F = 0, \quad \vec{u} = \frac{S(F)}{|\nabla F|} \nabla F$$

The fractional step method is applied to solve the equations. The explicit Euler in time and the central difference in space are used as the solution methodology of "non-advection phase". "Advection phase" is computed by the CIP method. The equations are solved until it reaches to the steady state with the convergence criterion.

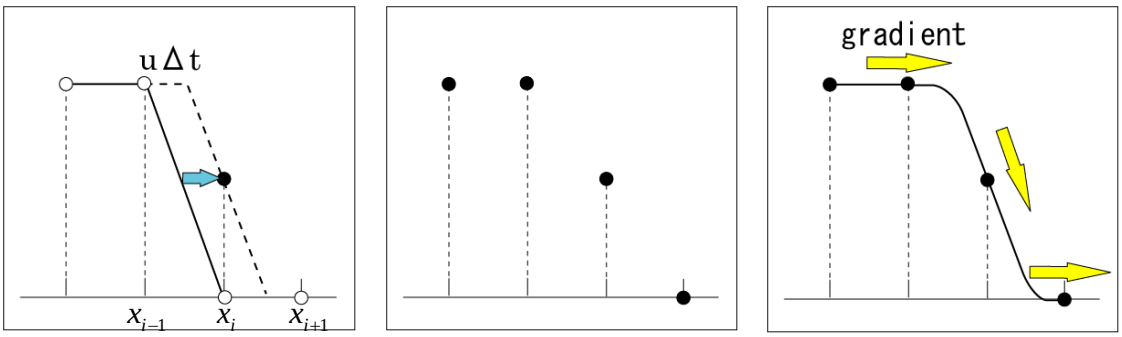

(a) Advected Profile (b) Only nodal values (c) Nodal values with gradients

Figure A. 1 The principle of CIP method

APPENDIX B

NUMERICAL IMPLIMENTATION OF THE MATERIAL POINT METHOD

A detailed derivation of a governing equation of the material point method (MPM) and several notes on numerical implementations of the method are presented in this section. The generalized material point method (GIMP) is of interest.

B.1 Derivation of Nodal Equation of Motion

A weak form of the equation of motion eq.(2.5.1) is written by

$$\int_\Omega \rho \frac{d\vec{v}_{solid}}{dt} \cdot \delta \mathbf{w} d\Omega + \int_\Omega \boldsymbol{\sigma} : \nabla \delta \mathbf{w} d\Omega = \int_{\partial\Omega} \boldsymbol{\tau} \cdot \delta \mathbf{w} dS + \int_\Omega \rho \mathbf{b} \cdot \delta \mathbf{w} d\Omega \qquad \text{(B.1.1)}$$

The equation is valid in continuum field whereas material properties and historical variables are stored on discrete material points. A mapping relation between material points and continuum field is required for the further computation.

B.1.1 Relation between variables on material points and continuum field

Any variable f_p defined on a material point is defined as a volume average of the variable on continuum field $f(\mathbf{x},t)$.

$$f_p = \frac{\int_\Omega f(\vec{x},t)\chi_p(\vec{x},t)d\Omega}{\int_\Omega \chi_p(\vec{x},t)d\Omega} = \frac{\int_\Omega f(\vec{x},t)\chi_p(\vec{x},t)d\Omega}{V_p} \qquad \text{(B.1.2)}$$

Taking summation of the equation for all material points reside the domain Ω gives the following relation.

$$\sum_{p=1}^{N_p} f_p V_p = \int_\Omega f(\vec{x},t)\sum_{p=1}^{N_p} \chi_p(\vec{x},t)d\Omega$$
$$\therefore \quad \sum_{p=1}^{N_p} f_p \int_\Omega \chi_p(\vec{x},t)d\Omega = \int_\Omega f(\vec{x},t)d\Omega \tag{B.1.3}$$

B.1.2 Nodal equation of motion

By using eq.(B.1.3), each term in eq.(B.1.1) can be represented by the following equations.

$$\int_\Omega \rho(\vec{x},t)\frac{d\vec{v}}{dt}\cdot\delta\mathbf{w}d\Omega = \int_\Omega \sum_{p=1}^{N_p}\rho_p \frac{d\vec{v}_p}{dt}\chi_p(\vec{x},t)\cdot\delta\mathbf{w}d\Omega = \sum_{p=1}^{N_p}\int_{\Omega\cap\Omega_p}\rho_p\frac{d\vec{v}_p}{dt}\chi_p(\vec{x},t)\cdot\delta\mathbf{w}d\Omega$$
$$\int_\Omega \boldsymbol{\sigma}(\vec{x},t):\nabla\delta\mathbf{w}d\Omega = \int_\Omega \sum_{p=1}^{N_p}\boldsymbol{\sigma}_p\chi_p(\vec{x},t):\nabla\delta\mathbf{w}d\Omega = \sum_{p=1}^{N_p}\int_{\Omega\cap\Omega_p}\boldsymbol{\sigma}_p\chi_p(\vec{x},t):\nabla\delta\mathbf{w}d\Omega \tag{B.1.4}$$
$$\int_\Omega \rho(\vec{x},t)\vec{b}\cdot\delta\mathbf{w}d\Omega = \int_\Omega \sum_{p=1}^{N_p}\rho_p\vec{b}\chi_p(\vec{x},t)\cdot\delta\mathbf{w}d\Omega = \sum_{p=1}^{N_p}\int_{\Omega\cap\Omega_p}\rho_p\vec{b}\chi_p(\vec{x},t)\cdot\delta\mathbf{w}d\Omega$$

Ω_p is again a support domain of each material point. Then, eq.(B.1.1) is rewritten by the following.

$$\sum_{p=1}^{N_p}\int_{\Omega\cap\Omega_p}\rho_p\frac{d\vec{v}_p}{dt}\chi_p(\vec{x},t)\cdot\delta\mathbf{w}d\Omega + \sum_{p=1}^{N_p}\int_{\Omega\cap\Omega_p}\boldsymbol{\sigma}_p\chi_p(\vec{x},t):\nabla\delta\mathbf{w}d\Omega$$
$$= \sum_{p=1}^{N_p}\int_{\Omega\cap\Omega_p}\rho_p\vec{b}\chi_p(\vec{x},t)\cdot\delta\mathbf{w}d\Omega + \int_{\partial\Omega}\boldsymbol{\tau}\cdot\delta\mathbf{w}dS \tag{B.1.5}$$

A weighting function $\delta\boldsymbol{w}$ needs to be specified to solve the equation. The choice of function is arbitrary, so a linear shape function $N_i(\mathbf{x})$ used in the usual FEM is typically selected in the MPM.

$$\delta\mathbf{w} = \sum_{i=1}^{nnod} N_i(\vec{x})\delta w_i \tag{B.1.6}$$

where *nnod* is the total number of nodes in the domain Ω. δw_i is only defined on nodal points, so its special gradient would be zero. That gives

$$\nabla\delta\mathbf{w} = \nabla\left(\sum_{i=1}^{nnod} N_i(\vec{x})\delta w_i\right) = \sum_{i=1}^{nnod}\nabla N_i(\vec{x})\delta w_i \tag{B.1.7}$$

$\delta\mathbf{w}$, $\nabla\delta\mathbf{w}$, and $\rho_p = m_p / V_p$ are now substituted into eq.(B.1.5). The first term is transformed by the following calculation process.

$$\begin{aligned}\sum_{p=1}^{N_p}\int_{\Omega\cap\Omega_p}\rho_p\frac{d\vec{v}_p}{dt}\chi_p(\vec{x},t)\cdot\delta\mathbf{w}d\Omega &= \sum_{i=1}^{nnod}\sum_{p=1}^{N_p}m_p\frac{d\vec{v}_p}{dt}\frac{1}{V_p}\int_{\Omega\cap\Omega_p}\chi_p(\vec{x},t)N_i(\vec{x})d\Omega\delta w_i \\ &= \sum_{i=1}^{nnod}\sum_{p=1}^{N_p}m_p\frac{d\vec{v}_p}{dt}\bar{S}_{vp}\delta w_i\end{aligned} \tag{B.1.8}$$

The second term is calculated by

$$\sum_{p=1}^{N_p}\int_{\Omega\cap\Omega_p}\boldsymbol{\sigma}_p\chi_p(\vec{x},t):\nabla\delta\mathbf{w}d\Omega = \sum_{i=1}^{nnod}\sum_{p=1}^{N_p}\boldsymbol{\sigma}_p\cdot\nabla\bar{S}_{vp}V_p\delta w_i \tag{B.1.9}$$

The third and fourth terms can be given by

$$\begin{aligned}&\sum_{p=1}^{N_p}\int_{\Omega\cap\Omega_p}\rho_p\vec{b}\chi_p(\vec{x},t)\cdot\delta\mathbf{w}d\Omega = \sum_{i=1}^{nnod}\sum_{p=1}^{N_p}m_p\vec{b}(\vec{x},t)\bar{S}_{vp}\delta w_i \\ &\int_{\partial\Omega}\vec{\tau}\cdot\delta\mathbf{w}dS = \sum_{i=1}^{nnod}\int_{\partial\Omega}\vec{\tau}\cdot N_i(\vec{x})dS\delta w_i\end{aligned} \tag{B.1.10}$$

By putting four terms all together, the following form is obtained for eq.(B.1.5).

$$\sum_{i=1}^{nnod}\left[\sum_{p=1}^{N_p}m_p\frac{d\vec{v}_p}{dt}\bar{S}_{vp} + \sum_{p=1}^{N_p}\boldsymbol{\sigma}_p\cdot\nabla\bar{S}_{vp}V_p - \sum_{p=1}^{N_p}m_p\vec{b}(\vec{x})\bar{S}_{vp} - \int_{\partial\Omega}\vec{\tau}\cdot N_i(\vec{x})dS\right]\delta w_i = 0 \tag{B.1.11}$$

The equation must be satisfied for arbitrary weighting function $\delta\mathbf{w}$. Then, the nodal equation of motion is obtained to be the following form.

$$\sum_{p=1}^{N_p}m_p\frac{d\vec{v}_p}{dt}\bar{S}_{vp} + \sum_{p=1}^{N_p}\boldsymbol{\sigma}_p\cdot\nabla\bar{S}_{vp}V_p - \sum_{p=1}^{N_p}m_p\vec{b}(\vec{x})\bar{S}_{vp} - \int_{\partial\Omega}\vec{\tau}\cdot N_i(\vec{x})dS = 0 \tag{B.1.12}$$

A particle characteristic function is defined such that the function has unity within l_pxl_p support domain where l_p is a side length of each material point as shown in Figure B. 1. Throughout this thesis, the material point is assumed to have a rectangular shape.

B.2 Stress Integration Algorithm

A stress increment needs to be computed based on eq.(2.2.7) with appropriate inelastic constitutive relation at every single time step. The radial return mapping method

[39] is applied in this thesis, and the numerical procedure is briefly presented in this section.

First, some useful expressions are derived. Eq.(2.2.7) is decomposed into the bulk and deviatoric component of stresses with elastic constitutive relation given by eq.(2.2.9).

$$\frac{d\boldsymbol{\sigma}}{dt} = \mathbf{C_0} : \frac{d\boldsymbol{\varepsilon}^e}{dt} = K\frac{d\varepsilon_{ii}}{dt}\mathbf{1} + 2G\frac{d\mathbf{e}^e}{dt} \tag{B.2.1}$$

K and G are related to E and ν by the following equations.

$$G = \frac{E}{2(1+\nu)}, \quad K = \frac{E}{3G(3G-E)} \tag{B.2.2}$$

1 is the second-order identity tensor, and $\mathbf{e}^e$ is the elastic part of the deviatoric strain defined by

$$e_{ij}^e = \varepsilon_{ij}^e - \frac{\varepsilon_{kk}^e}{3}\mathbf{1} \tag{B.2.3}$$

The deviatoric stress is only related to the deviatoric strain, and given by

$$\dot{s}_{ij} = 2G\dot{e}_{ij}^e \tag{B.2.4}$$

B.2.1 Elasto-perfectly-plasticity model

The numerical procedure of elasto-perfectly-plasticity model based on Mises yielding criterion with the associative flow is briefly described in this subsection.

B.2.1.1 The radial return mapping algorithm

(1) Elastic predictor

Assume all variables at time level n are already known, and incremental strain $\Delta\varepsilon_{n+1}$ at time level n+1is given. As a trial stress state, $\boldsymbol{\sigma}_{n+1}^{tr}$ is computed by assuming that $\Delta\varepsilon_{n+1}$ is composed of only elastic part. Trial stresses and strains are obtained by the following equations.

$$\begin{aligned}
\boldsymbol{\sigma}_{n+1}^{tr} &= \boldsymbol{\sigma}_n + \mathbf{C_0} : \Delta\boldsymbol{\varepsilon}_{n+1} \\
\mathbf{s}_{n+1}^{tr} &= \boldsymbol{\sigma}_{n+1}^{tr} - \frac{tr\left(\boldsymbol{\sigma}_{n+1}^{tr}\right)}{3}\mathbf{1} \\
\left(\boldsymbol{\varepsilon}_{n+1}^{e}\right)^{tr} &= \boldsymbol{\varepsilon}_n^{e} + \Delta\boldsymbol{\varepsilon}_{n+1} \\
\left(\boldsymbol{\varepsilon}_{n+1}^{p}\right)^{tr} &= \boldsymbol{\varepsilon}_n^{p}
\end{aligned} \tag{B.2.5}$$

(2) Examine yield criterion

Von Mises yield criterion eq.(2.2.11) is examined with the trial stress $\mathbf{s}_{n+1}^{tr}$. The following scenarios are expected.

(2-a) $f_Y\left(\mathbf{s}_{n+1}^{tr}\right) \le 0$

In this case, the trial state is the final state of stress and strain. Stress and strain are updated by

$$\begin{aligned}
\boldsymbol{\sigma}_{n+1} &= \boldsymbol{\sigma}_{n+1}^{tr} \\
\boldsymbol{\varepsilon}_{n+1}^{e} &= \left(\boldsymbol{\varepsilon}_{n+1}^{e}\right)^{tr} \\
\boldsymbol{\varepsilon}_{n+1}^{p} &= \left(\boldsymbol{\varepsilon}_{n+1}^{p}\right)^{tr}
\end{aligned} \tag{B.2.6}$$

Then, the stress integration procedure at time level n+1 is completed.

(2-b) $f_Y\left(\mathbf{s}_{n+1}^{tr}\right) > 0$

In this case, the states of stress and strain need to be corrected. Since plastic strain would be evolved, eq.(2.2.7) is written by the following form.

$$\frac{d\boldsymbol{\sigma}}{dt} = \mathbf{C_0} : \left(\frac{d\boldsymbol{\varepsilon}}{dt} - \frac{d\boldsymbol{\varepsilon}^{p}}{dt}\right) \tag{B.2.7}$$

The associative flow law represented by eq.(2.2.12) and eq.(B.2.4) are substitute into eq.(B.2.7), then the following equations are obtained.

$$\boldsymbol{\sigma}_{n+1} = \boldsymbol{\sigma}_n + \mathbf{C_0} : \left(\Delta\boldsymbol{\varepsilon}_{n+1} - \Delta\boldsymbol{\varepsilon}_{n+1}^{p}\right) = \boldsymbol{\sigma}_{n+1}^{tr} - \mathbf{C_0} : \Delta\boldsymbol{\varepsilon}_{n+1}^{p} \tag{B.2.8}$$

$$\mathbf{s}_{n+1} = \mathbf{s}_{n+1}^{tr} - 2G\Delta\boldsymbol{\varepsilon}_{n+1}^{p} = \mathbf{s}_{n+1}^{tr} - 2Gd\lambda\frac{\mathbf{s}_{n+1}}{\left\|\mathbf{s}_{n+1}\right\|} \tag{B.2.9}$$

Since G and $d\lambda$ are scalars, the relation of $\mathbf{s}_{n+1} // \mathbf{s}^{tr}_{n+1}$ is easily expected from eq.(B.2.9). Now the following unit tensor is defined.

$$\frac{\mathbf{s}_{n+1}}{\left\|\mathbf{s}_{n+1}\right\|} = \frac{\mathbf{s}^{tr}_{n+1}}{\left\|\mathbf{s}^{tr}_{n+1}\right\|} \equiv \mathbf{n}_{n+1} \tag{B.2.10}$$

Taking tensor contraction of eq.(B.2.9) with $\mathbf{n}_{n+1}$ gives

$$d\lambda = \frac{1}{2G}\left(\left\|\mathbf{s}^{tr}_{n+1}\right\| - \left\|\mathbf{s}_{n+1}\right\|\right) \tag{B.2.11}$$

Mises criterion gives the following relation under the plastic loading.

$$\left\|\mathbf{s}_{n+1}\right\| = \sqrt{\frac{2}{3}}\sigma_Y \tag{B.2.12}$$

Plastic multiplier $d\lambda$ is determined by eq.(B.2.11) and (B.2.12) as

$$d\lambda = \frac{1}{2G}\left(\left\|\mathbf{s}^{tr}_{n+1}\right\| - \sqrt{\frac{2}{3}}\sigma_Y\right) \tag{B.2.13}$$

The deviatoric stress $\mathbf{s}_{n+1}$ is updated such that

$$\mathbf{s}_{n+1} = \sqrt{\frac{2}{3}}\frac{\mathbf{s}^{tr}_{n+1}}{\left\|\mathbf{s}^{tr}_{n+1}\right\|}\sigma_Y \tag{B.2.14}$$

Using eq (B.2.14), a Cauchy stress and a plastic strain are also updated by

$$\begin{aligned}
\boldsymbol{\sigma}_{n+1} &= \mathbf{s}_{n+1} + \frac{tr\left(\boldsymbol{\sigma}^{tr}_{n+1}\right)}{3}\mathbf{1} \\
\Delta\boldsymbol{\varepsilon}^{p}_{n+1} &= \frac{1}{2G}\left(\mathbf{s}^{tr}_{n+1} - \mathbf{s}_{n+1}\right) \\
\boldsymbol{\varepsilon}^{p}_{n+1} &= \left(\boldsymbol{\varepsilon}^{p}_{n+1}\right)^{tr} + \Delta\boldsymbol{\varepsilon}^{p}_{n+1}
\end{aligned} \tag{B.2.15}$$

(3) Repeat procedure (1)-(2)

Since no iteration process is required in the algorithm, the method is efficient in terms of the numerical implementation and the computational time.

B.2.1.2 Hydrostatic stress in plain strain condition

As a side note, a derivation of hydrostatic stress in plane strain condition is briefly described in this subsection. It is trivial, but the derivation is omitted in the most textbook. Thus, it should be worth mentioning.

In the plane strain condition, $\sigma_{33}=\nu(\sigma_{11}+\sigma_{22})$ is satisfied. The hydrostatic stress is defined to be

$$\sigma_m = \frac{tr(\boldsymbol{\sigma})}{3} = \frac{1+\nu}{3}(\sigma_{11}+\sigma_{22}) \tag{B.2.16}$$

33 component of the plastic strain $d\varepsilon_{33}^{p}$ will be zero in the plane strain condition, so the associative flow rule gives the following relation.

$$0 = d\varepsilon_{33}^{p} = d\lambda \frac{s_{33}}{\|\mathbf{s}\|} = \frac{d\lambda}{\|\mathbf{s}\|}\frac{2\nu-1}{3}(\sigma_{11}+\sigma_{22}) \tag{B.2.17}$$

Since $(\sigma_{11}+\sigma_{22})$, $d\lambda$, and $\mathbf{s}$ are not always zero, $\nu=0.5$ is the required condition to satisfy eq.(B.2.17). The condition of $\nu=0.5$ is substituted into eq.(B.2.16), then it gives

$$\sigma_m = \frac{\sigma_{11}+\sigma_{22}}{2} \tag{B.2.18}$$

Plastic deformation is generally said to be incompressible. This is because $\nu=0.5$ is the essential condition if we assume the associative flow rule and plane strain condition.

B.2.2 Elasto-visco-plasticity model

A Perzyna type model [40] is used for the elasto-visco-perfectly plasticity model in this thesis. The radial return mapping method [39] is adopted as the stress integration algorithm. The numerical procedure of the stress integration is briefly described in the following subsection.

B.2.2.1 The radial return mapping algorithm

(1) Elastic predictor

Assume all variables at time level n are already known, and incremental strain $\Delta\varepsilon_{n+1}$ at time level n+1is given. As a trial stress state, $\boldsymbol{\sigma}_{n+1}^{tr}$ is computed by assuming that $\Delta\varepsilon_{n+1}$ is composed of only elastic part. Trial stresses and strains are obtained by the following equations.

$$\begin{aligned}
\boldsymbol{\sigma}_{n+1}^{tr} &= \boldsymbol{\sigma}_n + \mathbf{C_0} : \Delta\boldsymbol{\varepsilon}_{n+1} \\
\mathbf{s}_{n+1}^{tr} &= \boldsymbol{\sigma}_{n+1}^{tr} - \frac{tr\left(\boldsymbol{\sigma}_{n+1}^{tr}\right)}{3}\mathbf{1} \\
\left(\boldsymbol{\varepsilon}_{n+1}^{e}\right)^{tr} &= \boldsymbol{\varepsilon}_n^{e} + \Delta\boldsymbol{\varepsilon}_{n+1} \\
\left(\boldsymbol{\varepsilon}_{n+1}^{vp}\right)^{tr} &= \boldsymbol{\varepsilon}_n^{vp}
\end{aligned} \tag{B.2.19}$$

Where $\boldsymbol{\varepsilon}^{vp}$ denotes visco-plastic strain tensor.

(2) Examine the loading function

The loading function represented by eq.(2.2.13) is examined with the trial stress $\mathbf{s}_{n+1}^{tr}$. The following scenarios are expected.

(2-a) $f_Y\left(\mathbf{s}_{n+1}^{tr}\right) \le 0$

In this case, the trial state is the final state of stress and strain. Stress and strain are updated by

$$\begin{aligned}
\boldsymbol{\sigma}_{n+1} &= \boldsymbol{\sigma}_{n+1}^{tr} \\
\boldsymbol{\varepsilon}_{n+1}^{e} &= \left(\boldsymbol{\varepsilon}_{n+1}^{e}\right) \\
\boldsymbol{\varepsilon}_{n+1}^{vp} &= \left(\boldsymbol{\varepsilon}_{n+1}^{vp}\right)^{tr}
\end{aligned} \tag{B.2.20}$$

Stress integration procedure at time level n+1 is completed.

(2-b) $f_Y\left(\mathbf{s}_{n+1}^{tr}\right) > 0$

In this case, the states of stress and strain need to be corrected. Since viscoplastic strain would be evolved, eq.(2.2.7) is written by the following form.

$$\frac{d\boldsymbol{\sigma}}{dt} = \mathbf{C_0} : \left(\frac{d\boldsymbol{\varepsilon}}{dt} - \frac{d\boldsymbol{\varepsilon}^{vp}}{dt}\right) \tag{B.2.21}$$

Using backward-Euler scheme, the associative flow rule represented by eq.(2.2.14) with a consistency parameter defined by eq.(2.2.15) is descretized as

$$\frac{\boldsymbol{\varepsilon}_{n+1}^{vp}-\boldsymbol{\varepsilon}_{n}^{vp}}{\Delta t}=\gamma\frac{\partial f}{\partial\boldsymbol{\sigma}}=\frac{f_{n+1}}{\eta_{visc}}\mathbf{n}_{n+1}$$
$$\therefore\quad \boldsymbol{\varepsilon}_{n+1}^{vp}=\boldsymbol{\varepsilon}_{n}^{vp}+\frac{f_{n+1}}{\eta_{visc}}\Delta t\mathbf{n}_{n+1} \tag{B.2.22}$$

Discrete form of eq.(B.2.21) is represented by

$$\frac{\boldsymbol{\sigma}_{n+1}-\boldsymbol{\sigma}_{n}}{\Delta t}=\mathbf{C_0}:\left(\frac{\Delta\boldsymbol{\varepsilon}_{n+1}}{\Delta t}-\frac{\boldsymbol{\varepsilon}_{n+1}^{vp}-\boldsymbol{\varepsilon}_{n}^{vp}}{\Delta t}\right)$$
$$\therefore\quad \boldsymbol{\sigma}_{n+1}=\boldsymbol{\sigma}_{n+1}^{tr}-\mathbf{C_0}:\left(\boldsymbol{\varepsilon}_{n+1}^{vp}-\boldsymbol{\varepsilon}_{n}^{vp}\right) \tag{B.2.23}$$

From eq.(B.2.22), the visco-plastic strain $\boldsymbol{\varepsilon}^{vp}$ is only composed of the deviatoric part ($\mathbf{n}_{n+1}$ is given by the deviatoric part of the stress). Therefore, the visco-plastic strain develops the deviatoric part of the stress.

$$\begin{aligned}\mathbf{s}_{n+1}&=\mathbf{s}_{n+1}^{tr}-2G\left(\boldsymbol{\varepsilon}_{n+1}^{vp}-\boldsymbol{\varepsilon}_{n}^{vp}\right)\\&=\mathbf{s}_{n+1}^{tr}-\frac{2G\Delta t f_{n+1}}{\eta_{visc}}\mathbf{n}_{n+1}\end{aligned} \tag{B.2.24}$$

Same as eq.(B.2.9), $\mathbf{s}_{n+1}\,//\,\mathbf{s}_{n+1}^{tr}$ and $\mathbf{s}_{n+1}\,//\,\mathbf{n}_{n+1}$ are expected from this equation. By taking tensor contraction of eq.(B.2.24) with $\mathbf{n}_{n+1}$, it gives

$$\left\|\mathbf{s}_{n+1}\right\|=\left\|\mathbf{s}_{n+1}^{tr}\right\|-\frac{2G\Delta t f_{n+1}}{\eta_{visc}} \tag{B.2.25}$$

Unlike the plasticity model, the state of $f_{n+1}>0$ is allowed in the Perzyna type model. In order to compute new stress state, f_{n+1} needs to be determined. The loading function eq.(2.2.13) is transformed by the following way.

$$\begin{aligned}f_{n+1}&=\left\|\mathbf{s}_{n+1}\right\|-\sqrt{\frac{2}{3}}\sigma_Y=\left\|\mathbf{s}_{n+1}^{tr}\right\|-\frac{2G\Delta t f_{n+1}}{\eta_{visc}}-\sqrt{\frac{2}{3}}\sigma_Y\\f_{n+1}^{tr}&=\left\|\mathbf{s}_{n+1}^{tr}\right\|-\sqrt{\frac{2}{3}}\sigma_Y\end{aligned} \tag{B.2.26}$$

The above equations give the following relation between f_{n+1} and f_{n+1}^{tr}.

$$f_{n+1}=\frac{\eta_{visc}}{\eta_{visc}+2G\Delta t}\,f_{n+1}^{tr} \tag{B.2.27}$$

$\mathbf{s}_{n+1}$ is calculated by eq.(B.2.24) as

$$\mathbf{s}_{n+1} = \frac{\eta_{visc}}{\eta_{visc} + 2G\Delta t}\mathbf{s}_{n+1}^{tr} + \frac{2G\Delta t}{\eta_{visc} + 2G\Delta t}\sqrt{\frac{2}{3}}\sigma_Y \frac{\mathbf{s}_{n+1}^{tr}}{\left\|\mathbf{s}_{n+1}^{tr}\right\|} \tag{B.2.28}$$

New states of stress and visco-plastic strain are updated to be

$$\begin{aligned} \boldsymbol{\sigma}_{n+1} &= \mathbf{s}_{n+1} + \frac{tr\left(\boldsymbol{\sigma}_{n+1}^{tr}\right)}{3}\mathbf{1} \\ \Delta\boldsymbol{\varepsilon}_{n+1}^{vp} &= \frac{1}{2G}\left(\mathbf{s}_{n+1}^{tr} - \mathbf{s}_{n+1}\right) \\ \boldsymbol{\varepsilon}_{n+1}^{vp} &= \left(\boldsymbol{\varepsilon}_{n+1}^{vp}\right)^{tr} + \Delta\boldsymbol{\varepsilon}_{n+1}^{vp} \end{aligned} \tag{B.2.29}$$

(3) Repeat procedure (1)-(2)

From eq.(B.2.28), the unit of η_{visc} is [Pa.s] in international system of units (SI). The following relaxation time τ_{visc} is often defined for the convenience.

$$\tau_{visc} = \frac{\eta_{visc}}{2G} \tag{B.2.30}$$

Using the introduced parameter τ_{visc}, eq.(B.2.28) is rewritten by

$$\mathbf{s}_{n+1} = \frac{\tau_{visc}/\Delta t}{\tau_{visc}/\Delta t + 1}\mathbf{s}_{n+1}^{tr} + \frac{1}{\tau_{visc}/\Delta t + 1}\sqrt{\frac{2}{3}}\sigma_Y \frac{\mathbf{s}_{n+1}^{tr}}{\left\|\mathbf{s}_{n+1}^{tr}\right\|} \tag{B.2.31}$$

τ_{visc}=0 recovers rate-independent plasticity model presented in the preceding section.

B.3 Weighted Shape Function and its Gradient for 2-D

Two-dimensional expressions of weighted shape function and its gradient of defined in the GIMP are presented for the purpose of the numerical implementation.

The general expression of the two-dimensional particle characteristic function of the GIMP is written by the following form

$$\chi_p(x,y,t) = \begin{cases} 1 & for \;\; x,y \in \Omega_p \\ 0 & otherwise \end{cases} \tag{B.3.1}$$

Since a rectangular area shown in Figure B. 1 is assumed to be the support domain of each material point, eq.(B.3.1) is represented by the combination of one-dimensional particle characteristic function.

$$\chi_p(x,y,t) = \chi_p(x,t)\chi_p(y,t) \tag{B.3.2}$$

The two-dimensional nodal shape function is also written by the combination of one-dimensional shape function defined by eq.(2.5.18).

$$N_{ij}(x,y) = N_i(x)N_j(y) \tag{B.3.3}$$

Using eq.(B.3.2) and (B.3.3), the two-dimensional weighted shape function $\bar{S}_{vp}(x_p, y_p)$ is represented by the following equation.

$$\begin{aligned}
\bar{S}_{vp}(x,y) &= \frac{1}{V_p}\int_{\Omega\cap\Omega_p} N_{ij}(x,y)\chi_p(x,y)d\Omega \\
&= \frac{1}{l_p^2}\int_{\Omega\cap\Omega_p} N_i(x)N_j(y)\chi_p(x)\chi_p(y)d\Omega \\
&= \frac{1}{l_p}\int_{\Omega\cap\Omega_p} N_i(x)\chi_p(x)d\Omega\frac{1}{l_p}\int_{\Omega\cap\Omega_p} N_j(y)\chi_p(y)d\Omega \\
&= \bar{S}_{vp}(x)\bar{S}_{vp}(y)
\end{aligned} \tag{B.3.4}$$

The gradient of the weighted shape function $\nabla\bar{S}_{vp}(x_p, y_p)$is given by

$$\nabla\bar{S}_{vp} = \left(\frac{\partial}{\partial x}\bar{S}_{vp}(x,y), \frac{\partial}{\partial y}\bar{S}_{vp}(x,y)\right) \tag{B.3.5}$$

Each component of eq.(B.3.5) is calculated from eq.(B.3.4) as

$$\begin{aligned}
\frac{\partial}{\partial x}\bar{S}_{vp}(x,y) &= \frac{\partial}{\partial x}\left(\bar{S}_{vp}(x)\bar{S}_{vp}(y)\right) \\
&= \bar{S}_{vp}(y)\frac{\partial\bar{S}_{vp}(x)}{\partial x} \equiv \nabla\bar{S}_{vpx} \\
\frac{\partial}{\partial y}\bar{S}_{vp}(x,y) &= \frac{\partial}{\partial y}\left(\bar{S}_{vp}(x)\bar{S}_{vp}(y)\right) \\
&= \bar{S}_{vp}(x)\frac{\partial\bar{S}_{vp}(y)}{\partial y} \equiv \nabla\bar{S}_{vpy}
\end{aligned} \tag{B.3.6}$$

Derivatives of the weighted shape function with respect to *x* and *y* are calculated by the following way.

$$
\begin{aligned}
\nabla \bar{S}_{vpx} &= \frac{\partial}{\partial x}\left(\frac{1}{V_p} \int_{\Omega \cap \Omega_p} N_i(x,y)\chi_p(x,y) d\Omega \right) \\
&= \frac{\partial}{\partial x}\left(\frac{1}{V_p} \int_{\Omega \cap \Omega_p} N_i(x)N_i(y)\chi_p(x)\chi_p(y) d\Omega \right) \\
&= \frac{1}{l_p^2} \int_{y_p - l_p}^{y_p + l_p} \int_{x_p - l_p}^{x_p + l_p} \frac{\partial}{\partial x}\{N_i(x)\chi_p(x)\} N_i(y)\chi_p(y) dx dy \\
&= \frac{1}{l_p^2} \int_{x_p - l_p}^{x_p + l_p} \frac{\partial N_i(x)}{\partial x} \chi_p(x) dx \int_{y_p - l_p}^{y_p + l_p} N_i(y)\chi_p(y) dy \\
&= \nabla \bar{S}_{vp}(x) \bar{S}_{vp}(y) \\
\nabla \bar{S}_{vpy} &= \nabla \bar{S}_{vp}(y) \bar{S}_{vp}(x)
\end{aligned}
\tag{B.3.7}
$$

Eq.(B.3.4) and (B.3.7) are the specific forms of the two-dimensional weighted shape function and its gradient, and implemented in this thesis.

B.4 Dimensionless Equations of the MPM

In the actual computation, a phase-field equation, heat equation, and crystallographic orientation equation are non-dimensionalized by a relaxation time τ and an interface thickness W. In order to keep a consistency with those equations, dimensionless equations of the MPM analysis are constructed in this section.

For simplicity, let us consider the equation of motion eq.(2.2.5) without body force term.

$$
\frac{\partial v_i}{\partial t} = \frac{1}{\rho} \frac{\partial \sigma_{ij}}{\partial x_j} \tag{B.4.1}
$$

Constitutive relation is given by

$$
\sigma_{ij} = \frac{E}{1+\nu}\left(\frac{\nu}{1-2\nu} \varepsilon_{kk} \delta_{ij} + \varepsilon_{ij} \right) \tag{B.4.2}
$$

Same as the phase-field equation, a relaxation time τ and an interface thickness W are taken to be a time scale and a length scale, respectively. In addition to those scales, a scale for mass should be required. $\rho=\rho_s=\rho_l$ is assumed in the phase-field equation, so ρ_s is

used for the mass scaling. Using those scales, the following dimensionless variables are defined.

$$\rho = \rho_s \rho^*, \quad t = \tau t^*, \quad x = W x^* \tag{B.4.3}$$

Eq.(B.4.1) is non-dimensionlized with those scales as

$$\begin{aligned} &\frac{W}{\tau^2}\frac{\partial v_i^*}{\partial t^*} = \frac{1}{\rho_s \rho^* W}\frac{\partial \sigma_{ij}}{\partial x_j^*} \\ \therefore \quad &\frac{\partial v_i^*}{\partial t^*} = \frac{\partial}{\partial x_j^*}\left(\frac{\sigma_{ij}}{\rho_s W^2/\tau^2}\right) \\ &= \frac{\partial \sigma_{ij}^*}{\partial x_j^*} \end{aligned} \tag{B.4.4}$$

where dimensionless stress is defined by

$$\sigma_{ij}^* = \frac{\sigma_{ij}}{\rho_s W^2/\tau^2} \tag{B.4.5}$$

Same scaling of stress as eq.(B.4.5) is performed on eq.(B.4.2).

$$\sigma_{ij}^* = \frac{E}{(1+\nu)(\rho_s W^2/\tau^2)}\left(\frac{\nu}{1-2\nu}\varepsilon_{kk}\delta_{ij} + \varepsilon_{ij}\right) \tag{B.4.6}$$

From the equation, Young's modulus and yield stress has to be scaled by $\rho_s W^2/\tau^2$. Pure material is of the major interest in this thesis. For instance, a capillary length d=2.4x10^{-10}[m], a solid density ρ_s=2550[kg/m3], and a thermal diffusivity D=3.7x10^{-5}[m^2/s] are the typical values for pure aluminum [61]. From the parameter determination procedure of phase-field equation mentioned in chapter 2, W=1.3x10^{-9}[m] and τ=1.36x10^{-13}[s] are obtained if d/W=0.185 is chosen. This gives the dimensionless Young's modulus $E^*=E/(\rho_s W^2/\tau^2)$=0.317 for a typical value of E=70.6[GPa] at the room temperature. As already mentioned in chapter 2, the CFL condition has to be satisfied during the MPM analysis. Based on the above non-dimensionalization, a speed of sound within a solid body is transformed to the following with using eq.(2.5.21).

$$c_{solid} = \sqrt{\frac{K + 4G/3}{\rho}} = \sqrt{\frac{K^* + 4G^*/3}{\rho^*}\frac{\rho_s W^2}{\rho_s \tau^2}} = \sqrt{\frac{K^* + 4G^*/3}{\rho^*}}\frac{W}{\tau} \qquad \text{(B.4.7)}$$

Using the above usual properties for pure aluminum, a dimensionless value $K^*+4G^*/3=0.497$ and $\rho^*=1$ are obtained. In the actual computation, $\Delta x/W=0.4$ is basically used. This gives the CFL condition as

$$\Delta t \le \frac{\Delta x}{c_{solid}} \approx 0.57\tau \qquad \text{(B.4.8)}$$

For a stable computation, $\Delta t^*=\Delta t/\tau=0.01$ is used in this thesis.

In case of compression analysis, $H=800\Delta y$ is initially assigned as the height of the computational domain, and $\Delta y / W_0=0.4$ is also set. From the above material property for pure aluminum, $\Delta y=5.19 \times 10^{-10}$[m] and $H=4.15 \times 10^{-7}$[m] are the order of spatial length scales. $\tau_0=1.36\times 10^{-13}$[s] is also estimated from the above. Basically, wall displacement $\Delta u_y=1.0 \times 10^{-4}\Delta y$ [m/step]$=1.25 \times 10^{-7}$ [1/step] is applied in the computation, and time increment $\Delta t=0.01\tau_0$ is used. Thus, $d\varepsilon/dt=1.0\times 10^{8}$[1/sec] is the order of strain rate in this computation. In the work by Fuloria et al.[13], FEM deformation analysis of dendrite structure is performed under $d\varepsilon/dt=0.1$[1/sec].

B.5 Determination of Constitutive Behavior

B.5.1 Mechanical properties of metal at high temperature

In this thesis, a deformation analysis of solidifying dendritic structure at high temperature is of the great interest. Mechanical properties around melting point of the material should be appropriate for the analysis. As stated in the main chapter, metal at high temperature range behaves as visco-plastic material. In some research, phenomenologically determined constitutive model is applied to those kinds of material. For instance, Pokorny et al.[58] apply Cocks yielding criterion with associative flow rule. In their study, the dynamic yield stress is specified by

$$\sigma_{dy} = \sigma_0 \left(1 + \frac{\varepsilon_{eq}}{\varepsilon_0} \right)^n \left(1 + \frac{\dot{\varepsilon}_{eq}}{\dot{\varepsilon}_0} \right)^m \tag{B.5.1}$$

where σ_0 and $\varepsilon_0=\sigma_0/E$ are a reference stress and a reference strain. n is a hardening coefficient, $\dot{\varepsilon}_0 \approx 10^{-5}[1/s]$ is a temperature-dependent reference strain rate (due to a lack of available data, the value is arbitrarily defined), and m is the strain-rate-sensitivity coefficient. Mechanical properties used in the above model are estimated from available data [63]. The data indicates that Young's modulus at eutectic temperature is about 50GPa. The value is used for simulations in the main chapter. As also mentioned in [58], Poisson's ratio is almost independent of temperature, so a typical value 0.33 is used in this thesis. A static (reference) yield stress σ_0 varies with temperature. For example, Figure B. 4 plots stress-strain curves of copper single crystal for different temperature with constant strain rate $\dot{\varepsilon} = 5 \times 10^{-4}[1/s]$. Since a melting point of pure copper is about 1357[K], a static yield stress is the order of few MPa around the melting point. A static yield stress data in [58] also shows that its order is of few MPa. 5MPa defined in chapter 3 is reasonable value from those viewpoints.

B.5.2 Parameter determination of a Perzyna type visco-plasticity model

For elasto-perfectly-plasticity material model, Young's modulus, Poisson's ratio, and yield stress are material parameters should be determined. In addition to them, viscosity parameter or relaxation time should be specified for elasto-visco-plasticity material model. In chapter 2 and appendix B.2, Perzyna type model is introduced to consider the elasto-perfectly-visco-plasticity of the material behavior for its simplicity and applicability to large strain rate. However, its expression in eq.(2.2.12) and (2.2.13) is little bit complicated to obtain physical perspective of the model, i.e. a shape of stress-strain curve. In this subsection, a characteristic of the Perzyna type model for one-

dimensional uniaxial loading case and determination of model parameters are presented. Detailed derivations of equations are omitted (see [60]for details about derivations).

An evolution of visco-plastic strain in a general Perzyna type model is described by the following equation.

$$\dot{\varepsilon}_{ij}^{vp} = \gamma \langle \Phi(f_Y) \rangle \frac{\partial f_Y}{\partial \sigma_{ij}} \tag{B.5.2}$$

Here $\Phi(f_Y)$ is defined as a function of a static yielding function f_Y which is assumed to be independent of strain. For metallic material, it is typical to use von Mises yield criterion for the static yielding function. The form of f_Y in this thesis is

$$f_Y = \sqrt{s_{ij} : s_{ij}} - \sqrt{\frac{2}{3}}\sigma_Y \tag{B.5.3}$$

In case of one-dimensional uni-axial loading, eq.(B.5.3) should be given by

$$f_Y = \sqrt{\frac{2}{3}}(\sigma - \sigma_Y) \tag{B.5.4}$$

where σ is an uni-axial stress. Strain should be composed of elastic part and visco-plastic part of strain.

$$\dot{\varepsilon} = \frac{\dot{\sigma}}{E} + \dot{\varepsilon}^{vp} = \frac{\dot{\sigma}}{E} + \gamma \langle \Phi(\sigma - \sigma_Y) \rangle \tag{B.5.5}$$

In the Perzyna type model, for example, the following form of Φ is assumed.

$$\Phi(\sigma - \sigma_Y) = (\sigma - \sigma_Y)^m \tag{B.5.6}$$

Eq.(B.5.2) with eq.(B.5.6) is now turned out to be

$$\sigma = \sigma_Y + \left(\frac{\dot{\varepsilon}^{vp}}{\gamma} \right)^{1/m} \tag{B.5.7}$$

or

$$\dot{\varepsilon}^{vp} = \gamma (\sigma - \sigma_Y)^m \tag{B.5.8}$$

The equation indicates that stress can exceed the static yield stress (overstress) depending on visco-plastic strain rate. The dependency is adjusted by parameters γ and m.

Since a development of a specific constitutive relation is not of interest in this thesis, Φ is defined the same as the static yielding function, i.e. m=1, for its simplicity of numerical implementation (the actual implementation is already developed in appendix B.2).

$$\sigma = \sigma_Y + \frac{\dot{\varepsilon}^{vp}}{\gamma} \tag{B.5.9}$$

Although a development of a constitutive relation is not a subject of this study, plausible material behavior should be incorporated at least. Generally, strain rate and temperature dependent flow stress σ (dynamic yield stress) is described as the following empirical equation (see i.e. [66]).

$$\sigma = f\left\{\dot{\varepsilon}\exp\left(\frac{Q}{RT}\right)\right\} \tag{B.5.10}$$

where Q is an activation energy for plastic flow, R(=8.314J/(g.mol.K)) is an universal gas constant, and f denotes some empirically obtained function (stress-strain curve). Therefore, a function f depends on Arrhenius type term. At constant temperature, the following phenomenologically defined constitutive relation is often used.

$$\sigma = C\varepsilon^n\dot{\varepsilon}^m \tag{B.5.11}$$

where C, n and m are empirical parameters. When the imposed temperature to some metallic material is above their re-crystallization temperature (approximately one-half of absolute melting temperature), work-hardening effect and thermal softening effect is balanced on each other, so flow stress is saturated. In the case, the following empirical constitutive relation is often used.

$$\sigma = C\sinh^{-1}\left\{m\dot{\varepsilon}^n\exp\frac{b}{T}\right\} \tag{B.5.12}$$

C and m are constants, and b=Q/R defined in the above. Often $Z = \dot{\varepsilon}\exp(b/T)$ is called Zener-Hollomon parameter. When the value in the parenthesis is sufficiently small, the above equation is reduced to eq.(B.5.11). In any case, there is non-linear dependency of dynamic yield stress on strain rate. Thus, some approximation should be

required to represent those constitutive relation by eq.(B.5.9). Figure B. 5 plots stress-strain curves with different strain rate up to ~10^7[1/sec] for (a) polycrystalline aluminum and (b) high purity iron (99.99%Fe) [67]. Left panels are original graphs of the source [67], and they are plotted with logarithmic horizontal axis. Right panels are reproduced plots from the original graphs (left panels in the same figure) with normal horizontal axis. Basically, flow stress increases rapidly in the lower strain rate, so fitting data with eq.(B.5.9) in this regime is not suitable, i.e. γ~10^{-9}[1/(Pa.s)] (flow stress should be overestimated in the high strain rate). As a first approximation, a linear interpolation in high strain rate shown in the right panels is assumed in this thesis. From the fitting, model parameter γ in eq.(B.5.9) is 0.034[1/(Pa.s)] and 0.024[1/(Pa.s)] for aluminum and iron, respectively. The order of γ~10^{-2} [1/(Pa.s)] is assumed in this thesis. In other words, η_{visc} ~10^2 [Pa.s] is used. From eq.(B.2.30), i.e. $\tau_{visc}=\eta_{visc}/2G$, a relaxation time that it takes material mechanical response to decay to a static yield stress is the order of τ_{visc}~10^{-7}[sec] if the order of Young's modulus is several tens of GPa. It is sufficient to keep viscous effect during a whole computational time.

As a side note, for a structure which is composed of multiple grains, grain boundary strengthening or Hall-Petch strengthening is observed in the sense of macroscopic continuum mechanics.

$$\sigma = \sigma_0 + kd^{-1/2} \tag{B.5.13}$$

where σ_0 is the reference yield stress, k is a constant, and d is a size of grain. The equation indicates that smaller grains give more resistance to cause yielding (basically shear or sliding). A simulation model used in this thesis resolves a scale of microstructure, so the effect should be automatically included thorough contacts among grains approximately.

B.6 Specific Representation of Some Terms for an Actual Implementation

As a note for an actual numerical implementation, a detailed form of some terms is presented.

B.6.1 The velocity gradient $\nabla\bar{S}_{vp}\otimes\vec{v}$

The velocity gradient term $\nabla\bar{S}_{vp}\otimes\vec{v}$ is necessary to compute strain increment through a rate of deformation tensor. The term is represented by dyads. In the two-dimensional case, the term should be represented by the following form.

$$\nabla\bar{S}_{vp}\otimes\vec{v}_i=\begin{bmatrix} u_i\dfrac{\partial\bar{S}_{vp}}{\partial x} & u_i\dfrac{\partial\bar{S}_{vp}}{\partial y} \\ v_i\dfrac{\partial\bar{S}_{vp}}{\partial x} & v_i\dfrac{\partial\bar{S}_{vp}}{\partial y}\end{bmatrix} \tag{B.6.1}$$

where nodal velocity $\vec{v}_i=(u_i,v_i)$ is defined in this notation. With using the notation, a rate of deformation tensor at each material point should be given by

$$\begin{aligned}\dot{\boldsymbol{\varepsilon}}_p&=\sum_{i=1}^{nnod}\frac{1}{2}\left\{\overline{\nabla S_{vp}}\otimes\vec{v}_i+\left(\overline{\nabla S_{vp}}\otimes\vec{v}_i\right)^T\right\}\\&=\sum_{i=1}^{nnod}\begin{bmatrix} u_i\dfrac{\partial\overline{S_{vp}}}{\partial x} & \dfrac{1}{2}\left(\dfrac{\partial\overline{S_{vp}}}{\partial y}u_i+v_i\dfrac{\partial\overline{S_{vp}}}{\partial x}\right)\\ \dfrac{1}{2}\left(\dfrac{\partial\overline{S_{vp}}}{\partial y}u_i+v_i\dfrac{\partial\overline{S_{vp}}}{\partial x}\right) & v_i\dfrac{\partial\overline{S_{vp}}}{\partial y}\end{bmatrix}=\begin{bmatrix}\dot{\varepsilon}_{pxx} & \dot{\varepsilon}_{pxy}\\ \dot{\varepsilon}_{pxy} & \dot{\varepsilon}_{pyy}\end{bmatrix}\end{aligned} \tag{B.5.2}$$

B.6.2 Spin tensor $\boldsymbol{\omega}$

In order to correct the effect of rigid body rotation on stress tensor, Jaumann stress rate is used in our computation. In the expression, a spin tensor at each material point should be necessary. Using eq.(B.3.8), the following form should be obtained.

$$\boldsymbol{\omega}_p = \sum_{i=1}^{n} \frac{1}{2}\left[\nabla \bar{S}_{vp} \otimes \vec{v}_i - \left(\nabla \bar{S}_{vp} \otimes \vec{v}_i\right)^T\right]$$
$$= \begin{bmatrix} 0 & \frac{1}{2}\sum_{i=1}^{Nnod}\left(u_i \frac{\partial \bar{S}_{vp}}{\partial y} - v_i \frac{\partial \bar{S}_{vp}}{\partial x}\right) \\ -\frac{1}{2}\sum_{i=1}^{Nnod}\left(u_i \frac{\partial \bar{S}_{vp}}{\partial y} - v_i \frac{\partial \bar{S}_{vp}}{\partial x}\right) & 0 \end{bmatrix} \quad \text{(B.6.3)}$$

Using the expression, $\boldsymbol{\sigma}_p \cdot \boldsymbol{\omega}_p$ and $\boldsymbol{\omega}_p \cdot \boldsymbol{\sigma}_p$ should be given by the following equations.

$$\boldsymbol{\sigma}_p \cdot \boldsymbol{\omega}_p = \begin{bmatrix} -\frac{1}{2}\sigma_{pxy}\sum_{i=1}^{Nnod}\left(u_i \frac{\partial \bar{S}_{vp}}{\partial y} - v_i \frac{\partial \bar{S}_{vp}}{\partial x}\right) & \frac{1}{2}\sigma_{pxx}\sum_{i=1}^{Nnod}\left(u_i \frac{\partial \bar{S}_{vp}}{\partial y} - v_i \frac{\partial \bar{S}_{vp}}{\partial x}\right) \\ -\frac{1}{2}\sigma_{pyy}\sum_{i=1}^{Nnod}\left(u_i \frac{\partial \bar{S}_{vp}}{\partial y} - v_i \frac{\partial \bar{S}_{vp}}{\partial x}\right) & \frac{1}{2}\sigma_{pyx}\sum_{i=1}^{Nnod}\left(u_i \frac{\partial \bar{S}_{vp}}{\partial y} - v_i \frac{\partial \bar{S}_{vp}}{\partial x}\right) \end{bmatrix} \quad \text{(B.6.4)}$$

$$\boldsymbol{\omega}_p \cdot \boldsymbol{\sigma}_p = \begin{bmatrix} \frac{1}{2}\sigma_{pyx}\sum_{i=1}^{Nnod}\left(u_i \frac{\partial \bar{S}_{vp}}{\partial y} - v_i \frac{\partial \bar{S}_{vp}}{\partial x}\right) & \frac{1}{2}\sigma_{pyy}\sum_{i=1}^{Nnod}\left(u_i \frac{\partial \bar{S}_{vp}}{\partial y} - v_i \frac{\partial \bar{S}_{vp}}{\partial x}\right) \\ -\frac{1}{2}\sigma_{pxx}\sum_{i=1}^{Nnod}\left(u_i \frac{\partial \bar{S}_{vp}}{\partial y} - v_i \frac{\partial \bar{S}_{vp}}{\partial x}\right) & -\frac{1}{2}\sigma_{pxy}\sum_{i=1}^{Nnod}\left(u_i \frac{\partial \bar{S}_{vp}}{\partial y} - v_i \frac{\partial \bar{S}_{vp}}{\partial x}\right) \end{bmatrix} \quad \text{(B.6.5)}$$

Then, $(\boldsymbol{\omega}_p \cdot \boldsymbol{\sigma} - \boldsymbol{\sigma}_p \cdot \boldsymbol{\omega}_p)$ term is represented by the following equation.

$$\begin{aligned} &\boldsymbol{\omega}_p \cdot \boldsymbol{\sigma}_p - \boldsymbol{\sigma}_p \cdot \boldsymbol{\omega}_p = \begin{bmatrix} A_{11} & A_{12} \\ A_{21} & A_{22} \end{bmatrix} \\ &A_{11} = \sigma_{xy}\sum_{i=1}^{Nnod}\left(u_i \frac{\partial \bar{S}_{vp}}{\partial y} - v_i \frac{\partial \bar{S}_{vp}}{\partial x}\right) \\ &A_{22} = -A_{11} \\ &A_{12} = \frac{\sigma_{pyy} - \sigma_{pxx}}{2}\sum_{i=1}^{Nnod}\left(u_i \frac{\partial \bar{S}_{vp}}{\partial y} - v_i \frac{\partial \bar{S}_{vp}}{\partial x}\right) \\ &A_{21} = A_{12} \end{aligned} \quad \text{(B.6.6)}$$

B.6.3 Nodal internal force $\vec{f}_i^{\,\text{int}}$

If the following matrix notation of point stress is defined,

$$\boldsymbol{\sigma}_p = \begin{bmatrix} \sigma_{pxx} & \sigma_{pxy} \\ \sigma_{pxy} & \sigma_{pyy} \end{bmatrix} \quad \text{(B.6.7)}$$

Nodal internal force should be represented by

$$\vec{f}_i^{\,\mathrm{int}} = -\sum_{p=1}^{N_p} V_p \boldsymbol{\sigma}_p \cdot \overline{\nabla S_{vp}} = -\left(f_{ix}^{\mathrm{int}}, f_{iy}^{\mathrm{int}}\right)$$

$$f_{ix}^{\mathrm{int}} = \sum_{p=1}^{N_p} V_p \left(\overline{\nabla S_{vpx}}\sigma_{pxx} + \overline{\nabla S_{vpy}}\sigma_{pxy}\right) \tag{B.6.8}$$

$$f_{iy}^{\mathrm{int}} = \sum_{p=1}^{N_p} V_p \left(\overline{\nabla S_{vpx}}\sigma_{pxy} + \overline{\nabla S_{vpy}}\sigma_{pyy}\right)$$

B.6.4 Deformation gradient

Deformation gradient **F** denotes a mapping relation between reference (initial) and current configuration, and is used to update a volume associated with each material point in this thesis. A rate change of **F** is represented by the following equation.

$$\dot{\mathbf{F}} = \frac{d\mathbf{F}}{dt} = \frac{\partial \mathbf{v}}{\partial \mathbf{x}} \cdot \mathbf{F} \tag{B.6.9}$$

where $\partial\mathbf{v}/\partial\mathbf{x}$ is the velocity gradient tensor defined in the current configuration. The following equation can be derived for the discretized form of eq.(B.6.9) if the explicit Euler method is applied.

$$\mathbf{F}^{n+1} = \mathbf{F}^n + \left(\frac{\partial \mathbf{v}}{\partial \mathbf{x}}\right)^n \cdot \mathbf{F}^n \Delta t = \left\{\mathbf{I} + \left(\frac{\partial \mathbf{v}}{\partial \mathbf{x}}\right)^n \Delta t\right\} \cdot \mathbf{F}^n \tag{B.6.10}$$

Using the notation of a rate of deformation tensor in eq.(B.6.1), the equation should be represented by

$$\mathbf{F}^{n+1} = \begin{bmatrix} 1 + \sum_{i=1}^{nnod}\left(u_i \frac{\partial \overline{S_{vp}}}{\partial x}\right)^n \Delta t & \sum_{i=1}^{nnod}\left(u_i \frac{\partial \overline{S_{vp}}}{\partial y}\right)^n \Delta t \\ \sum_{i=1}^{nnod}\left(v_i \frac{\partial \overline{S_{vp}}}{\partial x}\right)^n \Delta t & 1 + \sum_{i=1}^{nnod}\left(v_i \frac{\partial \overline{S_{vp}}}{\partial y}\right)^n \Delta t \end{bmatrix} \begin{bmatrix} F_{11}^n & F_{12}^n \\ F_{21}^n & F_{22}^n \end{bmatrix} \tag{B.6.11}$$

B.7 Fragmentation

Although it is not included in the main chapter, a fragmentation should take place around contact surface and bridging part etc., and might affect morphological change of dendrite structure somehow as Flemings [2] points out. As well as a contact phenomenon

and a modification of solid structural model, a numerical implementation of a fragmentation of the solid structure is relatively easy by MPM. For instance, Ionescu et al.[62] set maximum tensile strain and shear strain as a criterion of the failure of the composite material. Since all historical variables are carried by each material point, the criterion is just imposed on each material point, i.e. stresses on a material point set to be zero if strains on the point exceed the maximum value.

As a simple test study, a tensile loading problem with dumbbell type specimen shown in Figure B. 2 is solved. The maximum equivalent (total) strain is set to be a criterion of fragment. An equivalent Mises strain is chosen for the strain measure and is defined by the following equation.

$$\varepsilon_{eq} = \sqrt{\frac{\left(\varepsilon_{xx} - \varepsilon_{yy}\right)^2 + \left(\varepsilon_{yy} - \varepsilon_{zz}\right)^2 + \left(\varepsilon_{zz} - \varepsilon_{xx}\right)^2}{2} + 3\left(\varepsilon_{xy}^2 + \varepsilon_{yz}^2 + \varepsilon_{zx}^2\right)} \qquad \text{(B.8.1)}$$

Same as the benchmark test described in section 2, a dumbbell shape test specimen is computationally created. Material properties of usual aluminum is assigned to it (E=69[GPa], ν=0.345, σ_Y=15[MPa], and ρ=2700[kg/m^3]) as a test study. Although it is a macroscopic value, typical breaking elongation of the material 30% is set to be a fragmentation criterion. Displacement boundary condition is imposed on both edges of the specimen. The displacement is increased linearly with time. Material properties of usual aluminum are assigned to the specimen. From some time step, a necking is formed in the middle of the specimen, and gradually stress is concentrated in the part.

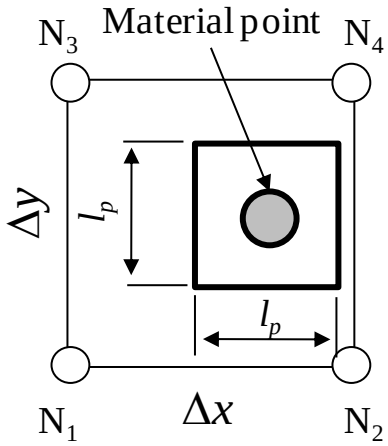

Figure B. 1 Schematic of volume associated with material point

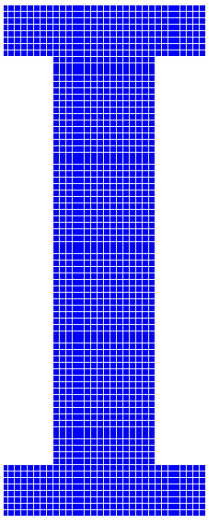

Figure B. 2 Allocation of material points for dumbbell type specimen model

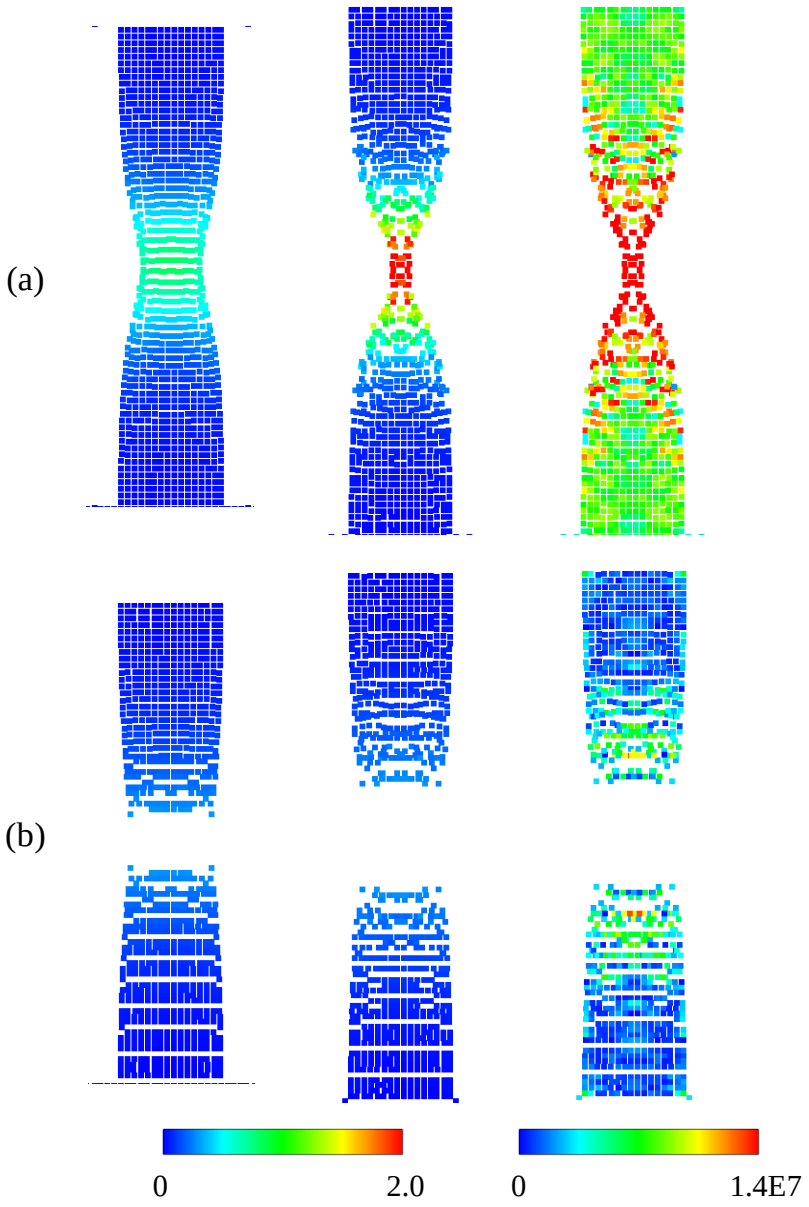

Figure B. 3 Contours of total strain (left two panels) and von Mises stress (right panels) for (a) without imposing fragment criterion and (b) with fragment criterion.

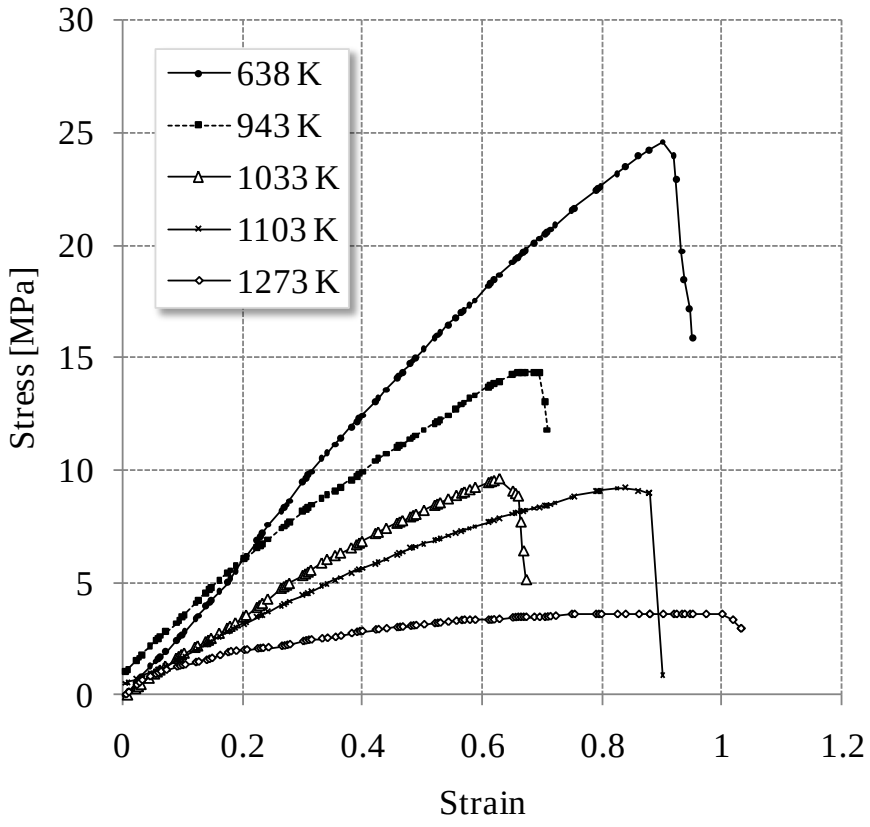

Figure B. 4 Stress-strain curves of copper single crystal as a function of temperature with $d\varepsilon/dt=5x10^{-4}[s^{-1}]$; The plots are reproduced from the source indicated below.

Source: Bauser M. et al. *Extrusion second edition*.**2006**,ASM international.

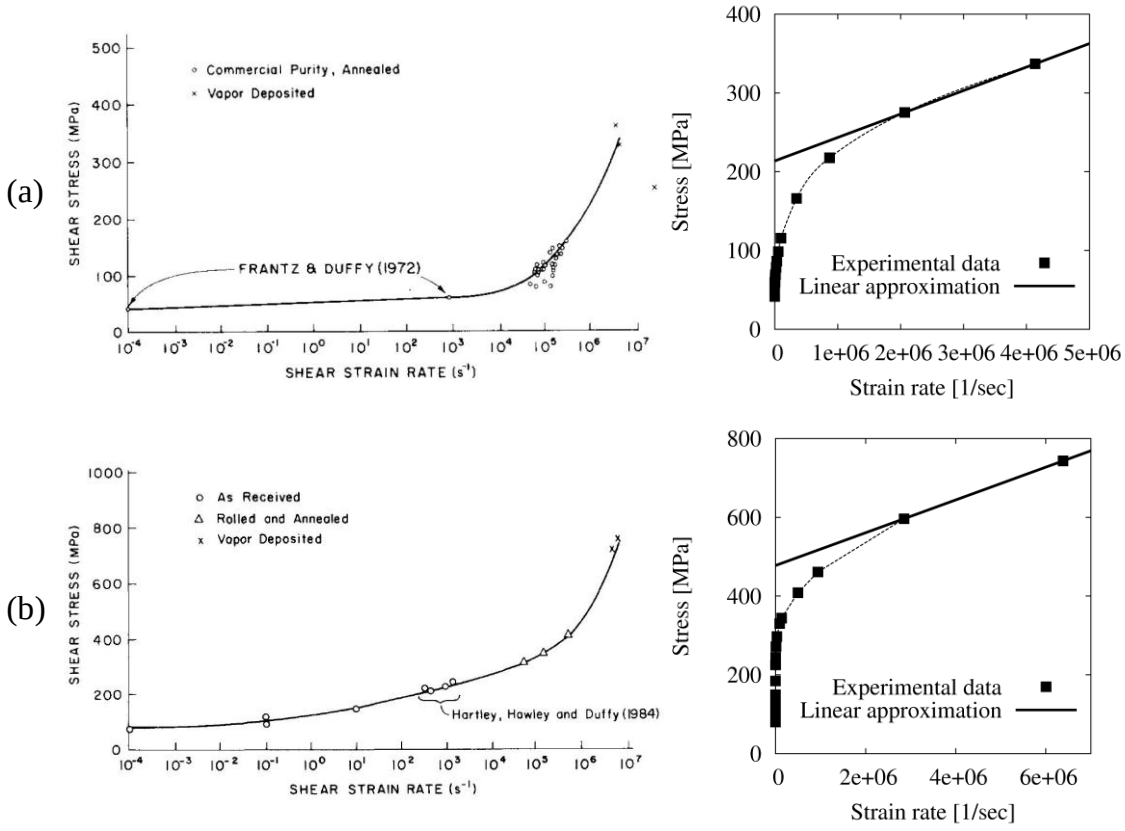

Figure B. 5 Strain rate dependency of dynamic yielding stress; (a) for polycrystalline aluminum; (b) for high purity iron (Fe 99.99%); Left panels: original plots of the source indicated below with logarithmic horizontal axis; Right panels: reproduced plots with normal horizontal axis. Approximated linear profiles are also presented.

Source: Klopp R.W. et al. *Mech.Mater*. **1985**,4, 375-385.

APPENDIX C

NUMERICAL IMPLIMENTATION OF POLYCRYSTALLINE PHASE-FIELD MODEL

Evolution equations for phase-field ϕ and crystallographic orientation α are presented in chapter 4. Some topics required for an actual numerical implementation are presented in this appendix.

C.1 Determination of Model Parameters

Model parameters η, s and ε_ϕ need to be specified in eq.(4.1.8) and (4.1.9). Basically, ε_ϕ and η relate to a grain boundary thickness of ϕ and α (a thickness which ϕ or α is allowed to vary), respectively. s affects on a phase-field ϕ at the center of the grain boundary. Plausible way to define the parameters needs to be constructed. Warren et al. [24] suggest the following guideline to determine the parameters.

(i) Assume typical value of latent heat per unit volume for metallic material as

$$L = 2 \times 10^9 [J/m^3] \tag{C.1.1}$$

The relation between a depth of double-well a and the above latent heat L is also assumed to be

$$a = \sqrt{L/2} \tag{C.1.2}$$

(ii) A characteristic length of grain boundary thickness is defined to be

$$\eta^* \equiv \eta / \sqrt{L} \tag{C.1.3}$$

As a plausible value of η^*, η^* =1.0x10^{-9}[m] is chosen.

(iii) Assume the following relation between and ε_ϕ and η.

$$\tilde{\varepsilon}_\phi = 1.875\tilde{\eta} \tag{C.1.4}$$

(iv) Choose the following relation between s and η.

$$\tilde{s} = 1.25\tilde{\eta} \tag{C.1.5}$$

The above model parameters have dimension. Dimensionless model parameters $\tilde{\varepsilon}_\phi$, $\tilde{\eta}$, and $\tilde{s}$ are obtained as follows with using a characteristic length l_0 and a reference energy density E_0 are used.

$$\tilde{\varepsilon}_\phi = \frac{\varepsilon_\pi}{\sqrt{E_0 l_0}} \tag{C.1.6}$$

$$\tilde{\eta} = \frac{\eta}{\sqrt{E_0 l_0}} \tag{C.1.7}$$

$$\tilde{s} = \frac{s}{E_0 l_0} \tag{C.1.8}$$

In the parameter determination by Warren et al.[24], $E_0=2a^2$ is used. With considering the similarity of KWC phase-field model with the phase-field model developed by Karma et al.[19] (see next section for more details), $E_0=a^2/2$ and $l_0=W_0$ are suitable choice for the non-dimensionalization.

C.2 Comparison of Polycrystalline Phase-field Model with the Phase-field Model of Single Dendritic Solidification Developed by Karma et al.

A phase-field model developed by Karma described in chapter 2 would be better to recover a simulation result obtained by sharp interface model. In this section, a similarity between the model and KWC phase-field model is examined. $\nabla\alpha = 0$ (no angle mismatch) is assumed throughout this section.

A phenomenological bulk free energy (dimensionless) by Karma et al.[19] is

$$f_K^*(\phi, \lambda\theta) = -\frac{\phi^2}{2} + \frac{\phi^4}{4} + \lambda\left(\phi - \frac{2}{3}\phi^3 + \frac{\phi^5}{5}\right)\theta \tag{C.2.1}$$

The one by Warren et al.[24] with type I function for $p(\phi)$ is

$$f_W(\phi,\theta) = \frac{a^2}{2}\left(-\frac{\phi^2}{2} + \frac{\phi^4}{4}\right) + \frac{a^2}{8} + \left\{\frac{15}{4}\left(\phi - \frac{2}{3}\phi^3 + \frac{\phi^5}{5}\right) + \frac{1}{2}\right\}\frac{L^2}{c_p T_m}\theta \tag{C.2.2}$$

As mentioned previously, a constant a has a dimension of [energy density]$^{1/2}$, and $a=\sqrt{L/2}$ is assumed for the parameter determination. Dimensionless eq.(C.2.2) by $a^2/4$ should be given by

$$f_W^*(\phi,\theta)=-\frac{\phi^2}{2}+\frac{\phi^4}{4}+\frac{1}{4}+\left\{15\left(\phi-\frac{2}{3}\phi^3+\frac{\phi^5}{5}\right)+8\right\}\frac{L}{c_pT_m}\theta \tag{C.2.3}$$

The variations of eq.(C.2.1) and (C.2.3) with respect to ϕ should be given by

$$\frac{\delta f_K^*}{\delta\phi}=-\phi\left(1-\phi^2\right)+\lambda\left(1-\phi^2\right)^2\theta \tag{C.2.4}$$

$$\frac{\delta f_W^*}{\delta\phi}=\frac{a^2}{2}\left[-\phi\left(1-\phi^2\right)+\frac{15L}{c_pT_m}\left(1-\phi^2\right)^2\theta\right] \tag{C.2.5}$$

In the research by Warren et al. [24], eq.(C.2.5) for isothermal case is simplified as

$$\frac{\delta f_W^*}{\delta\phi}=\frac{a^2}{2}\left[-\phi\left(1-\phi^2\right)+\frac{C}{2}\left(1-\phi^2\right)^2\right] \tag{C.2.6}$$

A constant C is defined for the computation. The form is quite similar to eq.(C.2.4), but is for isothermal case. Temperature dependency on double-well potential in KWC phase-field model is introduced by the following form.

$$\frac{\delta f_W^*}{\delta\phi}=\frac{a^2}{2}\left[-\left(1-\phi^2\right)\left\{\phi-\frac{2\kappa_1}{\pi}\tan^{-1}\left(\kappa_2\theta'\right)\right\}\right] \tag{C.2.7}$$

where $\theta'=(T-T_m)/T_m$ is dimensionless temperature which is different definition from the one used in this thesis. κ_1 and κ_2 are positive constants. The coefficient κ_1 is set to be $\kappa_1<1$ [18]. Since $-\pi/2\le\tan^{-1}x\le\pi/2$, minima of eq.(C.2.7) always stay within $-1\le\phi\le1$ by defining the function. Although slight differences exist between eq.(C.2.4) and (C.2.7), a basic characteristic of both equations is almost same , i.e. $\tan^{-1}(\kappa_2\theta')$ is almost linear with respect to θ around $T=T_m$. In this thesis, the form in eq.(C.2.1) is used for a

bulk free energy density f in a crystalline phase-field model in order to recover solutions by sharp interface model at least an absence of orientation mismatch.

Resulting phase-field equation by Warren et al. [24] should be the following form.

$$\tau_\phi \frac{\partial \phi}{\partial t} = \varepsilon_\phi^2 \nabla^2 \phi + \frac{a^2}{2}\left[\left(1-\phi^2\right)\left\{ \phi - \frac{2\kappa_1}{\pi}\tan^{-1}\left(\kappa_2 \theta'\right)\right\}\right] - 2\left(1+\phi\right)s\left|\nabla \alpha\right| - \left(1+\phi\right)\eta^2\left|\nabla \alpha\right|^2 \tag{C.2.8}$$

$E_0=a^2/2$ would be the suitable choice of reference energy density. Non-dimensionalization of eq.(C.2.8) with E_0 should be given by

$$\tau'_\phi \frac{\partial \phi}{\partial t} = \varepsilon'^2_\phi \nabla^2 \phi + \left(1-\phi^2\right)\left\{ \phi - \frac{2\kappa_1}{\pi}\tan^{-1}\left(\kappa_2 \theta'\right)\right\} - 2\left(1+\phi\right)s'\left|\nabla \alpha\right| - \left(1+\phi\right)\eta'^2\left|\nabla \alpha\right|^2 \tag{C.2.9}$$

where $\tau'_\phi=\tau_\phi/(a^2/2)$, $\varepsilon'_\phi=\varepsilon_\phi/(a^2/2)^{1/2}$, $s'=s/(a^2/4)$, and $\eta'=\eta/(a^2/2)^{1/2}$. By assuming $\tau'_\phi=\tau_0$ and $\varepsilon_\phi^2=W_0^2$, the following dimensionless equation (non-dimensionalized by τ_0 and W_0, i.e. $t'=t/\tau_0$, $\mathbf{x}'=\mathbf{x}/W_0$) should be obtained.

$$\frac{\partial \phi}{\partial t'} = \nabla'^2 \phi + \phi\left(1-\phi^2\right)\left\{ \phi - \frac{2\kappa_1}{\pi}\tan^{-1}\left(\kappa_2 \theta'\right)\right\} - 2\left(1+\phi\right)\tilde{s}\left|\nabla \alpha\right| - \left(1+\phi\right)\tilde{\eta}^2\left|\nabla \alpha\right|^2 \tag{C.2.10}$$

From the similarity of eq.(C.2.10) with the phase-field equation developed by Karma et al.[19], the following evolution equations are used in this thesis.

$$\frac{\partial \phi}{\partial t'} = \nabla'^2 \phi + \phi\left(1-\phi^2\right) - \lambda\left(1-\phi^2\right)^2\theta - 2\left(1+\phi\right)\tilde{s}\left|\nabla' \alpha\right| - \left(1+\phi\right)\tilde{\eta}^2\left|\nabla' \alpha\right|^2 \tag{C.2.11}$$

$$P'\tau'_\alpha \left(1+\phi\right)^2 \frac{\partial \alpha}{\partial t'} = \nabla'\cdot\left[\left(1+\phi\right)^2\left(\tilde{\eta}^2\nabla'\alpha + \tilde{s}\frac{\nabla'\alpha}{\left|\nabla'\alpha\right|}\right)\right] \tag{C.2.12}$$

where $t'=t/\tau_\phi$, $\mathbf{x}'=\mathbf{x}/W_0$, and $\tau'_\alpha=\tau_\alpha/\tau_\phi$ are defined. A coefficient P should be dimensionless, so a coefficient μ has the same unit as η. modified to P' as

$$P'\left(\tilde{\eta}\left|\nabla'\alpha\right|\right)=1-e^{-\beta\tilde{\eta}\left|\nabla'\alpha\right|}+\frac{\tilde{\mu}}{\tilde{\eta}}e^{-\beta\tilde{\eta}\left|\nabla'\alpha\right|} \quad \text{(C.2.13)}$$

$\tilde{\mu}=\mu/\left(\sqrt{E_0}l_0\right)$ would be a suitable nondimensinalization. For a heat equation, its expression is the same for both models. No modification for it should be required. From the above non-dimensionalization, the following relation among model parameters should be obtained.

$$\tilde{\eta}=\tilde{\varepsilon}_\phi/1.875 \quad \text{(C.2.14)}$$

$$\tilde{s}=\sqrt{2}\tilde{\varepsilon}_\phi/1.5 \quad \text{(C.2.15)}$$

From the parameters, a critical orientation mismatch should be $\Delta\alpha_c=1.06$.

Again, the model parameter determination is based on the guideline proposed by Warren et al.[24] and there is not a significant meaning on it.

C.2.1 Adding anisotropy

As represented by eq.(4.1.4), four-fold symmetry is introduced to phase-field equation to represent anisotropy. Since the anisotropy has to be included basing on crystal framework, cosine is computed with an angle of (φ-α). The treatment is completely same as the one developed in chapter 2.4.3. The same way of numerical implementation about the anisotropy term is simply applied to KWC phase-field model.

C.2.2 Validation: single dendrite growth with different orientation

As mentioned in the above, a polycrystalline phase-field model used in this study should have the same solutions obtained by a sharp interface model in case of no orientation mismatch. Test simulation is performed to confirm it in this section. A computational domain which is composed of 801x801 computational grids is prepared. Spacing of the grids is set to be $\Delta x/W_0$=0.4. A flux free boundary condition is imposed for phase-field, temperature, and orientation evolution equation. At the center of the

domain, a solid seed (ϕ=1 and θ=0 are imposed inside the seed. Otherwise, ϕ=-1 and θ=-0.55 is assigned) is allocated. ε=0.05, d_0/W_0=0.185, and D=3.0 are defined as model parameters. For one test case, α=0 is set all over the domain. For another case, α=π/4 is specified in the whole domain. In both cases, $|\nabla\alpha|$ is not expected in any region throughout the simulations.

Figure C. 3 upper panels show computed ϕ=0 contours at every 2500 steps for α=0 (left panel) and α=π/4 (right panel). In both cases, dendrite grows its main arms to the given orientation direction. Lower left panel of the same figure plots computed ϕ=0 contours of both conditions (the result of α=π/4 is rotated back for the comparison). Both contours correspond well with each other. A time history of tip velocity is shown in the lower right panel of the same figure. Tip velocities for both conditions are the same, and give the close value to the analytical one. Thus, the polycrystalline model developed in this thesis gives an exact solution at least when an orientation mismatch is absent.

C.3 Treatment of Singular Term in KWC Phase-field Model

KWC phase-field model includes a singular term, i.e. $\nabla\alpha/|\nabla\alpha|$. Since the term is inside of the divergence, $1/|\nabla\alpha|$ is assumed to be a diffusion coefficient. This means that infinitely large diffusion would be expected near $|\nabla\alpha|=0$. The term is necessary to keep α constant within each bulk grain, and to allow α to diffuse within grain boundary. However, some numerical cares need to handle it in an actual numerical implementation. Kobayashi et al.[68] introduce the following cut-off inverse function I_y.

$$\frac{1}{|\nabla\alpha|} \approx I_y\left(|\nabla\alpha|\right) = \begin{cases} \gamma_{\lim} & \text{for } 0 \le |\nabla\alpha| \le 1/\gamma_{\lim} \\ \dfrac{1}{|\nabla\alpha|} & \text{for } |\nabla\alpha| > 1/\gamma_{\lim} \end{cases} \qquad \text{(C.3.1)}$$

As shown in Figure C. 1, above some large value γ_{lim}, an original function $1/|\nabla\alpha|$ is cut off. An evolution equation of orientation field is solved by using the above cut-off

function with $\gamma_{lim}=10^8$ in this thesis. $\gamma_{lim}=10^8$ is actually still large value in the actual computation. Since a diffusion coefficient strongly affects on an acceptable time increment for a stable analysis of explicit time stepping method, the size of the time increment becomes very much small and unrealistic for an actual computation. In order to remove the restriction of the size of the time increment, SOR (Successive Over Relaxation) method which is an implicit method is adopted in this thesis.

C.4 Numerical Treatment of the Periodicity of the Angle Variable

Crystallographic orientation α appears in KWC phase-field model is defined as an angle between a direction of a crystal framework and x-axis fixed on the computational domain. α has an unit of angle, i.e. radian, and it has 2π periodicity. In the evolution equations of ϕ and α, the value α itself does not play a role, but the spatial variation of α does. Therefore, the difference of α among neighbor computational nodes as well as α itself should be kept in the range of 2π in the actual numerical computation. Otherwise, the computational result would be meaningless. A numerical treatment to keep α or its spatial difference $\Delta\alpha$ in the range of 2π is simple, and it is briefly described in the followings.

In this thesis, α and $\Delta\alpha$ is kept in the range of $-\pi<\alpha\leq\pi$. The following cases are considered.

(i) In case $\alpha>\pi$

Define the following integer $I_{\alpha\mathrm{mod}}$.

$$I_{\alpha\,\mathrm{mod}} = \mathrm{int}\left[\frac{\alpha-\pi}{2\pi}\right] \tag{C.4.1}$$

where a function "int" returns a quotient of inside the parenthesis. Then the corrected angle variable α_{corr} is represented by

$$\alpha_{corr} = \alpha - 2\pi\times\left(I_{\alpha\,\mathrm{mod}}+1\right) \tag{C.4.2}$$

(ii) In case$\alpha \leq \pi$

Define the following integer $I_{\alpha \mathrm{mod}}$.

$$I_{\alpha \,\mathrm{mod}} = \mathrm{int}\left[\frac{|\alpha + \pi|}{2\pi}\right] \tag{C.4.3}$$

Then the corrected angle variable α_{corr} is represented by

$$\alpha_{corr} = \alpha + 2\pi \times \left(I_{\alpha \,\mathrm{mod}} + 1\right) \tag{C.4.4}$$

In the above procedure, a notation of α is only presented, but the procedure also works with its spatial difference $\Delta\alpha$.

C.5 Validation of One-Dimensional Dry Boundary

In order to check a validity of a numerical program of KWC phase-field model in this thesis, one-dimensional dry boundary problem is chosen [24] since an analytical solution is available for it. Dry boundary here means that only solid phase is a stable phase in the system with using single-well potential, i.e.

$$f(\phi) = \frac{1}{8}(1-\phi)^2 \tag{C.5.1}$$

In this problem, evolution equations are nondimensionalized by the depth of the potential well, i.e. a coefficient "a", and the system is isothermal. η=0 is assumed to compare the numerical result with its analytical solution. Then the evolution equations in one-dimensional case are

$$\tau_\phi \frac{\partial \phi}{\partial t} = \varepsilon_\phi^2 \frac{d^2\phi}{dx^2} + 1 - \phi - 2s(1+\phi)\left|\frac{d\alpha}{dx}\right| \tag{C.5.2}$$

$$\tau_\alpha (1+\phi)^2 \frac{\partial \alpha}{\partial t} = s\frac{d}{dx}\left[(1+\phi)^2 \frac{d\alpha/dx}{|d\alpha/dx|}\right] \tag{C.5.3}$$

Steady solution of the above two equations is calculated by setting L.H.S. of the equations to be zero, and imposing the following Dirichlet boundary conditions.

$$\phi(\pm\infty)=1$$
$$\alpha(\pm\infty)=\pm\frac{\pi}{3} \tag{C.5.4}$$

Without going to details (see [24] for more details), the analytical solution is given by

$$\phi(x)=1-\frac{(1-\phi_0)}{2}\exp\left\{-\frac{|x|}{\varepsilon_\phi}\right\}$$
$$\alpha(x)=\begin{cases}\alpha_- & \text{for } -\infty<x<0\\ \alpha_+ & \text{for } 0<x<+\infty\end{cases} \tag{C.5.5}$$

where $\phi_0=\phi(0)$, and it is represented by

$$\phi_0=\frac{1-\Theta}{1+\Theta},\quad \Theta\equiv\frac{s\Delta\alpha}{\varepsilon_\phi} \tag{C.5.6}$$

Since basically ε_ϕ determines a diffuse interface thickness of ϕ, phase-field value at the center of the grain boundary, i.e. at x=0, depends on a parameter s and orientation mismatch $\Delta\alpha$. This is because $|\nabla\alpha|\neq 0$ reduces rate change of ϕ from eq.(C.5.2).

Now transient numerical simulation of eq.(C.5.2) and (C.5.3) is performed. Same parameter settings as Warren et al.[24] are used as s=1.0, ε_ϕ=0.01, γ=10^3, τ_ϕ=1.0, and τ_α=0.1. Calculation domain is defined in -0.5≤x≤0.5, and it is discretized by 100 computational grids. Δt=1.0x10^{-4} is defined, and the simulation is performed up to 10000 computational time steps. As shown in Figure C. 2, a numerical solution (solid line) corresponds well with an analytical solution given by eq.(C.5.5) for both phase-field and orientation field.

As a side note, if an explicit time stepping scheme is used to solve eq.(C.5.2) and (C.5.3), time increment has to be less than Δt=1.0x10^{-10} to obtain stable solution for this problem. That is not suitable to perform two-dimensional polycrystalline phase-field simulation.

C.6 Example: Multi Grain Growth with Thermal Noise

An introduction of thermal noise would be suitable to obtain more complex grain structure. Although an effect of the thermal noise is not mentioned in the paper [24], the term is introduced to perform a simulation of multiple grain growth by KWC phase-field model in this section. The simulation is for the check purpose of an availability of the noise term in the model.

Initially, 20 solid seeds are randomly allocated within a computational domain whose size is 2401x2401. Orientations are also assigned randomly to the seeds such that the value stays in the range of $-\pi/4 \leq \alpha \leq \pi/4$. $\Delta x/W_0=0.4$, $D=3.0$, $d_0/W_0=0.185$, $\varepsilon=0.05$, and $\Delta=0.55$ are set as the operating conditions. $F_u=1.0\text{x}10^{-3}$ is used as a strength of the thermal noise. Flux free boundary condition is imposed for phase-field, temperature, and orientation evolution equation. A cooling term represented in eq.(4.1.12) is arbitrary set to be $c=10$ and $\theta_0=-0.2$, and the term is activated after $t/\tau_0=550$.

As shown in Figure C. 4, multiple fluctuated dendrites evolve their structure, and impingements on each other take place after some time steps. Since dendrites have complex interface structure, formed grain boundaries also represented by complicated jagged lines, i.e. panels at $t/\tau_0=600\sim1000$. Once grain boundary is formed, diffusion process of orientation among impinging grains is observed. Some grains rotate and match their orientation to that of their neighbor.

From the above simulation result, thermal noise should be incorporated in the KWC phase-field model.

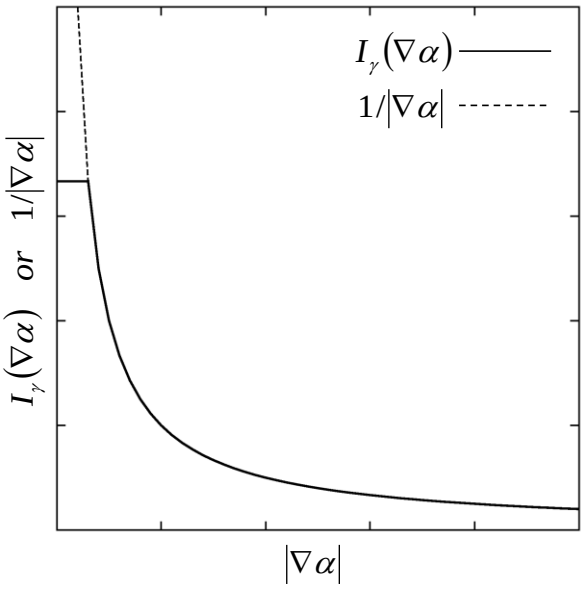

Figure C. 1 A schematic of cut-off inverse function; A dashed line represents an original function of $1/|\nabla\alpha|$ whereas a solid line plots the cut-off inverse function I_y; The original function is cut off at a sufficiently large value γ_{lim}.

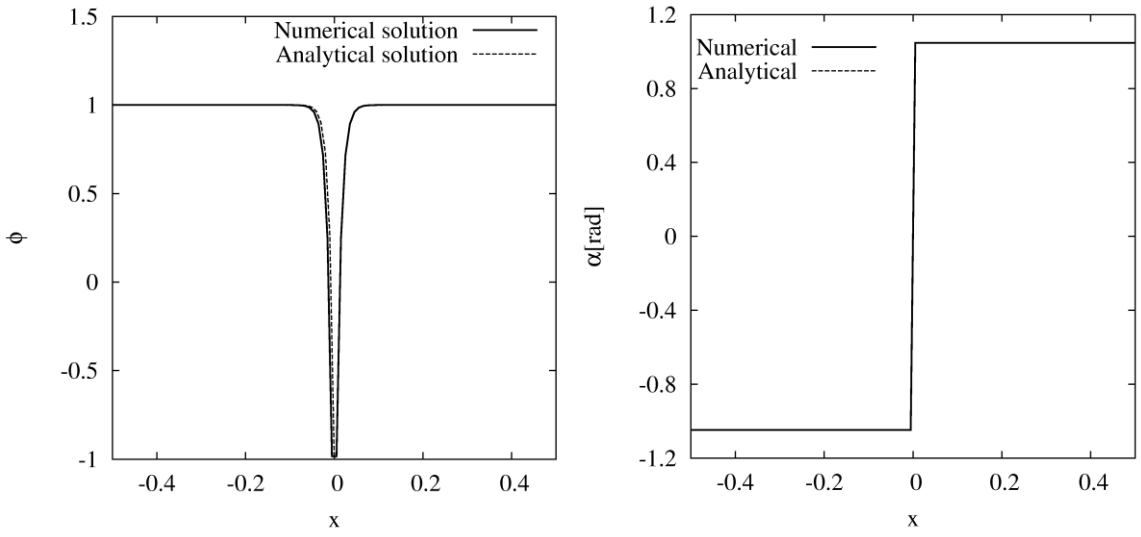

Figure C. 2 Line profiles of phase-field (left panel) and orientation field (right panel) of one-dimensional dry boundary validation problem; Solid and dashed line represent a numerical solution and an analytical solution, respectively.

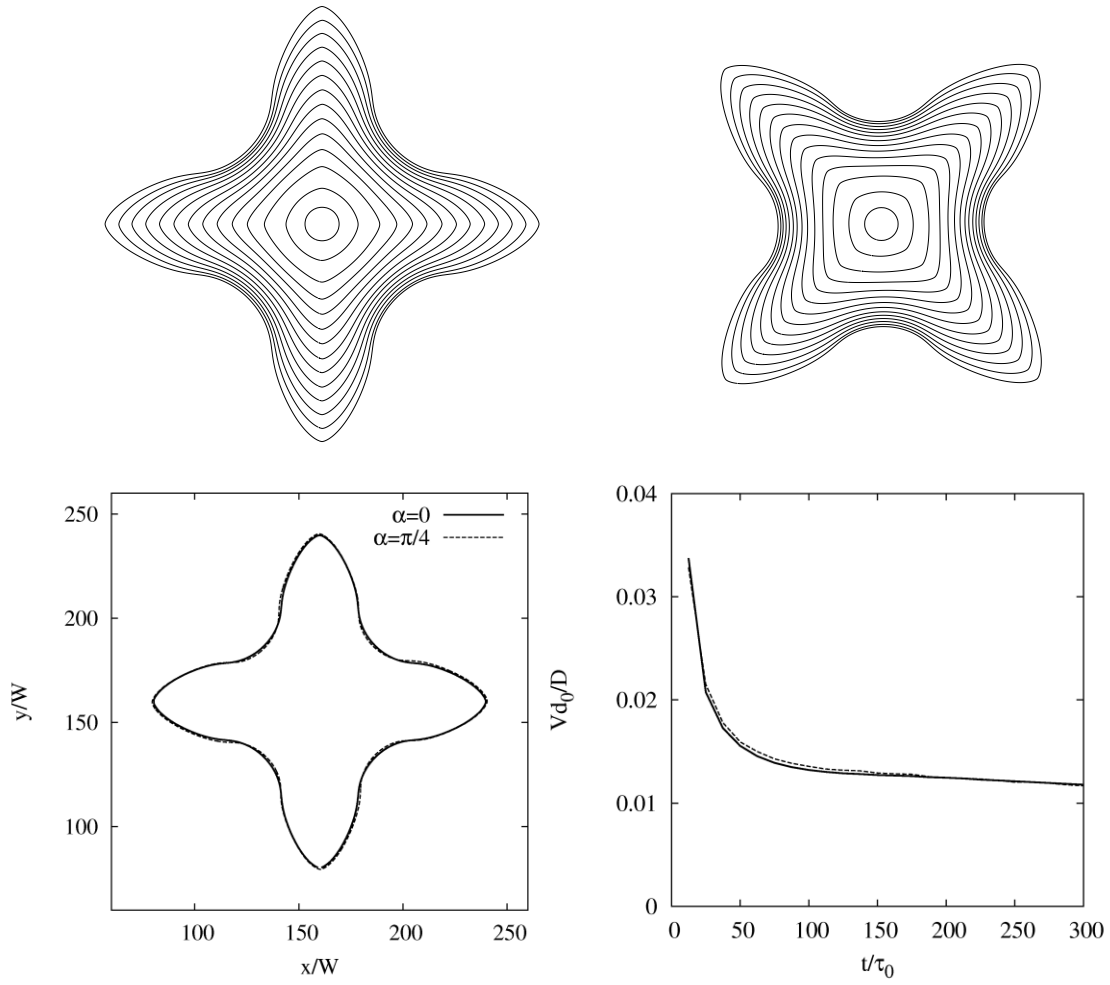

Figure C. 3 Time evolution of ϕ=0 contours at every 2500 steps for α=0 (upper left panel) and $\alpha=\pi/4$ (upper right panel); Lower left panel: comparison of ϕ=0 contours of α=0 and $\alpha=\pi/4$ at 25000 steps; lower right panel: a time history of dimensionless tip velocity.

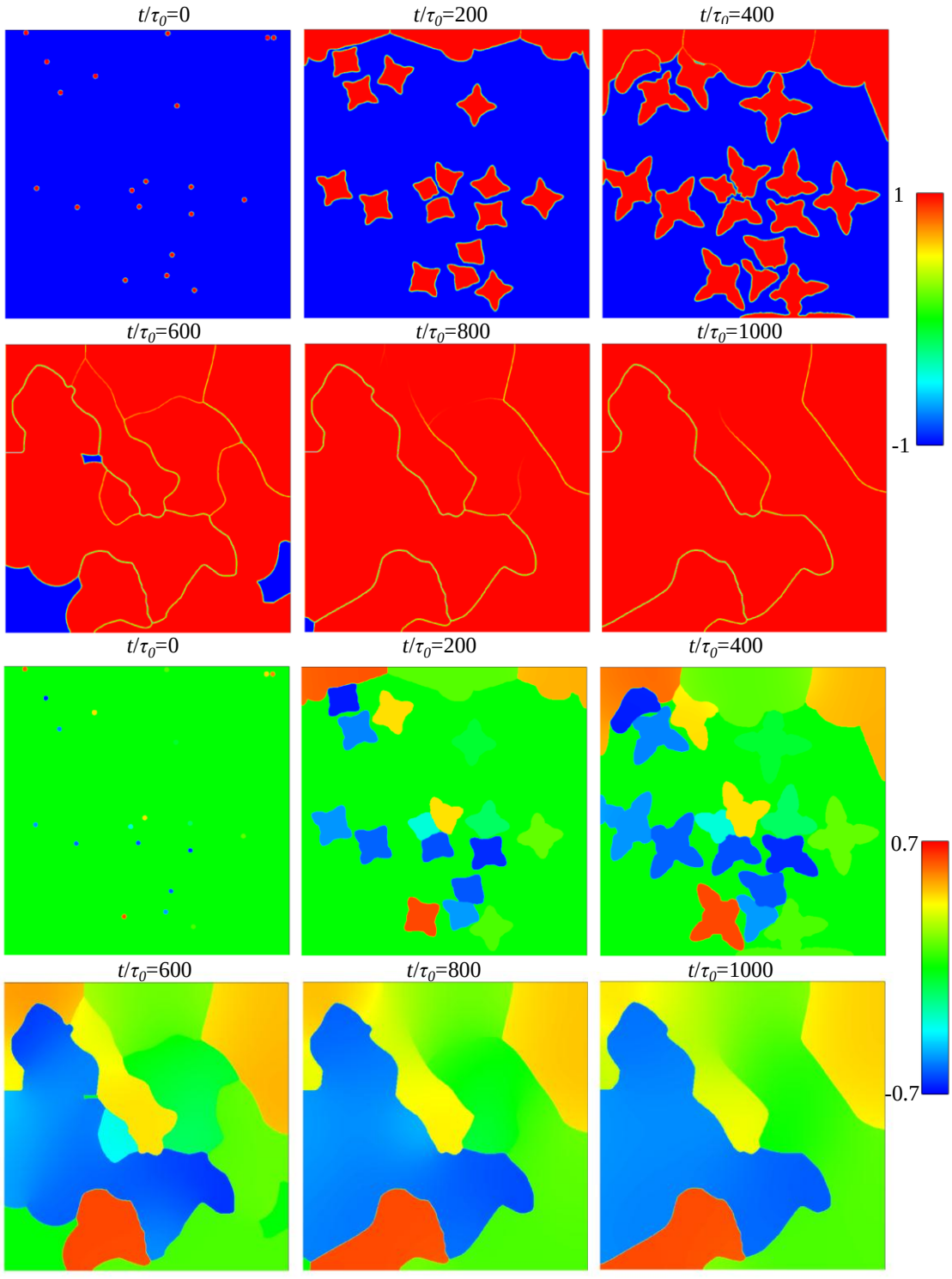

Figure C. 4 Multiple grain growth simulation with thermal noise by polycrystalline phase-field model; Upper panels: phase-field; Lower panels: crystallographic orientation; 20 seeds are randomly allocated, and orientation is assigned to them randomly at initial state.

REFERENCES

[1] J. A. Dantzig and M. Rappaz. *Solidification*. CRC press, 2009.

[2] M. Flemings. Behavior of metal alloys in the semisolid state. *Metall. Mater. Trans.*, 22B:269-293, 1991.

[3] Y. Sun. Phase-field simulation of microporosity formation in solidification. PhD thesis, The University of Iowa, 2006.

[4] A. Tewari M. Dighe, and A. M. Gokhale. Quantitative characterization of spatial arrangement of micropores in cast microstructures. Mater. Charact., 40:119-132, 1998.

[5] T. Kajitani, J. M. Drezet, and M. Rappaz. Numerical simulation of deformation-induced segregation in continuous casting of steel. *Metall. Mater. Trans. A*, 32A:1479-1491, 2001.

[6] B. Billia, J. Gastaldi, H. Nguyen-Thi, T. Schenk, G. Reinhart, N. Mangelinck, B. Grushko, H. Klein, J. Hartwig, and J. Baruchel. Growth structures, interface dynamics and stresses in metallic alloy solidification : in situ synchrotron X-ray Characterisation. *Trans. Indian Inst. Met*., 60:287-291, 2007.

[7] G. Reinhart, A. Buffet, H. Nguyen-Thi, B. Billlia, H. Jung, N. Mangelinck, N. Bergeon, T. Schenk, J. Hartwig, and J. Baruchel. In-situ and real-time analysis of the formation of strain and microstructure defects during solidification of Al-3.5 wt pct Ni alloys. *Metall. Mater. Trans. A*, 39A:865-874, 2008.

[8] M. G. Pokorny, C. A. Monroe, C. Beckermann, Z. Zhen, and N. Hort. Simulation of stresses during casting of binary magnesium-alminum alloys. *Metall. Mater. Trans. A*, 41A:3196-3207, 2010.

[9] S.Terzi, L. Salvo, M. Suery, N. Limodin, J.Adrien, E. Maire, Y. Pannier, M. Bornert, D. Bernard, M. Felberbaum, M. Rappaz, and E. Boller. In situ X-ray tomography observaion of inhomogeneous deformation in semi-solid aluminum alloys. *Scripta Mater.*, 61:449-452, 2009.

[10] L. A. Lalli. A model for deformation and segregation of solid-liquid mixtures. *Metall. Trans. A*,16A:1393-1403, 1985.

[11] C. A. Monroe. A modeling and experimental study of deformation and hot tearing in steel. PhD thesis, The University of Iowa, 2008.

[12] A. B. Phillion, S. L. Cockcroft, and P. D. Lee. A three-phase simulation of the effect of microstructural features on semi-solid tensile deformation. Acta Mater. 56:4328-4338, 2008.

[13] D. Fuloria and P. D. Lee. An X-ray microtomographic and finite element modeling approach for the prediction of semi-solid deformation behaviour in Al-Cu alloys. *Acta Mater*. 57:5554-5562, 2009

[14] S. O. Unverdi and G. Tryggvason. A front-tracking method for viscous, incompressible, multi-fluid flows. *J. Comput. Phys*.100:25-37, 1992.

[15] C. Hirt and B. Nichols. Volume of fluie (VOF) method for the dynamics of free boundaries. *J. Comput. Phys*. 39:201-225, 1981.

[16] S. Osher and R. Fedkiw. *Level set methods and dynamic implicit surfaces*. Springer, 2003.

[17] R. Fedkiw, T. Aslam, B. Merriman, and S. Osher. A non-oscillatory Eulerian approach in interfaces in multimaterial flows (the ghost fluid method). *J. Comput. Phys*.152:457-492, 1999.

[18] R. Kobayashi. Modeling and Numerical Simulations of Dendritic Crystal Growth. *Physica D*.63:410-423, 1993.

[19] A. Karma and W. J. Rappel. Quantitative phase-field modeling of dendritic growth in two and three dimensions. *Phys. Rev. E*.57:4323-4349, 1998.

[20] M. Plapp and A. Karma. Eutectic colony formation: a phase-field study. *Phys. rev. E*. 66:061608, 2002

[21] S. L. Wang, R. F. Sekerka, A. A. Wheeler, B. T. Murray, S. R. Coriell, R. J. Braun, and G. B. McFadden. Thermodynamically-consistent phase-field models for solidification. *Physica D*.69:189-200, 1993.

[22] T. Uehara, M. Fukui, and N. Ohno. Phase field simulations of stress distributions in solidification structures. *J. Cryst. Growth*.310:1331-1336, 2008.

[23] A. C. Powell, IV, and D. Dussault. Floating Solids : Combining Phase Field and Fluid-Structure Interactions. *Appl. Num. Anal. Comp. Math*. 2:157-166, 2005.

[24] J. A. Warren, R. Kobayashi, A. E. Lobkovsky, and W. C. Carter. Extending phase field models of solidification to polycrystalline materials. *Acta Mater*. 51:6035-6058, 2003.

[25] J. Berry, K. R. Elder, and M. Grant. Melting at dislocations and grain boundaries: A phase field crystal study. *Phys. Rev. B*.77:224114, 2008.

[26] R. A. Gingold and J. J. Monaghan. Smoothed particle hydrodynamics: theory and application to non-spherical stars. *Mon. Not. R. Astron. Soc*. 181:375-389, 1977.

[27] T. Belytschko, Y. Y. Lu, and L. Gu. Element free galerkin method. *Int. J. Numer. Methods Eng*. 37:229-256, 1994.

[28] C. Anderson and C. Greengard. On vortex methods. *SIAM J. Numer. Anal*. 22:413-440, 1985.

[29] J. U. Brackbill and H. M. Ruppel (1986). FLIP: A method for adaptive ly zoned, particle-in-cell calculations in two dimensions. *J. Comput. Phys*. 65:314-343, 1986.

[30] D. Sulsky, Z. Chen, and H. L. Schreyer. A particle method for history-dependent materials. *Comput. Methods Appl. Mech. Engrg*. 118:179-196, 1994.

[31] O. Borodin, D. Bedrov, G. D. Smith, J. Nairn, and S. Bardenhagen. Multiscale modeling of viscoelastic properties of polymer nanocomposites. *J. Polym. Sci*. 43:1005-1013, 2005

[32] I. Ionescu, J. E. Guilkey, M. Berzins, R. M. Kirby, and J. A. Weiss. Simulation of soft tissue failure using the material point method. *J. Biomech. Eng*. 128:917-924, 2006.

[33] S. G. Bardenhagen, J. U. Brackbill, and D. Sulsky. The material point method for granular materials. *Computer Methods Appl. Mech. Eng*. 187:529-541, 2000.

[34] J. E. Guilkey, T. Harman, A. Xia, B. Kashiwa, and P. McMurtry. An Eulerian-Lagrangian approach for large deformation fluid structure interaction problems, part 1: algorithm development. *Proc. 2nd Inter. Conf. on Fluid-Structure Interactions*, 2003.

[35] N. P. Daphalapurkar, H. Lu, D. Coker, and R. Komanduri. Simulation of dynamic crack growth using the generalized interpolation material point (GIMP) method. Int. J. Fract. 143:79-102, 2007.

[36] L. Beuth, T. Benz, and P. A. Vermeer. Large deformation analysis using a quasi-static material point method. *J. Theor. Appl. Mech*. 38:45-60, 2008.

[37] D. J. Benson. Computational methods in Lagrangian and Eulerian hydrocodes. *Comput, Method. Appl. M*. 99:235-394, 1992.

[38] O. C. Zienkiewicz and R. L. Taylor. *The finite element method volume 2 solid mechanics 5th edition*. Butterworth heinemann, 2000.

[39] R. D. Kreig and D. B. Kreig. Accuracies of numerical solution methods for the elastic-perfectly plastic model. *J. Pressure Vessel Technol*. 99:510-515, 1977.

[40] J. C. Simo and T. J. R. Hughes. *Computational inelasticity*. Springer-Verlag New York, Inc., 1997.

[41] Y. Sun and C. Beckermann. Sharp interface tracking using the phase-field equation. *J. Comput. Phys*. 220:626-653, 2007.

[42] H. Takewaki, A. Nishiguchi, and T. Yabe. Cubic Interpolated Pseudo-particle method for solving hyperbolic-type equation. *J. Comput. Phys*.61:261-268, 1985.

[43] F. Gibou, R.P. Fedkiw, L.Cheng, and M. Kang. A second-order-accurate symmetric discretization of the Poisson equation on irregular domains. *J. Comput. Phys*.176:205-227,2002.

[44] X. Tong, C. Beckermann, A. Karma, and Q. Li. Phase-field simulations of dendritic crystal growth in a forced flow. *Phys. Rev. E*.63:061601, 2001.

[45] S.G. Bardenhagen. Energy conservation error in the material point method for solid mechanics. *J. Comput. Phys*.180:383-403,2002.

[46] O. Buzzi, D.M. Pedroso, and A. Giacomini. Caveats on the implementation of the generalized material point method. *CMES*.1:1-21,2008.

[47] S.G. Bardenhagen and E.M. Kober. The generalized interpolation material point method. *CMES*.5:477-495,2004.

[48] H. Kolsky. *Stress waves in solids*. Oxford university press, 1953.

[49] D. Sulsky and H.L. Schreyer. Axisymmetric form of the material point method with applications to upsetting and Taylor impact problem. *Comput. Methods Appl. Mech. Engrg*.139:409-429,1996.

[50] R. Kobayashi, J.A. Warren, and W.C. Carter. Vector-valued phase field model for crystallization and grain boundary formation. *Physica D*.119:415-423,1998.

[51] I. Steinback, F. Pezzolla, B. Nestler, M. Seebelberg, R. Prieler, G.J. Schmitz, and J.L.L. Rezende. A phase field concept for multiphase systems. *Physica D*.94:135-147,1996.

[52] C. III Krill, and L. Chen. Computer simulation of 3-d grain growth using phase-field model. *Acta Mater*.50:3057-3073,2002.

[53] W. Hu and Z. Chen. A multi-mesh MPM for simulating the meshing process of spur gears. *Comput. Struct*.81:1991-2002,2003.

[54] P. Huang, X. Zhang, S. Ma, and X. Huang. Contact algorithms for the material point method in impact and penetration simulation. *Int. J. Numer. Meth. Engng*.85:498-517,2011.

[55] J.H. Ferziger and M.Peric. Computational methods for fluid dynamics 3rd edition. Springer. 2002.

[56] E. Stein, Rene de Borst, and T. J.R. Hughes. Encyclopedia of Computational Mechanics, volume 1 : Fundamentals. John Wiley & Sons, Ltd., 2004.

[57] D.M. Ingram, D.M. Causon, and C.G. Mingham. Developments in Cartesian cut cell methods. *Math. Comput. Simulat*.61:561-572,2003.

[58] M.G. Pokorny, C.A. Monroe, C. Beckermann, Z. Zhen, and N. Hort. Simulation of stresses during casting of binary magnesium-alminum alloys. *Metall. Mater. Trans. A*.41A:3196-3207,2010.

[59] A. Karma and W.J. Rappel. Phase-field model of dendritic sidebranching with thermal noise. *Phys. Rev. E.* 60:3614-3625,1999.

[60] P. Perzyna. Fundamental problems in viscoplasticity. *Advances in Applied Mechanics*. 9:243, 1966.

[61] W. Kurz and D.J. Fisher. *Fundamentals of solidification fourth revised edition*. Trans tech publications,1998.

[62] I. Ionescu, J.E. Guilkey, M. Berzins, R.M. Kirby, and J.A. Weiss. Simulation of soft tissue failure using the material point method. *J. Biomech. Eng-T. ASME*.128:917-924, 2006.

[63] R.S. Busk. *Magnesium Products Design*. Mareel Dekker Inc., New York, NY, 1987.

[64] M.Bauser, G.Sauer, and K. Siegert. *Extrusion second edition*. ASM international,2006.

[65] G.E.P. Box and M.E. Muller. A note on the generation of random normal deviates. *Ann. math. statist*.29:610-611,1958.

[66] J. Chakrabarty. *Theory of plasticity*. McGraw-Hill, 1987.

[67] R.W.Klopp, R.J. Clifton, and T.G. Shawki. Pressure-shear impact and the dynamic viscoplastic response of metals. *Mech. Mater*.4:375-385,1985.

[68] R. Kobayashi and Y. Giga. Equations with singular diffusivity. *J. Stat. Phys*.95:1187-1220,1999.

[69] W.T. Read and W. Shockley. Dislocation models of crystal grain boundaries. *Phys. Rev*. 78:275-289, 1950.

[70] G. Gottstein and L.S. Shvindlerman. *Grain boundary migration in metals 2nd edition*. CRC press,2010.

[71] L. Andersen, S.M. Andersen, and L. Damkilde. Selective integration in the material-point method. *Proceedings of the twenty second nordic seminar on computational mechanics*.125-128,2009.

[72] S.P. Timoshenko and J.N. Goodier. *Theory of elasticity third edition*. McGraw-Hill,1970.

[73] S. Andersen and L. Andersen. Analysis of spatial interpolation in the material-point-method. *Comput. Struct*. 88:506-518,2010.

[74] J. Dolbow and T. Belytschko. An introduction to programming the meshless element free Galerkin method. *Arch. Comput. Method E*. 5:207-241,1998.

[75] ANSYS, Inc. *ANSYS Commands Refference,* ANSYS Release 12.0,2009.

[76] Y. Sun and C. Beckermann. Effect of solid-liquid density change on dendrite tip velocity and shape selection. *J. Cryst. Growth*.311:4447-4453,2009.

[77] K. Dragnevski, A.M. Mullis, D.J.Walker, and R.F.Cochrane. Mechanical deformation of dendrites by fluid flow during the solidification of undercooled melts. *Acta Mater*. 50:3743-3755,2002.

[78] H. Garabedian and R.F. Strickland-Constable. Collision breeding of ice crystals. *J. Cryst. Growth*. 22: 188-192,1974.

[79] Y. Sun and C. Beckermann. Diffuse interface modeling of two-phase flows based on averaging mass and momentum equations. *Physica D*. 198:281-308,2004.

[80] T. Aoki and T. Yabe. Multi-dimensinal cubic interpolation ICF hydrodynamics simulation. *National Institute for fusion science.* NIFS series, NIFS-082, 1991.

[81] T. Yabe, T. Utsumi, and Y. Ogata. *CIP method* [in Japanese]. Morikita, 2003.

[82] R. Kobayashi and J.A. Warren. Modeling the formation and dynamics of polycrystals in 3D. *Physica A*. 356:127-132,2005.

[83] A. Gilmanov and S. Acharya. A hybrid immersed boundary and material point method for simulating 3D fluid-structure interaction problems. *Int. J. Numer. Meth. Fluid*. 56:2151-2177,2008.

[84] H. Tan and J.A. Nairn. Hierarchical, adaptive, material point method for dynamic energy release rate calculations. *Comput. Methods Appl. Mech. Engrg*. 191:2095-2109,2002.

[85] J.H. Jeong, N. Goldenfeld, and J.A. Dantzig. Phase field model for three-dimensional dendritic growth with fluid flow. *Phys. Rev. E*. 64:041602, 2001.

[86] G. Calilletaud, O. Diard, F. Feyel, and S. Forest. Computational crystal plasticity: from single crystal to homogenized polycrystals. *Technische Mechanik*. 23:130-145, 2003.